The Computations of Buoyant Fires and Fire Suppression

By

Heba Mustafa Ahmed Mohamed Mustafa

Under supervision of

Prof. Assaad R. Masri

Prof. Mattew Clearly

Dissertation submitted in fulfilment of the requirements
for the degree of
MASTER OF PHILOSOPHY

School of Aerospace, Mechanical and Mechatronic Engineering
The University of Sydney
Sydney, NSW 2006, Australia

July 2025

Statement of candidate

This is to certify that the content of this thesis, entitled "*The computations of buoyant fires and fire suppression*", is my own work during my Master of Philosophy candidature at the University of Sydney.

I certify that this thesis has not been submitted for any degree or other purposes.

I certify that the intellectual content of this thesis is the product of my own work and that all the assistance received in preparing this thesis and sources has been acknowledged.

……

Author: Heba Moustafa

Affectionately Dedicated

To

My first educators, my Dad and Mum, my beloved husband, Mohamed, and my adorable angels, Omar and Joudy

For their support, patience, and encouragement

That made this work possible

Acknowledgments

"وَقُلِ اعْمَلُوا فَسَيَرَى اللَّهُ عَمَلَكُمْ وَرَسُولُهُ وَالْمُؤْمِنُونَ"

First and foremost, I extend my heartfelt gratitude to God, Allah, for granting me the strength, patience, and opportunity to reach this milestone and complete this work in the field I am most passionate about.

I would like to express my sincere appreciation to those who have left a profound impact and a lasting imprint on my soul, my beloved mother Samia and my beloved father Mustafa. No words can truly capture the depth of my gratitude for their unwavering love, encouragement, and belief in me as I pursued my dreams.

I am deeply grateful to my supervisor, Professor Assaad Masri, for his invaluable guidance, steadfast support, and dedicated mentorship throughout the course of my Master's studies. His passion for research and academic excellence has been a constant source of inspiration. I am especially thankful to him for believing in me and giving me the opportunity to undertake this work. Without his encouragement, insight, and expertise, this research would not have been possible. I also extend my gratitude to members of USYD combustion team, more specifically the experimental team. This research reported in this thesis was supported by the award of a Research Training Program scholarship.

I would also like to sincerely thank my former manager, Mohamed Imran Sindauh, for his continuous support and the flexibility he provided. I am also thankful to the many senior engineers I have had the privilege to work with throughout my career.

Last, and most importantly, my deepest appreciation goes to my husband, Mohamed, for his unwavering encouragement, motivation, and belief in me. His support gave me light on the hardest days and inspired me to reach new heights and complete my Master's degree. To my beloved children, Omar and Joudy, your love and belief in me have been a powerful source of strength. You may be young, but your patience, understanding, and smiles gave me the courage to persevere through long nights and demanding days.

Finally, it is my sincere hope that the findings and contributions of this thesis will serve a meaningful purpose beyond the academic realm. I aspire for this work to contribute, even in a small way, to the advancement of fire safety practices and technologies. If, in the future, it helps protect lives or minimise the devastating impact of fire-related incidents, then I will consider this endeavour truly worthwhile and fulfilling.

Abstract

This thesis presents a comprehensive computational study of buoyant turbulent diffusion flames and water-based fire suppression, using a novel burner configuration developed at the University of Sydney. The research aims to advance current fire modelling practices by capturing the full progression of fire development from turbulence-enhanced flame formation to suppression dynamics. A key focus is placed on resolving the complex interplay between turbulence, combustion, and suppression effectiveness, particularly under varying injection strategies.

To validate the modelling framework, benchmark simulations of Sandia Flame D were performed using the ReactingFoam solver. The results demonstrated good agreement with experimental data and established the baseline performance of the numerical approach. The study then introduces the USYD Burner, a newly developed platform featuring a recessed perforated plate that enables controlled modulation of fuel-side turbulence without altering heat release rate. Numerical simulations using ANSYS Fluent and FireFOAM were conducted under both laminar and enhanced turbulence conditions, revealing clear changes in flame structure, mixing intensity, and velocity fields.

The study further explores suppression mechanisms using FireFOAM, where water mist is introduced through both top and bottom injection configurations. Large Eddy Simulation (LES) was employed to resolve the unsteady flow structures and accurately capture droplet flame interactions. Detailed injection parameters including droplet size distribution, mass flow rate, and injection direction were varied to evaluate their influence on suppression performance.

Overall, the simulations demonstrate that suppression effectiveness is highly dependent on aligning mist dynamics with flame structure and turbulence characteristics. The use of the USYD Burner allowed for precise boundary condition control and enhanced understanding of flame droplet interactions. This work contributes to the development of predictive fire suppression

models and provides a validated platform for future investigation of chemically enhanced mist systems and advanced suppression strategies.

Table of Contents

Table of Figures

1 Introduction

1.1 Background

Fire is a complex phenomenon arising from chemical reactions between fuel and oxygen, leading to the release of heat, light, and combustion products. While fire has played a critical role in human civilisation- producing warmth, light, and enabling industrial advancement, it has also posed severe risks when uncontrolled. Fires continue to cause substantial loss of life, property damage, and disruption across both urban and industrial environments. [5, 6]

In today's buildings, the complexity of building layouts, construction materials, and mechanical systems has introduced new challenges for fire safety engineering. Fires in these environments are influenced by the combined effects of heat transfer, fluid dynamics, combustion chemistry, and material response. Variables such as fuel composition, ventilation patterns, and the physical state of combustible materials can significantly alter how a fire ignites and propagates. For instance, solid fuels like timber exhibit different combustion behaviours compared to finely divided materials such as coal dust, which can become hazardous under certain conditions. This variability in fire dynamics highlights the need for a thorough understanding of key processes such as buoyancy-driven flow, turbulent mixing, and thermal radiation. [6, 7]

Among the most critical aspects of fire dynamics particularly in fires involving strong vertical heat release are buoyant turbulent flames, which occur when hot combustion gases rise due to density differences with the surrounding air. These flames are inherently unstable and highly sensitive to surrounding conditions. Their behaviour, structure, and development are governed by a complex interaction of turbulence, entrainment, radiation, and chemical kinetics, making them difficult to predict or control without advanced modelling techniques [5, 8, 9].

In recent years, computational fluid dynamics (CFD) [10] have become an indispensable tool in fire safety research. Numerical solvers such as ANSYS Fluent [11] and OpenFOAM [12] **(**FireFOAM and ReactingFOAM**)** offer the capability to simulate flame behaviour, combustion processes, and suppression mechanisms under a range of scenarios. Much of the current research isolates each stage of fire development, focusing separately on turbulence generation, flame propagation, or suppression effectiveness.

1.1.1 Fuel Types and Fire Behaviour

The nature of the fuel involved in combustion has a critical influence on the characteristics and progression of a fire. Different fuel types, solid, liquid, and gaseous exhibit distinct behaviours due to variations in physical state, volatility, heat of combustion, and how they mix with oxidisers. [5, 6]

Solid fuels, such as wood, plastics, or coal, typically undergo pyrolysis before combustion, with heat first decomposing the material to release flammable gases. The rate of heat transfer into the material, surface area, and thermal properties of the solid significantly affect ignition and flame spread. [6, 8, 13]

Liquid fuels, including hydrocarbons like gasoline, diesel, and ethanol, can form pool fires when spilled. Their combustion behaviour depends on volatility, boiling point, and evaporation rate. The vapour generated above the liquid surface mixes with air and ignites, producing diffusion flames. These fires are often intense, with high heat release rates and visible sooty flames. The spread of burning liquid over surfaces or through drainage systems poses unique suppression and containment challenges.[6]

Gaseous fuels, such as methane, propane, and hydrogen, are highly flammable and can form explosive mixtures with air. Their combustion tends to occur as premixed or diffusion flames depending on the mixing conditions. [6]

Each fuel type influences the flame structure, turbulence characteristics, heat transfer, and ultimately, the suppression strategy required. A thorough understanding of these behaviours is essential for developing accurate fire models and designing reliable mitigation systems in both open and confined environments.[14]

1.1.2 Environmental Influence on Fire Behaviour

While the characteristics of the fuel are critical in shaping fire behaviour, they do not act in isolation. Environmental conditions, including ambient temperature, ventilation, humidity, atmospheric pressure, and the geometry of the surrounding space, also play a significant role in how a fire ignites, spreads, and evolves. These variables influence key outcomes such as flame shape, thermal feedback, smoke movement, and the overall energy release rate [14, 15].

In both open and enclosed settings, the combined effect of these conditions can significantly alter fire growth and suppression outcomes. Capturing these environmental influences accurately is essential in computational fire modelling. Parameters such as boundary temperatures, inlet and outlet flow conditions, and radiation losses must be carefully defined to reflect real-world settings. The ability to model fire and environment interactions becomes especially important in cases where suppression systems must operate under variable or unpredictable conditions. Responding to these challenges, fire safety engineering has undergone substantial development in recent decades.

1.1.3 Fire Safety Advancements

Over the past several decades, significant advancements have been made in fire safety engineering. Improvements in building codes, materials, fire detection, and active suppression systems have reduced fire-related fatalities and property loss. However, as built environments become more complex, traditional prescriptive approaches are often insufficient. [6]

A performance-based approach, grounded in fire science and engineering principles, has increasingly been adopted. This shift relies on a deeper understanding of fire dynamics, combustion processes, heat transfer, fluid flow, and smoke movement as well as the interactions between fire and building systems. [14, 16]

Computational modelling plays a central role in this modern approach. Tools such as ANSYS Fluent and FireFOAM enable engineers to simulate various fire scenarios, assess the behaviour of flames under different conditions, and evaluate the performance of suppression systems. These models can incorporate turbulence, combustion chemistry, radiation, and multiphase flow in both confined and open environments.

1.1.4 Development of Fire Science

The scientific investigation of fire behaviour has historically relied on the advancement of mathematical and physical theories that describe combustion and heat transfer phenomena. Foundational contributions from several key scientific figures laid the groundwork for the emergence of fire science as a formal discipline. [6]

1 **Isaac Newton (17th century):**

Newton's laws of motion and universal gravitation established the theoretical basis for fluid dynamics, which is essential for analysing the movement of hot gases and flame propagation during a fire.

2 **Daniel Bernoulli (1738):**

Bernoulli's principle, which describes the relationship between pressure and velocity in fluid flow, provided critical insights into how fires influence and are influenced by surrounding airflow, including smoke and heat movement.

3 **Joseph Fourier (1822):**

Fourier's formulation of the heat conduction equation laid the foundation for understanding how thermal energy is transferred through solid materials, an essential aspect of predicting fire growth and structural response to heat.

4 **Ludwig Boltzmann (1872):**

Boltzmann's work in statistical mechanics contributed to the understanding of particle behaviour at the molecular level, offering fundamental insights into the processes underlying combustion reactions.

While these theoretical advancements were not initially intended for fire analysis, they later became essential tools in combustion science, enabling the development of models for flame propagation, heat transfer, and smoke movement. The increasing need for fire safety in industrialised societies eventually transformed combustion research into a more applied and multidisciplinary field.

The twentieth century witnessed substantial progress in fire safety and combustion modelling, with increased emphasis on understanding ignition, flame spread, and extinguishment mechanisms. Researchers such as Zeldovich, Semenov, and Damköhler advanced the study of flame structures and reaction kinetics, bridging theoretical combustion science with practical fire behaviour.

This era also saw the institutionalisation of fire safety through organisations such as the National Fire Protection Association (NFPA) and Underwriters Laboratories (UL). These

bodies were pivotal in developing fire safety standards and promoting systematic fire protection practices across residential, commercial, and industrial applications.

Despite ongoing funding challenges, these foundational developments continue to shape and improve fire safety engineering today. Their influence extends into the computational era, where tools such as Fire Dynamics Simulator (FDS) and FireFOAM incorporate the principles of fluid dynamics, heat transfer, and combustion to model complex fire scenarios.

1.2 Research Motivation

Understanding and predicting fire behaviour is a critical priority in both urban and industrial settings. The evolving complexity of modern infrastructure presents challenges that exceed the capabilities of conventional prescriptive fire protection methods, particularly in predicting and managing advanced fire behaviours. Fires involving buoyant turbulent flames present particular challenges due to their unstable nature and sensitivity to environmental conditions. These flames exhibit complex interactions between turbulence, combustion chemistry, heat transfer, and suppression systems, making them difficult to study experimentally and even harder to control in real-world situations.

While advancements in computational fluid dynamics (CFD) have enabled researchers to simulate individual components of fire behaviour such as turbulence generation, flame propagation, or suppression, most existing studies examine these phenomena in isolation attempts have been made to model the entire progression of a fire, from the initial turbulence-enhanced mixing, through flame development, to final suppression response, within a unified computational framework. This lack of integration limits our ability to fully visualise and understand the dynamics of fire as a system.

Furthermore, although experimental data from benchmark flames such as Sandia Flame D [1] and the Sydney burner [3] are available, they are typically used to validate only discrete

modelling stages. As a result, suppression models often do not account for the influence of upstream turbulence or burner geometry on suppression effectiveness creating a gap in both academic research and engineering application.

1.3 Computational Fire Modelling and Collaborative Research Efforts

1.3.1 Fire Dynamics Simulator (FDS) in Fire Research

The Fire Dynamics Simulator (FDS), developed by the National Institute of Standards and Technology (NIST), is one of the most established computational fluid dynamics (CFD) tools used in fire research. It is based on the Large Eddy Simulation (LES) approach and is specifically designed to simulate low-speed, thermally-driven flows associated with fire, smoke, and heat transfer.

Since its initial release in the early 2000s, FDS has been continually refined and validated against a wide range of experimental fire scenarios, supporting its use in both academic research and applied fire safety engineering.[17, 18] Across academic, governmental, and industrial sectors, FDS is commonly employed to analyse fire growth, smoke movement, sprinkler activation, and heat release.

To support the interpretation of simulation results, FDS is typically paired with Smokeview. Its dedicated visualisation tool used to display temperature fields, smoke layers, visibility, and other critical outputs.[19]

The reliability, open-access nature, and flexibility of FDS have contributed to its widespread use in performance-based design and its foundational role in global fire modelling initiatives. These attributes have also made FDS an important reference tool in community-driven benchmarking efforts such as the Measurement and Computation of Fire Phenomena (MaCFP) initiative, introduced in the next subsection.

1.3.2 Measurement and Computation of Fire Phenomena (MaCFP)

Significant progress in experimental techniques and computational modelling for fire research has been achieved over the past two decades. This progress builds on earlier international collaborations that date back to 1984, when leading researchers-initiated discussions that led to the establishment of the 1st International Symposium on Fire Safety Science, held in October 1985. The event also marked the founding of the International Association for Fire Safety Science (IAFSS), which continues to foster global research into fire dynamics and fire safety engineering.[11]

In support of community-driven model validation, the IAFSS launched the Measurement and Computation of Fire Phenomena (MaCFP) Working Group. The objective of MaCFP is to promote structured collaboration between experimentalists and computational modellers to identify knowledge gaps and develop a unified framework for assessing fire models. This initiative is endorsed by the IAFSS and operates through a series of open, international workshops [20].

The idea for the MaCFP initiative emerged during a session on benchmarking and data sharing held at the 11th IAFSS Symposium in 2014, where Professor Assaad Masri of the University of Sydney participated as a guest speaker. Following these discussions, a dedicated task group was established and formally recognised by the IAFSS in 2015 to support the creation of standard benchmark experiments for validating CFD fire models. This initiative guided the planning of the first MaCFP workshop held in Lund, Sweden, in 2017, and a second virtual event in 2021.[20]

The initial list of target experiments identified by the MaCFP Working Group includes five categories:

Category 1: Turbulent buoyant plumes; Key Focus: Buoyancy, turbulence (no combustion)

Category 2: Turbulent pool fires with gaseous fuel; Key Focus: Combustion of gaseous fuels

Category 3: Turbulent pool fires with liquid fuel; Key Focus: Evaporation, combustion, heat feedback

Category 4: Turbulent wall fires; Key Focus: Flame spread on vertical surfaces

Category 5: Flame extinction. Key Focus: Extinction, suppression, flame stability

The MaCFP data repository is publicly hosted on GitHub [21], providing open access to standardised experimental data and simulation results from participating modelling groups. The repository includes experimental descriptions, measurement uncertainties (where known), and structured ASCII datasets for direct use in model validation. The repository offers the experimental data in standard comma-delimited ASCII files, alongside simulation results submitted by participating modelling groups during the MaCFP-1 and MaCFP-2 workshops.

Among the canonical cases supported by MaCFP are the McCaffrey Flames and the Sandia Flames. The McCaffrey Flames[22] [23] are buoyant, turbulent diffusion flames generated from vertical, propane-fuelled burners under natural convection. These flames have been widely used to study plume behaviour, flame height, and centreline temperature across a range of heat release rates.

The Sandia Flames [1] are a set of non-premixed jet flame experiments conducted at Sandia National Laboratories. These cases provide high-resolution data for velocity, species concentration, and temperature, and serve as repeatable configurations for studying turbulent

mixing and combustion. Both datasets are included in the MaCFP repository and remain essential for benchmarking CFD models such as FDS and FireFOAM.

In addition to academic collaborations such as MaCFP, industrial organisations like **FM Global** have made substantial contributions to the advancement of computational fire modelling. A notable outcome of their research is the development and enhancement of FireFOAM [24], a solver within the OpenFOAM [12] framework specifically adapted for fire dynamics. FireFOAM integrates key physical phenomena including combustion**,** radiative heat transfer**,** turbulence**,** and suppression interactions**,** making it suitable for simulating realistic fire scenarios. FM Global's modelling strategy emphasises validation and benchmarking**,** with particular focus on sprinklered fires, flame suppression, and large-scale storage configurations. Their work has not only supported academic efforts such as MaCFP but has also been applied in practical engineering contexts to improve fire protection designs in industrial facilities.

1.3.3 Industrial Adoption and Support of the FireFOAM Solver

1.3.3.1 FM Global

FM Global is the principal developer of FireFOAM. Using the open-source OpenFOAM CFD toolkit as a base, FM Global created FireFOAM to simulate fire and explosion phenomena for loss-prevention research [25] FireFOAM serves as FM Global's flagship large-eddy simulation (LES) code for industrial fire scenarios.FM Global actively funds and maintains FireFOAM as part of its internal fire research program [26]

FM Global has actively collaborated with leading institutions to advance fire modelling. It partnered with Oak Ridge National Laboratory (ORNL) to run FireFOAM on high-performance computing platforms, including the Titan supercomputer, enabling large-scale simulations. ORNL experts helped optimise FireFOAM code, improving efficiency [27].

The National Institute of Standards and Technology (NIST) has acknowledged FM Global's FireFOAM development as beneficial to advancing NIST's own FDS fire model [28]

In 2011, the IAFSS Symposium [26] FM Global introduced FireFOAM to the scientific community through validation studies like "Large Eddy Simulation of Fire Plumes" (Yi Wang et al., Proc. Combustion Institute 2011) [29]. These case studies demonstrated FireFOAM ability to capture complex fire dynamics (combustion, soot, flame spread, suppression by sprinklers, etc.) in large-scale industrial scenarios. FM Global openly shares many of these research outcomes, aligning with its philosophy that improving fire modeling benefits industry. [12].

Oak Ridge National Laboratory [30] (ORNL) is a U.S. government research lab, not an industrial company, but it played a key supporting role by providing supercomputing resources and expertise to advance FireFOAM. ORNL's Oak Ridge Leadership Computing Facility (OLCF) granted FM Global access to the Titan supercomputer [31], simulations that had previously been considered computationally infeasible[27]. The success on Titan underscored

FireFOAM readiness for large-scale industrial fire scenarios (e.g. multi-story warehousing fires), bolstering confidence for other organizations to use FireFOAM for complex problems [32] [33].

1.3.3.2 RISE Fire Research (Sweden) – Validation for Industry Use

RISE Fire Research [34] [35](SP Fire Technology in Sweden) is an industrial-oriented research institute that has explored FireFOAM for fire safety engineering. RISE, together with Lund University, undertook independent verification and validation of FireFOAM as a tool for performance-based design in fire protection[36]. This project was funded by Swedish industry research funds to evaluate whether FireFOAM could be reliably used by fire consulting firms.

1.3.4 University of Maryland –in Fire Modelling and Research

The University of Maryland (UMD), through its Department of Fire Protection Engineering, has played a leading role in advancing fire modelling and experimental validation over the past decade. Since 2014, UMD has been at the forefront of collaborative research, particularly through the work of Professor Arnaud Trouvé and his group, who have been actively involved in the MaCFP (Measurement and Computation of Fire Phenomena) initiative. This effort, conducted in collaboration with UL Fire Safety Research Institute (UL FSRI) and other academic and government partners, focuses on validating fire models with laboratory-scale data including the McCaffrey buoyant plume and Sandia CH_4-air diffusion flames[22, 37]

UMD has contributed numerical datasets and modelling results to MaCFP workshops (2017, 2021), helping assess the performance of LES-based solvers such as FireFOAM and FDS in replicating complex fire behaviour. [20, 38, 39]

These contributions from the University of Maryland have played role in building computational knowledge and experimental foundations within the field of fire safety. Alongside international collaborations, such as MaCFP and projects with UL FSRI, these initiatives have helped shape a more integrated fire science community.

1.4 Gap Analysis

Significant progress has been made in the field of fire modelling through international efforts such as the Measurement and Computation of Fire Phenomena (MaCFP) initiative and large-scale industrial collaborations like those led by FM Global. These efforts have focused on computing the structure of buoyant flames under laboratory-controlled conditions, offering valuable benchmark datasets for validating numerical models.

While extremely useful, none of the burners studied refer to flames under controlled fuel turbulence. This is a significant gap considering the relevance of fuel turbulence in fire scenarios.

This thesis addresses these gaps by investigating a new burner configuration, the University of Sydney (USYD) Burner specifically designed to incorporate enhanced turbulence through a recessed perforated plate and to support flame suppression experiments under well-characterised boundary conditions. The USYD Burner allows for controlled modulation of turbulence intensity and precise specification of the suppressant's injection parameters.

Therefore, this study contributes to fire modelling research by:

- Introducing a new burner setup that adds the systematic study of fuel-generated turbulence on flame dynamics.
- Providing the comprehensive collective application of comprehensive analysis of flame development and suppression in a well characterised boundary condition.
- Simulating flame suppression under defined boundary conditions not previously addressed in MaCFP or FM Global scenarios.

1.5 Scope and Limitations

This study focuses on the computational modelling of buoyant fires and their suppression using OpenFOAM (FireFOAM and Reacting FOAM) and ANSYS Fluent. It simulates fire development under different turbulence and suppression configurations, aligned with experimental conditions from the Sydney University Combustion Lab.

While the aim is to provide a comprehensive visualisation of the fire process from turbulence generation to suppression. The research is subject to certain limitations. These include model assumptions, turbulence and combustion closures, and the availability and accuracy of experimental data for validation.

1.6 Thesis Structure

This thesis is organised into nine chapters, each representing a key stage in the development and validation of an integrated fire modelling framework. The chapters are structured to reflect the logical flow of the research, beginning with foundational concepts and literature, and progressing through numerical modelling, validation, and analysis.

Chapter 1: Introduction

This chapter presents the context and motivation for the study, highlighting the complexity of buoyant turbulent fires and the challenges associated with suppression modelling in modern infrastructure. It reviews the evolution of fire science, introduces key modelling tools and international collaborative efforts (e.g., MaCFP, FM Global), and identifies gaps in current approaches.

Chapter 2: Literature Review

This chapter presents a comprehensive overview of key concepts and previous research related to the numerical simulation of buoyant flames and fire suppression. It is divided into three main

sections. The first section outlines the fundamental principles of fire behaviour, with a particular focus on buoyant flame dynamics.

The second section reviews major experimental studies conducted in controlled laboratory settings to examine flame structure, turbulence interactions, and heat release. It includes benchmark datasets such as McCaffrey's plume model, Sandia Flame D, the NIST wall fire experiments, as well as recent studies on façade and pool fires.

The third section discusses significant computational studies using advanced fire modelling tools. It focuses on two widely adopted platforms: FDS (Fire Dynamics Simulator) developed by NIST and FireFOAM built on the OpenFOAM framework.

Chapter 3: Modelling and Methodology

Details the computational methods, governing equations, turbulence and combustion models, and numerical tools used in the study, including FireFOAM and ANSYS Fluent. It also describes the simulation setup and boundary conditions.

Chapter 4: Simulating Diffusion Flame- Sandia Flame D- Reacting Foam Solver.

This chapter aims to study and test the model using a well-known and simple configuration: the Sandia Flame D. It presents a numerical investigation of the well-established Sandia Flame D benchmark using the Reacting FOAM solver. The objective is to assess the solver's capability in modelling non-premixed turbulent diffusion flames under controlled conditions. The study focuses on capturing the flame structure, mixing dynamics, and combustion characteristics through detailed simulation. Numerical results are compared against experimental data to evaluate the accuracy of the turbulence and combustion models implemented. This validation step ensures the reliability of the simulation framework and establishes a solid foundation for the subsequent modelling stages of this research.

Chapter 5: Studying Flow Turbulence - USYD Burner -using Fluent ANSYS

This chapter introduces the University of Sydney (USYD) burner configuration, which features a perforated plate designed to enhance turbulence levels upstream of the flame region. The study presents numerical simulations of non-premixed methane-air flames generated using this burner under two distinct conditions: with and without turbulence enhancement. Using ANSYS Fluent, the chapter explores the impact of turbulence on flame behaviour by analysing the flame structure, velocity fields, and flow development.

Chapter 6: Studying the Diffusion Flame - USYD Burner - FireFOAM Solver.

This chapter presents the application of the FireFOAM solver to model buoyant diffusion flames generated by the University of Sydney (USYD) burner. The simulation investigates the influence of burner geometry and inlet turbulence conditions on flame structure, temperature distribution, and flow behaviour. The study aims to evaluate the predictive capabilities of FireFOAM by comparing numerical outcomes with those obtained from previous ANSYS Fluent simulations and available experimental observations.

Chapter 7: Flame Suppression of USYD Burner – using FireFOAM Solver.

This chapter integrates flame suppression modelling into the FireFOAM simulation framework, using the University of Sydney (USYD) burner as a reference case. It examines the interaction between the buoyant diffusion flame and different suppression configurations, with a focus on the effects of droplet injection methods, and boundary conditions. The results contribute to validating the numerical approach and enhance understanding of effective suppression strategies in turbulent fire scenarios.

Chapter 8 : Discussion Chapter

This chapter presents a comprehensive discussion of the key findings across all simulation and experimental chapters. It integrates results from the Sandia and USYD burner configurations, analysing the role of turbulence, flame structure, and suppression dynamics.

The chapter reflects on the implications of enhanced turbulence under controlled conditions and compares solver performance between FireFOAM and Fluent, highlighting the USYD Burner as a novel benchmark for coupled combustion-suppression studies.

Chapter 9: Conclusion, limitation and Future works

This chapter concludes the thesis by highlighting its main contributions to fire modelling and suppression research. It reviews the integration of high-fidelity simulations and experimental validation, reflects on modelling limitations, and proposes future directions such as using supercomputing for extended LES runs, implementing advanced chemical kinetics, and expanding the USYD Burner setup for complex fire scenarios. The chapter sets the groundwork for enhancing predictive suppression models in practical fire safety applications.

2 Literature review

2.1 Fire History

Fire, a complex phenomenon arising from chemical reactions between fuels and oxygen, is vital for many applications but also presents significant risks, resulting in substantial property damage and loss of life each year. Despite advancements in fire safety, challenges persist.[5, 7]

2.1.1 Understanding Fire Behaviour

Understanding fire behaviour is essential for developing effective prevention and suppression strategies. Various factors, such as fuel type, physical state, and the surrounding environment, significantly influence how a fire develops. For example, a log burns differently from wood chips, and coal dust can explode under specific conditions. [6, 13].

This complexity underscores the need for a deep understanding of heat transfer and fluid dynamics to effectively address fire safety challenges. Fire has been integral to human civilisation, providing essential benefits such as warmth, light, cooking, and industrial power. However, uncontrolled fires have always presented severe dangers. Historically, the focus has been more on utilising fire than preventing

2.2 Fire Behaviour and Buoyant Flames

2.2.1 Fire Behaviour in the Built Environment

Fire behaviour in buildings and industrial settings involves a complex interplay between fuel characteristics, ventilation, heat transfer, and environmental feedback. These factors influence the rate of flame spread, smoke development, and thermal impact on structural elements[6]. Predicting this behaviour remains challenging due to the dynamic nature of fire growth, particularly in enclosed or semi-confined spaces. A comprehensive understanding of these

mechanisms is essential for designing effective fire suppression systems and improving overall safety standards. [5, 6]

2.2.2 The Role of Turbulence in Fire Behaviour

Turbulence is a defining feature of many fire scenarios, particularly those driven by buoyancy. It enhances the mixing of fuel and air, increases combustion rates, and produces irregular flame structures. These effects contribute to rapid fire spread and make suppression more difficult. Turbulent flows also influence heat transfer and smoke movement, further complicating fire dynamics. To predict fire development and design efficient suppression systems, it is essential to incorporate turbulence modelling into fire simulations.[5, 6, 40]

2.2.3 Buoyant Flames and Their Characteristics

Buoyant flames occur when hot gases rise due to density differences with the cooler surrounding air. This natural convective movement creates strong fire plumes capable of transporting heat, smoke, and combustion products over considerable distances. The behaviour of buoyant flames is influenced by fuel properties, oxygen availability, and plume interactions, all of which determine flame height, turbulence intensity, and heat release. These flames are particularly challenging in large-scale fires due to their unpredictable nature, necessitating the use of advanced modelling tools to support fire safety design.[5, 40, 41]

2.3 Previous Experimental Studies on Laboratory-Based Flames

The study of turbulent buoyant flames remains a significant area in fire safety research, primarily due to the complex interactions between heat transfer, combustion chemistry, and buoyancy-driven flows. A range of experimental and numerical investigations has been conducted to explore flame structure, turbulence interactions, and heat release dynamics, both in open-air and enclosure fire scenarios as presented in Table 2.1.

Table 2.1 Previous Related Studies.

Author	Name	Citation
Quintiere, James G	Fundamentals of fire phenomena.	Quintiere [6]
Drysdale, Dougal.	An introduction to fire dynamics.	Drysdale [5]
Poinsot and Veynante	Theoretical and numerical combustion	Poinsot and Veynante [42]
Spalding	Mixing and chemical reaction in steady confined turbulent flames.	Spalding [43]
Heskestad	Luminous heights of turbulent diffusion flames	Heskestad [44]
Grant	Fire suppression by water sprays	Grant, Brenton and Drysdale [45]
Chao, B. H.	structure and extinction of diffusion flames with flame radiation	Chao, Law and T'ien [46]
Vilfayeau,	Large eddy simulation of suppression of turbulent line	Vilfayeau, Myers [41]
Verma	Measured and simulated temperature statistics in a buoyancy-driven turbulent line fire	Verma, White [47]

Ashgriz	An introduction to computational fluid dynamics: the Finite Volume Method	Ashgriz and Mostaghimi [48]
Vilfayeau	Large eddy simulation of suppression of turbulent line fires by base-injected water mist.	Vilfayeau, Myers [41]
Barlow	Effects of turbulence on species mass fractions in methane/air jet flames.	Barlow [49]

Classic works **McCaffrey (1983)** [22] and **Heskestad (2002)** [50] developed foundational empirical correlations to describe temperature, velocity, and entrainment behaviour in buoyant plumes, which continue to be employed as fire models.

Subsequent studies have explored the influence of burner geometry and turbulence enhancement methods on flame behaviour. **Dunn-Rankin et al.** (2009) [51] examined how variations in burner configuration affect flame stability and fuel-air mixing, noting that increased turbulence improves combustion efficiency while introducing instability.

The 1986 study by Smooke, Puri, and Seshadri[52] presents a detailed comparison between numerical simulations and experimental measurements of a counterflow diffusion flame formed by methane diluted with nitrogen and air also diluted with nitrogen. Using quartz microprobes and gas chromatography, the researchers measured stable species concentrations, while temperature profiles were obtained with coated thermocouples and corrected for radiation losses. Numerical simulations were performed using an adaptive nonlinear boundary value method with a detailed chemical kinetics mechanism involving 16 species and 46 reactions. The results showed excellent agreement between the calculated and measured profiles for major species such as CH_4, O_2, N_2, H_2O, and CO_2, as well as for the peak flame temperature. However, discrepancies in the H_2 and CO profiles were observed and attributed to the exclusion of C_2 hydrocarbon chemistry in the model. The study also explored the

influence of strain rate, transport processes, and boundary conditions, demonstrating that while some deviations existed, the numerical model effectively captured the key features of the flame structure, reinforcing the value of detailed simulations for understanding diffusion flame behaviour.

In 1992, Hamins et al. conducted a series of controlled laboratory-scale experiments titled [53] "Experimental Measurements of Heat and Mass Transfer from a Turbulent Diffusion Flame to a Vertical Wall". These were developed and published by the National Institute of Standards and Technology (NIST). The study focused on understanding the interaction between a methane-fuelled fire and an adjacent wall, particularly under free convection conditions.

The experimental setup featured a methane diffusion flame, produced by a circular burner placed near a vertical steel wall. Radiative and convective contributions to the wall heat flux were quantified using calibrated sensors. The experiments were primarily intended to provide high-quality validation data for computational models simulating flame-wall interactions, which are particularly relevant in the context of fire growth prediction and suppression modelling.

These data have become a benchmark dataset for validating computational fluid dynamics (CFD) models such as FireFOAM and have been widely cited in the literature due to their rigorous methodology and well-documented measurements. is widely referred to in the fire modelling community as the: Hamins /NIST Wall Flame Dataset.

In 1997, The Sandia Piloted [1, 54] CH_4/Air Flames dataset has undergone several stages of development to support collaborative efforts in validating turbulent non-premixed flame models. The original multi-scaler measurements were conducted in 1997 using a piloted methane/air jet flame burner developed at the University of Sydney. A preliminary release of the dataset limited to Flame D was made available prior to the third Turbulent Non-premixed Flames (TNF3) Workshop in 1998. In response to growing interest and model validation needs,

a more comprehensive release (Version 2.0) was issued in January 2003, providing full documentation and data for Flames C, D, E, and F. The most recent update, Release 2.1, was published in June 2007. This version incorporated an additional reference highlighting previously unpublished experimental insights, including 6000-shot records from Flame D. Throughout these releases, the dataset has remained a critical benchmark for evaluating scalar transport, extinction phenomena, and turbulent mixing in piloted turbulent diffusion flames. The benchmark used for the MaCFP (Measurement and Computation of Fire Phenomena) working group is the Sandia Piloted CH_4/Air Jet Flames, specifically Flames D and E from the TNF (Turbulent Non-premixed Flames) series.

Davis et al. (1993) [55] conducted a joint numerical and experimental study to investigate the dynamic behaviour of a low-speed buoyant jet diffusion flame, focusing on flame flickering and vortex structures. Using direct numerical simulation (DNS) based on the axisymmetric, compressible Navier–Stokes equations with a flame sheet model, the study excluded turbulence and radiation to isolate buoyancy effects. The simulations, performed using the QUICKEST finite-difference scheme and solved with FISHPAK routines, achieved up to 60 flickering cycles per CPU hour.

The experimental setup involved a coflowing propane/nitrogen jet flame, Mie scattering was used to visualise particles formed in the flame. Operating at fuel and air inlet velocities of 6.4 cm/s and 18 cm/s respectively, the flame exhibited flickering at 12–14 Hz. Both simulation and experiment showed good agreement in capturing large-scale vortex dynamics, flame bulging, tip detachment, and recirculation zones. The study also found that changes in coflow velocity caused abrupt shifts in flicker frequency, reproduced in both domains. Overall, this work demonstrated that simplified DNS models can reliably capture key buoyancy-driven features in laminar diffusion flames.

Following the foundational work by Smooke, Puri, and Seshadri on counterflow diffusion flames, the 2016 study by Reuter, et al [56] expanded the application of the counterflow burner configuration to investigate premixed cool flames, a combustion regime governed by low-temperature chemistry. Using ozone-assisted ignition, the researchers successfully stabilised self-sustaining dimethyl ether (DME)/oxygen premixed cool flames in a counterflow setup. This configuration enabled the exploration of ignition limits, extinction behaviour, flame hysteresis, and species distribution under varying strain rates and equivalence ratios. One key finding was that cool flames could persist beyond the extinction limit of hot flames, calling into question conventional definitions of extinction. Planar laser-induced fluorescence (PLIF) measurements of formaldehyde (CH_2O) showed that cool flames have significantly broader CH_2O profiles than hot flames, indicating their role as key intermediates. Furthermore, the propagation speed of cool flames exhibited weaker sensitivity to equivalence ratio changes compared to hot flames. Numerical simulations, based on detailed kinetic models, supported the experimental trends and provided insight into the dominant reaction pathways. This study presents a practical platform for studying cool flames and contributes to a deeper understanding of low-temperature combustion.

In 2004, Assaad R. Masri [57] and his colleagues conducted an experimental investigation into the compositional structure of swirl-stabilised turbulent non-premixed flames. The study used advanced laser diagnostics, including Raman scattering, Rayleigh scattering, and Laser-Induced Fluorescence (LIF), to obtain detailed, pointwise measurements of temperature and species such as OH, NO, CO, H_2, and CO_2. These measurements were carried out at the Combustion Research Facility, Sandia National Laboratories (USA), using a specially designed swirl burner. The burner allowed for different levels of swirl and fuel compositions, including pure methane, methane/hydrogen, and methane/air mixtures. Their results revealed that higher swirl numbers improve flame stability and enhance mixing, but they also lead to the appearance of locally unburnt or partially burnt regions, especially near the outer radial zones. These

findings were visualised through colour-coded scatter plots in mixture fraction space, offering insight into the strong coupling between fluid mechanics and combustion chemistry. The full dataset, which includes temperature, flow, and chemical composition fields, was made available for model validation, supporting the development of reliable computational combustion models.

University of Maryland & FM Global Research

The University of Maryland's Department of Fire Protection Engineering (FPE) has a longstanding history of conducting experimental studies in fire dynamics and safety. Established in 1956, the department has been a pioneer in fire protection education and research.

One notable laboratory-based experimental study was conducted by Duny et al. (2016)[58] to investigate vertical fire spread along combustible façades under controlled conditions. The tests aimed to generate high-quality experimental data for validating numerical fire models. A 2.5 m × 4.9 m façade was exposed to a 1500–1567 kW wood crib fire, simulating post-flashover conditions. Three configurations were tested: an inert calcium silicate façade, and two façades clad with 18 mm thick plywood (Birch and Okoumé) [58].

Heat release rate (HRR) was measured via both mass loss and oxygen consumption methods, while thermocouples and radiometers monitored temperature and heat flux. Results showed that while both wood types added approximately 500 kW to the HRR compared to the inert façade, the Birch cladding exhibited significantly greater vertical flame spread and higher peak façade temperatures, reaching 800°C at 3.2 m above the opening. This study highlights the critical influence of material properties on fire spread and provides a valuable benchmark for validating CFD fire models under realistic façade conditions.

In 2015, the University of Waterloo made a significant contribution to the field of fire safety engineering through a detailed investigation into wind-blown pool fires, focusing on the geometry of flames under varying wind conditions. Conducted by Lam and Weckman, the second part of their two-part study published in the *Fire Safety Journal* offered an in-depth comparison between experimental measurements and semi-empirical correlations for key flame characteristics namely flame drag, flame tilt, and flame length. The experiments were carried out on 2 m diameter Jet-A pool fires subjected to crosswinds ranging from 3 to 10 m/s,

using temperature-based analysis rather than visual imaging alone, a methodological improvement over many prior studies. The results revealed limitations in existing correlations, particularly under high wind conditions, and highlighted the importance of factors such as fuel vapour density, air entrainment, and heat release rate in influencing flame behaviour. The study called for enhanced modelling approaches that account for the dynamic interplay between wind momentum and buoyancy, reinforcing the University of Waterloo's role in advancing the understanding of fire plume dynamics and fire hazard prediction. [59, 60]

In 2016, DiDomizio and Weckman [61] from the University of Waterloo conducted a comprehensive evaluation of various methodologies for determining gas analyser delay times in cone calorimeter fire tests. The accuracy of delay time correction is critical for calculating heat release rates using oxygen consumption calorimetry. The standard ASTM E1354 method was found to produce inconsistent results, particularly due to thermal lag in the stack thermocouple and inadequate consideration of analyser response dynamics. The study compared four calibration techniques: the ASTM E1354 method, the apparent response method, the square wave approach, and a novel gas injection method. Among these, the gas injection technique yielded the most accurate and consistent results by directly tracking gas concentration changes and accounting for both transit and response times. The authors proposed an exponential model to relate delay time to the initial gas production rate, especially for CO and CO_2. Their findings underscored the importance of selecting appropriate calibration methods based on material type and combustion behaviour, offering valuable guidance for improving the reliability of cone calorimeter data in fire testing.[61]

Together, these experimental investigations, which span diffusion flames, turbulent jet flames, façade fire testing, and cone calorimeter measurements, have significantly advanced the empirical understanding of flame behaviour under varied thermal, chemical, and boundary conditions. They provide critical benchmark datasets for validating computational models, guiding the development of accurate fire simulation tools, and enhancing our insight into

mechanisms such as ignition delay, flame-wall interaction, and combustion stability. While this review does not exhaustively cover every available dataset in the literature it aims to highlight the most relevant studies. The following section presents the numerical modelling framework employed in this study, focusing on buoyant fire dynamics and suppression processes under controlled and realistic conditions.

2.4 Previous numerical study of Computational Fire Modelling Studies

2.4.1 Pioneering CFD Fire Modelling:

The emergence of computational fluid dynamics (CFD) as a viable tool for fire modelling can be traced back to the mid-1970s, as discussed by Cox[62], when increasing computational power enabled the numerical solution of governing equations for momentum, energy, and mass transport. Early efforts in the 1980s and 1990s laid the foundation for the development of contemporary fire simulation tools. These foundational models predominantly employed Reynolds-Averaged Navier–Stokes (RANS) approaches to simulate turbulent buoyant flows, combustion processes, and heat transfer mechanisms within fire scenarios.

One of the early landmark contributions to RANS-based fire modelling was presented by Cox in 1994 [62]**,** who outlined the scientific and practical challenges involved in modelling turbulent buoyant fires. The study provided a clear distinction between zone models based on simplified compartment assumptions and more advanced field models, which utilise computational fluid dynamics (CFD) techniques to resolve localised fire behaviours through the solution of conservation equations. The development of field models, as outlined by Cox, made it possible to simulate complex fire behaviours such as the trench effect observed during the Kings Cross Underground fire phenomena that could not be captured by simplified methods. The work laid a crucial foundation for subsequent developments in tools like FDS and FireFOAM.

In parallel with RANS-based CFD efforts, another influential contribution was made by Karlsson and Magnusson (1991) [63], who developed a physically based numerical model for simulating room fire growth involving combustible wall linings. Although their approach did not employ RANS or URANS formulations, it represented a critical step towards integrated fire modelling. Their model utilised key material parameters, such as thermal inertia, ignition temperature, flame spread coefficient, and heat release rate constants, derived from standard

bench-scale tests to predict full-scale compartment fire behaviour. The simulation incorporated sub models for gas temperature rise, flame spread dynamics, heat transfer to walls, and total heat release rate. One of the major outcomes of their work was a regression-based empirical equation for flashover time, which achieved a coefficient of determination (R^2) of 0.98 against simulation results. While not a CFD model in the strict sense, this study bridged bench-scale testing with predictive room-scale modelling and advanced the concept of performance-based material classification, reinforcing the broader transition toward simulation-based fire safety engineering.

These early modelling efforts demonstrated that fire behaviour could be predicted using physics-based simulations rather than relying solely on empirical methods. They also laid the foundation for modern CFD tools used in fire safety engineering today. A detailed overview and evaluation of these pioneering contributions are presented in the review by Novozhilov (2001) [64], which highlights how these initial RANS-based models influenced the development of advanced fire simulation frameworks, including those used in performance-based design.

2.4.2 NIST's FDS (Fire Dynamics Simulator) Solver for Simulating Compartment Fires

The Fire Dynamics Simulator (FDS), developed by the National Institute of Standards and Technology (NIST), is a CFD-based tool used to simulate fire-driven flows under low-speed, thermally dominated conditions. Introduced in the early 2000s, FDS integrates Large Eddy Simulation (LES) with a low-Mach number formulation of the Navier-Stokes equations to model key fire phenomena, including heat release, flame spread, smoke transport, and sprinkler response. Paired with the visualisation software Smokeview, FDS has been extensively validated against experimental data and continues to evolve through international research collaboration. It is widely adopted in fire safety engineering for performance-based design, forensic analysis, and large-scale fire assessments.[65]

In 2008 study, Dr Arnaud Trouvé [66] from the University of Maryland critically examined the numerical and modelling challenges associated with simulating large-scale pool fires using Computational Fluid Dynamics (CFD). The study focused on the limitations of traditional CFD models, particularly the Fire Dynamics Simulator (FDS) in capturing complex flame geometries, flame extinction, soot production, and radiative losses as pool diameters increase. It was found [67] that traditional modelling approaches in FDS5 failed to account for scale-dependent changes in combustion efficiency, soot yield, and radiant fraction. To address this, a modified version of FDS (FDS5m) was introduced, incorporating enhanced flame extinction modelling that considers flow time scales, fuel vitiation, and radiative cooling. Numerical simulations of propylene pool fires across a wide range of burner sizes (0.4 to 40 m) demonstrated that large-scale fires are poorly ventilated and consist of multiple, thinner flame structures requiring high grid resolution (up to 300 grid cells per pool diameter). The updated model showed improved predictions of combustion efficiency and soot emissions, supporting the hypothesis that flame extinction under slow mixing and strong radiative cooling is a dominant mechanism in large-scale pool fires. The study highlighted the need for refined

combustion models and high-resolution meshes to accurately represent the physics of fire growth and smoke production at field scales. [67]

In 2013, Silvia Tavelli and colleagues from Politecnico di Milano [68] conducted a numerical study using Fire Dynamics Simulator (FDS) to analyse the consequences of pool fires in confined environments, including rooms and tunnels. The research aimed to validate FDS predictions against experimental data and assess its suitability for simulating complex fire dynamics. The study involved small-scale room fires, full-scale tunnel fires, and laboratory-scale tunnel experiments. Results showed that FDS reliably reproduced temperature and smoke behaviour, particularly when accurate boundary conditions and ventilation settings were applied. The study confirmed the importance of modelling ventilation, wall properties, and geometric configurations to predict smoke movement, back layering, and flame spread. Overall, the work demonstrated the effectiveness of CFD modelling in designing fire protection and ventilation systems for confined spaces. [68]

In 2017, Wang et al. [69] from Ulster University conducted a numerical and experimental study using Fire Dynamics Simulator (FDS) to investigate flame height and horizontal flame spread from small pool fires under ceilings. The study introduced a correlation based on the stoichiometric mixture fraction to define continuous flame height and assess flame extent beneath the ceiling. Results showed good agreement with existing experimental data and highlighted the influence of ceiling height on air entrainment and flame behaviour. The findings support the use of FDS in predicting flame spread under ceilings and developing dimensionless correlations for fire safety design. [69]

In 2019**,** Gianmaria Pio and colleagues [70] from the University of Bologna conducted a numerical study using the Fire Dynamics Simulator (FDS) to evaluate small-scale LNG pool fires, focusing on the effects of pool diameter and fuel composition (methane, ethane, and propane). The study aimed to improve understanding of key fire characteristics including heat

release rate (HRR), flame height, burning rate, and thermal radiation for safety distance assessment. The Thomas correlation, which estimates flame height based on mass burning rate and pool diameter, was validated against simulation results and found to perform reliably across all mixtures and sizes. However, existing models for predicting radiative heat flux were not adequate, particularly for multi-component LNG mixtures. To overcome this, the authors introduced new empirical correlations in exponential form, fitted to FDS results and incorporating fuel composition and pool size using specific constants (B, C_1, C_2), which account for the effects of pool diameter and fuel composition on radiation decay with distance. These improved accuracy in estimating thermal radiation intensity, especially for mixtures with higher concentrations of ethane and propane.

The findings highlight the importance of using realistic gas compositions rather than pure methane for conservative safety assessments.[70]

2.4.3 OpenFOAM-Based FireFOAM Solver for Simulating Compartment Fires

The second part of this numerical investigation adopts FireFOAM, an open-source solver developed by FM Global, a leading industrial research organisation specialising in property loss prevention and fire safety engineering. Built within the OpenFOAM computational framework, FireFOAM was specifically designed to simulate fire-related phenomena, including buoyant fire plumes, combustion, and thermal radiation, using a Large Eddy Simulation (LES) approach. This solver integrates key sub-models such as the Eddy Dissipation Concept (EDC) for turbulent combustion, the Discrete Ordinates Method (DOM) for radiation heat transfer, and a one-equation eddy viscosity model for sub-grid turbulence closure.[12, 25, 30]

In 2010, Trouvé and Wang [71] , from the Department of Fire Protection Engineering at the University of Maryland and FM Global Research Division respectively, demonstrated the capability of Large Eddy Simulation (LES) techniques for modelling compartment fire dynamics, highlighting the importance of resolving complex multi-physics interactions including pyrolysis, buoyancy-driven turbulence, combustion, soot formation, and thermal radiation. The study reviewed two benchmark solvers FDS (developed by NIST) and FireFOAM (developed by FM Global) both of which are open-source tools widely used in fire research and engineering.

The authors [71] presented LES results for two representative scenarios: a full-scale compartment fire (the Dalmarnock test) and a canonical methane pool fire. The Dalmarnock test simulation captured the fire development through flashover and the transition to under-ventilated conditions. FDS effectively reproduced the global fire behaviour, including heat release rate trends and flame spread, although local temperature and heat flux predictions showed limitations due to simplified pyrolysis models.

In contrast, FireFOAM simulations of small-scale pool fires demonstrated strong agreement with experimental correlations by McCaffrey, particularly in plume temperature, velocity, and mass flow rate profiles. These simulations provided insight into buoyancy-dominated flame structures and validated LES performance at laboratory scale.

The paper [71] emphasised that while LES-based CFD tools offer significant predictive potential, challenges remain in modelling subgrid-scale combustion, accurate thermal feedback, flame extinction, and soot dynamics. The study called for enhanced pyrolysis models, turbulence-radiation interaction treatment, and the use of high-fidelity experimental data for further validation.

In 2013, Ren et al. (2013) [72] at the University of Maryland, conducted a numerical investigation using Large Eddy Simulation (LES) to study vertical turbulent wall fires, focusing on the interplay between turbulence, combustion, and heat transfer mechanisms. The simulation employed a non-premixed flame model with the Smagorinsky subgrid-scale turbulence model to resolve large-scale eddies while accounting for chemical reactions and thermal radiation. The results demonstrated that LES could effectively capture key flow structures, temperature distributions, and flame behaviours along vertical walls subjected to buoyant fire conditions.

The study validated the simulation results against experimental data, showing good agreement in temperature and heat flux profiles along the wall. The LES approach provided improved accuracy over traditional Reynolds-Averaged Navier–Stokes (RANS) methods in predicting transient and spatially-evolving features of wall fires. This work illustrates the capacity of LES to model complex fire dynamics near solid surfaces and highlights the importance of coupling turbulence with combustion and radiative heat transfer to replicate real-world fire behaviours.

In 2013, To enhance the predictive capability of computational fire suppression models, Meredith et al. (2013)[73] developed a coupled numerical framework within OpenFOAM to

simulate the interaction of sprinkler water with solid surfaces during fire events. The model extends the FireFOAM solver by integrating a detailed surface film transport module based on mass, momentum, and energy conservation equations. The water-film model operates on a two-dimensional mesh over the solid surfaces, capturing the effects of impingement, film flow, vaporisation, and thermal interactions with both the wall and surrounding gas phase.

The implementation assumes a thin-film approximation, enabling efficient resolution of surface-normal transport processes without resorting to computationally intensive volume-of-fluid methods. Interfacial phenomena such as thermocapillary forces, partial wetting, and vapor recoil pressure are also accounted for. Validation of the model was conducted through experimental studies involving water flow over a heated vertical steel panel exposed to varying radiative heat fluxes (5–33 kW/m²). Results demonstrated accurate predictions of film behaviour, temperature profiles, and vaporisation rates, confirming the model's robustness in simulating suppression-related surface cooling mechanisms.

In 2016, in a notable study conducted by Vilfayeau et al. at the University of Maryland [74], the performance of advanced flame extinction and reignition models was evaluated through large eddy simulations (LES) of a buoyant, turbulent, methane-fuelled line fire subjected to air-nitrogen co-flow conditions. Implemented within the FireFOAM solver, the extinction model was based on a critical Damköhler number, while the reignition model relied on a critical gas temperature. The experimental setup allowed for controlled variation of oxygen levels, revealing an extinction limit at 12.2% O_2. The LES simulations, performed with a refined computational mesh, successfully captured the transition from sustained combustion to extinction, predicting a numerical extinction limit at 11% O_2. The model was validated against global combustion efficiency data and spatially resolved temperature and oxygen profiles. This work not only demonstrated the predictive capabilities of FireFOAM in modelling gas-based

suppression but also laid the groundwork for future investigations involving thermal radiation and water-based suppression systems.

In 2017, Sedano et al. from Universidad de los Andes and Universidad del Valle [75] conducted a study to assess the performance of the fireFoam solver within OpenFOAM for simulating a small-scale methanol pool fire, originally studied experimentally by Weckman and Strong (1996). The simulation employed Large Eddy Simulation (LES) for turbulence and the Eddy Dissipation Concept (EDC) for combustion modelling, incorporating simplified chemical kinetics and radiation using the Discrete Ordinates Model. The study evaluated mesh sensitivity using four grid resolutions, revealing that a medium mesh (2 million cells) offered a good balance between accuracy and computational cost, with flame height predictions differing by less than 3% from experimental data. Results showed reasonable agreement with experimental temperature and velocity profiles, particularly in the far-field region of the flame.

Despite some discrepancies in maximum temperature predictions and contour shapes, the model captured key fire behaviours and demonstrated mesh convergence. The authors concluded that fireFoam is a suitable and cost-effective CFD tool for simulating pool fires and could be extended to larger-scale turbulent fire scenarios.[75]

In a 2018, Duy Le [76] as part of his Master's research at the University of Waterloo, Canda. His work focused on evaluating the predictive capabilities of the FireFOAM solver for large-scale, confined compartment fires. By comparing numerical results with detailed experimental data from the PRISME Integral Test 4, Le demonstrated that FireFOAM could accurately capture key fire dynamics such as temperature, pressure, species concentration, and doorway velocity. However, the study also identified areas for future improvement. It recommended refining the combustion model by incorporating finite-rate chemistry to better capture reaction kinetics and improving turbulence modelling using more advanced sub-grid scale models or hybrid RANS–LES approaches. The study also highlighted the need for more accurate wall

treatment strategies to improve heat transfer predictions near boundaries. These findings contributed to a better understanding of the solver's current strengths while guiding future development [76].

In 2021, Mohamed M. Ahmed and Trouvé [38] from the University of Maryland conducted a comprehensive study to evaluate the capability of Large Eddy Simulation (LES) in modelling the flame structure and thermal feedback mechanisms of a medium-scale methanol pool fire. The researchers employed the FireFOAM solver within a wall-resolved LES framework, focusing on capturing the complex buoyancy-driven dynamics and gas-to-liquid heat transfer occurring near the fuel surface. Their work, which forms part of the efforts by the IAFSS MaCFP Working Group to validate computational fire models, is notable for its detailed grid sensitivity analysis and for comparing simplified and advanced radiation modelling approaches. The study provides critical insights into the spatial resolution required to resolve boundary-layer instabilities and accurately predict thermal feedback in pool fire scenarios. [38]

In 2025, Ahmed Abdalhamid, et al [77] from the University of Waterloo conducted a comprehensive numerical study of a medium-scale ethanol pool fire using Large Eddy Simulation (LES) integrated with the Conditional Source-Term Estimation (CSE) framework. This work represented the first numerical application of CSE with soot modelling to simulate a buoyant turbulent flame, addressing key fire dynamics phenomena including turbulence chemistry radiation interactions. Two semi-empirical soot models based on the Laminar Smoke Point (LSP) concept were implemented and assessed. The first model included a temperature-sensitive oxidation term and a higher soot nucleation rate, which enabled it to better capture the formation and consumption of soot within the flame. In contrast, the second model used simplified oxidation kinetics and did not strongly respond to local flame temperature, resulting in an underprediction of soot concentrations. These differences in underlying assumptions largely explain the discrepancy between the two models' predictions. Detailed combustion

chemistry was incorporated via Trajectory Generated Low-Dimensional Manifolds (TGLDM), and radiation modelling employed the Radiative Transfer Equation (RTE) using the Weighted Sum of Gray Gases (WSGG) approach.
The simulation outcomes were benchmarked against experimental data from the MaCFP working group, showing strong agreement in flame height, gas species concentrations, soot mass fractions, and radiative heat fluxes. The first soot model provided closer alignment with measured values, particularly for temperature and soot predictions, while the second model underpredicted soot concentrations. Overall, this study demonstrated the effectiveness of the LES-CSE framework for advancing the predictive accuracy of fire modelling, particularly for lightly sooting fuels like ethanol. [77]

In recent years, suppression modelling has progressed through CFD simulations of sprinkler and mist systems.

Kim et al. (2003) [78] conducted both experimental and numerical investigations to assess the effectiveness of water mist systems in suppressing fires within enclosed spaces. The research provided insights into the dynamics of fire suppression and the interactions between water mist droplets and fire behaviour. FireFOAM has also been extended by Suard et al. (2016) to incorporate spray injection and heat absorption models, supporting coupled simulation of multiphase flow and suppression dynamics. However, these studies often rely on predefined fire scenarios and seldom account for upstream burner effects or varying turbulence intensities.

These upstream factors significantly affect fire behaviour and suppression efficiency. The burner setup determines the initial velocity profile, flame geometry, and thermal stratification, all of which influence droplet trajectories and mist penetration. Turbulence intensity alters the flame surface area and enhances entrainment, which governs how well droplets evaporate, absorb heat, and displace oxygen in the flame zone. Ignoring such dynamics can result in oversimplified suppression models. Therefore, accurate assessment of suppression

mechanisms requires the incorporation of upstream flow characteristics and turbulence-driven mixing to reflect the real complexity of mist–flame interactions.

In summary, significant progress has been made in the field of fire modelling through international efforts such as the Measurement and Computation of Fire Phenomena (MaCFP) initiative and large-scale industrial collaborations like those led by FM Global. These initiatives have successfully developed valuable benchmark datasets, advancing the understanding of buoyant flame structures under controlled laboratory conditions. Foundational studies, including the McCaffrey Flames and the Sandia Flames, have provided critical datasets for validating computational fire models and continue to be highly regarded within the research community.

Despite the extensive development of experimental configurations, many canonical-scale studies introduce complexities at the fuel surface that are difficult to resolve. Accurate modelling often requires capturing species transport within porous materials, such as bronze burners, or quantifying surface energy balances in pool fires. To simplify this, empirical wall functions developed for non-reactive flows are frequently applied, although they introduce significant uncertainties when extended to fire scenarios. Furthermore, turbulence generation in buoyant flames is typically governed by fuel and boundary conditions, limiting the ability to systematically control turbulence intensity in traditional setups.

To address these challenges, this thesis introduces a new burner configuration, the University of Sydney (USYD) Burner, specifically designed to enhance turbulence generation through a recessed perforated plate while maintaining well-characterised boundary conditions. The USYD Burner enables the controlled modulation of turbulence intensity and facilitates flame suppression experiments under precisely specified operating conditions. Accordingly, the present study contributes to fire modelling research by:

i. Introducing a new burner setup that enables the systematic study of fuel-generated turbulence effects on flame structure and dynamics.

ii. Providing a comprehensive framework for analysing flame development and suppression under carefully defined and quantified boundary conditions.

iii. Simulating suppression processes within a buoyant diffusion flame.

3 Model Setup

3.1 Introduction

Diffusion flames, characterised by the gradual mixing of fuel and oxidiser, play a fundamental role in combustion science. Understanding these flames is particularly crucial in fire safety and suppression applications, as they are frequently encountered in various industrial and safety-related scenarios. OpenFOAM (Open Field Operation and Manipulation) is a comprehensive CFD software package designed to simulate a wide range of phenomena, including thermodynamics, fluid dynamics, and chemical reactions. Understanding the computational foundations of fluid dynamics is essential in numerical modelling, as discussed in Street [79], Anderson [80], and Versteeg [81].

OpenFOAM is an open-source CFD platform widely used to model complex physical phenomena, including fluid flow, thermodynamics, and combustion. Developed in C++, it comprises over 250 applications, divided into solvers for physics-based simulations and utilities for pre-processing and post-processing tasks. Its implementation of the finite volume method allows for the discretisation and solution of partial differential equations over structured or unstructured meshes, offering substantial flexibility for complex geometries.

Solvers: These applications address specific challenges in fluid and continuum mechanics, conducting the core calculations required to simulate various physical processes.

Utilities: These tools support data manipulation throughout the simulation workflow, including mesh generation, data extraction, and post-processing analysis.

Open FOAM boasts a rich toolbox of solvers catering to diverse combustion phenomena. However, for non-premixed flames, the focus of this study, selecting the optimal solver becomes a critical step as it significantly impacts the accuracy of simulation results, ultimately

influencing the validity of the conclusions drawn. This selection process can be particularly challenging for those new to Open FOAM combustion simulations.

To navigate this critical selection process effectively, a comprehensive investigation was undertaken and detailed in section 3.5, focusing on two key aspects to gain a thorough understanding of available solver options within Open FOAM:

Current Combustion Models in Open FOAM: To ensure the selection of the most appropriate solver for simulating the non-premixed flame within the USYD Burner, a comprehensive review of the combustion models available within the Open FOAM framework was conducted (Section 3.2). This review carefully assessed the capabilities and limitations of each model. By critically evaluating these models, we gained a clear understanding of the available options and their suitability for non-premixed flame simulations.

Applications in Combustion Studies: A review of existing literature on combustion simulations using Open FOAM was conducted. This analysis provided valuable insights into how researchers have utilized different solvers for various combustion scenarios.

This section also presents the fundamental governing equations required for simulating reacting flows. These include the transport equations for continuity, momentum, species transport, and energy. Given that simulations often rely on time- or ensemble-averaged values, relevant averaging techniques are also introduced to support the sub-models discussed in Section 3.2.

3.2 OpenFOAM Solvers for Non-Premixed Flames:

OpenFOAM offers a diverse suite of solvers tailored to the simulation of non-premixed combustion, each suited to specific flow conditions and modelling objectives. The key solvers relevant to this study include:

ReactingFoam Solver: This foundational solver is commonly used for non-premixed flame simulations, providing a base framework for modelling combustion with chemical reactions.

rhoReactingFoam Solver: Enhancing the capabilities of ReactingFoam, this solver uses a density-based thermodynamics package. It is particularly well-suited for compressible flows where pressure-based approaches may have limitations.

rhoReactingBuoyantFoam Solver: An extension of rhoReactingFoam, this solver includes buoyancy effects by explicitly accounting for gravitational forces. It is ideal for simulating flames influenced by natural convection, such as buoyant plume behaviour observed in many fire scenarios.

fireFoam Solver: Designed specifically for fire modelling, this solver supports non-premixed flames and includes advanced features such as soot formation, radiation modelling, and fire suppression capabilities.

3.3 Governing Equations for Reacting Flows:

During simulations of reacting flows, the interplay between chemical reactions and fluid dynamics results in several key effects within the computational domain:

Fluid Composition Changes: Ongoing chemical reactions alter the species composition, resulting in the continuous formation and depletion of reactants and products. This, in turn, affects the overall molecular mass of the fluid mixture.

Pressure and Temperature Fluctuations: Reacting flows particularly those involving compressible gases exhibit changes in density due to shifts in temperature and pressure, further influencing the flow field.

To capture these phenomena accurately, governing equations that incorporate variable density effects are employed. The foundational formulations for mass, momentum, and energy conservation are established in works by Anderson [80] , Versteeg [81], Patankar [82], and accounting for varying density are defined as Biswas and Eswaran [83], and Kadar [84].

Continuity Equation

The continuity equation for variable density flows is given by:

$$\frac{\partial \rho}{\partial t} + \nabla.(\rho u) = 0$$

Equation 3-1

Where:

ρ is the density [kg/m³],

t is time [s],

u is the velocity vector [m/s].

Momentum Equation:

The momentum equation considering the variable density is:

$$\frac{\delta(\rho u)}{\delta t} + \nabla.(\rho u u) = -\nabla_p + \nabla._\tau + f$$

Equation 3-2

Where:

P: is the pressure.

τ : is the stress tensor.

f: is the body forces (e.g., gravity)

The specific form of the momentum equation for variable density flow is:

$$\frac{\delta(\rho u_i}{\delta t} + \frac{\delta(\rho u_i u_j)}{\delta x_j} = \frac{\delta p}{\delta x_i} + \frac{\delta}{\delta x_j}(\mu\left(\frac{\delta u_i}{\delta x_j} + \frac{\delta u_j}{\delta x_i} - \frac{2}{3}\delta_{ij}\frac{\delta u_k}{\delta x_k}\right))$$

Equation 3-3

Where:

u_j : is the Cartesian velocity component.

x_i : is the Cartesian direction.

μ : is the dynamic viscosity.

δ_{ij} : is the Kronecker delta,

Energy Equation:

The energy equation for a reacting flow is:

$$\frac{\delta(\rho E)}{\delta t} + \nabla.(up) + \nabla.(k\nabla \mathrm{T}) + \phi + \sum_i (J_i h_i) + \dot{q}$$

Equation 3-4

Where:

E: is the total energy per mass.

k: is the thermal conductivity.

T: is the temperature.

Φ: represents viscous dissipation.

h_i: is the specific enthalpy of species of i.

$\dot{q}$: is the heat release due to chemical reaction.

Mixture Density

The density of a reacting gas mixture is determined using the ideal gas law:

$$\rho = \frac{pM_{avg}}{RT}$$

Equation 3-5

Where:

$M_{avg} = \frac{1}{\sum \frac{Y_i}{M_i}}$ is the average molar mass of the mixture.

Y_i: is the mass fraction of chemical species i.

R: is the universal gas constant.

T: is the temperature.

Dynamic Viscosity – Sutherland's Law

For laminar flows, dynamic viscosity can be estimated using Sutherland's law:

$$\mu = A_s(\frac{T}{T_s})^{3/2}\frac{T_s + C}{T + C}$$

Equation 3-6

Where:

A_s and T_s are species- specific constants, and C is Sutherland's constant.

Energy Transport Equation

Temperature distribution is essential for capturing thermodynamic properties and chemical kinetics. The energy transport equation is defined as [48, 80]:

$$\underbrace{\frac{\delta(\rho h)}{\delta t}}_{\text{Enthalpy term}} + \underbrace{\frac{\delta(\rho h u_j)}{\delta x_j}}_{\text{Convection term}} = \underbrace{\frac{\delta}{\delta x_j}(\frac{\lambda}{Pr}\frac{\delta h}{\delta x_j})}_{\text{Conduction term}} + \underbrace{\mu(\frac{1}{Sc} - \frac{1}{Pr})\sum h_i \frac{\delta Y_i}{\delta x_j}}_{\text{Diffusion term}} + \underbrace{S_{rad}}_{\text{Radiation term}} + \underbrace{S_{comb}}_{\text{Combustion term}}$$

Equation 3-7

Where:

Pr: is the Prandtl number of the mixture.

Sc: is the species Schmidt number.

S_{rad}: is the radiation source term.

λ: is the thermal conductivity

h: is the sensible enthalpy

S_{comb}: is the combustion source term.

3.4 Turbulence modelling in Burner Simulations

In the field of Computational Fluid Dynamics (CFD) [80], Street [79], and [85], accurately representing turbulent flow dynamics is essential for achieving reliable results, especially when simulating combustion processes. Turbulence models offer varying levels of complexity and accuracy, catering to the specific requirements of different simulations.

This study represents the combustion characteristics of the Sandia and Sydney burners using OpenFOAM. Two distinct solution platforms were chosen from the available options within OpenFOAM. Each model selection was based on its strengths and its suitability for capturing the specific flow features of the respective burner geometry.

Reynolds-Averaged Navier-Stokes (RANS) Model in the Sandia Burner Study

For the Sandia burner study, the Reynolds-Averaged Navier–Stokes (RAS) approach with the standard k–ε model was adopted. This model, widely used in engineering applications, where the turbulence is averaged, and the model provides general predictions of turbulence via two equations: one for turbulent kinetic energy (k) and one for its dissipation rate (ϵ\epsilon).

The RANS model averages the turbulent fluctuations, solving for the mean flow fields alongside equations for turbulent kinetic energy (k) and its dissipation rate (ϵ\epsilon). This model is particularly effective for simulations where the flow is relatively homogeneous and isotropic, but it may not capture complex flow structures accurately, particularly in regions with high anisotropy near solid boundaries.

Application: The RANS model was well-suited for the Sandia burner, where the flow field remains relatively uniform and does not exhibit strong anisotropy and it may not capture complex flow structures accurately, particularly in regions with high anisotropy near solid boundaries

Limitations: The k-ε model may not effectively replicate complex or anisotropic turbulence patterns, such as those found in swirling flows or near solid boundaries where turbulence displays significant anisotropy.

Large Eddy Simulation (LES) Model

Turbulence Modelling: In LES, the large-scale eddies are resolved directly, while the smaller scales, where turbulence tends to be more isotropic, are modelled. [86] [87], and [88]

This approach enables more accurate representation of turbulence–combustion interactions, particularly in highly unsteady and anisotropic flows. The k-equation - sub-grid model commonly used in LES simplifies the estimation of unresolved turbulent kinetic energy, improving model performance without excessive computational cost.

LES is particularly well-suited for capturing the complex flow dynamics often seen in turblent flames, where large-scale structures dominate. Its higher fidelity makes it a preferred choice for detailed simulations involving strong turbulence–flame interactions and boundary layer effects

Large Eddy Simulation (LES) - Sydney Burner Study

In contrast, the Sydney burner case employed the Large Eddy Simulation (LES) technique due to the presence of significant large-scale turbulent structures. LES resolves the larger energy-containing eddies directly, while modelling the smaller, sub-grid scale motions using a simplified approach. Specifically, the *k*-equation sub-grid scale model was applied, which solves a transport equation for sub-grid turbulent kinetic energy (k_{sgs}) as expressed in Ren [89]

$$\underbrace{\frac{\partial(\bar{\rho}k_{sgs})}{\partial t}}_{\text{Time Derivative Term}} + \underbrace{\frac{\partial(\bar{\rho}k_{sgs}\widetilde{u_i})}{\partial x_i}}_{\text{Convection Term}} - \underbrace{\frac{\partial}{\partial x_i}\left(\bar{\rho}(v + v_{sgs})\frac{\partial k_{sgs}}{\partial x_i}\right)}_{\text{Diffusion Term}} = \underbrace{-\bar{\rho}(\frac{2}{3}\left(k_{sgs} + v_{sgs}\frac{\partial \tilde{u}_k}{\partial x_k}\right)\frac{\partial \widetilde{u_i}}{\partial x_i}}_{\text{Production Term}} \underbrace{- 2v_{sgs}\widetilde{S_{ij}}\widetilde{S_{ij}})}_{\text{Dissipation Term}} \underbrace{- \varepsilon_{sgs}}_{\text{SGS Dissipation Term}}$$

Equation 3-8

- **Time Derivative Term:**

This term represents temporal change of sub-grid kinetic energy. It reflects how the turbulent kinetic energy accumulates or dissipates in a fluid parcel as time progresses.

- **Convection Term**:

This term accounts for the transport due to mean velocity. It illustrates how k_{sgs} is conveyed across the fluid by the mean flow.

- **Diffusion Term:**

This term reflects the spreading of sub grid-scale turbulent kinetic energy across the fluid, influenced by molecular viscosity (v) and sub-grid scale turbulent viscosity (v_{sgs}). It represents how k_{sgs}diffuses through the fluid due to velocity gradients.

- **Production Term:**

This term represents the generation of turbulent kinetic energy through the interaction of turbulent stresses with the mean flow.

.**• Dissipation Term:**

This term represents the dissipation of turbulent kinetic energy due to the viscous effects at the sub-grid scale.

• SGS Dissipation Term:

This term represents the rate at which sub-grid scale turbulence kinetic energy is converted into thermal energy at unresolved scales.

This simulation approach directly resolves major turbulent eddies while modelling the smaller, more isotropic scales of turbulence. The choice of LES was driven by its capability to deliver high-fidelity simulations crucial for capturing large-scale turbulent structures and their interactions with mean flow. The enhanced resolution provided by LES is vital for accurately predicting the intricate dynamics of turbulent flows within the burner.

The decision to transition from RANS to LES for the Sydney burner was driven by the need for a more detailed and accurate representation of the turbulent and reactive flows. Despite the higher computational demands of the LES model, its ability to more accurately resolve critical flow features justified its use. The comparative analysis of both models indicated that while the RANS model provides a good first approximation, LES offers superior detail and accuracy, essential for the complex interactions in combustion simulations.

This detailed approach ensures that our simulations not only adhere to theoretical expectations but are also grounded in practical applicability, providing a robust platform for further research and development in combustion technology [48, 80].

3.5 Combustion and Reaction modelling

Combustion modelling in CFD bridges fuel properties, chemical kinetics, and fire dynamics. In OpenFOAM, solvers like reactingFoam, rhoReactingFoam, and fireFoam support non-premixed turbulent combustion simulations for gaseous hydrocarbon fuels. This section outlines the combustion models applied in the Sandia and Sydney burner studies and the reasoning behind each selection.

Eddy Dissipation Model (EDM)

The EDM assumes chemical reactions are much faster than turbulent mixing. Combustion occurs instantaneously once fuel and oxidiser are sufficiently mixed. In this model, reaction rates are governed by turbulent mixing, not chemical kinetics.

In FireFOAM, combustion is modelled using the universal approach of a global combustion equation, supplemented by the Eddy Dissipation Model (EDM) Magnussen and Hjertager [90] . The reaction rate is defined by:

$$\dot{q} = min\left(\frac{\tilde{Y}_F \tilde{Y}_O}{\tau_{turb}}, C_{EDM}\rho\right)$$

Equation 3-9

Where:

C_{EDM}: the modelling coefficient.

$\tilde{Y}_F \tilde{Y}_O$: the mass fractions of fuel and oxygen, respectively.

Application:

Used in the Sydney burner study, EDM offers computational efficiency and is suitable for engineering-scale simulations where simplified chemistry is acceptable.

Eddy Dissipation Concept (EDC)

The Eddy Dissipation Concept (EDC) model is a sophisticated approach used in computational fluid dynamics to model the interactions between turbulence and chemical reactions, particularly in combustion processes. Developed by Magnussen and Hjertager [90], the EDC model is predicated on the premise that the rate of combustion is controlled by the rate at which turbulent eddies dissipate their energy.

At the heart of the EDC model is the assumption that turbulent eddies, particularly the smallest and most energetic ones, are the primary sites for chemical reactions. These fine structures are where turbulent kinetic energy is converted into thermal energy through molecular movements. The EDC model distinguishes itself by considering both the effects of mixing and chemical kinetics on the reaction rates. It utilizes the lesser of the two rates derived from these effects to determine the overall reaction rate. This dual consideration ensures that the model can accurately simulate scenarios where either mixing or chemical kinetics dominates the combustion process.

In practical terms, the EDC model divides the combustion domain into two distinct zones: the fine structures, where the reactions occur, and the surrounding bulk flow. This division enables the EDC model to provide a detailed simulation of combustion dynamics, making it particularly valuable for studies involving complex interactions between turbulence and reactive flows.

The reaction rate for a species in the EDC model as detail in Magnussen and Hjertager [90], Kadar [84] and can be given by:

$$\overline{\omega_c} = \rho . \frac{\min(\tilde{Y}_{C_nH_mO_p;} \tilde{Y}_{\frac{O_2}{r_s}})}{\tau_t}$$

Equation 3-10

Where:

$\overline{\omega_c}$: is the mass reaction rate.

$\tilde{Y}_{C_nH_mO_p;} \tilde{Y}_{O_2}$: represent the filtered mass fractions of the fuel and Oxygen, respectively.

r_s: is the stoichiometric ratio.

ρ: is the fluid density.

τ_t: is the turbulent time scale, reflecting the time it takes for eddies to dissipate their energy, and mix the reactants effectively.

Application:

Chosen for the Sandia burner study to capture detailed flame chemistry essential for research-level combustion analysis.

Partially Stirred Reactor (PaSR)

Beside the Eddy Dissipation Concept (EDC) and Eddy Dissipation Model (EDM) in turbulent combustion, another significant model is the Partially Stirred Reactor (PaSR). The PaSR model bridges the gap between perfectly stirred reactors and laminar flame let models by considering partial mixing within cells. It separates each cell into reacting and non-reacting zones, allowing for local reaction dynamics.

The Partially Stirred Reactor (PaSR) model operates under the assumption that the reactor, or combustion zone, exhibits partial mixing characteristics. This model positions itself between the extremes of a Perfectly Stirred Reactor (PSR), where complete mixing is assumed, and scenarios akin to laminar flow, where mixing is minimal. This intermediate approach allows

for the realistic simulation of practical combustion systems, such as internal combustion engines and industrial furnaces, where both turbulence and reaction rates significantly influence the overall combustion process. This configuration is the basis for calculating reaction rates in the PaSR model Lia [91]

.

$$\widetilde{\omega}_s = k\frac{\bar{\rho}(\tilde{Y}_s - \tilde{Y}_s^*)}{\tau_{mix}(1-k)}$$

Equation 3-11

Where:

$\widetilde{\omega}_s$: mean reaction rate for species.

k: is the mass fraction of the reacting cell region.

$\tilde{Y}_s$: is the Favre-averaged mass fraction of species s in the computational cell.

$\tilde{Y}_s^*$: is target mass fraction of species s in the reacting region.

Mass fraction k is defined as detail in Kadar [84] as

$$k = \frac{\tau_c}{\tau_c + \tau_{mix}}$$

Equation 3-12

Where:

τ_c: is the chemical time scale.

τ_{mix}: is the turbulent mixing time scale.

$$\tau_{mix} = C_{mix}\sqrt{\frac{\mu_{eff}}{\bar{\rho}\tilde{\varepsilon}}}$$

Equation 3-13

Where:

C_{mix}: is a coefficient used to adjust the turbulent mixing time scale.

μ_{eff}: is the effective dynamic viscosity.

3.6 Radiation modelling

Radiative heat transfer is a significant mechanism in fire scenarios, particularly in large-scale fires where radiation dominates over conduction and convection. The Stefan–Boltzmann law, as described by Wellons [92] , governs blackbody radiation and is critical for understanding radiative heat loss:

$$\frac{P_{rad}}{A_s} = \epsilon\sigma T^4$$

Equation 3-14

Where:

$\frac{P_{rad}}{A_s}$: is the rate of the released energy per area (W/m²).

σ: is the Stefan Boltzmann constant (5.67 x 10^{-8} W/m²K⁴)

T: is the surface temperature (K).

ϵ:is the emissivity constant, = 1 for an ideal blackbody.

In real fire simulations, the Radiative Transfer Equation (RTE) describes how radiation propagates through a participating medium, accounting for absorption, emission, and scattering:

$$\frac{dI(\lambda,\vec{s})}{ds} = -\mathrm{k}(\lambda,\vec{s})I(\lambda,\vec{s}) + j(\lambda,\vec{s}) + \int_{\Omega} I\left(\lambda,\overrightarrow{s'}\right)p(\vec{s},\vec{s}')d\Omega'$$

Equation 3-15

Where:

$I(\lambda, \overrightarrow{s'})$: is the spectral radiation intensity at wavelength λ along path $\overrightarrow{s'}$.

$\frac{dI}{ds}$: is the rate of change of intensity along the path.

$k(\lambda, \vec{s})$: is the absorption coefficient.

$j(\lambda, \vec{s})$: is the emission term, representing the amount of radiation emitted per unit and wavelength.

In this study, radiation modelling is simplified by assuming a non-absorbing, non-scattering medium, with radiative losses defined as a fixed fraction of the heat released. This optically thin approximation is acceptable for the methane-fuelled flames investigated here, which are only weakly sooting, and the effects of soot are considered negligible.

FireFOAM addresses radiation transport using a finite volume implementation of the Discrete Ordinates Method (DOM), as described by J.C.CHAI [93]. This approach offers a practical compromise between accuracy and computational efficiency, particularly in large-scale turbulent fire simulation

3.7 Flame suppression modelling

In FireFOAM, fire suppression via water sprays is modelled using a classical Lagrangian particle tracking approach [94], where the liquid phase is treated as discrete spherical droplets. These droplets are injected into the computational domain with predefined velocity, size distribution, and flow rate settings. The solver tracks each droplet's trajectory and incorporates two-way coupling, allowing for the exchange of momentum, heat, and mass between the droplets and the gas phase.

A fundamental assumption in this model is that of dilute spray conditions, the dispersed liquid volume is small relative to the gas volume, and droplet–droplet interactions are neglected. This simplification is valid for spray suppression scenarios and significantly reduces computational cost while still capturing the key physics of droplet–gas interactions.

The Lagrangian-based modelling involves several critical steps:

Droplet Injection: Here, water droplets are introduced into the simulated environment based on pre-defined settings. These settings specify the size distribution of the droplets, their initial velocity, and the rate at which they are injected.

Trajectory Tracking: The model then tracks the individual path of each droplet within the simulation domain. This is achieved by solving the equations of motion, which consider forces acting on the droplets such as drag from the gas, gravity, and buoyancy. Their motion is governed by Newton's second law, considering forces such as drag, gravity, and buoyancy as described Patankar [82]:

$$\frac{\delta u}{\delta t} = F$$

Equation 3-16

Where:

u is the velocity of the droplet

F: is the forces acting on the droplet, including drag, gravity, and possibly buoyancy.

2. Heat and Mass Transfer

As droplets travel through the high-temperature gas, they absorb thermal energy and undergo evaporation. This phase change is the core suppression mechanism, as it reduces gas temperature and disrupts combustion. The heat transfer rate is given by Çengel and Ghajar [95]:

$$\frac{dT_d}{dt} = \frac{hA(T_g - T_d)}{m_d C_p}$$

Equation 3-17

Where:

T_d: is the droplet temperature.

T_g: is the gas temperature.

h: is the heat transfer coefficient.

m_d: is the mass of the droplet, and $C_p$is the specific heat capacity of the droplet.

and the mass transfer (evaporation) is expressed as:

$$\frac{d_{m_d}}{dt} = -\frac{KA(Y_g - Y_d)}{L_v}$$

Equation 3-18

Where:

K: is the mass transfer coefficient.

Y_g and Y_d: are the vapor mass fractions in the gas and at the droplet surface, respectively.

L_v:is the latent heat of vaporization.

3. Two-Way Coupling with the Gas Phase

The interaction between the spray and the surrounding gas is modelled through source terms in the gas-phase equations, accounting for:

Heat Exchange:

$$S_h = \sum hA(T_g - T_d)$$

Equation 3-19

h: heat transfer coefficient between the gas and the droplet.

A: surface area of the droplet.

T_g: $Temperature\ of\ the\ gas\ phase.$

T_d: $Temperature\ of\ the\ droplet.$

Mass Exchange:

$$S_v = \sum kA(Y_g - Y_d)$$

Equation 3-20

k: Mass transfer coefficient between the gas and the droplet.

A: Surface area of the droplet.

Y_g: Mass fraction of the species in the gas phase.

Y_d: Mass fraction of the species in the droplet

These source terms reflect the thermal and mass influence of the droplets on the surrounding fire environment, crucial for modelling the suppression effect.

3.8 Literature Benchmarking and Solver Selection Rationale

A review of recent literature indicates that ReactingFoam and FireFOAM are the most frequently used solvers in OpenFOAM for simulating non-premixed combustion. Although variants such as rhoReactingFoam are available, they are less commonly applied in fire-related studies.

This subsection summarises the latest developments in OpenFOAM-based combustion research, focusing on non-premixed flame modelling from 2010 onwards. Table 3.1 presents a collection of benchmark studies, highlighting key solver choices, case descriptions, and relevant sub-models. These references help frame the modelling strategies adopted in this thesis, particularly in relation to buoyancy- and momentum-driven flames.

A recurring pattern in the literature reveals that ReactingFoam is predominantly employed for momentum-driven combustion, typically involving high fuel injection velocities. In contrast, FireFOAM is often selected for buoyancy-driven flames, where the natural rise of hot gases plays a dominant role in flame dynamics.

Evaluation of Momentum and Buoyancy Forces Using Froude Number

The momentum and buoyancy forces can be evaluated using the Froude number (Fr) as described in details in Ho¨ hne [96]. The Froude number is a dimensionless parameter that compares inertial forces (momentum) to gravitational forces (buoyancy) and is given by:

$$F_r = \frac{U_f}{\sqrt{gl}} = \frac{momentum\ forces}{gravity\ forces}$$

Equation 3-21

Where:

F_r: Froude number

U: is the characteristic of the fuel inlet velocity.

g: is the acceleration due to gravity.

l: is the characteristic length.

When the Froude number is close to 1, both momentum and buoyancy forces have a similar impact. Values below 1 indicate that buoyancy forces dominate the flow, while values above 1 suggest that momentum forces are more significant. [96],and Wu [97] present the higher Froude numbers indicate momentum-dominated flows, while lower Froude numbers indicate buoyancy-dominated flows

Solver Selection Justified by Froude Analysis

From Table 3.1, a correlation emerges between solver selection and Froude number range:

- ReactingFoam is typically applied to combustor-type geometries, where fuel is injected at high velocities, resulting in high Fr values. These scenarios prioritise momentum effects, which dominate the combustion dynamics.
- FireFOAM, on the other hand, is associated with low-velocity flames such as pool fires or natural convection scenarios, where buoyancy dominates. These cases show lower Fr values, aligning with the solver's strength in modelling radiation, soot, and suppression mechanisms in open or semi-confined environments.

Application in the Present Study

This thesis adopts a dual-solver strategy based on the nature of each burner:

- Sandia Burner (Chapter 4): Simulated using ReactingFoam, appropriate for high-velocity, momentum-driven conditions (pilot velocities up to 11.2 m/s).
- Sydney Burner and flame suppression Cases (Chapters 6 and 7): Simulated using FireFOAM, due to the lower inlet velocity and stronger influence of buoyant plume development. FireFOAM also supports the integration of suppression models.

Authors	Year	University	Case Description	Combustion Solver	Froude number	Reference.
Jingxuan Li, Yu Xiaa, Aimee S. Morgans, Xingsi Han	2017	Imperial College London, UK Beihang University, China Nanjing University Astronautics, China	Prediction of combustion for a combustor with a long flame	ReactingFoam	9.1	Li, Xia [98]
Sedano, Lopez, Ladino, Munoz	2017	Universidad de los Andes, Colombia	Small-scale pool fire	FireFOAM	.01	Camilo Andrés, López [75]

Table 3.1 an overview of the selected references, emphasizing non-premixed combustion simulations performed with OpenFOAM

4 Studying a Diffusion Flame- Sandia burner – Using reacting Foam Solver

4.1 Introduction

In Chapter 3, the fundamental principles of combustion and the computational capabilities of OpenFOAM solvers were discussed, with a particular emphasis on ReactingFoam and FireFoam for simulating momentum- and buoyancy-dominated flame scenarios. The chapter also highlighted the importance of selecting an appropriate solver based on the dominant physical mechanisms influencing flame behaviour.

To support the development and validation of combustion models, Sandia National Laboratories conducted extensive measurements on a series of flames during the 1999 International Workshop on Measurement and Computation of Turbulent Non premixed Flames [54]. These well documented experimental flames, known as "Sandia Flames," have become benchmark cases in the combustion research community due to the availability of detailed, high-fidelity experimental datasets.

This chapter applies the ReactingFoam solver to simulate the Sandia Flame D, a controlled, well characterised diffusion flame widely used for validating numerical models. The goal is to demonstrate the accuracy and capability of ReactingFoam in predicting key combustion features under controlled conditions. The chapter outlines the computational setup, including geometry, mesh generation, boundary conditions, and the specific combustion and turbulence models implemented within ReactingFoam.

Sandia Flames D, E, and F are specifically designed to examine combustion behaviour under increasing fuel jet velocities and conditions conducive to local extinction. In this study, Flame D (as illustrated in Figure 4-2) is selected due to its stable flame structure and the availability of extensive validation data.

Simulation results will be compared with experimental measurements to evaluate model performance and establish a reliable baseline before applying the framework to more complex scenarios using FireFOAM in subsequent chapters.

4.2 Sandia Flame D Experimental Setup

The Sandia Flame D configuration, as detailed in the works of Barlow and colleagues [99] [100] [101] [4], is a well-established benchmark for turbulent combustion model validation. Developed at Sandia National Laboratories, this experimental setup involves the ignition of a partially premixed CH_4/air jet using a surrounding pilot flame. The burner, illustrated in Figure 4-1, consists of two concentric cylinders: a central fuel nozzle and an annular pilot jet. The Sandia Flame series adopted burner geometries originally established in piloted flame studies at both Sydney University and Sandia [5]. Extensive scalar measurements such as temperature, N_2, O_2, H_2O, CO_2, CO, and OH were obtained along the centreline (x/d = 5, 10, 15, ..., 80) and in radial profiles (x/d = 1, 2, 3, 7.5, 15). Detailed descriptions of the burner design, flow parameters, and diagnostic methods are available in references [100] [101] [4] [1]

4.3 Sandia Flame D: Computational Domain

The computational domain for the Sandia Flame D case is designed to replicate the experimental burner geometry and operating conditions as accurately as possible. Figure 4.1 and Figure 4.2 illustrate the physical setup and provide a magnified view of the inlet region for clarity as illustrated in TNF workshop [1].

As shown in Figure 4.3, the burner consists of three concentric flow regions:

- The main jet, coloured red, exits from the central nozzle and has a diameter of 7.2 mm. This jet introduces a premixed methane air mixture, with a volumetric composition of 25% CH_4 and 75% air.
- The pilot jet, represented in purple, surrounds the main jet and supplies combustion products from laminar flames stabilised on a perforated plate upstream of the jet exit plane.
- The co-flow region, shown in blue, envelops the entire burner assembly and delivers ambient air to replicate surrounding environmental conditions.

Figure 4-1 Sandia/TUD Piloted CH4/Air Jet Flames[1, 2]

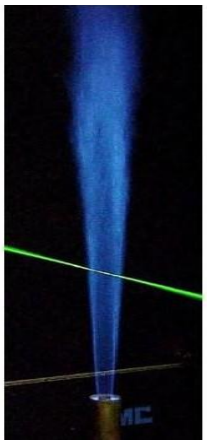

Figure 4-2 Sandia Flame D [1, 2, 4]

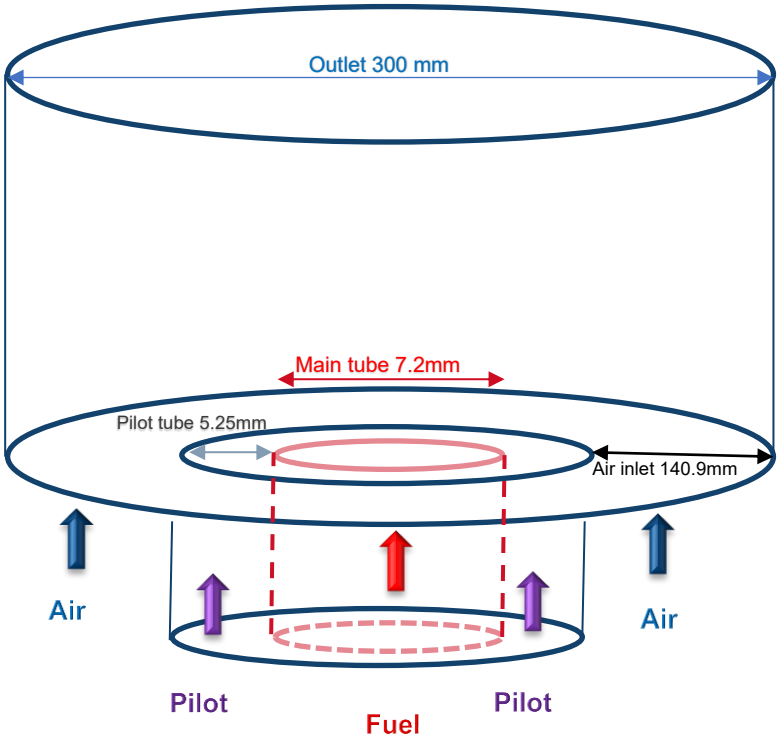

Figure 4-3 A simple schematic of the flame and the surroundings.

A physical wall separates the pilot and main jets, while an outer wall encompasses the full burner assembly. This setup is consistent with the Sandia Flame D configuration used in experimental investigations and is crucial for achieving accurate numerical simulations.

The specific boundary conditions applied to each of these flow regions are summarised in Table 4.2. These include velocity profiles, temperature, and species concentrations, which reflect the conditions established in the experimental dataset.

Figures 4.1 and 4.2 also highlight the geometric details of the burner, including the symmetry axis, domain size, and boundary locations, to support accurate grid generation and solver stability during numerical simulations.

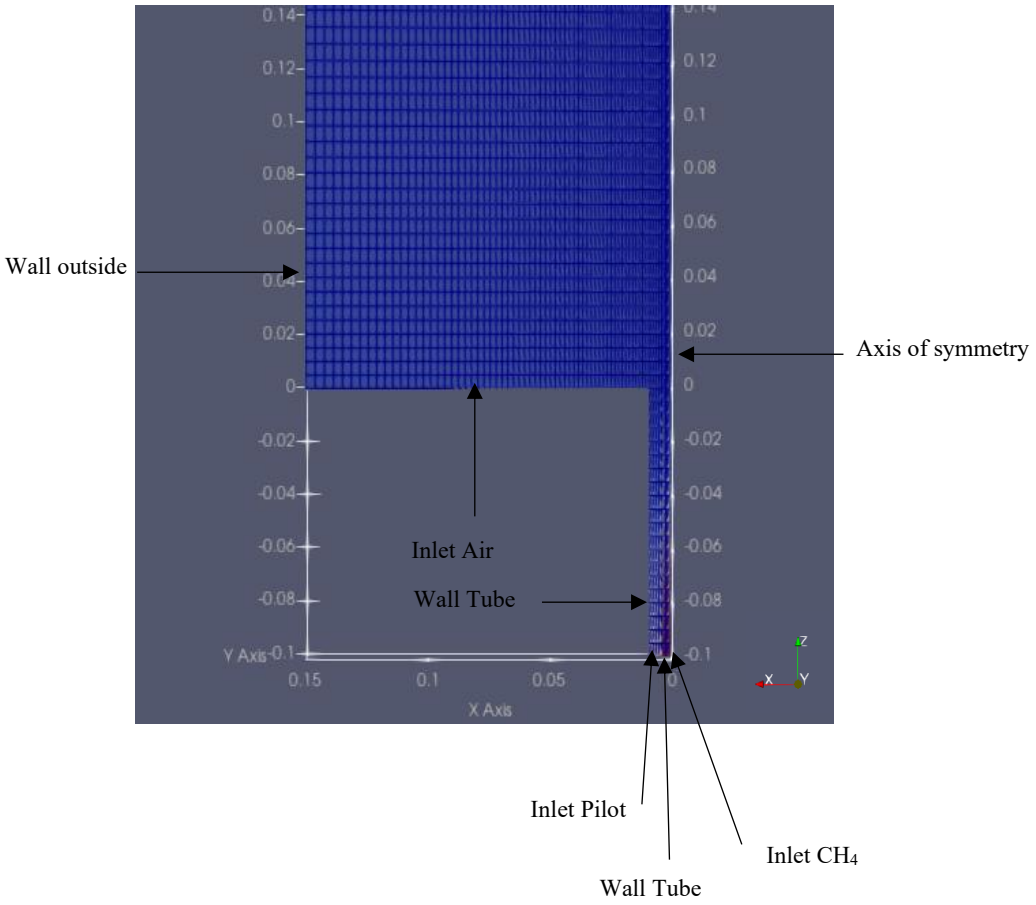

Figure 4-4 Sandia burner- inlet region.

4.3.1 Two-Dimensional Computational Mesh

Although OpenFOAM is inherently a three-dimensional solver, this case study employs a two-dimensional (2D) mesh to improve computational efficiency while preserving the essential flow and combustion characteristics. This simplification is achieved by applying specific boundary conditions such as `"empty"` or `"wedge"`, which effectively reduce the simulation to a 2D axisymmetric domain.

In this study, the Sandia Flame D configuration was modelled using a 2D axisymmetric wedge mesh in OpenFOAM. This approach involves using a narrow angular section (typically 5° or less) of the full cylindrical domain Axisymmetry is not enforced explicitly through coordinate transformation into cylindrical form but is instead approximated by setting the side boundaries to wedge type and the central axis to empty, which mimics rotational symmetry in OpenFOAM.

This is consistent with previous validated research such as the work of Kannan et al. (2022) [102], who successfully simulated the same burner using reactingFoam with an axisymmetric domain. Although the governing equations in OpenFOAM's reactingFoam solver are written in Cartesian coordinates, the axisymmetric nature of the flow is correctly enforced through the mesh design and the use of appropriate wedge and axis boundary conditions. As demonstrated in the referenced study, this approach allows for accurate resolution of axisymmetric flame structures while maintaining computational efficiency.

The structured mesh used in this study is shown in Figure 4.5 and comprises approximately 4,500 cells, predominantly hexahedral elements, with the exception of prismatic cells located near the symmetry axis. The mesh has been carefully constructed to accurately capture the geometric features of the burner and ensure appropriate resolution in key regions such as the flame zone, inlet jets, and mixing layers.

As depicted in Figures 4.4 and 4.5, the CH_4/air mixture inlet is positioned nearest to the axis of symmetry in the y-direction. It is followed by the pilot jet inlet, separated from the main jet by a physical wall boundary, which prevents premature mixing of the gas streams. A similar wall is placed around the pilot jet inlet, and both walls are assigned the same boundary condition within the simulation setup.

The outermost boundary, labelled as the "outside wall," does not represent a physical structure but rather the extent of the simulated air domain. Ambient air enters the computational domain through the interface between the burner and the outside wall, simulating the co-flow conditions observed in the experimental setup. The outlet boundary is located at the far end of the computational domain, allowing products of combustion and entrained air to exit the system.

This 2D mesh configuration strikes a balance between computational economy and modelling fidelity, enabling the investigation of key flow and combustion dynamics within a feasible time frame.

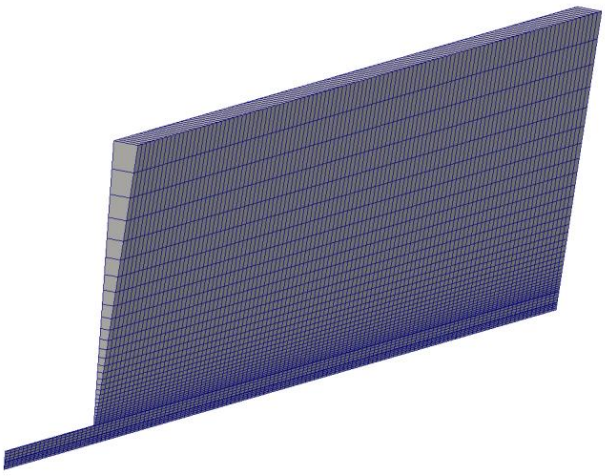

Figure 4-5 Sandia Burner- two-dimensional domain. [1]

4.4 Turbulence–Combustion Modelling of Sandia Flame D Using PaSR and k-ε in reactingFoam

The Sandia Flame D is a well-established turbulent non-premixed jet flame that serves as a benchmark for validating combustion and turbulence models in numerical fire simulations. In this study, the simulation is conducted using the reactingFoam solver in OpenFOAM, with the Partially Stirred Reactor (PaSR) model for combustion and the standard k-ε turbulence model. This sub-section outlines the rationale for selecting these models and describes their numerical implementation.

4.4.1 Model Selection

Turbulence - Combustion Interaction (PaSR):

The PaSR model is particularly suitable for simulating turbulent non-premixed Sandia flame-D, which has the lowest degree of turbulence-chemistry interaction given that it further from stoich stoichiometric conditions than the other flames (E, F). It assumes that only a fraction of the flow reacts at any given moment, with the reaction rate governed by both the chemical kinetics and turbulence timescales. This hybrid approach makes it effective for capturing the essential behaviour of diffusion flames such as Sandia Flame D, where moderate to high turbulence levels dominate combustion dynamics. [42, 85, 103]

RANS-Based Turbulence Model (k-ε):

The standard k-ε model, a two-equation Reynolds-Averaged Navier–Stokes (RANS) approach, is selected due to its computational efficiency and compatibility with reactingFoam. Although it does not resolve transient flow features like LES (Large Eddy Simulation) (FireFOAM solver), it provides a practical compromise for engineering applications by predicting the average flame shape, turbulent kinetic energy (k), and its dissipation rate (ε). This enables stable numerical performance and effective coupling with the PaSR combustion model. [81, 104]

4.4.2 Numerical Implementation in reactingFoam

Within the reactingFoam solver, the PaSR model operates by dividing each computational cell into reacting and non-reacting zones. The reacting portion is assumed to behave as a perfectly stirred reactor, allowing for the immediate completion of reactions, while the non-reacting part contributes to the overall mixing process. The solver integrates this with the turbulence model to determine the turbulence-chemistry interaction timescale, which governs reaction progress.

The k-ε turbulence model calculates turbulent viscosity and enhances the resolution of flow properties required by the combustion model. This configuration, combining the PaSR model with k-ε under reactingFoam, has been widely adopted in literature as a robust and computationally efficient method for initial validation against benchmark flames like Sandia Flame D.

4.5 Sandia Flame D: Boundary conditions

Boundary Conditions

In computational fluid dynamics (CFD), accurately specifying boundary conditions (BCs) at the edges of the computational domain is critical. These conditions govern how the fluid interacts with domain boundaries and play a vital role in determining the stability and realism of the solution.

For the Sandia Flame D simulation, boundary conditions were carefully assigned to replicate experimental settings and ensure convergence and physical accuracy. The prescribed boundary conditions are summarised in Table 4.2 and Table 4.3

Inlet Conditions

The jets (main, pilot, and co-flow air) were modelled with Dirichlet boundary conditions, using the fixedValue keyword in OpenFOAM. These explicitly define the velocity vectors, temperature, and species mass fractions at the inlet boundaries.

Other Boundaries:

For all other boundaries, a zero-gradient condition ("zeroGradient" keyword) is applied to these variables (velocities, temperatures, and mass fractions), signifying Neumann boundary conditions. This implies minimal to no change in these properties across these boundaries.

Table 4.3 details the remaining boundary conditions. Notably, pressure uses a Neumann condition at the inlet and a Dirichlet condition at the outlet. This approach is often preferred for pressure to enhance numerical stability during the simulation.

Turbulence Quantities

Turbulence modelling requires additional boundary conditions at the inlets, based on standard formulations widely adopted in the literature[1, 105-107]

Turbulent Kinetic Energy: The turbulent kinetic energy (k) at the inlets is set using the "turbulentIntensityKineticEnergyInlet" boundary condition. This condition calculates k based on a specified turbulent intensity value (I). The formula used for this calculation is:

$$k = \frac{3}{2}(|U|.I)^{2}$$

Equation 4-1

Where:

$|U|$: Magnitude of the velocity vector.

I: Turbulent intensity.

Turbulent Dissipation Rate: The turbulent dissipation rate (ε) at the inlets is set using the "turbulentMixingLengthDissipationRateInlet" boundary condition, which calculates ε as:

$$\varepsilon = C_{\mu}^{.75}\frac{k^{1.5}}{L}$$

Equation 4-2

Where:

ε: Turbulent dissipation rate.

C_{μ}: Turbulent viscosity constant (typically set to .09).

k:. Turbulent kinetic energy.

L: Characteristic length scale.

Turbulent Thermal Diffusivity: The turbulent thermal diffusivity (α_t) is not explicitly set but rather calculated during the simulation based on the turbulent transport equation:

$$\alpha_t = \frac{\mu_t}{P_{r\,t}}$$

Equation 4-3

$$\mu_t = \rho C_\mu \frac{k^2}{\varepsilon}$$

Equation 4-4

Where:

α_t: Turbulent thermal diffusivity.

μ_t: Turbulent viscosity.

$P_{r\,t}$: Turbulent Prandtl number.

Turbulent Thermal Diffusivity	α_t
Turbulent Dynamic Viscosity	μ_t
Turbulent Kinetic Energy	k
Turbulent intensity	I
Magnitude of the velocity vector	|U|
Turbulent Dissipation Rate	ε
Turbulent Prandtl Number	($P_{r\,t}$

Table 4.1 table of nomenclature

Wall Patches

Wall patches (labelled "wall") in the domain utilise wall functions for turbulent quantities to approximate near-wall effects without requiring extremely fine mesh resolution. The following are applied:

- Turbulent kinetic energy (k)
- Dissipation rate (ε)
- Thermal diffusivity (α_t)
- Dynamic viscosity (μ_t)

Side Patches

For 2D simulations, wedge boundary conditions were applied to the `"side"` patches, enabling axisymmetric simulation with only a narrow wedge of the full geometry. This significantly reduces computational cost while preserving physical accuracy.

Summary of Physical Properties and Conditions

Table 4.2 presents the experimental inlet conditions adopted from the Sandia Flame D dataset, including temperature, axial velocity, and species mass fractions for the main jet, pilot jet, and co-flow air stream. These values serve as reference inputs for the numerical model. Table 4.3 outlines the boundary conditions prescribed in the numerical simulation for each patch, including pressure, velocity profile, turbulence intensity (via turbulent kinetic energy and length scale), and wall functions for thermal and momentum variables. The wall and outlet conditions follow standard OpenFOAM boundary condition conventions to ensure stable simulation of the turbulent diffusion flame.

	Temperature (K)	Velocity (m/s)	Mass compositions				
			CH_4	O_2	H_2O	CO_2	N_2
Main jet	294	(49.6,0,0)	.1561	0.1966	0	0	0.6473
Pilot jet	1880	(11.4,0,0)	0	0.054	0.0942	0.1098	.742
Air Flow	291	(.9,0,0)	0	0.23	0	0	.77

Table 4.2 Physical properties - Sandia D experimental boundary conditions

WF: WallFunction

	Pressure (Pa)	Velocity (m/s)	k Turbulent kinetic energy	ε Turbulent dissipation rate	μ_t Dynamic viscosity	α_t Thermal diffusivity
inletCH4	*zeroGradient*	*(0 0 49.6)*	$I = 0.0458$	$L = 0.000504$	*calculated*	*calculated*
inletPilot	*zeroGradient*	*(0 0 11.4)*	$I = 0.0628$	$L = 0.000735$	*calculated*	*calculated*
inletAir	*zeroGradient*	*(0 0 0.9)*	$I = 0.0471$	$L = 0.019677$	*calculated*	*calculated*
WallTube	*zeroGradient*	*noSlip*	*kqRWF*	*epsilonWF*	*mutWF*	*alphatWF*
WallOutside	*zeroGradient*	*zeroGradient*	*kqRWF*	*epsilonWF*	*mutWF*	*alphatWF*
outlet	100000	*calculated*	*inletOutlet*	*zeroGradient*	*calculated*	*calculated*

Table 4.3 Sandia D the boundary conditions prescribed in the numerical simulation

Time Stepping for Stable Simulations

The simulation employed the PISO (Pressure-Implicit with Splitting of Operators) algorithm, which requires careful time step management to ensure numerical stability. A key parameter is the Courant number (C).

$$C = \frac{u\Delta t}{\Delta x}$$

Equation 4-5

Where:

- U is the local velocity,
- Δx is the cell size,
- Δt is the time step.

Smaller cells require smaller time steps, which enhances accuracy but increases computational time. This presents a trade-off between precision and efficiency.

Accuracy vs. Computation Time

While smaller cells enhance accuracy, they come at a cost:

Increased Computation Time: Simulations with very fine meshes necessitate many time steps to reach a solution, significantly increasing computation time. This can become a bottleneck for complex simulations.

Local Time Stepping

OpenFOAM offers Local Time Stepping (LTS), unlike the global time step approach, LTS calculates a unique time step for each cell based on the Courant number.

By using cell-specific time steps, LTS can potentially achieve steady-state solutions more efficiently compared to a global time step approach, particularly for problems with varying flow characteristics or heat sources Pang [108]

4.6 Sandia Flame D: Chemical Reaction Mechanism

The simulation employs a simplified reaction mechanism based on the GRI-3.0 library [109]. This library provides a comprehensive set of chemical reactions and thermodynamic data for combustion processes. However, to improve computational efficiency, the mechanism used here focuses specifically on methane combustion and neglects all reactions involving nitrogen (N2). This reduced mechanism includes 36 species participating in 219 chemical reactions.

4.7 Sandia Flame D: Mesh Refinement Strategy

Computational Fluid Dynamics (CFD) simulations require the discretisation of the computational domain into a finite number of control volumes or mesh cells. The accuracy of simulation results is strongly influenced by the mesh resolution, particularly in turbulent reacting flows where the interplay between turbulence and combustion introduces highly complex and multiscale phenomena.

A finer mesh enables more precise resolution of velocity gradients, scalar fields, and flame structure. However, increasing mesh density substantially raises the computational cost, both in terms of memory usage and simulation time. Therefore, a trade-off must be achieved between maintaining sufficient accuracy and ensuring computational efficiency.

To address this, the present study implemented a block-based mesh refinement strategy. The approach commenced with a base mesh consisting of approximately 4,500 structured hexahedral cells. Two levels of progressive refinement were applied, focusing specifically on regions of critical importance namely, the burner exit and flame zone, where the interaction between turbulent mixing and chemical reactions is most prominent.

The refinement strategy resulted in the following mesh resolutions:

Base mesh: ~4,500 cells

First refined mesh: ~10,120 cells

Second refined mesh: ~24,300 cells

Each refinement level was designed to enhance the spatial resolution of the solution in areas with steep gradients and complex flow features, while keeping the peripheral regions coarser to conserve computational resources.

The effectiveness of this refinement strategy will be assessed through a mesh convergence study, which will be presented in a subsequent section. That section will include a comparative analysis of key physical quantities across the three mesh levels, along with plots illustrating the influence of mesh resolution on simulation results.

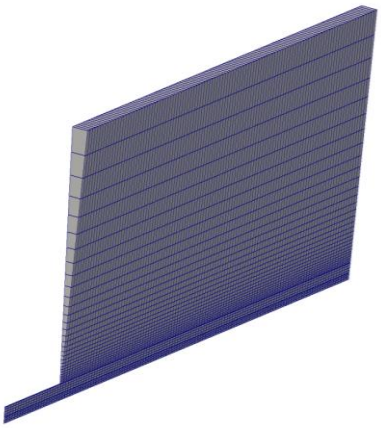

Figure 4-6 Sandia burner - 4500 cells.[1]

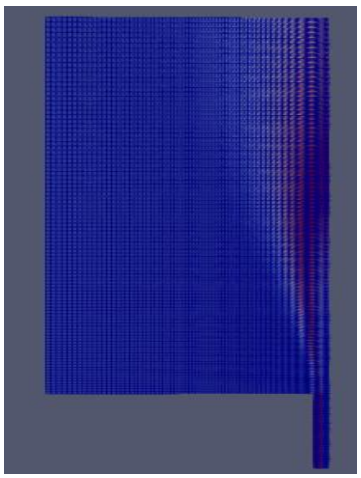

Figure 4-7 Sandia burner - 10120 cells.

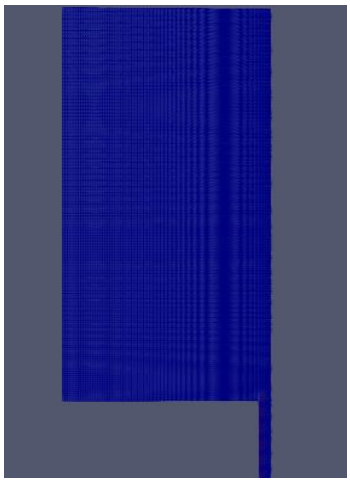

Figure 4-8 Sandia burner - 24300 cells.

4.8 Sandia Flame D: Simulation setting

The simulation of the Sandia Flame D was conducted using OpenFOAM's reactingFoam **solver**, which is specifically designed for compressible, turbulent, reacting flows with species transport. The simulation setup includes a combination of numerical schemes, turbulence modelling, and chemical kinetics solvers tailored to balance stability, accuracy, and computational efficiency. A summary of the simulation settings is provided in Table 4.4 and described below:

4.8.1 Chemistry Settings

The simulation considers methane-air combustion, with nitrogen (N_2) defined as the inert species. A reduced chemical mechanism is implemented, as detailed in Section 4.5, focusing exclusively on hydrocarbon combustion.

The chemical source terms are solved using an ODE-based solver, with the following tolerances for numerical accuracy:

Absolute tolerance (absTol): 1×10^{-12}
Relative tolerance (relTol): 1×10^{-7}
Initial chemical time step: 1×10^{-7} seconds

4.8.2 Turbulence Modelling

The Reynolds-Averaged Navier–Stokes (RANS) approach is employed using the standard k–ε turbulence model, as specified in the `RASProperties` file.

4.8.3 PIMPLE Algorithm

The solver uses a PIMPLE algorithm, which combines the advantages of PISO and SIMPLE algorithms. This method is particularly suited for transient flows with moderate to large time steps, offering a balance between computational efficiency and numerical stability. In the present study, the PIMPLE algorithm is adopted to ensure accurate pressure-velocity coupling in unsteady flame simulations.

nOuterCorrectors: 3: defines the number of PIMPLE iterations per time step, allowing for better convergence of non-linear terms.

nCorrectors: 1: sets the number of PISO pressure corrector steps within each outer iteration.

4.8.4 Solvers for Equations

Pressure (p): Solved using the PCG (Preconditioned Conjugate Gradient) method.

Other variables (e.g., velocity **U**, enthalpy **h**, turbulent kinetic energy **k**, dissipation rate **ε**, and species mass fractions $\mathbf{Y_i}$): Solved using PBiCGStab (Preconditioned Bi-Conjugate Gradient Stabilised) method.

Category	Setting / Value
Chemistry	
Inert Species	**N_2**
Chemistry Solver	**ODE-based**
Absolute Tolerance	**1×10^{-12}**
Relative Tolerance	**1×10^{-7}**
Initial Time Step	**1×10^{-7}**
Turbulence Model	**RANS – k–ε model**
PIMPLE Algorithm	
nOuterCorrectors	**3**
nCorrectors	**1**
Linear Solvers	
Pressure (p)	**PCG**
U, h, k, ε, Y_i	**PBiCGStab**
Numerical Schemes	
Time Derivative	**localEuler**
Gradient Scheme	**Gauss linear**
Divergence Scheme	**Gauss linear**
Laplacian Scheme	**Gauss linear orthogonal**
Interpolation Scheme	**linear**
snGrad Scheme	**orthogonal**

Table 4.4 Numerical setting for Sandia Burner-flame D

4.9 Sandia Flame D: Simulations results

The Sandia Flame D dataset provides high-quality experimental data essential for validating numerical simulations. The dataset includes measurements of:

Species mass fractions
Temperature
Velocity
Turbulent kinetic energy

These were recorded at various axial positions along the flame, from the burner exit at x/d = 1 to the flame tip at x/d = 75, where x is the axial distance from the burner exit and d is the diameter of the main jet nozzle (7.2 mm). Radial profiles of each variable were collected at these positions and scaled by the jet diameter to ensure consistent spatial reference.

At each selected axial location (x/d), simulation results are compared along the radial direction (r/d), where r is the radial distance from the burner axis and d is the main jet nozzle diameter

To establish a stable initial condition for the flow field before considering combustion, all Sandia Flame D simulations were run for an initial 1500 Local Time Stepping (LTS) iterations with the chemical reactions turned off. This allows the simulation to reach a steady-state solution for the fluid dynamics without the complexities of chemical heat release.

Once a converged cold flow profile was achieved, the chemical reactions were activated in the simulations. The simulations then continued for an additional 5000 LTS iterations to capture the full effects of combustion on the flow field and temperature distribution.

Two axial positions—x/d = 1 and x/d = 15 were selected for detailed analysis. Line sampling of 1000 points was applied at each location to extract high-resolution profiles for comparison with experimental data. The results are presented in the following subsections.

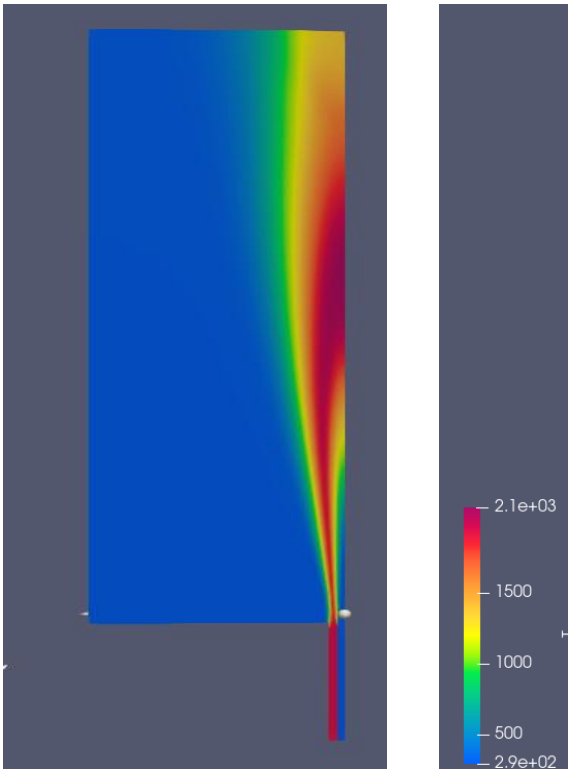

Figure 4-9 Sandia Flame D flame shape.

4.9.1 Temperature

Figures 4.10 and 4.11 present the temperature profiles from the simulations compared to experimental measurements at **x/d = 1** and **x/d = 15**. These comparisons were conducted for three mesh configurations:

- **Original mesh**: 4500 cells
- **Refined-1**: 10120 cells
- **Refined-2**: 24300 cells

These plots demonstrate how well the numerical results match the experimental data and the impact of mesh refinement on simulation accuracy.

4.9.1.1 Temperature at x/d=1:

The experimental data (T (Exp.)): The experimental data show a peak temperature near 1800 K and shows a clear radial distribution.

The original mesh (4500 cells): captures the overall trend but underestimates the peak and outer profile.

The Refined-1 mesh (10120 cells): Shows improved alignment with experimental data, especially near the peak temperature.

The Refined-2 mesh (24300 cells): shows minimal improvement beyond Refined-1. This suggests that the mesh resolution achieved with Refine-1 is sufficient to capture the temperature distribution within the methane-air jet flame for the present study.

4.9.1.2 Temperature at x/d=15:

The experimental data: Displays a peak around 1800 K with a broader distribution.

The original Model (4500 cells): Demonstrates significant deviations, especially in the peak region and the outer edges.

The Refined-1 mesh (10120 cells): Provides the most accurate results, almost overlapping with the experimental data.

The Refined-2 mesh (24300 cells): The transition from Refine-1 (10120 cells) to Refine-2 (24300 cells) does not yield significant improvements in the temperature profiles. However, the simulation results tend to underpredict temperature values at radial distances greater than r/d = 1.5 compared to the experimental data, as seen in Figure 4.11. These differences may be attributed to limitations of the RANS turbulence model in capturing fine-scale mixing at the flame periphery. These findings suggest that Refined- 1 (10120 cells) provides sufficient resolution to accurately model temperature distribution in the flame.

T(Exp)	Temperature values- experimental results-[2, 4]
T(O)-4500 cells	Temperature value-Original model-4500 cells.
Refine-1	Temperature value-Refine-1-10120 cells
Refine-2	Temperature value-Refine-1-24300 cells

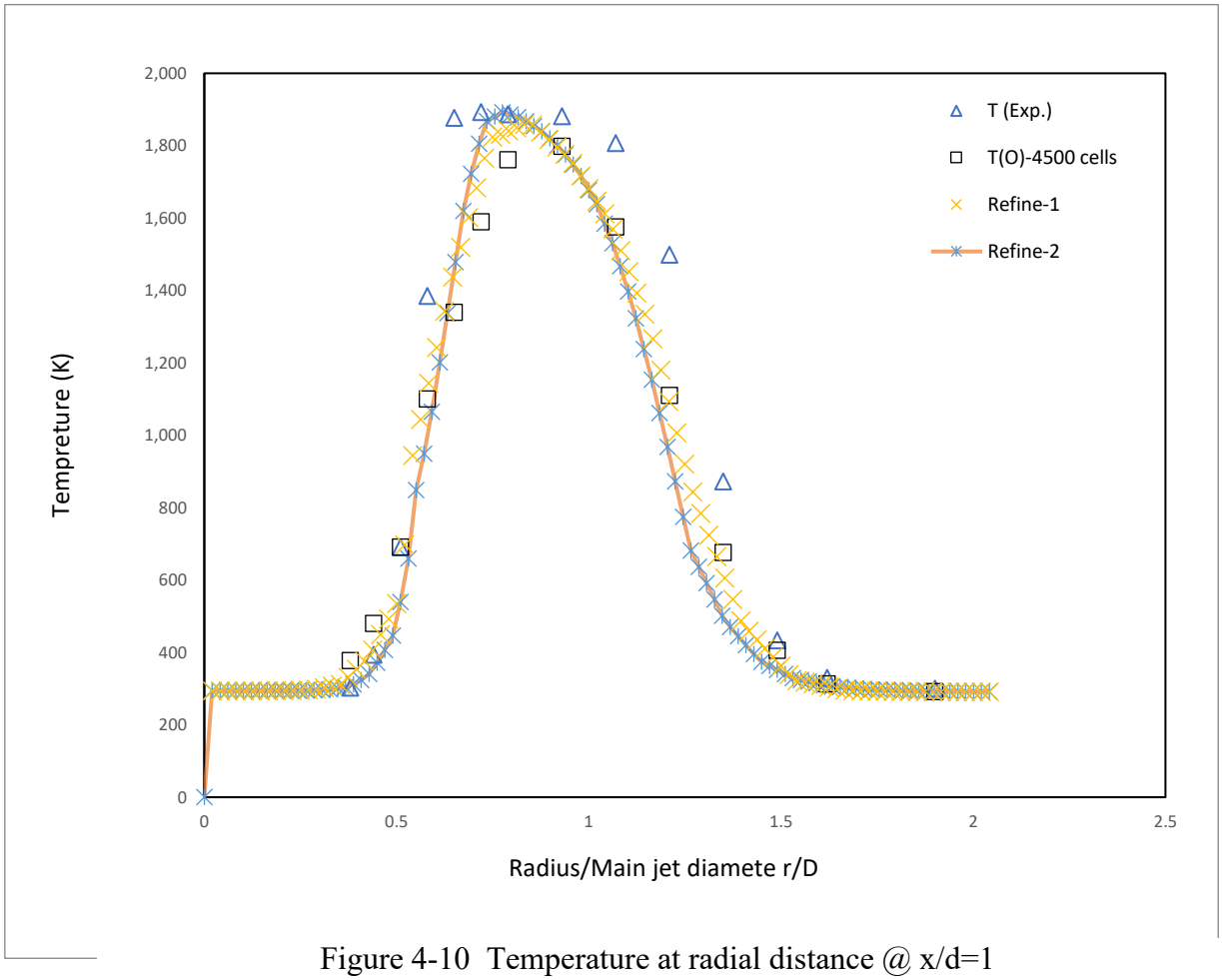

Figure 4-10 Temperature at radial distance @ x/d=1

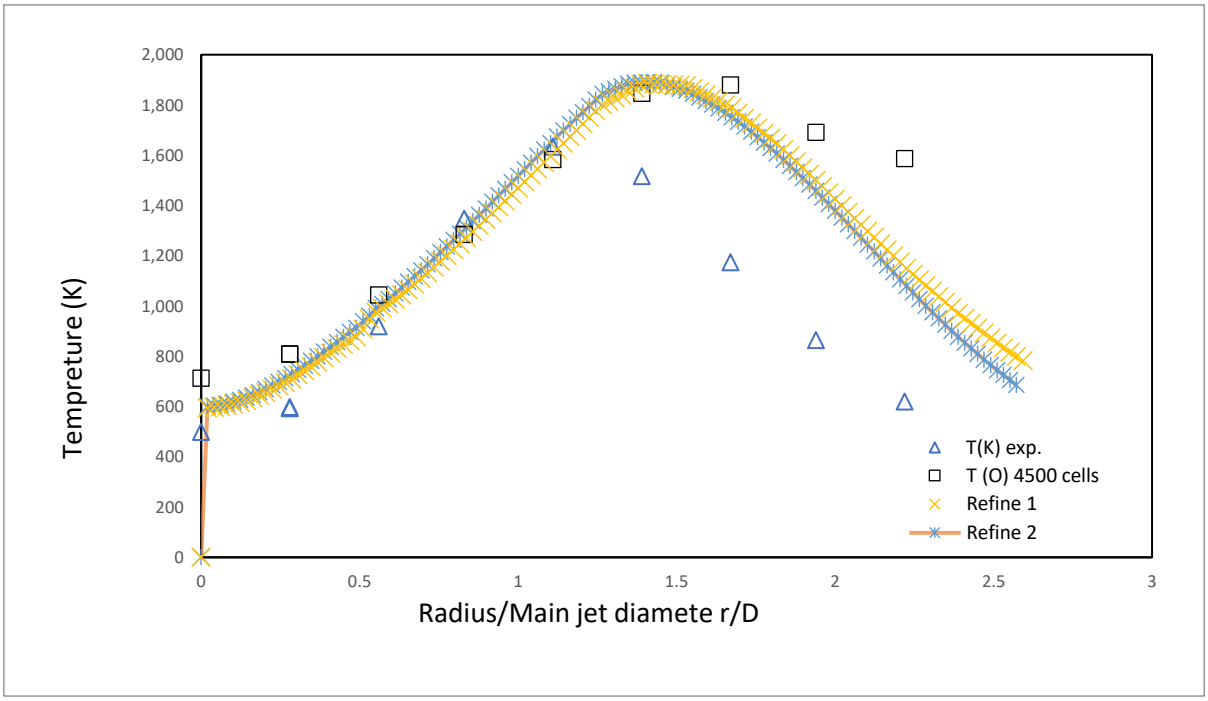

Figure 4-11 Temperature at radial distance @x/d=15

4.9.2 O_2 mass fraction

Figure 4-12, and Figure 4-13 show the O_2 mass fraction profiles at x/d = 1 and x/d = 15. To validate the numerical simulations, the mass fraction profiles of O2 at two axial positions, were compared against experimental data.

The comparisons included the original model with 4500 cells, the first refinement with 10120 cells, and the second refinement with 24300 cells. These plots demonstrate how well the numerical results match the experimental data and the impact of mesh refinement on simulation accuracy.

It is important to note that the O2 mass fraction is expected to decrease significantly within the flame zone due to consumption during the combustion process. This is reflected in both the experimental data and the simulation results. However, some discrepancies are observed, particularly near the centreline (axis of symmetry) of the flame.

4.9.2.1 Mass Fraction of O2 at x/d=1:

The experimental data: The O2 concentration shows a clear radial distribution, with a peak value around 0.22.

The original Model (4500 cells): Captures the general trend but deviates from experimental data, particularly in the inner and outer regions.

The Refined-1 mesh (10120 cells): Matches the experimental data closely, with minimal deviation, indicating the refinement's effectiveness

The Refined-2 mesh (24300 cells): The transition from Refine-1 (10120 cells) to Refine-2 (24300 cells) does not yield significant improvements in the profile.

4.9.2.2 Mass Fraction of O2 at x/d=15

The experimental data: Displays a peak around 0.21 with a broader distribution.

The original model: Demonstrates significant deviations, especially in the inner and outer edges.

The Refined-1 mesh : Shows better accuracy, closely following the experimental trend.

The Refined-2 mesh: The transition from Refine-1 (10120 cells) to Refine-2 (24300 cells) does not result in notable improvements in the profile.

The Refined-1 mesh: Shows better accuracy, closely following the experimental trend. Nonetheless, the simulation slightly overpredicts the O_2 mass fraction near the axis of symmetry ($r/d < 0.5$) and underpredicts it in the outer radial regions ($r/d > 1.5$), indicating that further improvements in modelling near-field turbulence and radial diffusion could be beneficial.

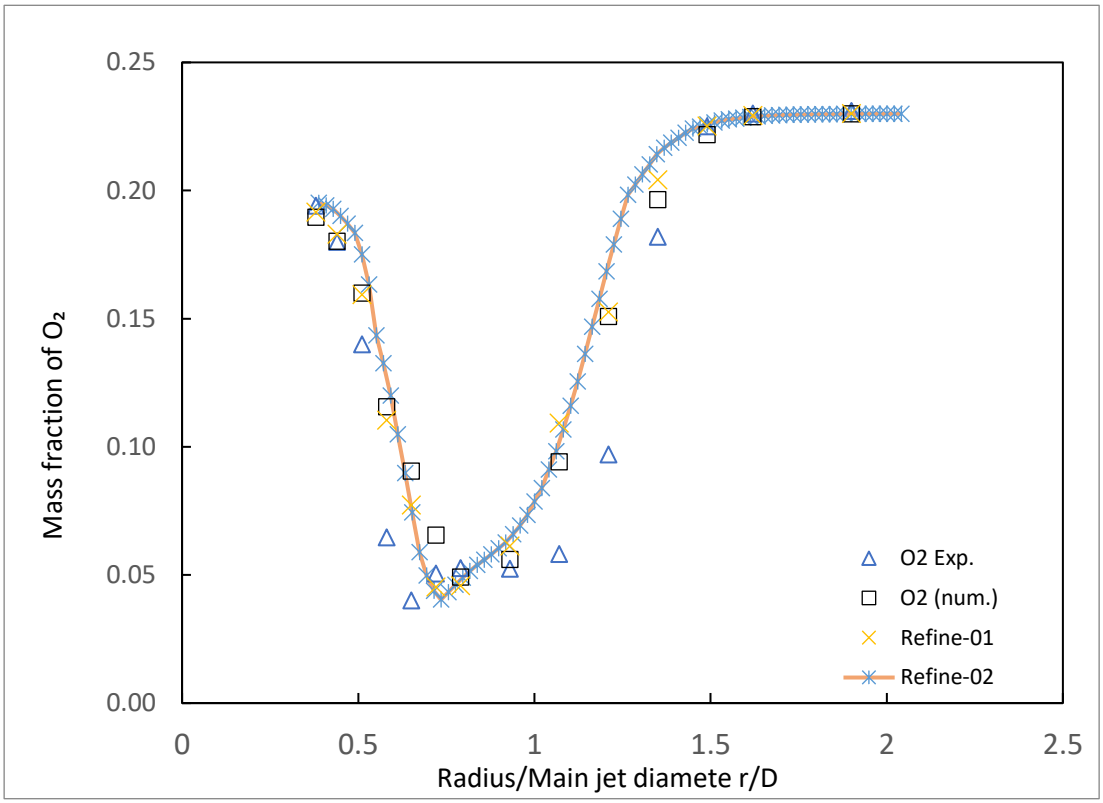

Figure 4-12 Mass fraction of O_2 at radial distance @X/D=1

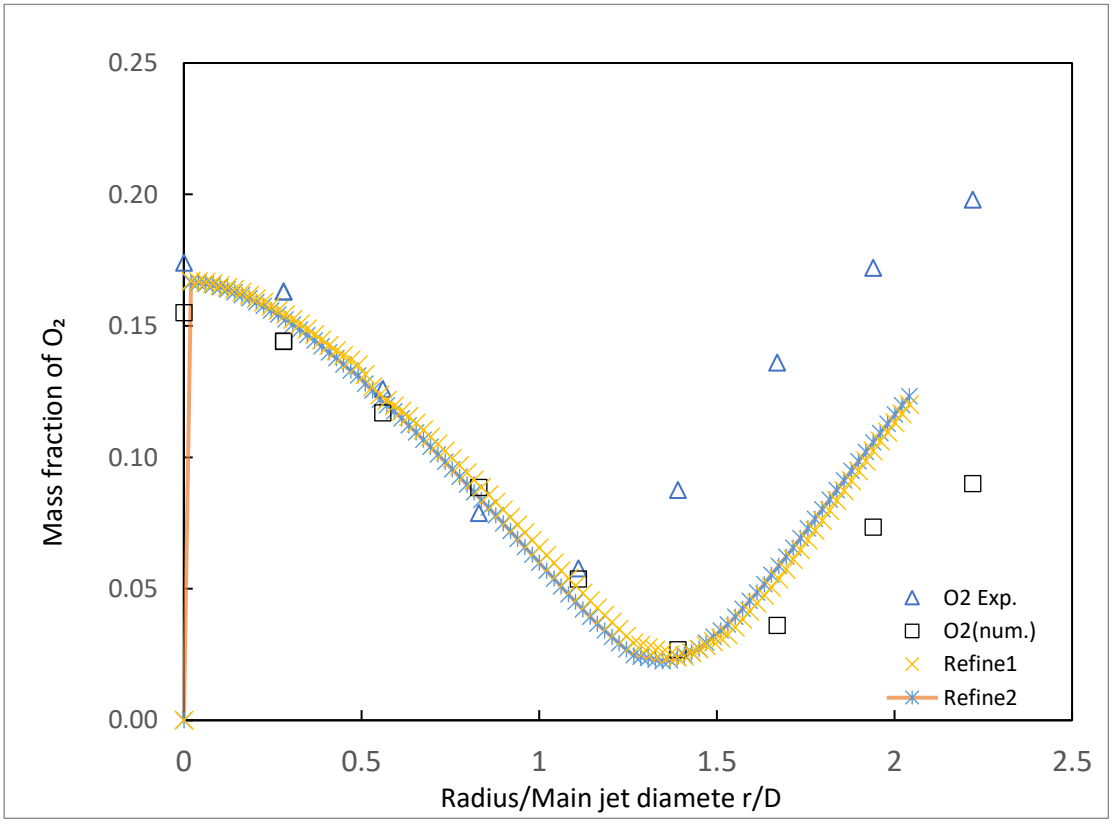

Figure 4-13 Mass fraction of O_2 at radial distance @X/D=15

4.9.3 CO_2 mass fraction

Figures 4-14 and 4-15 the CO_2 mass fraction profiles at x/d = 1 and x/d = 15.

4.9.3.1 CO_2 Mass Fraction at x/d=1

The experimental data: Shows a significant increase in CO2 concentration radially outward from the centreline.

The original model (4500 cells): Captures the overall trend but underestimates CO2 concentration near the centreline and richer fuel regions.

The Refined-1 mesh (10120 cells) and Refined-2 (24300 cells): Both show similar results, indicating that Refine-1 is sufficient for capturing CO2 profiles at this position. However, small deviations persist at radial distances beyond r/D > 1.5, where the simulation slightly overestimates CO_2 concentration compared to experimental results. This discrepancy may be attributed to the limitations of RANS in modelling the slow diffusion of combustion products in the outer, low-turbulence region of the plume**.**

4.9.3.2 CO_2 Mass Fraction at x/d=15

The experimental data: Demonstrates higher CO_2 concentrations in the product region compared to the preheat zone.

The simulation Results: Both refinements (Refine-1 and Refine-2) show similar trends but slightly underestimate CO_2 near the centreline.

Nonetheless, the simulation results slightly diverge from the experimental profile beyond r/D > 1.8, where a downward trend in experimental CO_2 is not fully captured in the numerical results. This could result from residual numerical diffusion or simplified combustion chemistry in the reactingFoam solver**.**

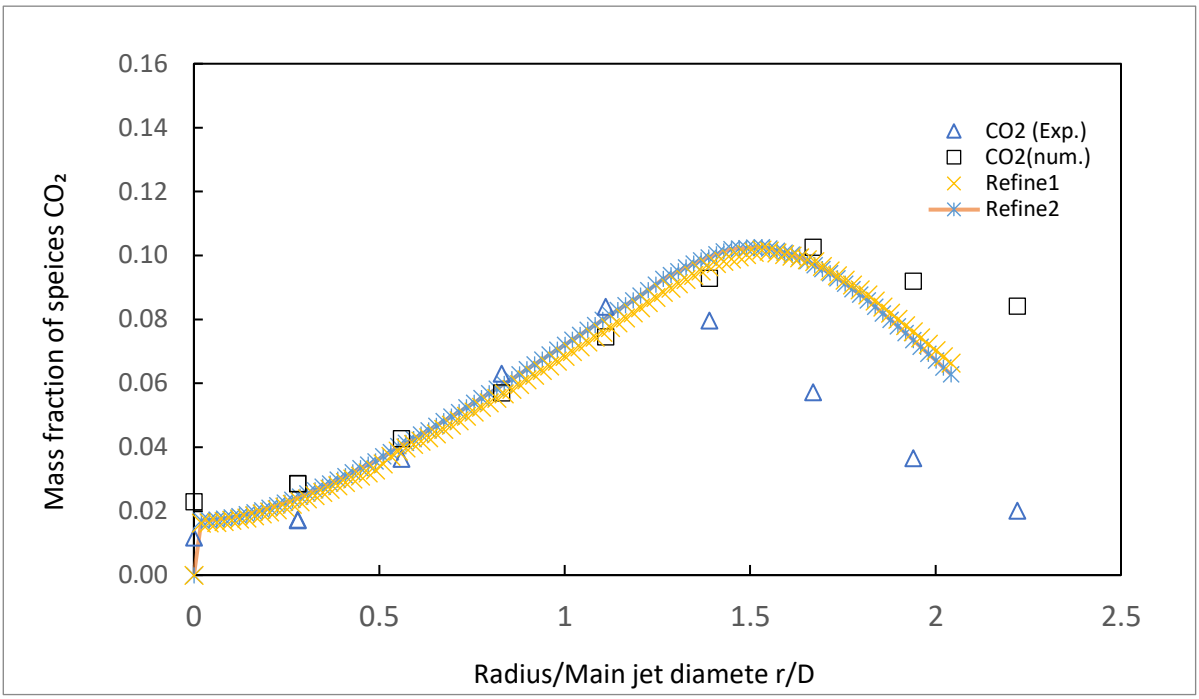

Figure 4-15 Mass fraction of CO_2 @ X/D=15

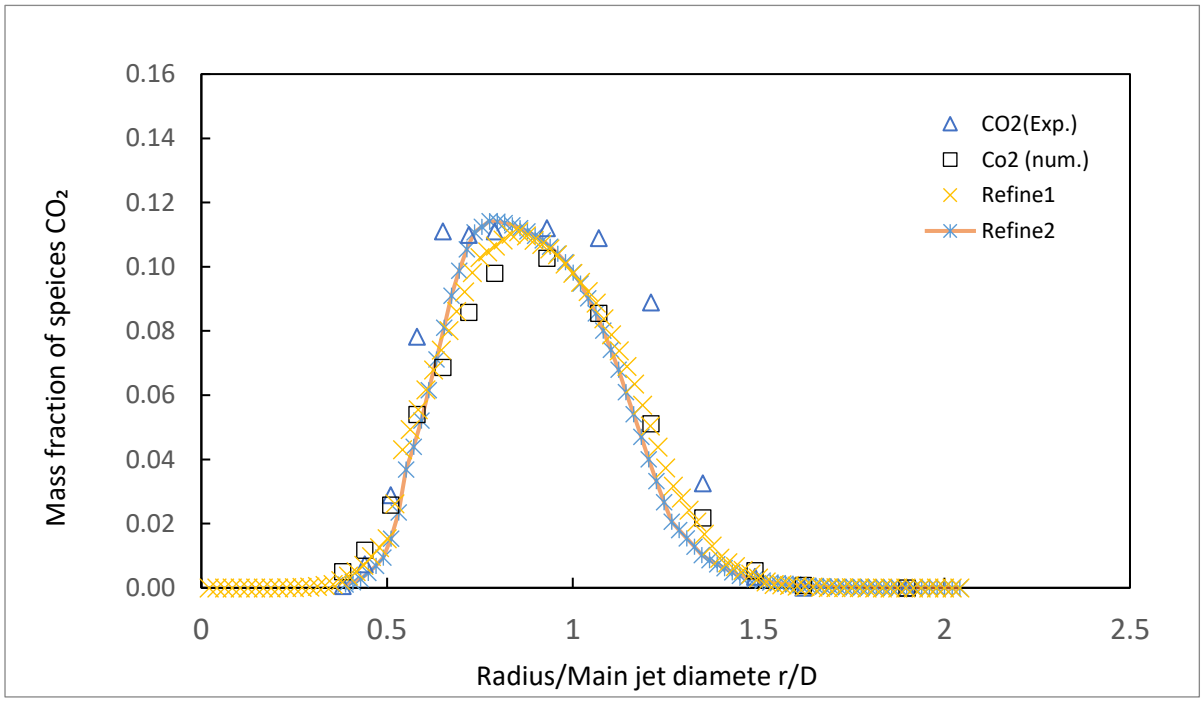

Figure 4-14 Mass fraction of CO_2 at radial distance @X/D=1

4.9.4 CH_4 mass fraction

Figure 4-16 and Figure 4-17illustrate the CH4 mass fraction profiles obtained from the simulations alongside the experimental data for the methane-air jet flame.

4.9.4.1 CH_4 Mass Fraction at x/d=1

The experimental: Shows a sharp decrease in CH4 concentration radially outward from the centreline.

The original model: Captures the trend but underestimates CH4 near the centreline.

The Refined-1 (10120 cells) and Refined-2 (24300 cells): Closely match the experimental data, indicating that Refine-1's resolution is sufficient.

4.9.4.2 CH_4 Mass Fraction at Radial Distance x/d=15

The experimental data (CH4 (Exp.)): Exhibits a gradual decrease in CH4 concentration radially outward.

The Simulation Results: Both refinements (Refined-1 and Refined-2) show similar trends but slightly underestimate CH4 near the centreline. Large CH4 concentration gradients cause numerical diffusion due to the finite cell count in the computational domain.

The simulations generally follow expected CH_4 consumption patterns, and Refined-1 proves sufficient to resolve key features.

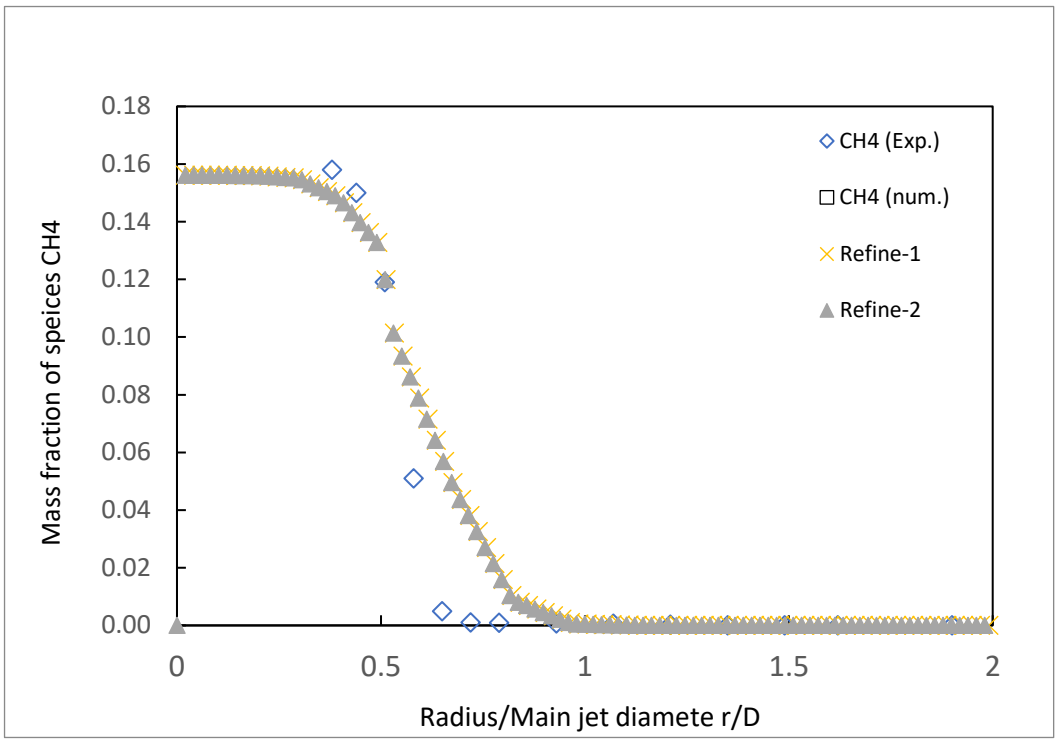

Figure 4-16 Mass fraction of CH_4 @ X/D=1

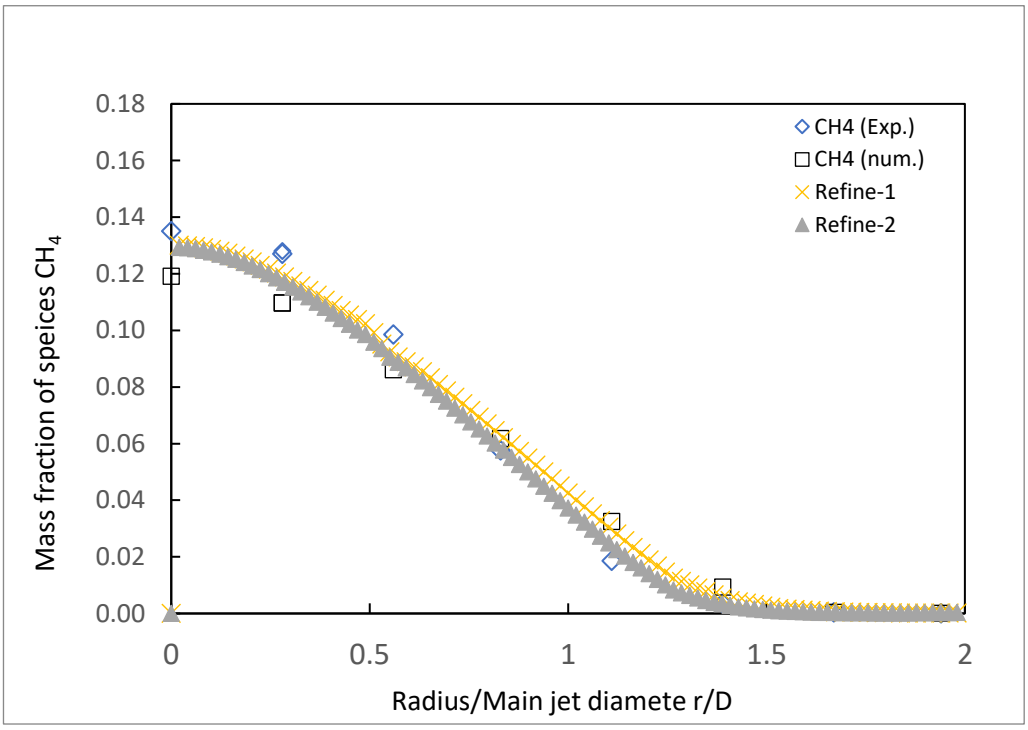

Figure 4-17 Mass fraction of CH_4 @ X/D=15

4.10 Sandia Flame D: Conclusion

This chapter presented the results of simulating the Sandia Flame D using the reactingFoam solver. The study compared numerical predictions of temperature, and species mass fractions of O_2, CO_2, and CH_4 against experimental data.

Overall, the simulations demonstrated good agreement with experimental trends, particularly in the preheat and reaction zones. The temperature predictions showed high accuracy when using the Refined-1 mesh (10120 cells), indicating that this resolution effectively captures thermal gradients within the flame. Nonetheless, some deviations were observed, especially at larger radial distances ($r/d > 1.5$) in the temperature field at $x/d = 15$ (Figure 4.11), where the simulations underpredicted peak temperatures near the flame periphery.

For species predictions, while the simulations followed the expected trends, noticeable deviations were also found. In particular, CO_2 mass fraction profiles showed discrepancies at radial distances beyond $r/d > 1.5$ in Figure 4.14 and $r/d > 1.8$ in Figure 4.15, where the numerical results slightly overpredicted or failed to follow the decline seen in experimental data. Similar minor deviations were also observed in O_2 predictions near the centreline and outer regions.

These deviations are likely due to model limitations, including the use of the RANS turbulence model, which tends to oversimplify the flow fluctuations, numerical diffusion effects due to mesh resolution, and the simplified combustion chemistry used in the reactingFoam solver**.**

It is also worth noting that the experimental data used for comparison were obtained using laser diagnostics such as Rayleigh scattering for temperature and Raman spectroscopy for species measurements. These measurement limitations may contribute to the minor deviations observed in the simulation results.

Importantly, the transition from Refined-1 to Refined-2 did not result in significant improvements, suggesting that Refined-1 provides an optimal balance between accuracy and computational cost for this study.

4.11 Transition to USYD Burner Simulation Using LES-Based Modelling &Fluent ANSYS:

The simulation of Sandia Flame D in this chapter has provided a valuable baseline for validating combustion and turbulence models using a well-established, simple, and reproducible configuration. By employing the reactingFoam solver with the PaSR combustion model and the k-ε RANS turbulence model, the numerical framework has demonstrated its ability to capture key features of non-premixed turbulent jet flames. This validation step serves as an essential foundation for advancing to more complex and realistic fire scenarios.

However, the Sandia flame represents an idealised laboratory case with well-characterised boundary conditions and moderate turbulence. In contrast, the next stage of this study focuses on the USYD burner, which introduces enhanced turbulence through perforated plates and a more practical burner configuration. To accurately simulate the strong buoyancy effects, swirling structures, and transient flame dynamics observed in the USYD burner, it is necessary to adopt a higher-fidelity turbulence modelling approach.

Therefore, the study now transitions from RANS-based reactingFoam to the FireFOAM solver, which supports Large Eddy Simulation (LES). LES resolves the large-scale, energy-carrying eddies directly, making it more suitable for capturing the unsteady flow behaviour, velocity fluctuations, and vortex interactions present in the USYD burner. In addition, FireFOAM provides a more comprehensive treatment of radiation and combustion coupling, allowing for a more realistic representation of buoyant flame growth and suppression performance under flow conditions.

5 Studying Flow Turbulence-USYD Burner – using ANSYS Fluent.

5.1 Introduction

Fire dynamics and heat transfer arise from the complex interaction between energy release and buoyancy induced flow fields. This interaction involves turbulent mixing, mass transport, flame radiation, gas-phase chemistry, and soot formation, all of which occur over relatively short spatial scales. These processes manifest in observable fire characteristics such as flame height, entrainment rates, thermal feedback, burning rates, global radiative fractions, and soot volume fractions, which are critical parameters in computational modelling.

Historically, many of these fire characteristics have been represented through empirical correlations, which offer computational efficiency but are limited in their generalisability across diverse fire scenarios. To improve the predictive capability and reliability of fire models, locally resolved simulations based on well-designed experiments are required. These experiments must include well-characterised boundary conditions and provide detailed physical measurements.

Recent research has placed emphasis on validating sub-models used in computational fluid dynamics (CFD) by employing comprehensive experimental datasets that capture turbulent velocity fields, temperature distributions, radiation, and soot generation. Diffusion flames, characterised by the mixing of fuel and oxidiser, are particularly important in this context as they dominate many real-world fire scenarios. Understanding the structure and behaviour of diffusion flames is critical for designing effective fire suppression and safety systems.

In 2014, Meares and Masri [110] developed a modified piloted burner at the University of Sydney to investigate turbulent partially premixed flames with inhomogeneous mixture distributions. The burner employed two concentric tubes, one for fuel and the other for air, both enclosed by an annular pilot flame. By adjusting the axial position of the inner tube relative to the burner exit, the degree of fuel–air premixing could be controlled, allowing the generation of spatial gradients in the mixture fraction. This inhomogeneity was shown to enhance flame stability, particularly at intermediate recessions, by promoting the formation of locally burnable pockets. While this configuration provided valuable insights into stratified combustion regimes, the present study focuses on a different burner design that explores buoyancy-driven turbulent diffusion flames without the use of a pilot flame or concentric flow elements [110].

The present study adopts a modified experimental setup referred to as the modern USYD Burner. It employs a buoyancy-driven configuration equipped with a recessed perforated plate. This plate produces multiple fine fuel jets that induce high shear and generate adjustable turbulence levels. By varying the recess distance of the plate within an outer jacket, the turbulence intensity at the burner exit can be systematically altered without changing the bulk fuel velocity and the Froude number. This capability makes the burner particularly well suited for investigating buoyancy-turbulence interactions under controlled, reproducible conditions. The burner's operation remains within a buoyancy-dominated regime by maintaining relatively low fuel flow rates This burner has been characterised under non-reacting cold flow conditions using Laser Doppler Velocimetry (LDV), as conducted by Xiao, Gupta [3] , who quantitatively evaluated the turbulence characteristics at the exit plane.

This chapter presents the findings from the initial stage of the research, focusing on CFD modelling using ANSYS Fluent. The objective is to examine the influence of the perforated plate on turbulence generation within the burner tube. Simulations were conducted for two configurations, one with and one without the perforated plate while the Froude number is kept constant, to evaluate its effect on turbulence intensity and mixing behaviour. Enhancing turbulence at the outlet of the inner fuel tube is hypothesised to improve fuel-air mixing efficiency downstream.

Turbulence is characterised using two key parameters: Turbulent Kinetic Energy (TKE) and Root Mean Square (RMS) velocity, both of which provide detailed insight into flow fluctuations and turbulence intensity. These metrics serve as the basis for evaluating the perforated plate's effectiveness.

The chapter outlines the CFD modelling approach, including domain setup, boundary conditions, meshing strategies, and simulation parameters. It then presents a comparative analysis of the simulation results, highlighting the turbulence profiles for both configurations. The findings offer important insights into the role of structural modifications in shaping turbulent flow behaviour and mixing performance.

In summary, this chapter lays the groundwork for understanding the impact of engineered turbulence on combustion dynamics. The insights gained here inform the direction of the next research phase, which will employ the FireFOAM solver to simulate combustion processes.

5.2 Methodology

This burner configuration has been developed to enable the investigation of interactions between turbulence and buoyancy in flames. It offers well controlled fuel turbulence conditions and clearly defined boundary parameters, making it suitable for systematic study and numerical validation.

5.2.1 Burner design

The USYD burner is constructed from three brass components and has an internal diameter of 35 mm and a wall thickness of 2.5 mm. The assembly delivers a vertical fuel jet that generates buoyant flames under a range of flow and turbulence condition. The fuel employed is compressed natural gas (CNG), with a composition measured and reported by Xiao, Gupta [3], consisting of 88.8 percent methane (CH_4), 7.8 percent ethylene (C_2H_4), 1.9 percent carbon dioxide (CO_2), and 1.2 percent nitrogen (N_2). To stabilise the flame, the burner is installed within a wind tunnel that supplies a uniform co-flow of ambient air.

A key design feature of the burner is the inclusion of a perforated brass plate, engineered to enhance turbulence levels downstream of the burner exit. The plate has a thickness of 8 mm and contains 25 circular holes, each with a diameter of 1 mm. It is mounted on a manually adjustable sliding rail system that allows it to move axially along the burner tube. This rail guide mechanism enables the plate to be recessed up to 100 mm upstream of the burner exit and secured in position during testing. This adjustability enables precise control over the distance between the plate and the exit plane, denoted as Lr.

A schematic of the burner tube is provided in Figure 5-1 and discussed by by Xiao, Gupta [3]. The tube, labelled as item 1, has an internal diameter of 30 mm, a wall thickness of 2.5 mm, and a total length of 150 mm. The perforated plate, labelled as item 2, is designed to be repositioned along the axial direction of the tube to control the turbulence intensity at the burner outlet. When installed, high-velocity fuel jets pass through the plate's small holes, generating significant shear forces and enhancing turbulence levels downstream. These effects are investigated by comparing flow characteristics in simulations both with and without the plate installed, as also discussed in detail by Xiao, Gupta [3]

The three-dimensional geometry was constructed using ANSYS SpaceClaim, with the computational domain filling the interior volume of the burner tube and the perforated plate. This setup enables accurate simulation of fluid flow dynamics, as illustrated in Figure 5-2.

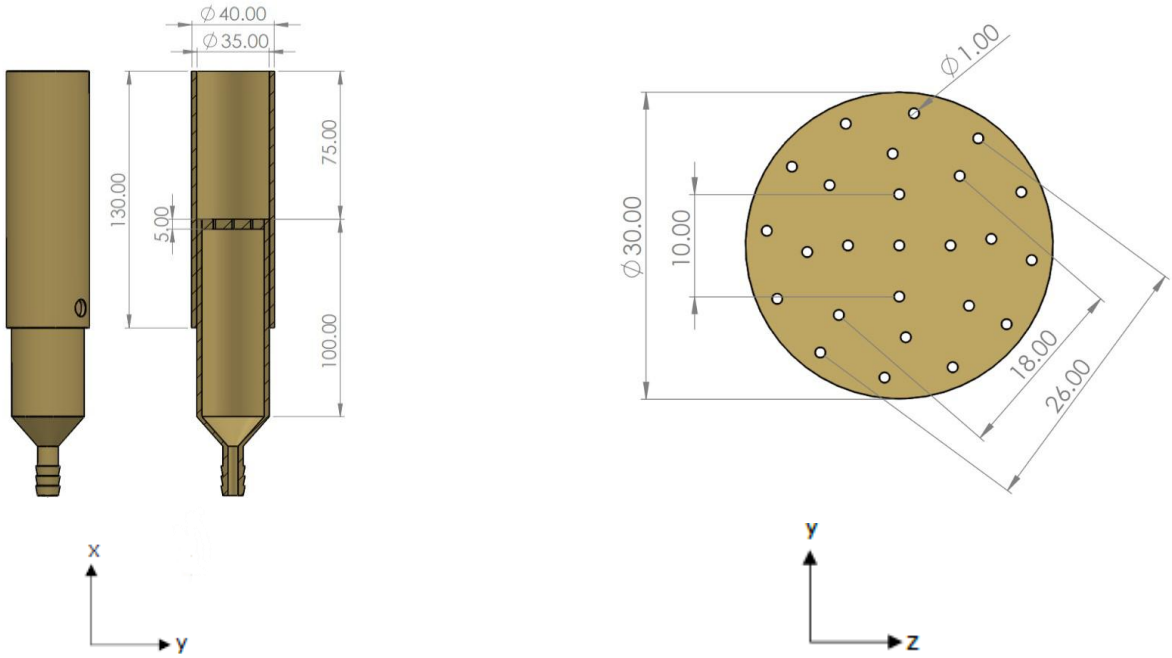

Figure 5-1 Schematic of the burner assembly [3]

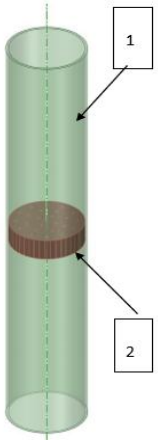

Figure 5-2 Tube schematic with the perforated plate.

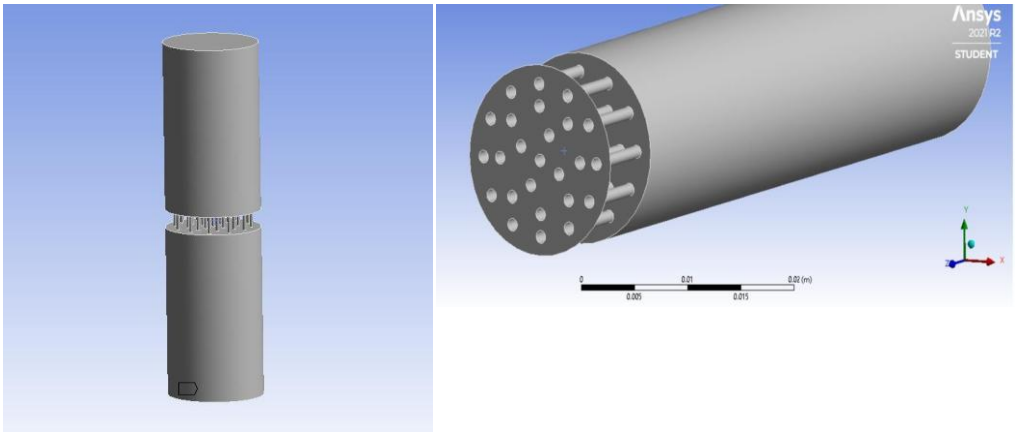

Figure 5-3 Fluid Volume-burner domain.

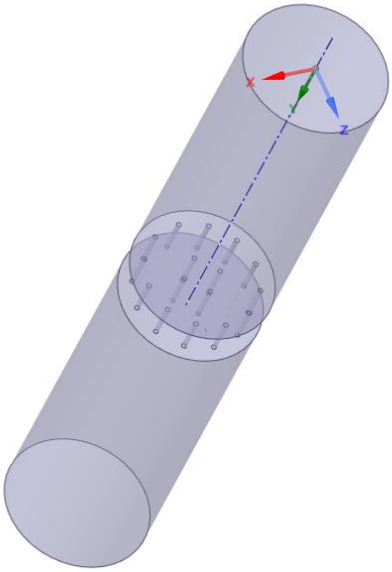

The perforated plate is mounted on a sliding mechanism, allowing it to be recessed up to 100 mm upstream of the burner exit plane, denoted as Lr. When in place, the small holes in the plate generate high-velocity jets that induce strong shear layers, producing elevated levels of fuel-side turbulence. For a fixed bulk fuel velocity, varying the recess distance Lr allows for precise control of the turbulence intensity at the burner outlet. This mechanism enables generation of high turbulence levels within buoyancy-driven flames without altering the Froude number.

The fire Froude number is a fundamental non-dimensional parameter that characterises the relative influence of inertial and buoyant forces in turbulent jet diffusion flames. It is typically introduced in its simplified form as:

$$F_r = \frac{U_f}{\sqrt{gl}} = \frac{momentum\ forces}{gravity\ forces}$$

Equation 5-1

This simple form has been widely adopted to distinguish between different combustion regimes. A detailed classification of this transition was developed by Delichatsios (1993) [111], who derived a comprehensive scaling framework for jet diffusion flames covering the full spectrum from buoyancy- to momentum-controlled regimes. His analysis provided a robust correlation for flame height and entrainment based on a fire Froude number that incorporates both thermal and momentum flux terms.

The present study adopts a modified Froude number that accounts for temperature rise and density variation, following the approach of Delichatsios (1993) [111]. This extended form is given in Equation 5-2 and quantifies the flow behaves with respect to the diameter of the burner exit plane.

Both the Froude number (Equation 5-2) and the heat release rate (Equation 5-3) are directly controlled by the fuel mass flow rate. The fire Froude number characterises the balance between inertial and buoyant forces at the burner outlet, while the heat release rate represents the total energy released assuming complete combustion. These are calculated using the following equations:

$$F_{rf} = U_s/[(S+1)^{\frac{3}{2}} \left(\frac{\rho s}{\rho o}\right)^{1/4} \left(\frac{\Delta T_f}{T_o} \; g d_s\right)^{1/2}$$ Equation 5-2

$$Q = \Delta H_c \, m_f$$ Equation 5-3

Fr_f	Buoyancy-momentum flame Froude Number.
u_s	Nozzle fuel flow velocity.
S	Stoichiometric mass air-to-fuel ratio.
ρ_s	Fuel density at the nozzle.
ρ_o	Ambient air density
ΔT_f	Mean peak flame temperature rise.
T_o	Ambient temperature.
g	Gravitational acceleration.
ds	Nozzle diameter.
Q	Heat release rate.
ΔH_c	Heat of combustion
m_f	Fuel mass flow rate

To ensure stable flame operation, the burner parameters were optimised to prevent flame lift-off or blow-off. This involved controlling the fuel flow rate, the air co-flow velocity, and the recess distance of the perforated plate. A fixed recess distance of 75 mm was chosen for all cases, and two different heat release rates, ranging 20 and 40 kW, were examined to assess the impact of varying energy input on turbulence and flow behaviour.

The co-flow system operates under standard laboratory atmospheric conditions, delivering filtered ambient air at a controlled velocity of approximately 0.2 m/s to stabilise the flame.

The fuel flow rates and resulting Froude numbers for each test case are presented in Table 5.1, which also includes additional key parameters such as Reynolds numbers and dimensionless heat release rates to facilitate comprehensive flow characterisation.

In the present study, as reported by Xiao et al. [3], Laser Doppler Velocimetry (LDV)

measurements were conducted at the jet exit plane under non-reacting conditions to evaluate turbulence intensity for selected flame configurations. Specifically, for the 20 kW and 40 kW cases with the turbulence generator plate installed, the measurements revealed a significant enhancement in near-field turbulence. These measurements were conducted using Laser Doppler Velocimetry (LDV), focusing on the axial and radial velocity components at the burner exit plane. At 20 kW, the turbulence intensity reached approximately 70%, while at 40 kW, it exceeded 100%, indicating a substantial rise in velocity fluctuations induced by the perforated plate. These findings, detailed in Section 3 of Xiao et al. (2023) [3], demonstrate the effectiveness of the perforated plate in increasing turbulence intensity.

Table 5.1-Burner Operation Conditions with plate.

Heat Release Rate (Q) [kW]	***Fuel Flow Rate (mf)[L/min]***	**Froude Number (Frf)**	**Fuel Exit Velocity (vin) [m/s]**
20	36.6	.0127	.634
40	73.2	.0254	1.268

5.3 Meshing

Following the completion of the three-dimensional geometry in ANSYS SpaceClaim, the next step was to generate the computational mesh. A mesh sensitivity analysis was carried out by testing a range of element sizes to assess their effect on solution accuracy and to confirm mesh independence. The detailed results of this analysis are presented in Section 5.7.

The following element sizes were examined:

0.025m 0.0125m .00152m .00120m

Among these, the element size of 0.00152 was selected as an optimal configuration for achieving a balance between computational efficiency and solution accuracy. For this mesh size, the computational domain contained approximately 753,000 elements. A representation of this mesh configuration is shown in Figure 5-4

Mesh adaptation was also applied during the refinement process and will be discussed in Section 5.7, which focuses on accuracy assessment and mesh convergence. The mesh quality

and convergence analysis were primarily conducted for the burner configuration without the perforated plate, serving as the baseline for subsequent comparative studies.

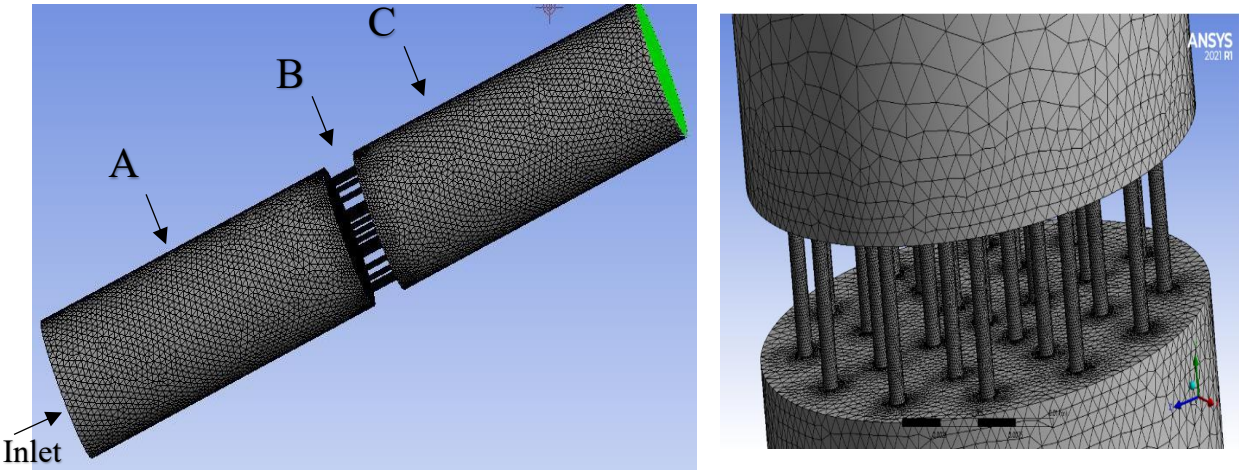

Figure 5-4 Basic mapped face mesh of the burner.

5.4 Processing, Boundary Conditions & Solver Details

To analyse the turbulence characteristics within the burner tube, the standard k–ε (k-epsilon) turbulence model was implemented in ANSYS Fluent. This model was selected due to its reliability and efficiency in capturing turbulent flows in internal ducted configurations. The simulations aimed to compare the velocity and turbulence fields in cases both with and without the perforated plate installed.

The primary quantity of interest is the turbulence level, defined as the ratio of the root mean square (RMS) of velocity fluctuations to the mean velocity. To compute this, instantaneous velocity values were recorded at each time step during the transient simulation. These were subsequently post-processed to obtain the time-averaged velocity U_{mean} and the RMS velocity U_{rms}

Although the turbulence kinetic energy (k) is available directly from Fluent's output, the RMS velocity is calculated manually using the relationships below:

$$U_{mean} = \frac{U_{ins1} + U_{ins2} + U_{ins3} + \cdots + i}{\sum U_{ins.}} \qquad \text{Equation 5-4}$$

$$U_{rms} = 2K^{.5} \qquad \text{Equation 5-5}$$

Where:

U_{ins}: Instantaneous velocity at each location.

K: Turbulence kinetic energy.

The turbulence level is calculated by the ratio between U_{rms} and $U_{mean.}$

$$Turblence\ level = \frac{U_{rms}}{U_{mean}} \qquad \text{Equation 5-6}$$

This non-dimensional parameter provides a direct measure of velocity fluctuation intensity and enables a comparative evaluation of turbulent mixing between the burner configuration**s.**

5.5 Model conditions & Properties:

The numerical simulations were performed for two heat release rate (HRR) cases: 20 kW and 40 kW. The geometric configuration, mesh resolution, and solver settings were kept consistent across both cases. Key simulation parameters are summarised in Table 5.2 and Table 5.3

Case 1: Q=20 kW, V_{in} = .863 m/s & m_f = 36.6 L/min

Parameter	**Value**		
Element Size	.00152		
Number of Elements	753,153	**Solver scheme**	Second order upwind
Number of Elements after adaption method.	2,552,562	**Spatial discretisation - momentum**	Second order upwind
Turbulence Model	K-epsilon-standard	**Kinetic Energy**	Second order upwind
Fluid	Methane CH4	**Residual convergence criteria**	1e-05
Tube Material	Steel	**Time step**	.01s
Inlet Velocity (m/s)	.83	**No. of time step**	200
Inlet pressure	50Kpa		

Table 5.2 Simulation Parameters for HRR = 20 kW

Case 2: Q=40 kW, V_{in}= 1.73 m/s & m_f = 73.2 L/min

Element Size	**.00152**		
Number of Elements	753,153	**Solver scheme**	Second order upwind
Number of Elements after adaption method.	2,552,562	**Momentum**	Second order upwind
Model	K-epsilon-standard	**Kinetic Energy**	Second order upwind
Fluid	Methane CH4	**Residual convergence criteria**	1e-05
Tube Material	Steel	**Time step**	.01s
Inlet Velocity (m/s)	1.73	**No. of time step**	200
Inlet pressure	50Kpa		

Table 5.3 Parameters of the burner model @HRR=40KW

5.6 Accuracy& convergence

To ensure the reliability and accuracy of the numerical solution, several validation checks were performed. This included residual independence, grid size independence, and mesh adaptation. Each check was designed to verify that the results are not significantly influenced by solver settings or grid resolution. The primary parameter used to assess consistency was the radial velocity profile at the outlet, which is sensitive to variations in both numerical and spatial settings.

Residual Independence Check

This involves monitoring the residuals, which are measures of the solution's convergence. Low and stable residuals indicate that the numerical solution is approaching a steady state. Ensuring that the residuals are independent of further iterations confirms that the solution is reliable.

Grid Size Independence Check

Grid independence was verified by comparing simulation results across multiple mesh resolutions. As described in Section 5.7.2, mesh sizes ranging from coarse to refined were tested to determine whether further refinement would result in significant changes to the velocity field. The grid size was considered acceptable once the radial velocity profiles stabilised, indicating that the numerical solution no longer depended on mesh resolution. This ensured that the computational model was sufficiently resolved for the purposes of the study.

Mesh Adaptation

Mesh adaptation involves refining the mesh in regions where higher accuracy is required, based on preliminary solutions. This ensures that critical areas with steep gradients or complex flow features are adequately resolved. The adapted mesh is then used to achieve more accurate results without excessively increasing computational cost.

The parameter used to verify independence and accuracy will be the radial velocity profile at the outlet, ensuring consistency across different checks.

5.6.1 Residual Independency check

To validate the accuracy of the solution, we aim to obtain suitable residuals for the specific grid size by starting with an initial residual value of 10−3 and monitoring its value individually. The following residual values were tested:

1x10-3 1x10-4 1x10-5 1x10-6

The velocity profile at the outlet resembles a parabolic profile for the non-plate case when the residuals were set to 1×10−3. However, as the residuals were decreased, the velocity profile appeared to be more influenced by the generated turbulence. Regarding the solution's accuracy and independence from the residual values, it is evident that the velocity profiles for 1×10−5 and 1×10 −6 are quite similar, as shown in Figure 5-5. Therefore, using residuals of 1×10−5 is sufficiently accurate and more time-efficient compared to 1×10−6.

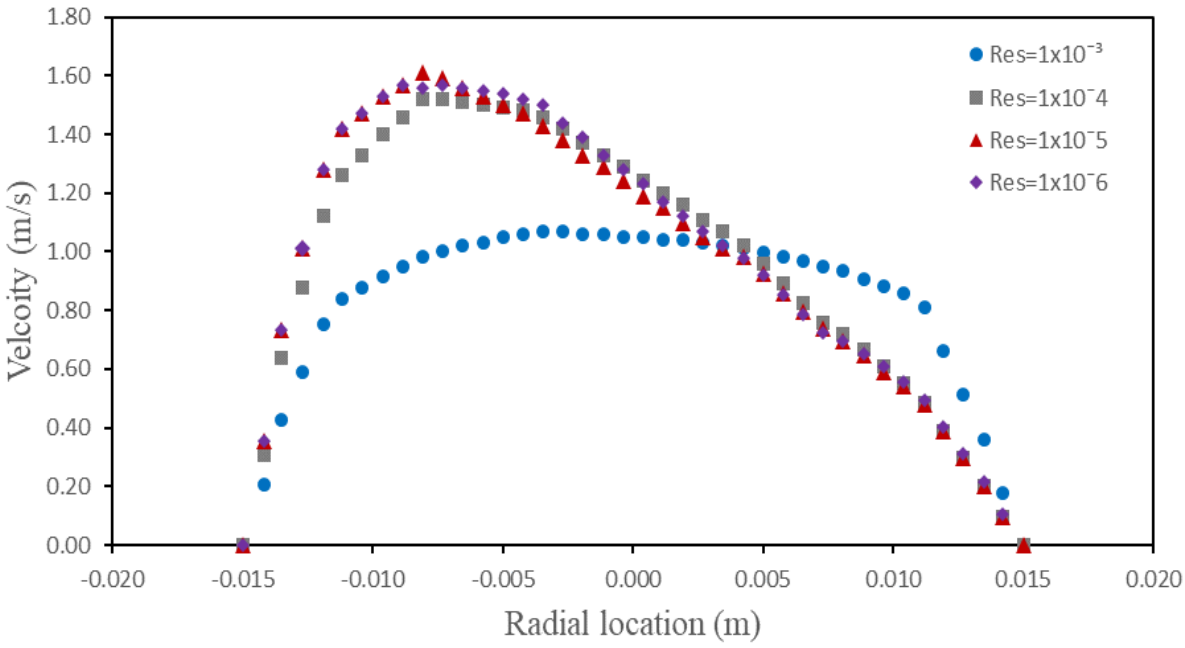

Figure 5-5 Velocity Profile at the outlet of the tube with the perforated plate for the different tested residual values.

5.6.2 Grid Independence check

To verify the independence of the numerical solution from grid resolution, simulations were performed using a range of mesh sizes. The tested element sizes included 0.025, 0.0125, 0.0018, and 0.00152. The corresponding velocity profiles were compared to determine the sensitivity of the results to mesh refinement, as shown in Figure 5-6.

The analysis indicated that beyond an element size of 0.00152, no significant changes in the velocity profile were observed. This confirmed that the mesh was sufficiently fine to capture the key flow features, and that further refinement would not yield considerable improvements. Therefore, an element size of 0.00152 was selected for the final simulations, ensuring both accuracy and computational efficiency.

Figure 5-6 presents the axial velocity profiles extracted at the burner outlet (z = 150 mm), plotted along the radial direction across the tube diameter. The asymmetry observed in the coarse mesh cases (H = 0.025 m and 0.0125 m) is attributed to under-resolved shear layers and wall effects. In contrast, the profiles obtained with finer meshes (H = 0.0018 m and 0.00152 m) exhibit more symmetric and smoother velocity distributions, confirming that mesh convergence has been achieved.

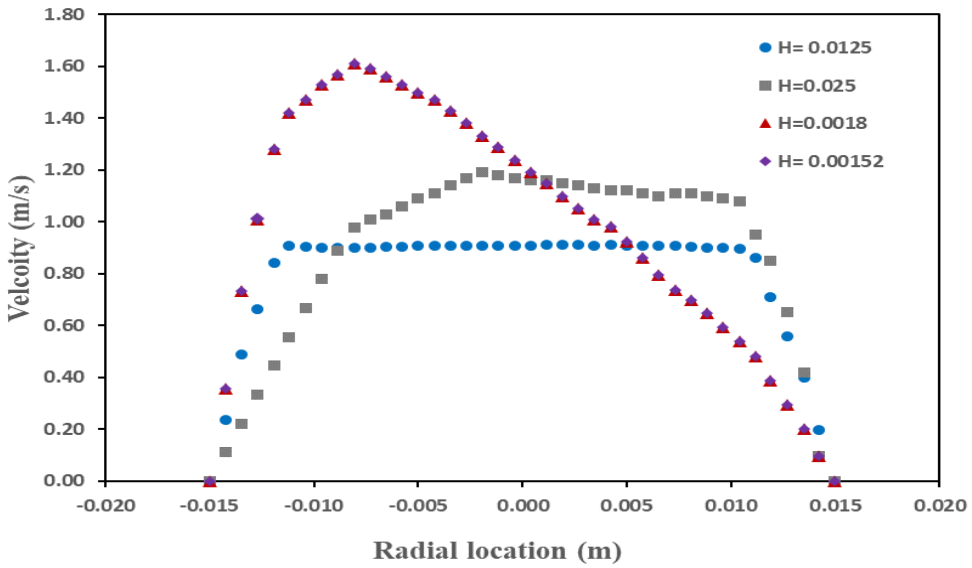

Figure 5-6 Velocity at the outlet of the tube versus the different tested element size.

5.6.3 Grid Adaption Method

To further enhance the accuracy of the solution, a grid adaptation technique was applied. This method focuses on refining the mesh in critical regions where high velocity gradients or complex flow interactions occur, such as near the perforated plate and along the wall boundaries.

As shown in Figure 5-7, the mesh was refined in the regions of interest based on flow field indicators from preliminary simulations. The initial mesh consisted of approximately 750,000 elements. Following adaptation, the total number of elements increased to approximately 2,000,000, allowing for improved resolution without the need for uniform refinement across the entire domain.

This adaptive strategy ensures that the mesh density is increased only where necessary, enabling the accurate capture of turbulence structures and shear layers while maintaining manageable computational costs.

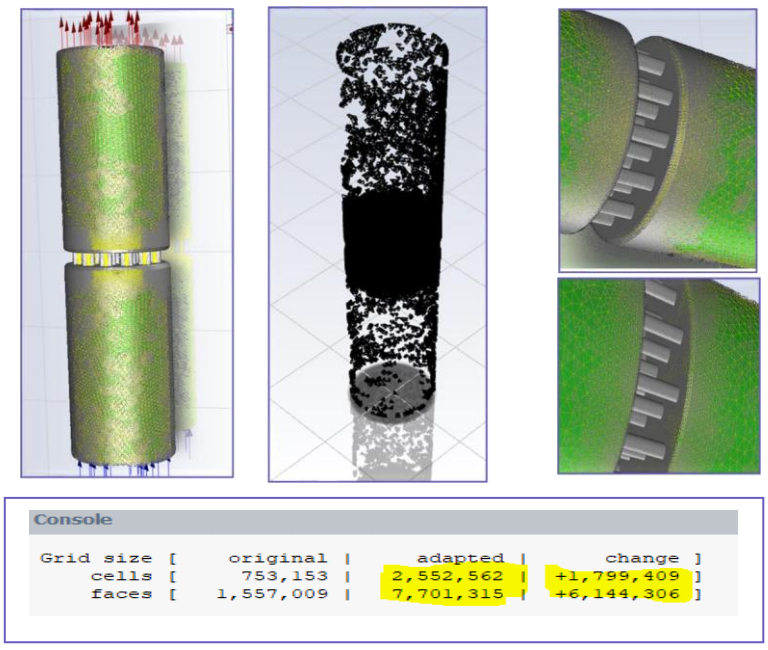

Figure 5-7 The result of the adaption method.

5.7 Post processing, results, and discussion

This section presents the results of the numerical simulations, which are divided into two primary categories:

Flow in a Vertical Tube without the Plate.

Flow in a Vertical Tube with the Plate.

While the experimental study investigated five different flow conditions by varying the heat release rate and turbulence intensity, this numerical analysis focuses on two representative cases only:

Q = 20 kW and Q = 40 kW, corresponding to flames F3 and F5 in the experimental dataset [112]

5.7.1 Flow in the tube without plate

The first case examines flow behaviour in the absence of the perforated plate. Figure 5-8 presents the velocity contours and streamlines inside the burner. The results show that the flow is dominated by a parabolic profile with minimal turbulence, which is expected in the absence of internal obstructions or shear-inducing features. The streamline patterns reflect smooth, laminar-like flow conditions within the vertical tube (part C in Figure 5-4).

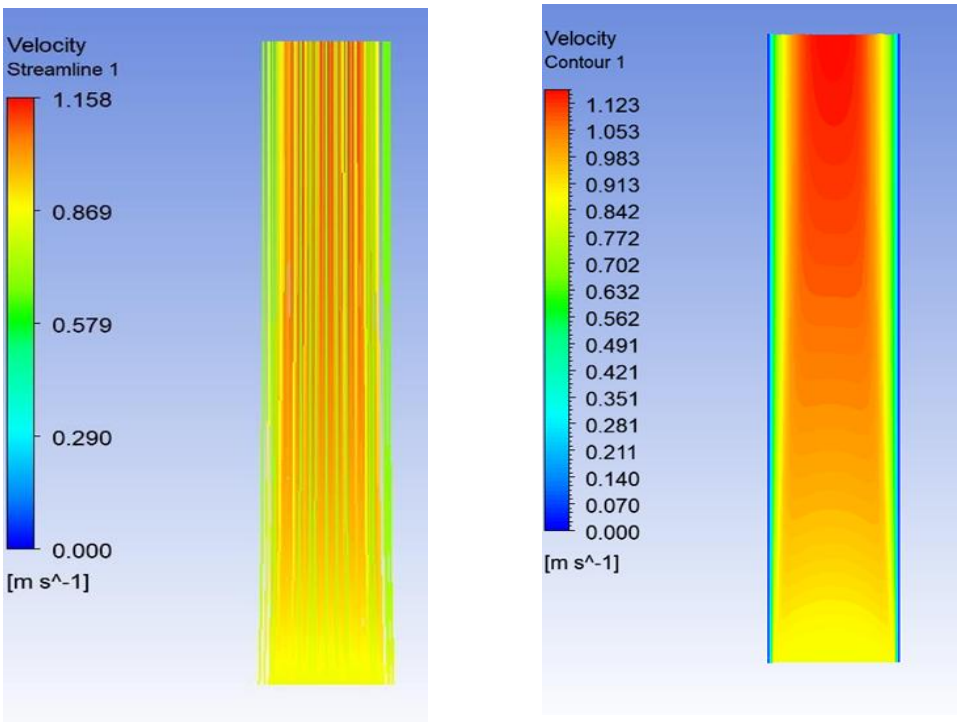

Figure 5-8 Streamlines (right) and velocity contour (left) for the flow in the tube without the plate.

5.7.1.1 Velocity profile at the outlet of the burner

To quantify the turbulence level at the burner outlet, the RMS velocity U_{rms} was calculated based on the turbulence kinetic energy obtained from Fluent, and compared with the mean velocity

$U_{mean.}$ These values were evaluated along a line placed at the outlet plane, enabling the computation of the turbulence level using Equation 5-4 Equation 5-5

Case 1: Q=20 kW, V_{in} = .863 m/s & m_f = 36.6 L/min

Figure 5-9 presents the axial velocity profile and RMS axial velocity at the outlet of the tube without the perforated plate. The mean velocity profile exhibits a typical parabolic distribution, characteristic of fully developed pipe flow. The RMS velocity, derived from turbulence kinetic energy. The calculated turbulence level indicates limited fluctuations across the profile, consistent with low-turbulence flow.

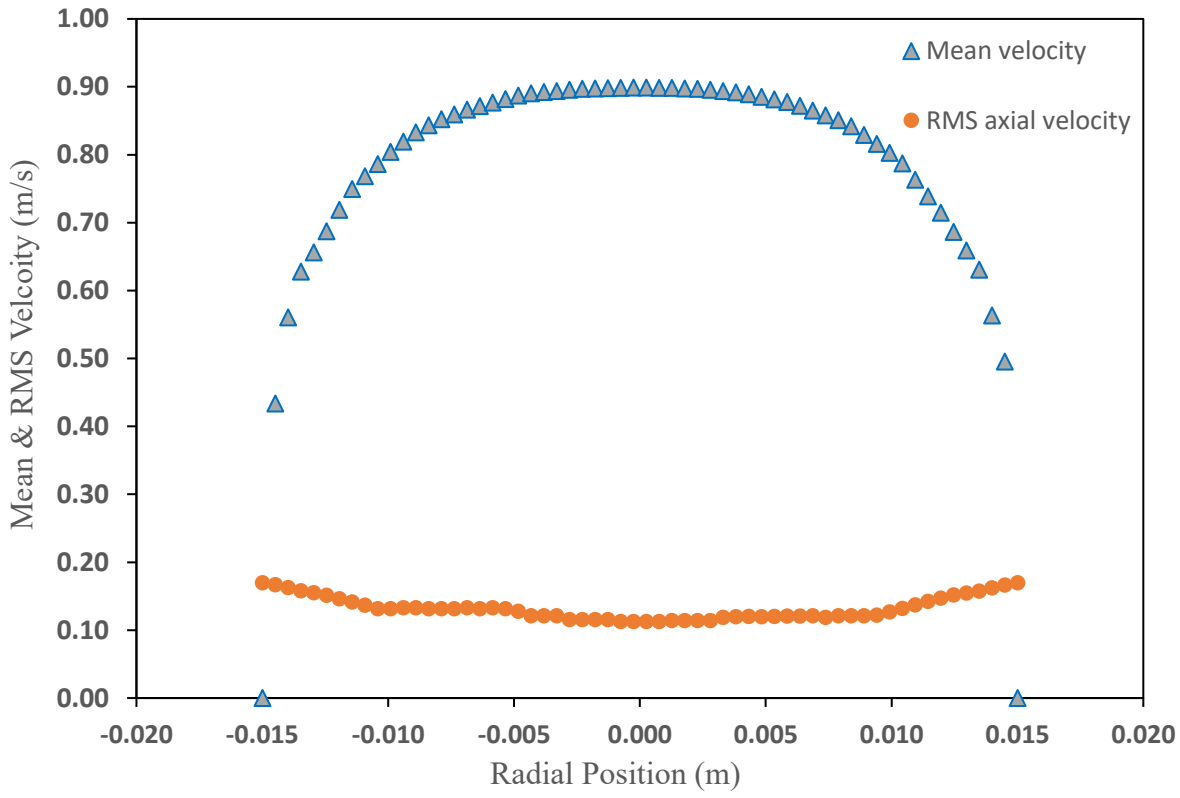

Figure 5-9 Mean velocity & RMS axial velocity profile at the outlet of the tube without the plate.

Case 2: Q=40 kW, V_{in}= 1.73 m/s & m_f = 73.2 L/min

Figure 5-10 displays the outlet velocity profile for this higher energy case, which maintains a parabolic shape. The RMS velocity, remains relatively low, with the turbulence levels slightly elevated due to the increased inlet velocity and energy input.

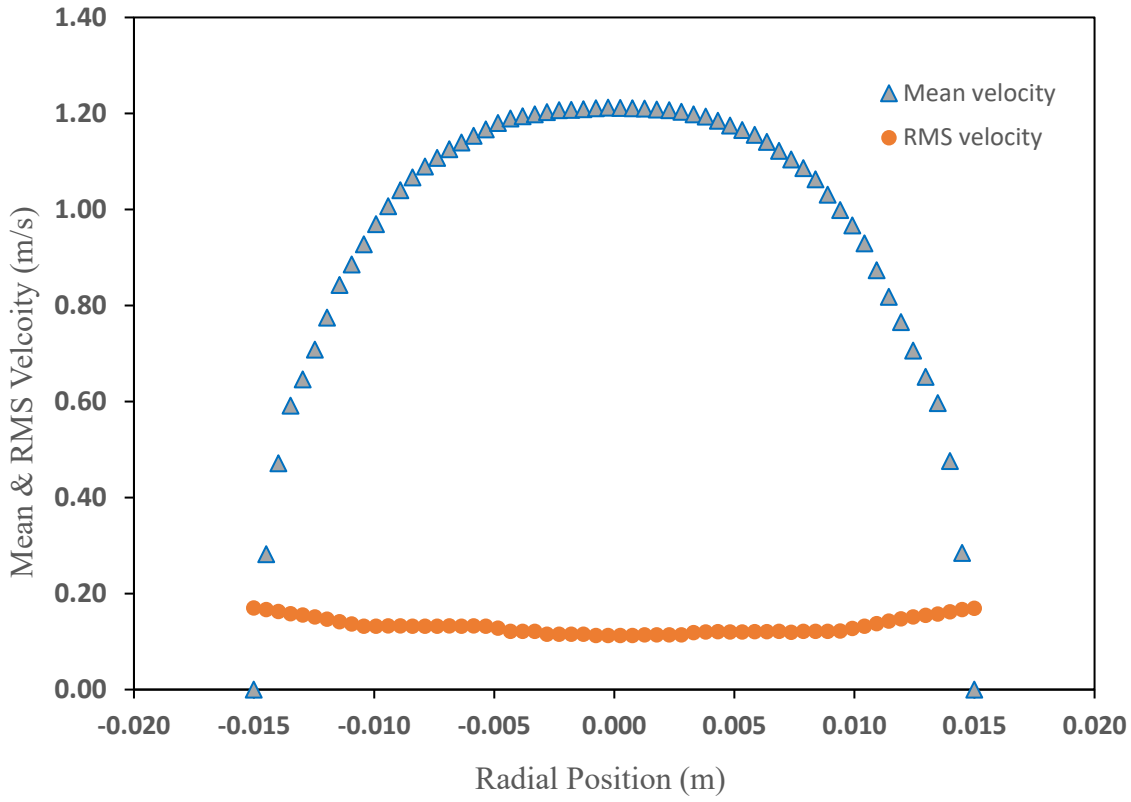

Figure 5-10 Mean velocity & RMS axial velocity profile at the outlet of the tube without the plate.

Comparison Between Numerical and Experimental Velocity Profiles

Figure 5-11 & Figure 5-12 present a comparison between the numerical and experimental mean velocity profiles at the outlet for both heat release rates.

For Q = 20 kW (Figure 5-11):

The numerical results (shown in light blue circles) align closely with experimental data (blue circles), confirming that the model accurately reproduces the parabolic flow profile expected in such cases.

For Q = 40 kW (Figure 5-12):

The numerical data (grey circles) once again follow the same trend as the experimental results (grey squares), validating the simulation's ability to capture key flow behaviours under higher HRR conditions.

While some differences are observed, particularly in the central region and near the burner wall, these are within expected bounds given the use of the standard k–epsilon model. Minor deviations may be attributed to increased flow complexity at higher turbulence intensities and limitations in resolving near-wall effects. Nonetheless, the velocity profile maintains good overall agreement in shape and magnitude, supporting the reliability of the simulation setup.

These comparisons demonstrate that the standard k-epsilon model, combined with the chosen mesh resolution and solver settings, provides reliable predictions of velocity distributions in the burner without the perforated plate.

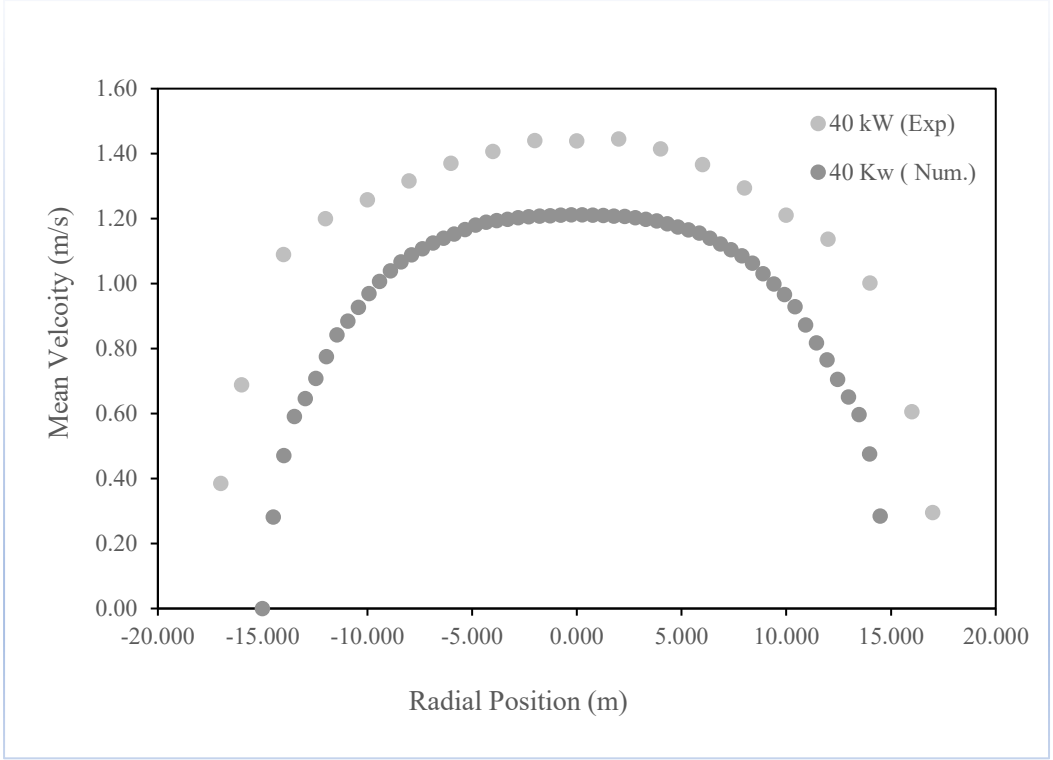

Figure 5-11 U mean numerically and experimental at the outlet of the tube without the plate-40kW

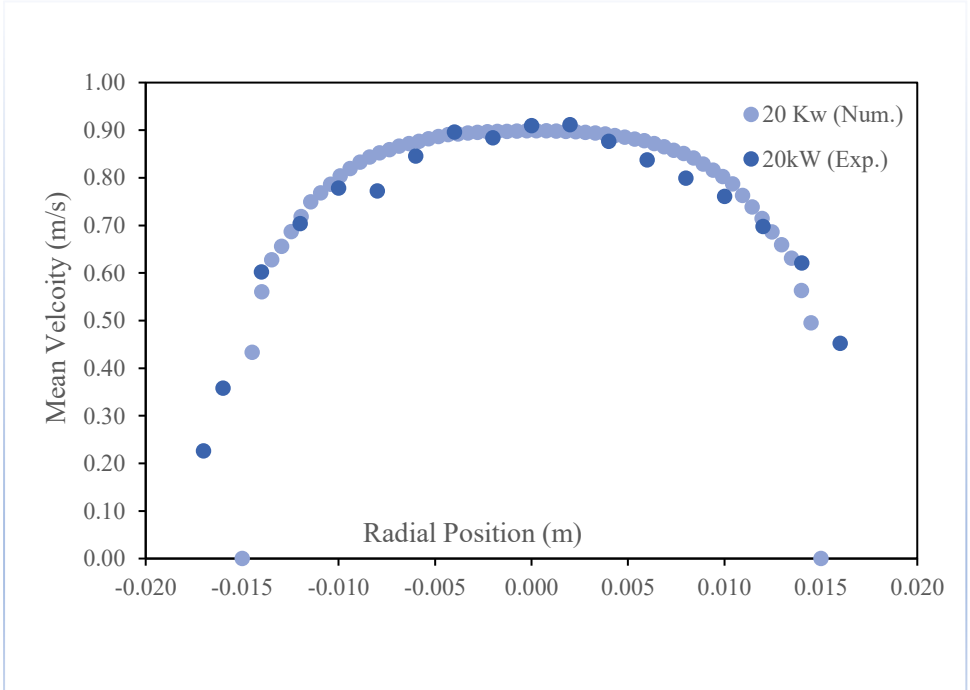

Figure 5-12 U mean numerically and experimental at the outlet of the tube without the plate-20kW

5.7.2 Flow in the Tube with the Perforated Plate

This section explores the impact of the perforated plate on the flow field using the validated numerical setup and optimum mesh settings established earlier. Figure 5-13 shows the streamlines within the burner tube when the plate is introduced.

The presence of the perforated plate leads to significant disruption of the flow, as evidenced by the development of small-scale vortices and increased velocity fluctuations. The micro-jets emerging from the 1 mm diameter holes reach velocities up to 40 m/s, generating strong shear regions that enhance turbulence intensity within the burner.

These effects are further observed in the outlet velocity profiles, where a noticeable deviation from the parabolic pattern occurs, especially in regions near the walls.

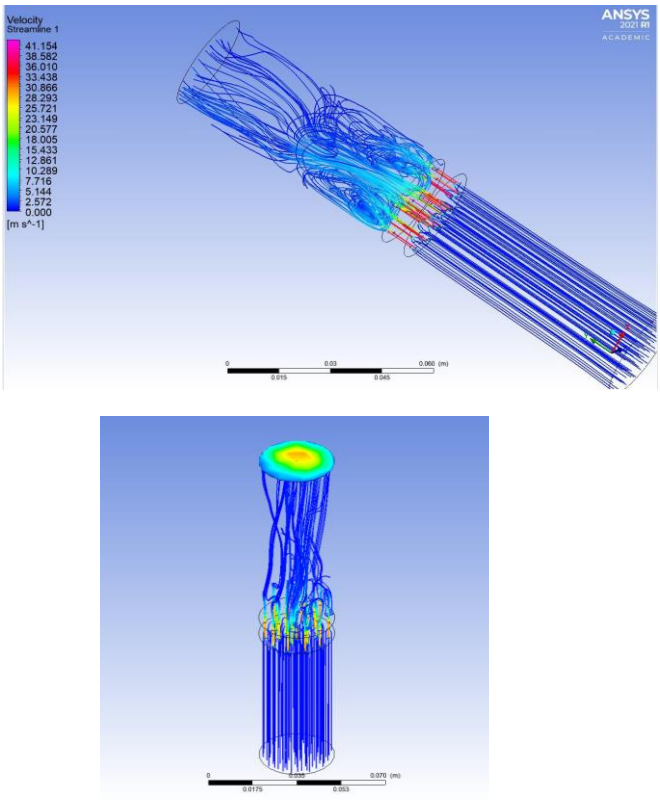

Figure 5-13 streamlines and velocity contour for the flow in the tube with the plate (k-epsilon)

5.7.2.1 Case 1: Velocity at the outlet for Q=20 kW

Figure 5-14 presents the radial velocity distributions for both mean and RMS velocities. The mean velocity peaks near the burner walls, reaching approximately 0.95 m/s, while the centreline velocity decreases to around 0.7 m/s. The RMS velocity (U_{rms}) follows a similar trend, with values ranging from 0.6 m/s at the centre to approximately 0.85 m/s near the outer boundaries. This profile indicates strong turbulence generation as a result of the perforated plate.

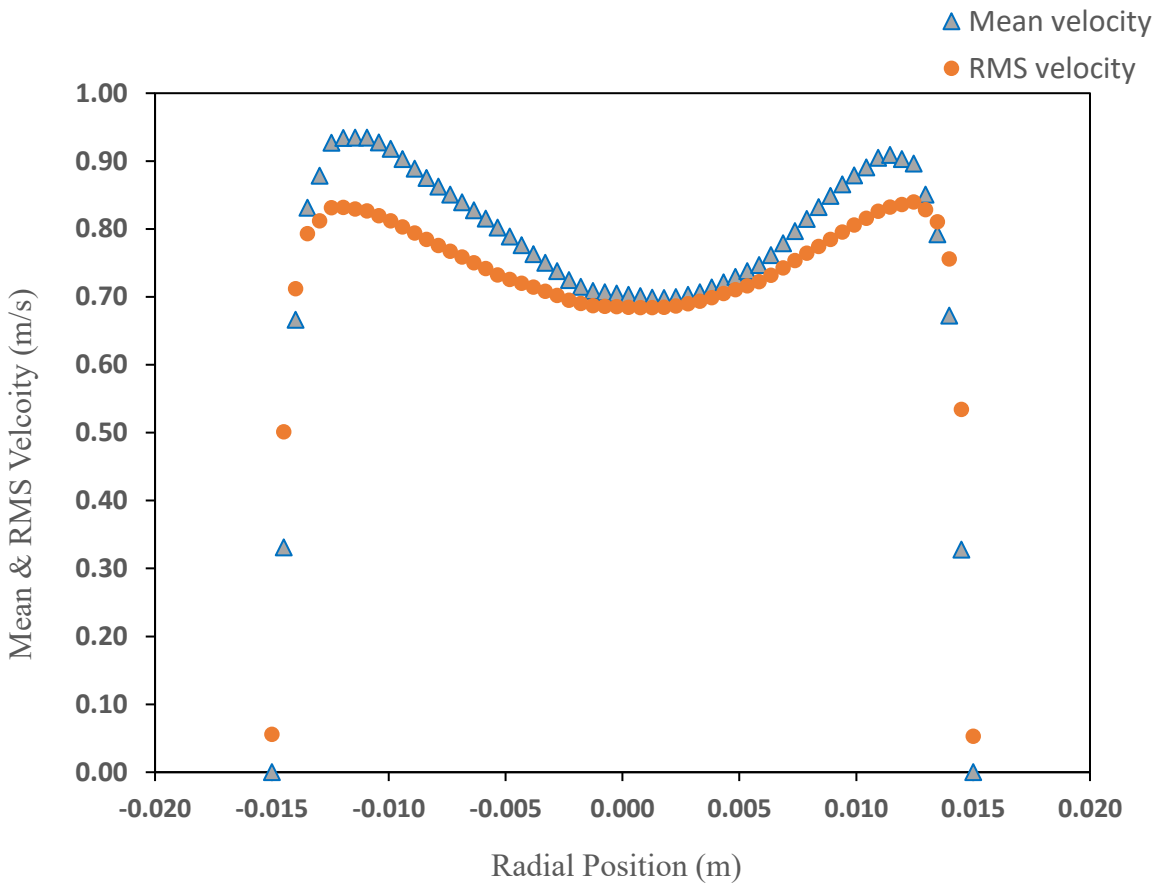

Figure 5-14 Mean velocity & RMS axial velocity profile at the outlet of the tube with the plate.

5.7.2.2 Case 2: Velocity Profile at the outlet for Q=40 kW

Figure 5-15 illustrates the outlet velocity distributions for the higher heat release rate case.

Mean Velocity (U_{mean}) Profile:

The profile peaks near the wall region at approximately 1.6 m/s and decreases toward the centreline to around 1.0 m/s.

RMS Velocity (U_{rms}) Profile:

The U_{rms} profile demonstrates higher turbulence intensity near the walls, with values ranging from approximately 1.0 m/s at the centre to about 1.6 m/s near the walls.

These findings confirm that the perforated plate significantly alters the flow structure, enhancing turbulence and modifying the velocity field across the burner outlet. The impact is more pronounced at higher HRRs due to the greater energy input, which contributes to intensified shear and mixing effects.

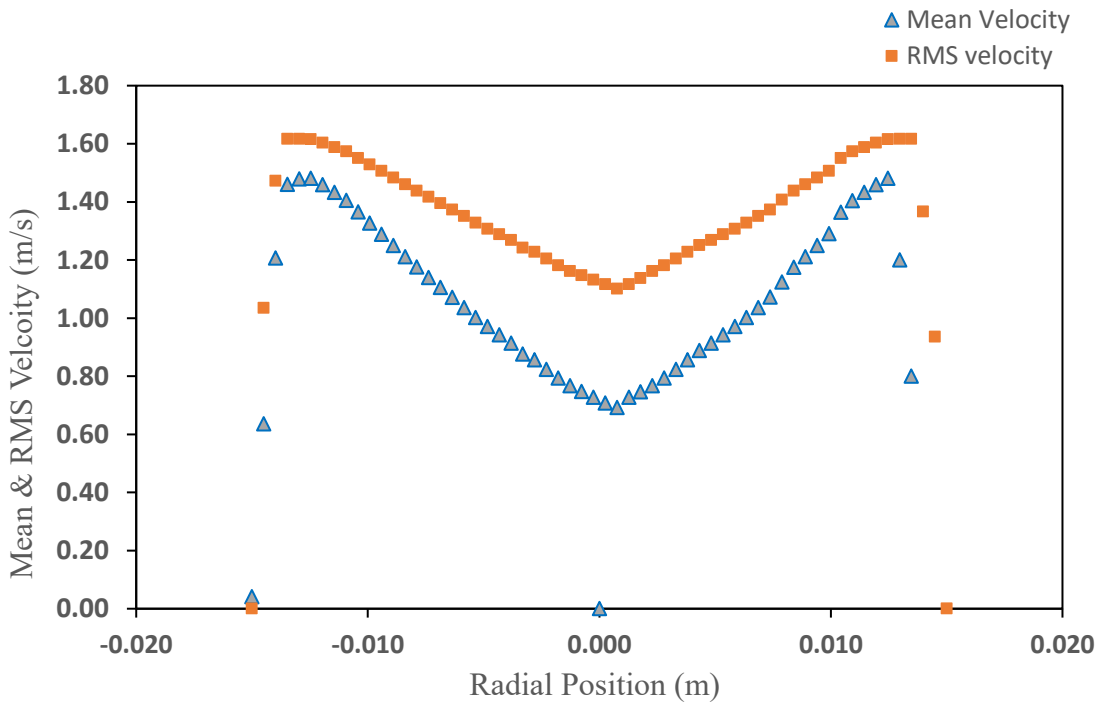

Figure 5-15 Mean velocity & RMS axial velocity profile at the outlet of the tube with the plate.

5.8 Velocity Profile Analysis

The velocity profiles at the burner outlet were analysed for both heat release rate cases (Q = 20 kW and Q = 40 kW), with a focus on the distribution of mean and root mean square (RMS) velocities across the burner radius.

Case 1: Q = 20 kW

The mean velocity (Umean) profile exhibited a peak value of approximately 0.95 m/s near the burner walls, while the velocity at the centre dropped to around 0.7 m/s. This parabolic distribution indicates a strong influence of wall shear and boundary layer formation. The RMS velocity (Urms) varied between 0.6 m/s at the centre and approximately 0.85 m/s near the walls, demonstrating enhanced turbulence intensity near the boundaries.

Case 2: Q = 40 kW

The overall shape of the velocity profile remained similar to Case 1; however, the magnitudes increased due to the higher fuel flow rate and thermal energy input. The mean velocity peaked at approximately 1.6 m/s near the walls and reduced to around 1.0 m/s at the centre. Similarly, the RMS velocity ranged from 1.0 m/s at the centre to approximately 1.6 m/s near the outer boundaries. These results confirm that increased heat release rate leads to higher turbulence levels and more pronounced shear effects.

5.9 Validation with Experimental Data

Validation is a fundamental aspect of computational fluid dynamics (CFD), ensuring that the numerical results are representative of real-world physical phenomena. In this study, validation was performed by comparing the CFD results obtained from ANSYS Fluent with experimental data provided by the Sydney University Combustion Research Group [3].

The comparison focused primarily on mean velocity and RMS velocity distributions at the burner outlet. The numerical predictions were evaluated against experimental measurements to assess the model's fidelity. Any discrepancies observed were used to inform potential refinements to the turbulence model and mesh resolution, thereby improving the model's predictive capability in simulating buoyant turbulent flames.

A comprehensive summary of the measurement procedures and associated uncertainties can be found in Xiao et al. (2023) [3]. and in the referenced publication, providing essential context for interpreting the observed trends and discrepancies.

5.9.1.1 Analysis of Case 1 (Q = 20 kW)

Figure 5-16 and Figure 5-17 illustrate the comparison between the experimental and numerical results for the mean velocity and the root mean square (RMS) velocity.

Mean Velocity: As shown in Figure 5-16, the numerical velocity profile closely matches the experimental data. Peak velocities of approximately 0.95 m/s were observed near the walls, while the centreline velocity was around 0.7 m/s. The strong agreement across the radial domain indicates that the numerical model effectively captures the mean flow characteristics under low heat release conditions.

RMS Velocity: Figure 5-17 shows the RMS velocity comparison. The simulated Urms profile closely follows the experimental trend, with values ranging from 0.6 m/s at the centre to approximately 0.85 m/s near the wall. A slight deviation is noted at the outermost regions, which may be attributed to measurement uncertainty or limitations in turbulence modelling near the wall boundaries.

5.9.2 Analysis of Case 2 (Q = 40 kW):

Figure 5-18 and Figure 5-19 illustrate the comparison of velocity profiles at the outlet for the higher heat release rate.

Mean Velocity: Figure 5-18 demonstrates that the numerical simulation accurately replicates the experimental behaviour, even under higher energy input conditions. The mean velocity reached approximately 1.6 m/s near the walls and 1.0 m/s at the centre, reflecting increased momentum associated with the higher mass flow rate.

RMS Velocity: As shown in Figure 5-19, the Urms results from the simulations again demonstrated good agreement with the experimental measurements, particularly near the walls where higher turbulence is expected. The Urms ranged from 1.0 m/s at the centre to 1.6 m/s near the walls.

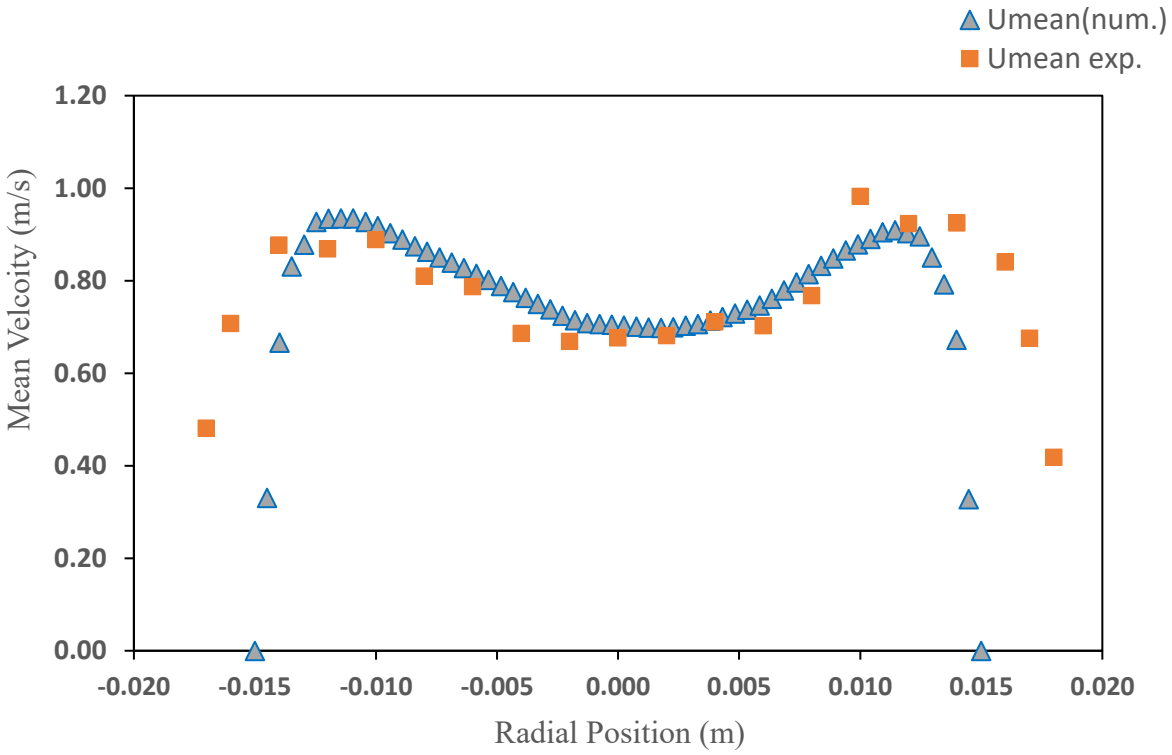

Figure 5-16 U_{mean} at the outlet of the tube with the plate for the numerical and experimental data for Q=20kW.

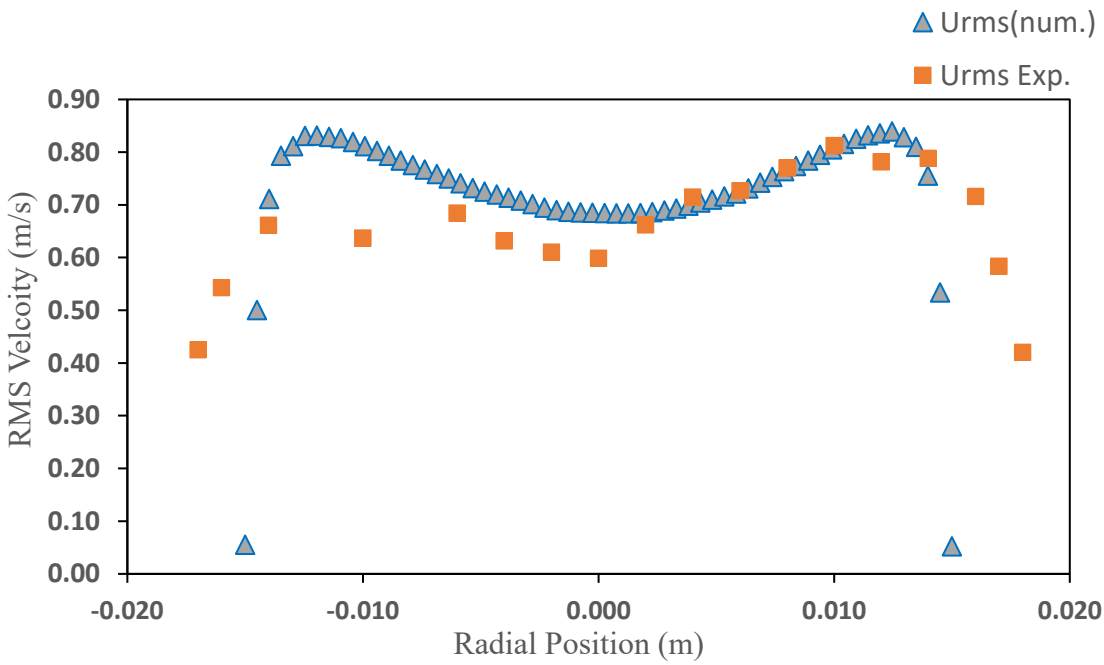

Figure 5-17 U_{rms} at the outlet of the tube with the plate for the numerical and experimental data for Q=20kW

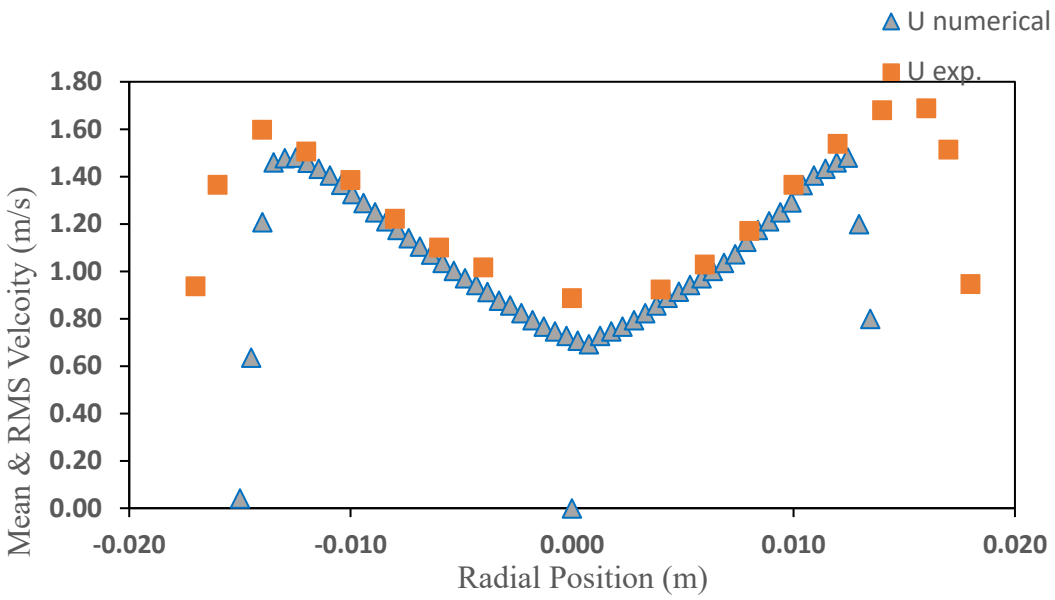

Figure 5-18 U_{mean} at the outlet of the tube with the plate for the numerical and experimental data for Q=40kW

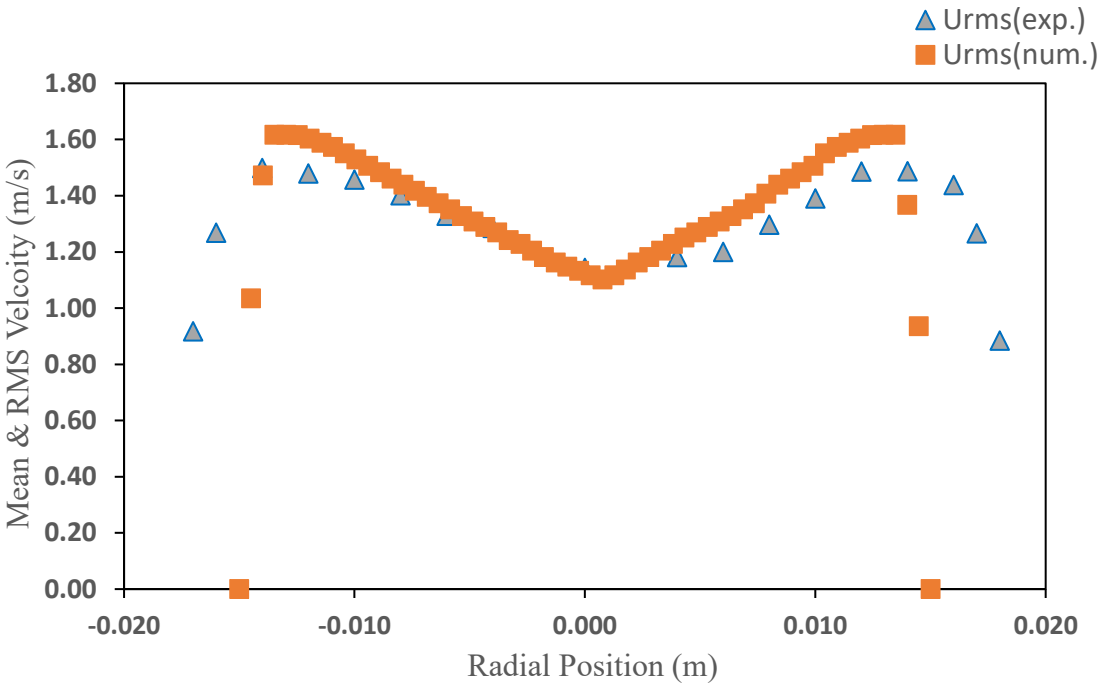

Figure 5-19 Urms at the outlet of the tube with the plate for the numerical and experimental data for Q=40kW

5.10 Discussion

The comparison between numerical and experimental results has confirmed the validity of the computational model across both low and high heat release rates (20 kW and 40 kW). The simulated mean and RMS velocity profiles closely matched the experimental measurements, particularly at the burner outlet where turbulence levels were highest. These findings demonstrate that the applied standard k–ε turbulence model and refined mesh configuration are capable of accurately capturing the flow dynamics in buoyant flame scenarios, both with and without the turbulence-generating perforated plate.

For the case without the perforated plate, both the experimental and numerical velocity profiles displayed a parabolic distribution, with minimal turbulence intensity. This behaviour is consistent with expectations for flow in a smooth, unobstructed duct, where the absence of shear-inducing geometries results in relatively laminar-like conditions. The turbulence level remained low across the radial profile, reinforcing the assumption of minimal fuel-side turbulence in the absence of the plate.

In contrast, the presence of the perforated plate substantially altered the flow field. The high-velocity micro-jets generated by the 1 mm diameter holes introduced strong localised shear regions, which significantly increased the turbulence intensity near the burner walls. This was confirmed by both the numerical simulations and experimental measurements, with RMS velocity values increasing notably at the outer edges of the burner outlet. These findings support the conclusion that the perforated plate serves as an effective mechanism for generating controlled turbulence in buoyant flame environments.

The study also highlighted the importance of mesh refinement, residual convergence, and mesh independence in ensuring the stability and accuracy of the numerical results. By performing a mesh sensitivity analysis and validating simulation outputs with experimental data, the numerical setup proved to be reliable and robust under different flow conditions.

From a practical perspective, the enhanced turbulence resulting from the perforated plate has significant implications for combustion efficiency and fire suppression applications. Increased

turbulence promotes improved mixing of fuel and oxidiser, which may lead to more efficient and cleaner combustion, as well as improved predictability in flame behaviour. This is particularly relevant for engineering applications where accurate modelling of turbulent mixing and flame spread is critical.

Finally, the successful validation of this CFD approach provides a solid foundation for the next stage of this research, which will involve modelling combustion and suppression dynamics using the FireFOAM solver under buoyancy-driven conditions. The validated flow field simulations presented in this chapter form the groundwork for future investigation into flame structure and suppression strategies in complex fire environments.

6 Studying the Diffusion Flame - USYD Burner - FireFOAM Solver.

6.1 Introduction

This chapter presents the numerical simulation of the USYD Burner using **FireFOAM**[30], a dedicated reacting flow solver within the OpenFOAM [12] computational platform. OpenFOAM (Open Field Operation and Manipulation) is a widely adopted open-source computational fluid dynamics (CFD) software package that employs the finite volume method to solve systems of partial differential equations on arbitrary unstructured meshes. It supports a diverse range of physical models and offers flexibility for implementing customised solvers, making it highly suitable for academic research.

FireFOAM is specifically developed to simulate fire-related phenomena, including combustion, buoyant flows, thermal radiation, and species transport. Its capabilities enable the modelling of complex interactions between turbulent flow fields, chemical reactions, and heat transfer processes that define buoyant diffusion flames.

Key features of FireFOAM that support its application in this study include:

Open-Source Customisability: Access to source code allows users to modify solver behaviour, physical models, and numerical methods, making it adaptable to specific research needs.

Multiphysics Modelling: FireFOAM incorporates advanced sub-models for turbulence, radiation, combustion, and multiphase interactions, enabling comprehensive simulation of real fire conditions.

Computational Cost Efficiency: The absence of licensing fees makes FireFOAM a cost-effective solution for conducting high-resolution, parametric studies.

This chapter aims to replicate the buoyant diffusion flame conditions observed experimentally in the USYD Burner [3] [112]. Using the FireFOAM solver, the simulation explores flame structure, temperature distribution, and species transport under buoyancy-driven combustion. The numerical results are then compared with experimental data to assess model accuracy and validate the solver's capability in reproducing key fire behaviour characteristics.

6.2 Methodology

This section outlines the numerical methodology used to simulate the diffusion flame within the University of Sydney Burner (USYD Burner) using FireFOAM.

The simulation process involved defining the computational domain, selecting suitable turbulence and combustion models, and specifying solver schemes and boundary conditions tailored to buoyancy-driven, non-premixed combustion scenarios. A summary of the core methodological components is presented below.

6.2.1 FireFOAM Solver Overview:

FireFOAM is an advanced reacting flow solver based on the Favre-filtered compressible Navier–Stokes equations under the Large Eddy Simulation (LES) framework. Developed as part of OpenFOAM [113, 114],and further enhanced by research institutions and FM Global [24].

FireFOAM is designed to capture the complex coupling between fluid flow, heat transfer, and chemical reactions. It solves the Favre-filtered, compressible Navier–Stokes equations under the Large Eddy Simulation (LES**)** framework, enabling it to resolve large-scale turbulent structures while modelling smaller eddies through sub-grid scale turbulence models Poinsot and Veynante [42] It supports multi physics simulations including:

Turbulent combustion modelling: FireFOAM incorporates combustion models capable of representing diffusion flames, premixed flames, and partially premixed regimes [9]

Radiative heat transfer using participating media models.

Soot formation and pyrolysis relevant to fire behaviour. [10]

Multiphase interaction capabilities FireFOAM includes modules for simulating water sprays, droplets, and liquid transport within fires, which relevant for suppression system design and analysis.

In this study, FireFOAM is employed to simulate the buoyancy-driven diffusion flame produced by The University of Sydney Burner (USYD Burner). The solver's ability to resolve turbulent structures, model complex thermochemical behaviour, and account for radiative and convective heat transfer makes it an appropriate tool for capturing the essential dynamics of uncontrolled, diffusion-dominated flames.

6.2.2 Geometry and Mesh Setup

The geometry and mesh used for the USYD Burner simulation in FireFOAM followed the same configuration outlined in Chapter 5. The computational domain captured the internal flow region of the burner, including the fuel inlet, burner walls, and outlet section. A structured mesh was applied, with additional refinement introduced in areas expected to exhibit high gradients, such as the burner exit and flame zone. Mesh quality and independence were confirmed through preliminary tests, as described earlier in Section 5. No further changes to the geometry or meshing strategy were necessary for this simulation.

6.2.3 Governing equations

The FireFOAM solver is based on the Favre-filtered formulation of the fundamental conservation equations, which include mass, momentum, sensible enthalpy, and species transport. These equations are designed to resolve the large-scale turbulent structures within reactive flows, using the Large Eddy Simulation (LES) approach. The following governing

equations, as described as described by Poinsot and Veynante [42] which are solved by FireFOAM:

Mass Conservation:

$$\frac{\partial \bar{\rho}}{\partial t} + \frac{\partial \left(\bar{\rho}\tilde{u}_j\right)}{\partial x_j} = 0 \qquad \text{Equation 6-1}$$

Momentum Conservation:

$$\frac{\partial(\bar{\rho}\tilde{u}_i)}{\partial t} + \frac{\partial(\bar{\rho}\tilde{u}_i\tilde{u}_j)}{\partial x_j} = \frac{\partial \bar{p}}{\partial x_i} + \frac{\partial}{\partial x_j}\left(\left(\bar{\rho}(\nu + \nu_{SGS})\left(\frac{\partial \tilde{u}_i}{\partial x_j} + \frac{\partial \tilde{u}_j}{\partial x_i} - \frac{2}{3}\delta_{ij}\frac{\partial \bar{u}_k}{\partial x_k}\right)\right)\right) + \bar{\rho}g_i$$

Equation 6-2

Sensible Enthalpy Transport:

$$\frac{\partial(\bar{\rho}\tilde{h}_s)}{\partial t} + \frac{\partial(\bar{\rho}\tilde{u}_j\tilde{h}_s)}{\partial x_j} = \frac{D\bar{p}}{Dt} + \frac{\partial}{\partial x_j}\left(\bar{\rho}\left(\alpha + \frac{\nu_{SGS}}{P_{r\,SGS}}\right)\frac{\partial \tilde{h}_s}{\partial x_j}\right) + \overline{\dot{\omega}'''_{h_s}} - \overline{\dot{q}'''_r}$$

Equation 6-3

Species Mass Fraction:

$$\frac{\partial(\bar{\rho}\tilde{Y}_k)}{\partial t} + \frac{\partial(\bar{\rho}\tilde{u}_j\tilde{Y}_k)}{\partial x_j} = \frac{\partial}{\partial x_j}\left(\bar{\rho}\left(D_{Y_K} + \frac{\nu_{SGS}}{S_{c\,SGS}}\right)\frac{\partial \tilde{Y}_k}{\partial x_j}\right) + \overline{\dot{\omega}'''_{Y_k}}$$

Equation 6-4

Where:

$\bar{\rho}$	Favre-averaged density
$\tilde{u}_i$	Favre-averaged velocity component
$\bar{p}$	Favre-averaged pressure
ν	Kinematic viscosity
ν_{SGS}	Sub-grid scale viscosity
δ_{ij}	Kronecker delta
g_i	Gravitational acceleration
$\tilde{h}_s$	Favre-averaged sensible enthalpy
Pr_{SGS}	Sub-grid Prandtl number
D_{Y_K}	Mass diffusivity of species k
$\overline{\dot{\omega}'''_{Y_k}}$	represents the volumetric heat release rate (HRR).
~	represents the Favre filter operator.
$\dot{\omega}'''_{h_s}$	represents the rate of change of the sensible enthalpy due to the reactions.
$\overline{\dot{q}'''_r}$	represents the radiation source term.
$\frac{\partial(\bar{\rho}\tilde{u}_j\tilde{h}_s)}{\partial x_j}$	represents the convection (or advection) of sensible enthalpy.
$\frac{D\bar{p}}{Dt}$	represents the substantial derivative of pressure, indicating the rate of change of pressure experienced by a moving fluid element.

Lewis Number Assumption:

In this study, the Lewis number is assumed to be unity. It is defined as the ratio of thermal diffusivity to mass diffusivity of a species:

$$L_{e_k}=\frac{\alpha}{D_{Y_K}}=\frac{thermal\ diffusivity}{mass\ diffusivity\ of\ species\ k}$$

Equation 6-5

6.2.4 Solver Settings and Numerical Schemes

FireFOAM utilises the PIMPLE algorithm, which combines elements of the PISO (Pressure Implicit with Splitting of Operators) and SIMPLE (Semi-Implicit Method for Pressure-Linked Equations) algorithms for effective pressure-velocity coupling Hrvoje [115]. This approach enables stable and accurate simulations.

6.2.5 Turbulence Models

In Large Eddy Simulation (LES), the larger turbulence scales are directly resolved by the computational grid, while the effects of smaller, sub-grid scales are modelled. The primary function of the turbulence model is to estimate the sub-grid scale (SGS) viscosity **(**ν_{sgs}**)**, which accounts for the energy dissipation occurring at scales smaller than the grid resolution.

The effectiveness of the SGS model depends heavily on the grid resolution. Coarser grids, which cannot capture finer turbulent structures, rely more on the turbulence model to simulate these effects. In this study, because the grid resolution is sufficiently refined, the influence of the specific turbulence model on the calculated SGS viscosity becomes less significant. However, the turbulence model remains essential in determining the turbulent mixing time scale, which is a key parameter in combustion modelling.

Beyond this, the turbulence model is critical for determining the mixing time scale needed in the combustion model. Each turbulence model, such as the one-equation eddy-viscosity model

and the WALE model, offers unique strengths and weaknesses, making the choice of model important. In this study, we employ the one-equation eddy viscosity model, which has previously demonstrated success in similar configurations.

One-Equation Eddy Viscosity Model:

To accurately represent the influence of unresolved turbulence in LES, this study employs the One-Equation Eddy Viscosity Model. This approach introduces a transport equation for the sub-grid scale turbulent kinetic energy ($\boldsymbol{k_{sgs}}$), which forms the basis for calculating the sub-grid scale dissipation rate ($\boldsymbol{\epsilon_{sgs}}$), eddy viscosity (v_{sgs}), and other associated turbulence quantities. By solving this single equation for $\boldsymbol{k_{sgs}}$, the model provides a more detailed and dynamic description of the sub-grid scale energy transfer, particularly useful in reacting flows where small-scale turbulence significantly influences combustion behaviour. The subsequent sections outline each key term and their formulation as implemented in the present FireFOAM simulation of the USYD burner.

Sub-grid Scale Turbulent Kinetic Energy ($\boldsymbol{k_{sgs}}$):

The one-equation eddy viscosity model is used to represent sub-grid scale (SGS) turbulence in Large Eddy Simulation (LES). It focuses on computing the SGS turbulent kinetic energy k_{sgs} which is essential for accounting for the influence of unresolved small-scale turbulent motions. This model provides a practical approach to capturing the dynamics of turbulent eddies that are smaller than the computational grid resolution [8]

The transport equation k_{sgs} is given by:

$$\frac{\partial(\bar{\rho}k_{sgs})}{\partial t}+\frac{\partial(\rho\tilde{k}_{sgs}\widetilde{u_i})}{\partial x_i}=\frac{\partial}{\partial x_i}\left(\bar{\rho}\left(v+v_{sgs}\right)\frac{\partial\tilde{k}_{sgs}}{\partial x_i}\right)+P-\rho\epsilon_{\ sgs}$$

Equation 6-6

Where:

ρ: the density

v: the kinematic viscosity

v_{sgs}: the sub-grid scale viscosity.

P: the production term of SGS kinetic energy.

$\epsilon_{\ sgs}$: the SGS dissipation rate.

SGS Eddy Dissipation Rate (ϵ_{sgs}):

The dissipation rate of sub-grid scale turbulent kinetic energy $\epsilon_{\ sgs}$ is calculated using the following expression [42]:

$$\epsilon_{\ sgs}=\ C_\epsilon\frac{k_{sgs}^{2/3}}{\Delta}$$

Equation 6-7

Where:

C_ϵ: the model constant

Δ : represents the characteristic filter width, typically related to the grid cell size.

SGS Eddy Viscosity:

The SGS viscosity is calculated from the SGS turbulent kinetic energy as [42]:

$$v_{sgs}=C_k\sqrt{k_{sgs}}\Delta$$

Equation 6-8

Where:

C_k: the model constant.

Production term (P):

The production term P in the sub-grid scale kinetic energy equation accounts for the transfer of energy from resolved scales to sub-grid scales. It is computed as:

$$P = -\frac{2}{3}\bar{\rho}\left(k_{sgs} + v_{sgs}\frac{\partial \tilde{u}_k}{\partial x_k}\right)\frac{\partial \tilde{u}_\iota}{\partial x_i} + 2\rho v_{sgs}\widetilde{S_{\iota J}}\widetilde{S_{\iota J}}$$

Equation 6-9

Where:

$\widetilde{S_{\iota J}}$: the resolved strain rate tenso

$\widetilde{u_\iota}$ and $\tilde{u}_k$: are the resolved velocity components

$\bar{\rho}$: the filtered density

Turbulent Mixing Time Scale(τ_{sgs}):

The turbulent mixing time scale, which is used in the combustion model, is defined as:

$$\tau_{sgs} = \frac{k_{sgs}}{\epsilon_{sgs}} = \frac{1}{c_\epsilon} \frac{\Delta}{\sqrt{k_{sgs}}}$$

Equation 6-10

Where:

c_ϵ: a model constant.

Δ:the local filter width related to the grid resolution.

6.2.6 Combustion model

Fire simulations frequently involve turbulent diffusion flames, where the fuel and oxidiser are not completely premixed prior to ignition. Instead, combustion occurs progressively as these components mix within the turbulent flow field. In such flames, the combustion rate is predominantly governed by the turbulent mixing time scale, rather than by the intrinsic chemical reaction rates. Since turbulent mixing is generally much faster than chemical kinetics in most fire scenarios, the influence of reaction time becomes negligible.

To model this behaviour effectively, **FireFOAM** adopts the Eddy Dissipation Model **(EDM)**, which is particularly well-suited for representing combustion under turbulence-dominated conditions. EDM captures the reality that large-scale fire combustion is largely mixing-limited, making it highly appropriate for the simulation of **diffusion flames** in fire safety applications.

Before introducing EDM, it is useful to briefly describe the Eddy Break-Up **(EBU)** model, which serves as a conceptual foundation for many turbulence–chemistry interaction models. The EBU model, introduced by Spalding [43], was developed for premixed turbulent flames and operates under the fast-chemistry assumption, where fuel and oxidiser react

instantaneously upon mixing. Under this assumption, the reaction rate is primarily determined by the turbulence-induced mixing rate.

The mean chemical reaction rate in the EBU model is given by:

$$\omega_f = -C_{EBU}\sqrt{\frac{Y_f''^2}{\tau_t}}$$

Equation 6-11

Where:

C_{EBU}: is a model coefficient.

$Y_f''^2$: is the variance of the mixture fraction of the fuel,

The characteristic turbulence time $\tau_t$is defined as:

$$\tau_t = \frac{\kappa}{\epsilon}$$

Equation 6-12

Where:

$\kappa\ and\ \epsilon$ are the Favre-averaged turbulent kinetic energy and the dissipation rate respectively.

The Eddy Dissipation Model (EDM), proposed by Magnussen and Hjertager. [90], extends this approach to include both premixed and diffusion flames. Unlike the EBU model which is based on the variance of the fuel mixture fraction, EDM focuses on the limiting reactant in the system.

In lean mixtures, fuel is typically the deficient species.

In rich mixtures, oxygen becomes the limiting component.

The EDM equation calculate the mean chemical reaction rate (ω_f) as detail in Wang, Chatterjee and de Ris [29] by considering:

Y_f: is the mean chemical reaction rate.

Y_0: is the oxidizer.

Y_p: are the products.

τ_t: is the turbulent mixing time.

s: is the stoichiometric mass ratio of oxidizer to fuel.

$$\omega_f = -C_{EDM}(\frac{Y_f}{\tau_t}, \frac{Y_0}{s\tau_t}, \frac{Y_p}{(1+s)\tau_t})$$

Equation 6-13

In FireFOAM, the EDM is implemented in a slightly modified manner, particularly in how it interacts with the global reaction equations. Rather than resolving detailed kinetics or intermediate species, FireFOAM employs a single-step global reaction to represent the conversion of fuel and oxidiser into combustion products. Although this simplification does not capture detailed chemistry, it effectively represents the dominant flame behaviour and is well suited to fire-scale simulations.

6.2.7 Radiation model

In the FireFOAM solver, thermal radiation needs to be considered for accurately simulating in fire scenarios. The FireFOAM solver uses the finite volume discrete ordinates model (fvDOM)

To solve the radiative heat transfer equation. This approach tackles the radiative heat transfer equation by dividing the directions of radiation travel into a finite specific number of discrete directions, allowing for detailed calculations of radiative heat transfer in complex fire geometries.

Key Components of the Radiation Model in FireFOAM:

Finite Volume Discrete Ordinates Model (fvDOM):

Solves the RTE by dividing the radiation field into discrete angular segments, allowing for directional calculation of radiative fluxes within the domain.

Weighted Sum of Gray Gases Model (WSGG):

Used to approximate the absorption and emission behaviour of combustion gases. The WSGG model simplifies the spectral complexity of gas radiation by using a limited set of grey gases, providing a computationally efficient solution.

Initially, radiation effects were excluded from the simulation. As a result, the flame temperature approached the adiabatic flame temperature, with values reaching approximately 2200 K. While this is consistent with idealised conditions, it neglects radiative heat losses that naturally occur in real fire environments.

6.2.7.1 Simplified Radiation Assumptions

To produce a more realistic thermal representation of the flame, radiation modelling was subsequently enabled using simplified assumptions, including:

Direct Radiation Path "Non-Scattering":

This assumption indicates that the medium through which radiation travels does not disperse the radiation in various directions. Accounting for scattering can complicate the calculations due to the need to consider multiple directions and interactions.

Non-Absorbing: This means that the medium does not absorb the radiative energy passing through it. In reality, many gases can absorb radiation, but this simplification ignores such effects to reduce computational complexity.

Global radiative heat loss fraction: A fixed value of 23 percent was applied, based on previous studies by White, Link [116], and Vilfayeau, Myers [41]. This fraction represents the proportion of energy released during combustion that is lost through radiation.

These simplifications serve as an intermediate modelling approach, offering a balance between highly detailed radiation transport methods and completely adiabatic assumptions. This is particularly suitable for scenarios with minimal soot production, as is the case in methane-fuelled flames. Methane combustion typically generates low amounts of soot, which reduces the influence of particulate radiation and justifies the exclusion of soot effects from the model.

6.2.8 Simulation Results with and without Radiation Model

To investigate the impact of radiative heat transfer on flame characteristics, simulations were performed both with and without the radiation model enabled.

6.2.8.1 Without Radiation Model:

When radiation effects were excluded, the simulation predicted a peak flame temperature of approximately 2200 K, which is in close agreement with the theoretical adiabatic flame temperature of methane-air mixtures (approximately 2240 K). This consistency confirms that, under adiabatic conditions, the thermal energy release in the FireFOAM simulation aligns with expected combustion theory.

6.2.8.2 With Radiation Model Enabled:

Activating the radiation model resulted in a substantial reduction in peak flame temperature, with values dropping to approximately 1800 K. This reduction of around 23% in peak temperature reflects the energy losses due to radiative heat transfer. The inclusion of radiation provides a more realistic representation of actual fire conditions, where heat is dissipated not only through convection and conduction but also through radiative emission.

6.2.8.3 Conclusion

The inclusion of radiation effects revealed a notable difference in predicted flame temperature, reinforcing the importance of radiative heat transfer in fire modelling. By accounting for radiative losses, the simulation offers a more accurate estimate of flame behaviour and thermal feedback.

With peak temperatures around 1800 K, the results align well with theoretical expectations, considering the 2240 K adiabatic baseline and the 23% radiative heat loss. This modelling approach strikes a practical balance between computational efficiency and physical accuracy, making it well suited for studying methane-fuelled diffusion flames in fire dynamics research.

6.3 Simulation Setup

6.3.1 Setting Up the Burner Simulation:

This subsection outlines the configuration process for simulating the buoyant diffusion flame in the USYD Burner using FireFOAM. The setup includes defining the computational domain, geometry, mesh generation, and boundary conditions. The model replicates the burner configuration used in the experimental studies conducted at the University of Sydney [112]

6.3.2 Computational Domain and Grid Independence:

6.3.2.1 Geometry and Domain Construction

The computational domain is centred around the burner exit and extends vertically into the wind tunnel to capture the buoyancy-driven flow development. The burner geometry consists of a 35 mm internal diameter (ID) brass tube, with a 2.5 mm wall thickness, through which compressed natural gas (CNG) is introduced. The fuel composition comprises 88.8% CH_4, 7.8% C_2H_4, 1.9% CO_2, and 1.2% N_2. The domain height is set to 1000 mm to accommodate the full flame development. The burner outlet and the surrounding air inlet are shown in Figure 6-1 and Figure 6-2, respectively.

Figure 6-3 provides a visual reference for the USYD burner flame observed during experimental testing. The image illustrates the nature of the vertical flame and turbulence features that are simulated in this chapter using FireFOAM.

The numerical analysis presented in this chapter focuses on a case with a heat release rate (HRR) of 20 kW, corresponding to **Flame F3** in the experimental campaign described in Chapter 5. [112]

By selecting this case, the numerical model captures a representative intermediate flame with moderate turbulence intensity, allowing meaningful comparison with experimental measurements in terms of temperature distribution, species concentration, and flame structure. The boundary and operating conditions in the simulation are configured accordingly to reflect these values.

To minimise computational cost, a 2D domain was used with structured meshing. A block-structured mesh was adopted, which facilitates refinement and quality control.

Three mesh resolutions were tested to ensure grid independence:

O (22,500 cells) – Initial coarse mesh.

Re-1 (160,000 cells) – Medium refinement.

Re-2 (250,000 cells) – High refinement.

By comparing the key results from each mesh (e.g. temperature and species profiles), mesh Re-1 was selected for further analysis due to its balance of accuracy and computational efficiency.

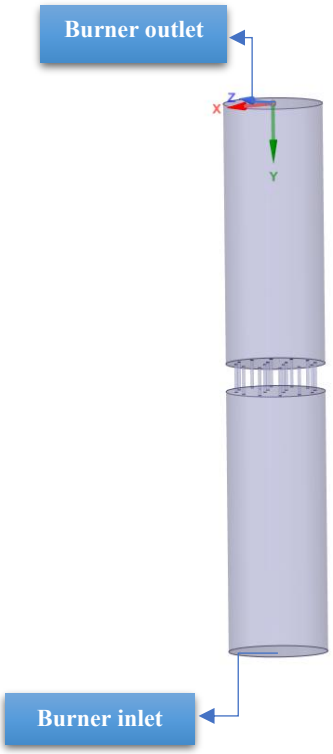

Figure 6-1 Fluid Volume-burner

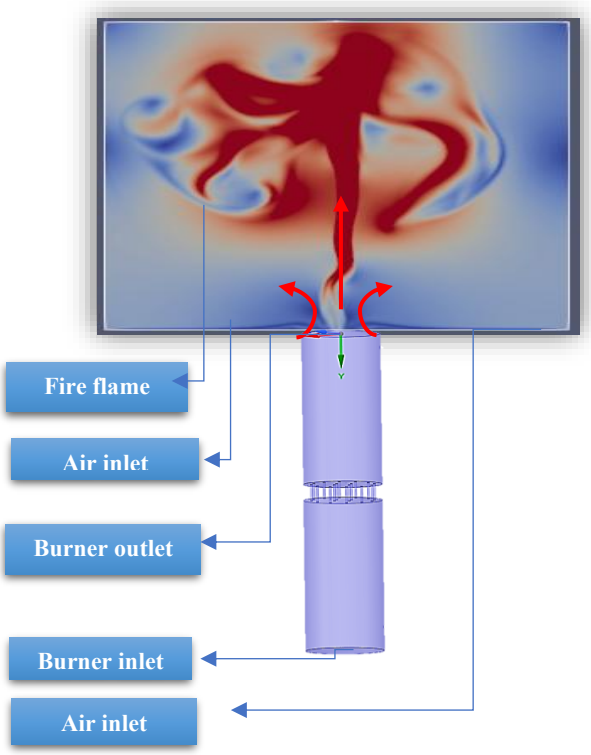

Figure 6-2 Computational domain of combustion model

Figure 6-3 Sydney Burner-Fire Flame.

6.3.3 Burner Design Analysis

6.3.3.1 Burner Configuration

The design and operational principles of the University of Sydney Burner (USYD Burner) were presented in detail in Chapter 5, where the burner geometry, perforated plate design, and its role in controlling turbulence levels were extensively discussed.

To support clarity and maintain fluency in this chapter, a brief summary is provided. The burner is constructed from brass, with an internal diameter of 35 mm and a wall thickness of 2.5 mm. It is designed to deliver a vertical fuel jet, producing buoyancy-driven flames under controlled conditions.

The burner is supplied with Compressed Natural Gas (CNG), comprising:

88.8% Methane (CH_4)

7.8% Ethylene (C_2H_4)

1.9% Carbon Dioxide (CO_2)

1.2% Nitrogen (N_2)

A key design feature is the perforated brass plate, 8 mm thick with 25 evenly spaced 1 mm diameter holes.

6.3.3.2 Burner Operation and Control

As discussed in Chapter 5, the turbulence characteristics at the burner exit are controlled primarily through two mechanisms: the fuel flow rate and the adjustable recess position of the perforated plate. The turbulence level increases significantly with the introduction of the plate due to high shear generated by the micro-jets, even when the bulk fuel velocity remains unchanged.

The experimental studies conducted by the experimental team demonstrated that turbulence levels rise considerably, from 0.135 m/s to 1.873 m/s RMS, as a direct result of the burner geometry. This confirms that the increase in turbulence is not solely due to higher fuel flow rates but is strongly influenced by the introduction of the turbulence-generating plate. These findings validate the USYD burner design as an effective platform for controlling and studying flame turbulence.

In this numerical study, the fuel flow rate was set to replicate the experimental case for a 20 kW heat release rate. A plate recess distance of 75 mm was selected, consistent with the experimental configuration used for flames F2 to F5.

This configuration is especially significant, as the level of turbulence has been shown to affect several aspects of flame behaviour. The experiments revealed that greater turbulence levels lead to delayed soot formation and a reduction in soot intensity. This supports the suitability of the USYD burner for exploring the complex interactions between turbulence and combustion in buoyant diffusion flames.

6.3.3.3 Operating Conditions:

The burner was operated within a wind tunnel environment under standard atmospheric conditions to ensure flame stability and reproducibility. A co-flow velocity of approximately 0.2 m/s was applied to maintain a steady ambient air stream surrounding the flame and to minimise external disturbances. The fuel flow rates and resulting Froude numbers for each test case are presented in Table 6.1

Table 6.1 Burner Operation Conditions with plate.

Heat Release Rate (Q) [kW]	***Fuel Flow Rate (mf)[L/min]***	**Froude Number (Frf)**	**Fuel Exit Velocity (vin) [m/s]**
20	36.6	.0127	.634

6.3.4 Boundary conditions

In CFD simulations, boundary conditions (BCs) define how variables like velocity, pressure, and temperature behave at the domain limits. For the USYD Burner, appropriate Dirichlet and Neumann conditions were assigned across inlet, outlet, and wall boundaries to replicate the physical setup.

Table 6.2 summarises the physical boundary conditions for temperature, pressure, velocity, and mass compositions at the burner and surrounding air. ZeroGradient (zG) conditions were applied where appropriate to allow natural flow development.

Table 6.3 details the turbulence-related boundary conditions. Turbulence kinetic energy and dissipation settings were based on experimental turbulence intensity estimates. The remaining boundary conditions are shown in Table 6.4

	Temperature (K)	Pressure (pa)	Velocity (m/s)	Mass compositions		
				CH4	O2	N2
Burner inlet	300	calculated	Exporting from the fluent ANSYS-burner model	1.0 Total flow rate advective diffusive	0	Calculated
Air Flow	zG	zG	(0,0.2,0)	zG	0.23	.77
Outlet and side	inletOutlet	101325	zG	zG	Calculated	Calculated

zG - zeroGradient
Velocity expressed in (axial, radial, tangential) components.

Table 6.2 Physical properties – SYD-burner - boundary conditions

	Pressure (Pa)	Velocity (m/s)	Turbulent kinetic energy	FSDomega	p_rgh
Inlet Burner(CH4)	calculated	Exporting from the fluent ANSYS-burner model.	I = 0.10	calculated	fixedFluxPressure
inletAir	calculated	(0 0 0.2)	I = 0.0471	calculated	fixedFluxPressure
frontAndBack	zeroGradient	noSlip	zeroGradient	zeroGradient	zeroGradient
Sides	zeroGradient	zeroGradient	inletOutlet	inletOutlet	zeroGradient
outlet	101325	calculated	inletOutlet	inletOutlet	calculated

Table 6.3 USYD Burner- boundary conditions

TurbulenceProperties	LES	kEqn
Chemistry	inertSpecie fuel	N_2 CH_4
Chemistry solver	on odeCoeffs initialChemicalTimeStep	 Rosenbrock34 absTol =1e-12; relTol .01 1e-07
PIMPLE	nOuterCorrectors nCorrectors	1 2
solver	rho| p| G p_rgh| Ii | U|h|k| FSDomega | Yi	PCG GAMG PBiCGStab
scheme	ddtSchemes gradSchemes divScheme laplacianSchemes interpolationSchemes snGradSchemes	Euler Gauss linear Gauss linear corrected linear corrected

Table 6.4 Numerical setting for USYD. Burner.

6.3.5 Residual Convergency Check

FireFOAM, like many CFD solvers, employs an iterative process to solve complex simulations. At each time step, the solver updates key variables such as velocity, pressure, temperature, and species mass fractions until a stable and accurate solution is achieved.

This convergence process is monitored by tracking the residuals, which represent the differences between successive iterations of the governing equations. As the solution becomes more accurate, these residuals decrease. FireFOAM allows users to define convergence thresholds for each variable, and the simulation progresses until all residuals fall below the specified tolerances.

In the initial simulations, a residual tolerance of 10^{-6} was applied. The results showed rapid convergence, with residuals typically decreasing to values between 10^{-7} and 10^{-8} in a single

iteration per time step. To ensure the independence of the solution from the chosen residual threshold, a stricter criterion of 10^{-9} was tested. Under this setting, some variables required two or three iterations per time step to converge.

Despite this increased strictness in convergence tolerance, the simulation results remained consistent across all test cases. This residual analysis was conducted for the 20 kW flame configuration, representing a mid-range turbulence condition with a perforated plate length ratio (Lr) of 75 mm. The computational domain was defined within a bounding box of (−0.5, 0, −0.01) m to (0.5, 1, 0.01) m and discretised into approximately 160,000 cells and 321,602 points, ensuring adequate spatial resolution near the flame zone. A second-order backward time integration scheme was employed, and boundary conditions were held constant across all tests.

These tests demonstrate that the simulation outcomes are robust across a range of residual tolerances. Accordingly, a residual threshold of 10^{-6} is considered sufficient for maintaining result accuracy while optimising computational cost. This threshold is therefore adopted for all subsequent simulations.

The Figure 6-4 illustrates the RMS axial velocity distribution across the burner exit plane for residual convergence thresholds of 10^{-6}, 10^{-7}, 10^{-8}, and 10^{-9}. Despite differences in solver tolerances, the resulting velocity profiles are nearly identical, with peak values of approximately 0.95 m/s near the burner edges and a minimum of about 0.7 m/s at the centerline. These results confirm the robustness of the simulation outcomes and support the choice of 10^{-6} as a reliable convergence criterion.

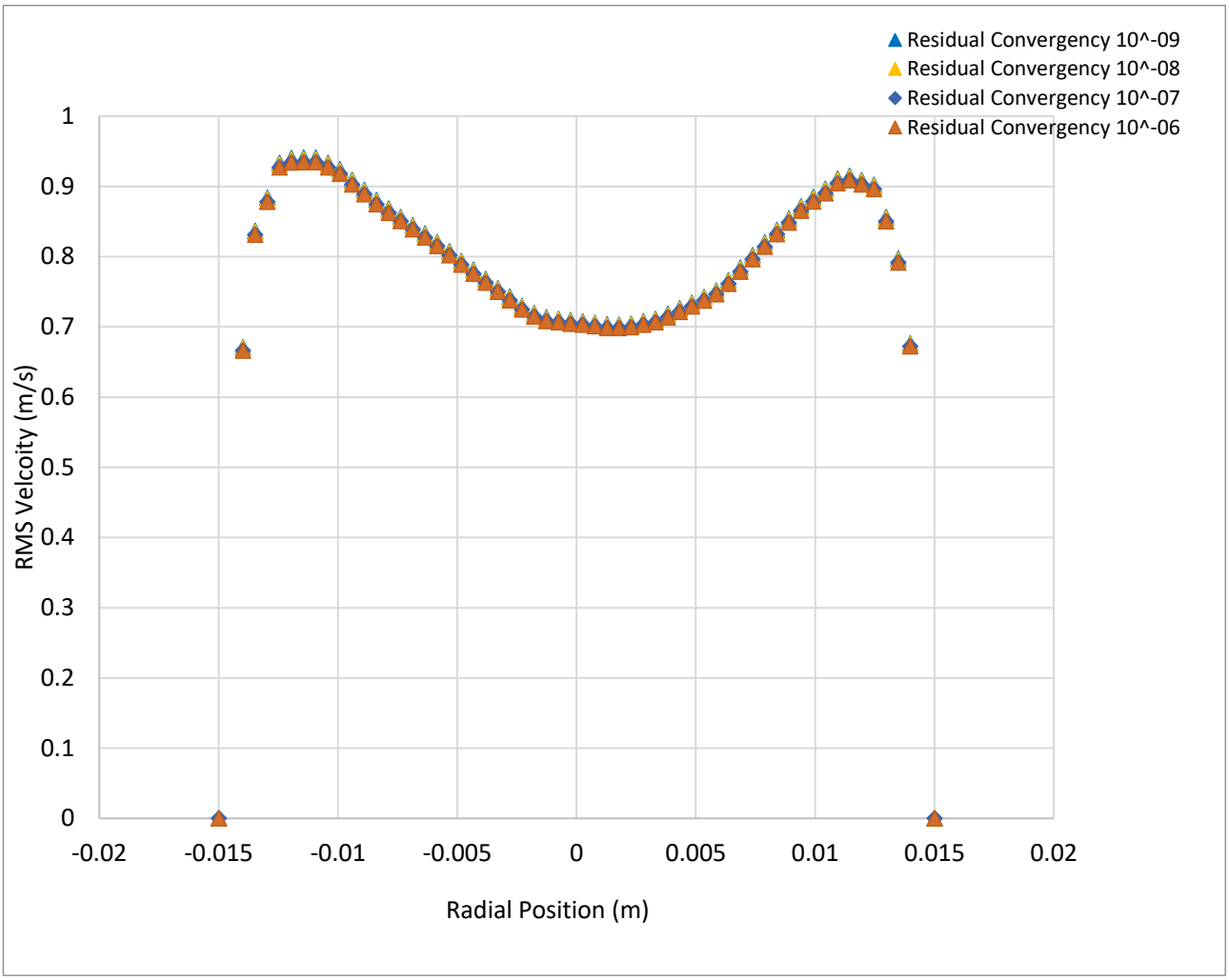

Figure 6-4 Residual Independence Check

6.4 Velocity profile with and without perforated plate.

This subsection evaluates the combustion model performance by comparing the velocity profile at the burner exit under two configurations: with and without the perforated plate. These comparisons are essential for validating the FireFOAM simulation results against both ANSYS Fluent predictions and experimental measurements from the USYD Burner setup.

The key objective is to assess the capability of FireFOAM to replicate the observed trends in velocity distribution, particularly in relation to peak velocities and flow behaviour near the burner wall, where turbulence is most pronounced. The simulations were conducted for the heat release rate (HRR) of **20 kW**, consistent with the experimental baseline.

Flow Without Perforated Plate

As shown in Figure 6-5 and Figure 6-7, the velocity profile obtained from FireFOAM and Fluent displays a near-parabolic shape, with the highest velocities recorded at the centreline of the burner. The experimental data points also follow this trend, although some deviations are noted at the outer radial positions. These differences may stem from measurement limitations or unaccounted disturbances in the experimental setup.

Flow With Perforated Plate

In contrast, the configuration with the perforated plate exhibits a markedly different velocity profile. Figure 6-6 and Figure 6-8 illustrate a double-peaked or "M-shaped" velocity distribution, with velocity maxima near the burner walls. This profile is indicative of shear-layer formation induced by high-velocity micro-jets from the plate. Both FireFOAM and Fluent simulations successfully capture this characteristic pattern, aligning closely with experimental measurements.

Table 6.5 -Velocity profile with/without perforated plate

	Flow in the burner without plate	Flow in the burner with plate
Streamlines of the fuel in the tube.	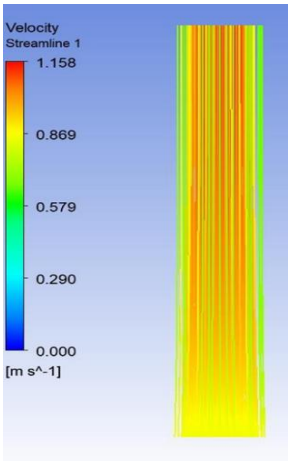 Figure 6-5 Streamlines for the flow in the tube without the plate.	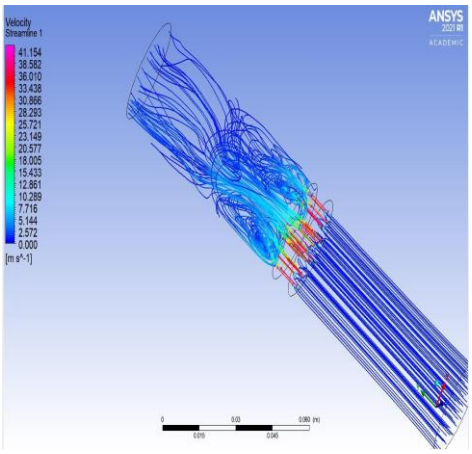 Figure 6-6 Streamlines for the flow in the tube with the plate.
Mean Velocity profile at the exit of the burner.	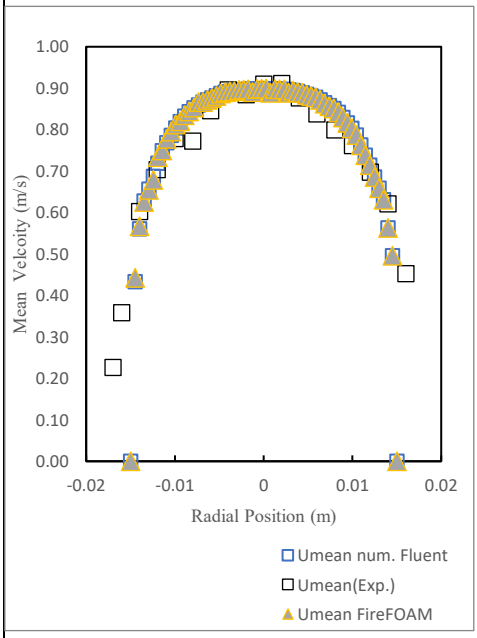 Figure 6-7 Mean Velocity profile at the exit of the burner.	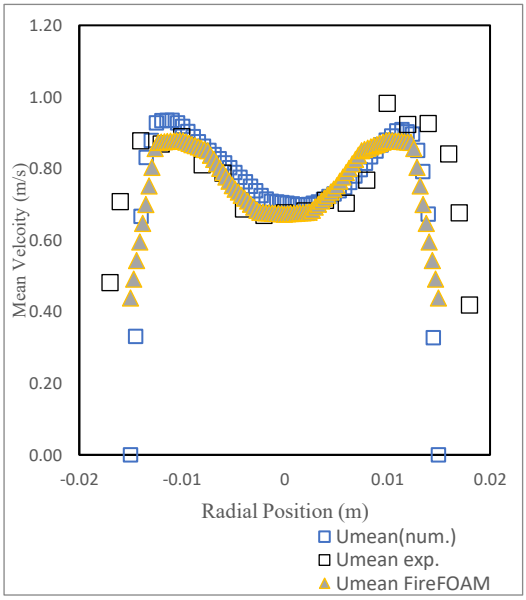 Figure 6-8 Mean Velocity profile at the exit of the burner.

Results	The mean velocity profile of the fuel at the exit of the burner without a plate shows a distinct pattern, which serves as a critical benchmark for evaluating the effectiveness and accuracy of different simulation models. A comparison of the data from the graph showcases good agreement between the experimental results and those obtained from both Fluent and FireFOAM simulations.	The comparison of mean velocity profiles among experimental data, ANSYS Fluent simulations, and FireFOAM results demonstrates a good alignment, particularly in the characterization of peak velocities. The peak values across the datasets closely correspond, underscoring the capability of both computational models to effectively replicate the observed experimental trends.
	The peak velocity observed aligns closely across the experimental data and simulations, suggesting that both FireFOAM and Fluent accurately represent the physical phenomena occurring near the burner exit.	The peak velocity values, indicative of the highest mean velocities observed within the flow, show a substantial agreement across all three methods. suggesting that both ANSYS Fluent and FireFOAM accurately capture the flow dynamics, especially in terms of peak velocity and flow direction. The close agreement between simulated peak velocities, flow directions, and near-wall behavior confirm the effectiveness of the simulation approaches.

6.5 Post-Processing Strategy

Post-processing was conducted using ParaView in conjunction with OpenFOAM built-in utilities. A combination of visualisation and quantitative tools was employed to analyse the flame characteristics and validate the numerical results.

Line probes were placed along the burner's centreline and selected radial cross-sections to extract data on velocity, temperature, and species mass fractions. These probes provided detailed profiles at multiple heights above the burner exit, enabling an examination of spatial flame development.

Contour plots of temperature and major species concentrations (CH_4, O_2, CO_2) were generated to evaluate the structure of the diffusion flame and the extent of combustion. These visualisations were used to interpret flame shape, mixing behaviour, and reaction zones.

The Plot Over Line tool was applied at specific axial positions (notably Y = 0.5 m and Y = 0.9 m) to extract numerical data for comparison with corresponding outputs from Fluent simulations and experimental datasets.

6.6 Results and Discussion:

6.6.1 Flame Characteristics: Temperature Distribution

Figure 6-9 presents the vertical temperature distribution captured through FireFOAM simulations. Peak temperatures reached approximately 1900 K when radiation was included, aligning with methane combustion theory under a 23% radiative heat loss assumption. The temperature decreases towards the flame tip due to convective and radiative dissipation.

Figure 6-10 illustrates the temperature contour. Blue regions (300–800 K) indicate ambient air and unburned fuel, while red to orange zones (1500–2000 K) mark the main combustion region. Yellow zones (~2200 K) represent near-adiabatic flame temperatures.

The flame displays a tongue-like shape with discernible vortex structures, indicating strong buoyancy effects and unsteady mixing. These patterns affirm the LES model's capacity to resolve the transient dynamics typical of turbulent diffusion flames.

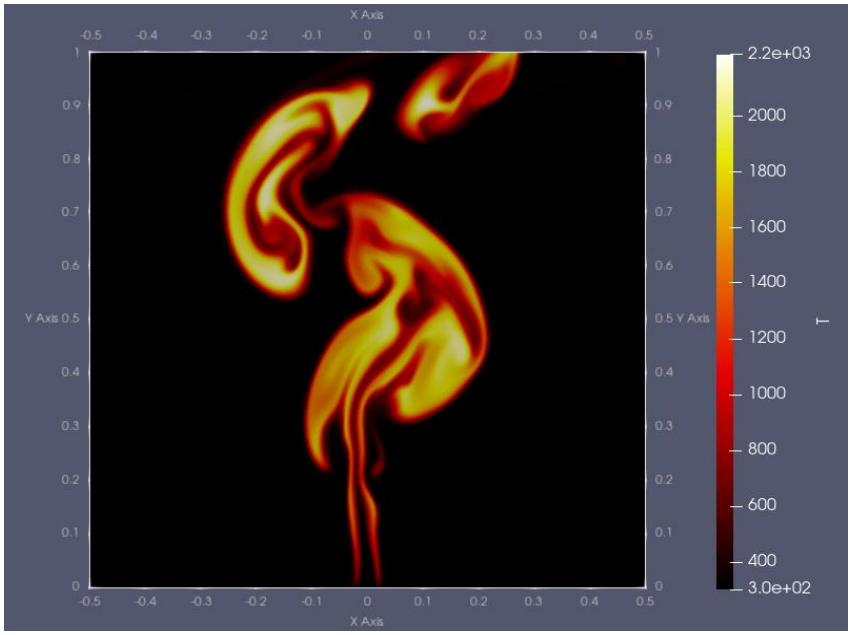

Figure 6-9 Temperature distribution

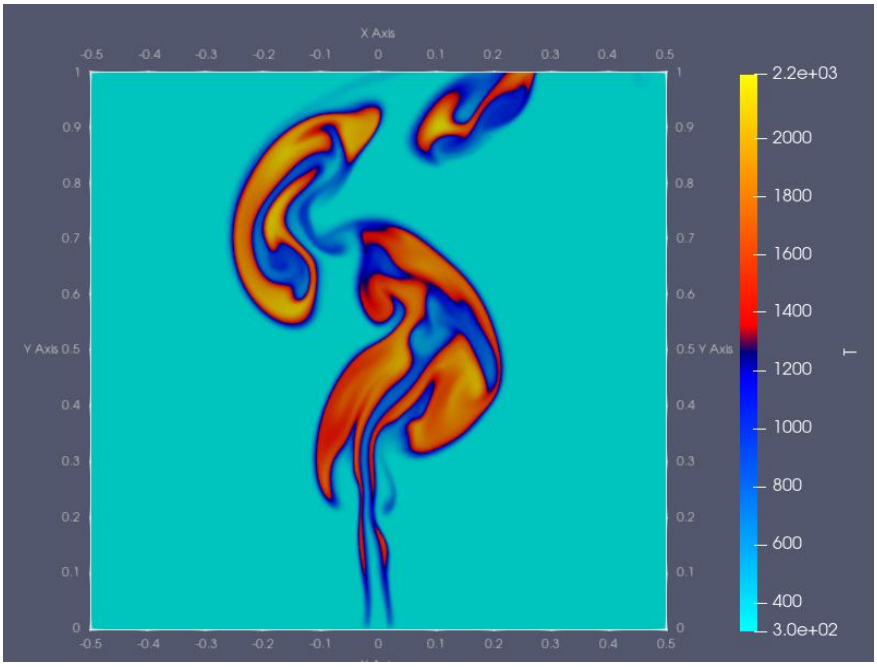

Figure 6-10 Temperature Contour of the USYD

Burner Flame

6.6.2 Flame Pinch-Off Instability

In the present study, the numerical simulation was configured to replicate the experimental Flame F2 case, which corresponds to a 20 kW fire with the turbulence-generating plate in place. Temperature contour results from the simulation reveal a distinct necking of the flame, followed by the formation of vortex-like structures, indicative of flame pinch-off behaviour. This behaviour is consistent with the experimental findings reported by Xiao et al. (2023) [112], where time-resolved OH-PLIF and soot scattering images show periodic flame pinch-off at the third axial window. Specifically, the experimental results for F2 illustrate a symmetrical narrowing at the flame neck, followed by detachment and upward advection of a flame pocket, occurring within a narrow time interval. The observed temperature gradients and the rolling structures in the numerical contour align with this pinch-off sequence, capturing the transition from a stabilised flame to periodic detachment driven by buoyancy and turbulence interaction

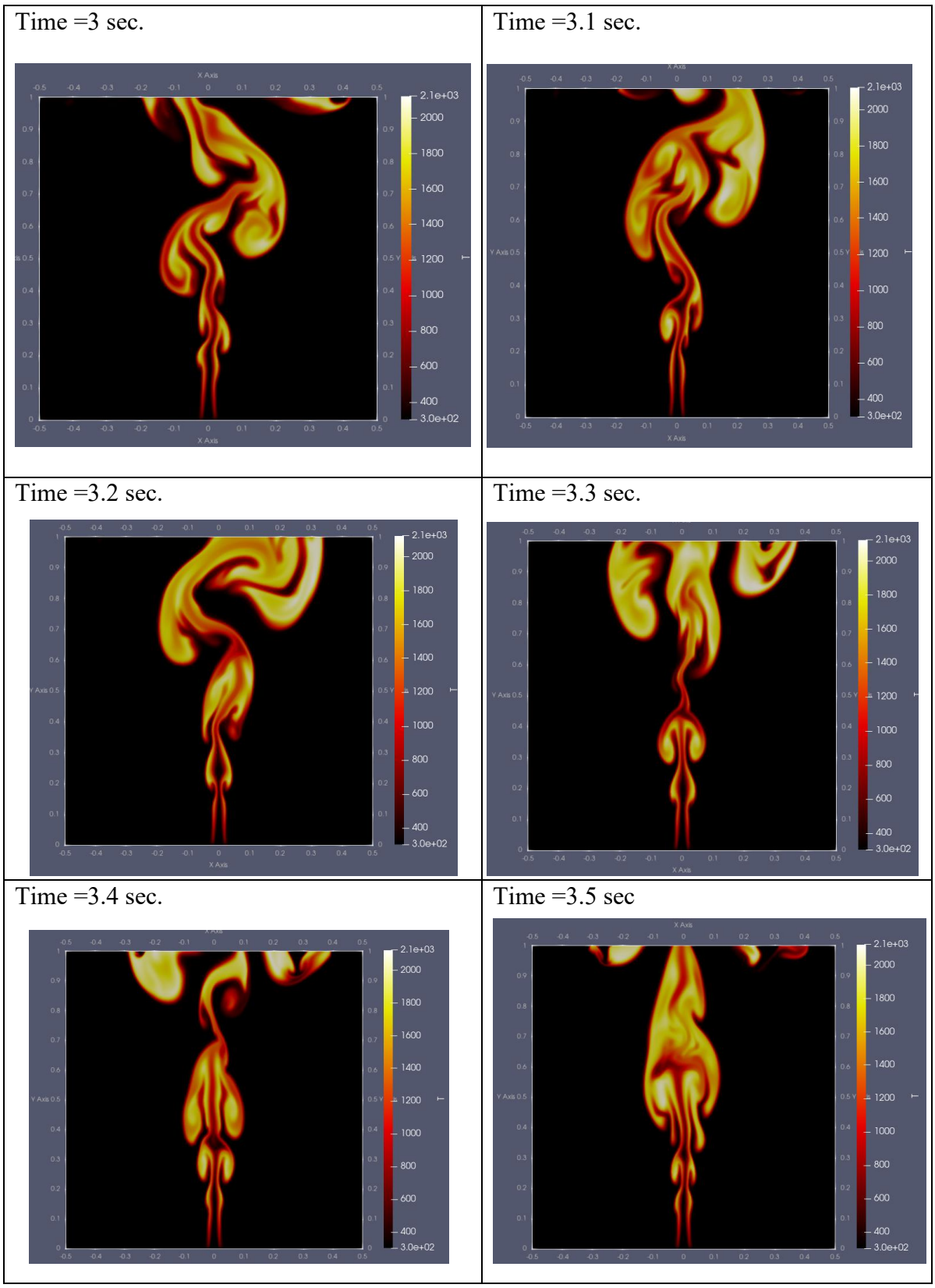

Figure 6-11 Time-resolved temperature contours showing the flame pinch-off evolution for the 20 kW case (3.0 s to 3.5 s).

To visualise the flame pinch-off process more clearly, Figure 6-10 presents a series of time-resolved temperature contours from 3.0 to 3.5 seconds. These snapshots show the dynamic evolution of the flame structure under the influence of buoyancy and induced turbulence. At 3.0–3.2 s, the flame base remains attached to the burner, with a stable shape and smooth thermal gradients. However, as the sequence progresses to 3.3–3.4 s, a narrowing is observed near the mid-height of the flame, forming a distinct neck. This marks the onset of pinch-off. By 3.5 s, the upper portion of the flame appears to have separated and is being convected upward, indicating the detachment of a flame pocket. This pattern is in agreement with the flame pinch-off behaviour described experimentally by Xiao et al [112]. The results confirm that the pinch-off process, caused by flow instabilities and buoyancy effects, can be captured using the FireFOAM model.

6.6.3 Flame Structure and Flow Dynamics

The numerical simulation of Flame F2 shows a tongue-shaped flame structure, which is commonly seen in buoyant turbulent diffusion flames. Near the burner, the flame appears stable and vertically aligned, forming what is referred to as the near-laminar region As the flame rises, it begins to curve and develop rolling structures due to the mixing between hot combustion gases and surrounding air This interaction generates vortical structures (swirling flows) that influence the flame's shape and motion.

This pattern matches what is seen in the experimental DSLR image of Flame 2 (see Figure 4.3 in [112]), where the flame grows vertically and then curves as it rises. Both the simulation and experiment exhibit a repeating puffing motion, identified as puffing instability, which is driven by buoyancy and turbulent mixing.

In the mid-flame region, the simulation reveals a necking zone, where the flame becomes narrow and constricted. This is the region where the flame may begin to detach, a process known as pinch-off. The top portion of the flame sometimes separates and is advected upwards

as a flame pocket. Since this case (F2) has low turbulence, the flame stays mostly symmetrical on both sides. This means it follows the varicose pinch-off mode, as described by Xiao in chapter 4 [112]. Overall, the simulation shows the same changes in flame structure and flow seen in the experiment from a stable base to a dynamic and puffing flame affected by buoyancy and air movement.

6.6.4 Flame Height

Flame height was determined as the vertical distance from the burner exit (y = 0 m) to the highest point where flame temperature exceeded 1000–1500 K. The FireFOAM simulation estimated a flame height of approximately 0.95 m, consistent with the behaviour expected from buoyant diffusion flames.

Experimental Reference

Experimental studies using the USYD Burner reported a mean flame height of 0.67 m for the 20 kW methane-fuelled case, known as Flame F3 [112].

The longer flame height predicted by the FireFOAM simulation can be attributed to two key modelling approaches. Firstly, the simulation incorporates radiative heat transfer using methods such as the finite volume discrete ordinates method (FVDOM) coupled with the weighted-sum-of-grey-gases model (WSGGM), which enhances the vertical spread of thermal energy and contributes to an extended flame appearance (Zhou et al.,) [117]. This radiative heat loss modelling allows a more accurate representation of thermal buoyancy effects compared to purely convective models. Secondly, the flame height in this study is defined using a temperature-based criterion, identifying regions where the local temperature exceeds a specific threshold. As demonstrated by Zhang et al.) [118], a temperature-based definition of flame height captures a wider zone of elevated thermal activity, including lower-luminosity regions not apparent in visual observations based on flame intermittency. The use of a temperature threshold-based definition (1000–1500 K) was selected to capture the thermal

extent of the flame consistent with previous numerical studies. The ~30–40% discrepancy observed here aligns with reported differences in Zhang et al. [118] and reflects the inclusion of low-luminosity, thermally active regions in the simulation.

Consequently, the simulated flame appears longer than that recorded in experimental imaging relying solely on visual flame boundaries.

Impact of Turbulence: With and Without Perforated Plate

To investigate the effect of turbulence on flame structure, two configurations were compared.

Without the Perforated Plate: As illustrated in Figure 6-13,

the flame showed a smooth and symmetrical shape with limited wrinkling. Combustion appeared more stable, with reduced turbulence.

With the Perforated Plate: As illustrated in Figure 6-12, the presence of high-velocity jets introduced strong shear, producing a more wrinkled and elongated flame front. Enhanced turbulence led to more intense combustion and a taller flame, along with greater unsteadiness.

Velocity contours and species concentration profiles supported these observations. The presence of vortex structures and increased upward gas motion confirmed the influence of turbulence on flame shape and behaviour.

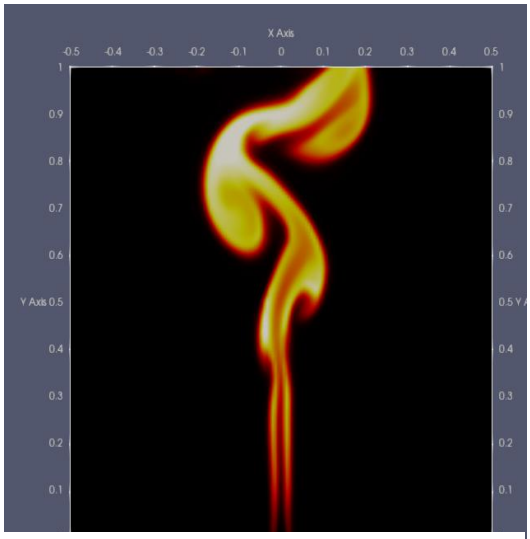

Figure 6-13 Fire Flame contour without perforated plate

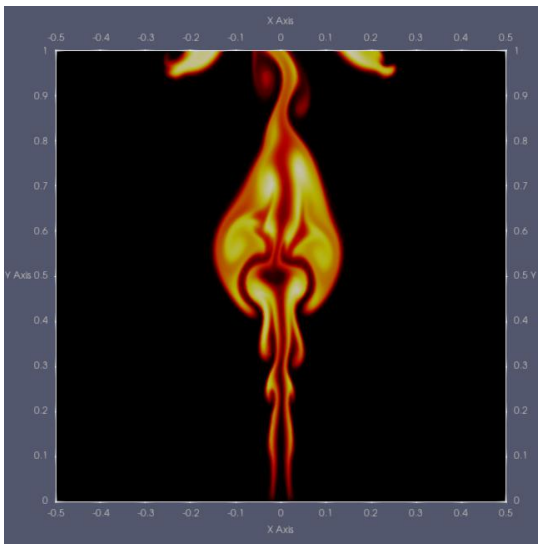

Figure 6-12 Fire Flame with perforated plate.

Conclusion

The simulation predicted a flame height of 0.95 m, which falls within the expected range for buoyant flames when accounting for the different definition used (temperature threshold versus visual intermittency.

Method	Flame Height (m)	Observation Type	Remarks
FireFOAM Simulation	0.95	Numerical	Based on temperature >1000–1500 K
Experimental (F3)	0.67	Experimental	Measured with 50% flame intermittency

Table 6.6 Flame Height Comparison Table

6.6.5 Species Concentration Profiles

To further evaluate flame characteristics, the distribution of temperature and major species (O_2, CO_2, CH_4) was examined at two critical axial positions within the flame: Y = 0.60 m (near mid-flame height) and Y = 0.90 m (near the flame tip). These positions were selected to capture both the core combustion behaviour and the burnout characteristics of the diffusion flame. Data were extracted using the *Plot Over Line* tool in ParaView, where each profile was sampled radially across the flame from X = −0.3 m to X = 0.3 m at a fixed height (Y = 0.6 m or Y = 0.9 m) and Z = 0.01 m, with a uniform sampling resolution of 500 points.

Although direct experimental measurements for species mass fractions (O_2, CO_2, CH_4) were not available for this study, the FireFOAM simulation results provide valuable insight into the combustion process. The resulting profiles exhibit physically consistent trends, including oxygen depletion, carbon dioxide formation, and methane consumption along the flame axis. These behaviours reflect expected chemical gradients within a buoyant diffusion flame and support the model's ability to capture species transport and reaction dynamics under the defined operating conditions.

.

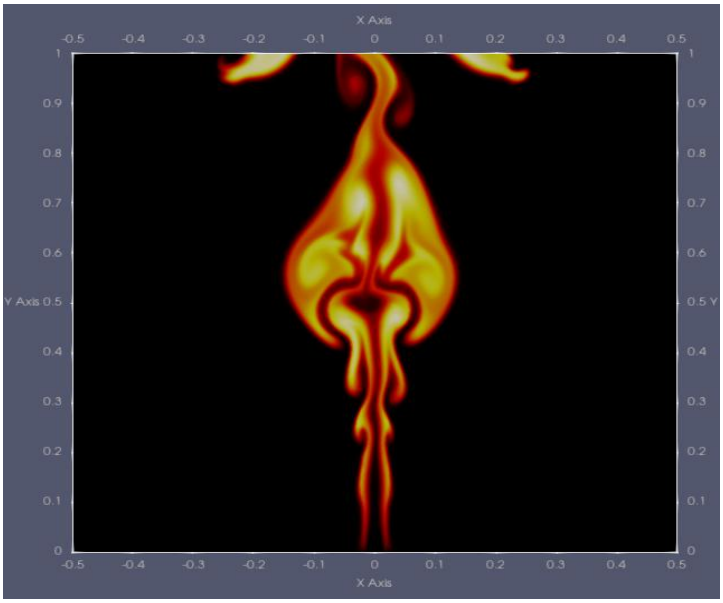

Figure 6-14 Fire Flame with perforated plate.

6.6.5.1 At Y = 0.6 m (Mid-Flame Region)

At this axial location, the radial distribution of flame properties reflects the main combustion zone of the buoyant diffusion flame. As illustrated in Figure 6-15, the sampling line intersects the central region of the flame, capturing gradients in species concentration and temperature influenced by intense chemical reactions and turbulent mixing. This region is particularly important for evaluating the effectiveness of fuel-oxidiser mixing, flame symmetry, and the completeness of combustion.

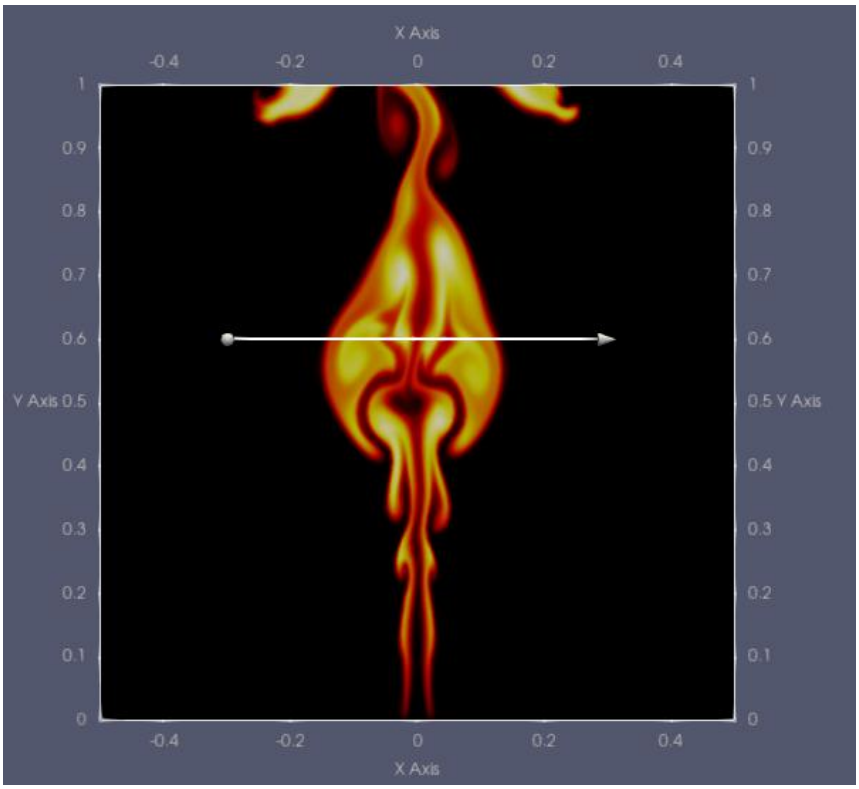

Figure 6-15 Sampling Line at Y = 0.6 m across the Mid-Flame Region

Temperature Profile:

The radial temperature distribution at Y = 0.6 m (see Figure 6-16) exhibits a characteristic double-peak structure, with two local maxima reaching approximately 2000–2100 K on either side of the centreline. This indicates a hollow-core flame structure, where combustion is more intense in the annular regions. The central dip, which reaches approximately 1000 K, corresponds to the fuel-rich core, where combustion is still developing due to limited mixing with oxygen. This is a typical feature in turbulent non-premixed diffusion flames.

O_2 Mass Fraction:

As shown in Figure 6-16**,** the oxygen mass fraction profile displays distinct depletion at radial positions that coincide with the temperature peaks. The lowest mass fractions fall to approximately 0.02–0.03, which aligns with the zones of peak combustion. Oxygen levels increase outward to ~0.07–0.08, highlighting ambient air entrainment and confirming reduced oxidiser availability at the centreline. This distribution supports the formation of a toroidal reaction zone where combustion is concentrated

CO_2 Mass Fraction:

The carbon dioxide concentration peaks just off the centreline, closely following the high-temperature regions as seen in Figure 6-16. Peak CO_2 values reach approximately 0.13, with values decreasing toward the centre and the outer radial limits, confirming the location of the primary reaction region and the production of combustion products where fuel and oxygen are best mixed.

CH_4 Mass Fraction:

As illustrated in Figure 6-16, methane concentration is highest at the flame core, with a pronounced central peak of approximately 0.45. The profile decreases steeply in the radial direction, dropping to less than 0.05 toward the flame edges. This confirms that unburnt fuel

accumulates in the centreline region, where oxygen is insufficient, while combustion progressively consumes methane as it mixes with entrained air outward.

Interpretation:

The combined analysis of the temperature and species mass fraction profiles at Y = 0.6 m reflects the characteristic structure of a buoyancy-driven turbulent diffusion flame. The presence of peak temperature and CO_2 concentrations in annular regions, accompanied by oxygen depletion and a centralised methane core, indicates the formation of a toroidal reaction zone surrounding a fuel-rich centreline. This flame structure suggests that combustion predominantly occurs in the outer zones where fuel and oxidiser are better mixed, while the inner core remains relatively unmixed and cooler. These trends align with established theoretical and experimental descriptions of diffusion flame behaviour and confirm that the FireFOAM simulation reliably captures the coupled dynamics of species transport, mixing, and combustion processes under buoyant conditions.

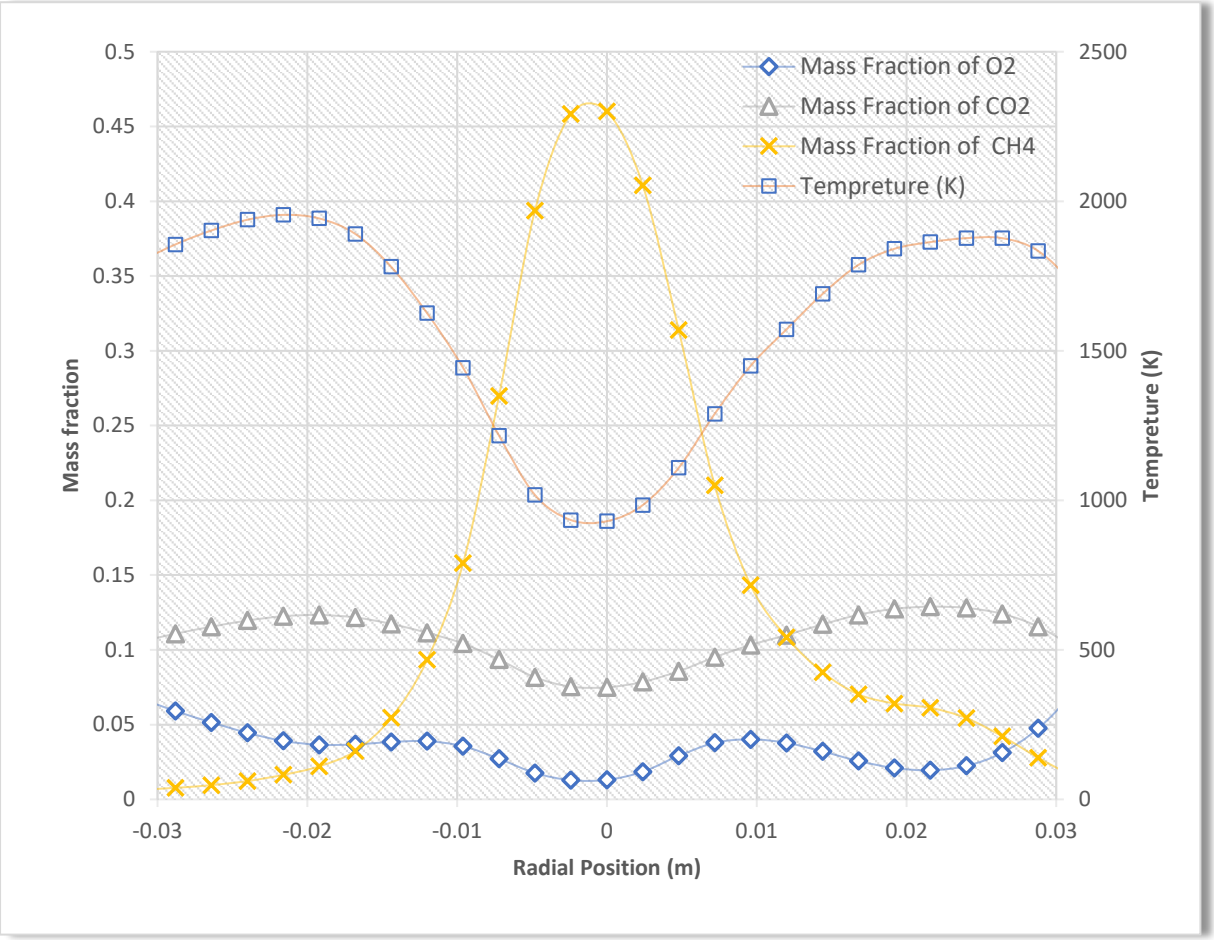

Figure 6-16 Radial Profiles of Species Mass Fractions and Temperature

6.6.5.2 At Y = 0.9 m (Flame Tip Region)

At this axial position, near the flame tip, the combustion process is largely complete. The temperature and species profiles reveal the residual effects of mixing, radiation, and post-flame gas dynamics.

Temperature Profile

At Y = 0.9 m, the radial temperature profile (Figure 6-17) shows a broader and less pronounced double-peak structure compared to the mid-flame region. Maximum temperatures on either side of the centreline reach approximately 1500–1600 K, while the central temperature dips to around 1200 K. The overall reduction in peak temperature values and flattening of the profile indicate a weakened combustion intensity near the flame tip, consistent with the burnout stage of the flame where fuel and oxidiser have been largely consumed.

O_2 Mass Fraction

The oxygen profile in Figure 6-17, shows significant radial variation, with low mass fractions (~0.02) near the centreline gradually increasing toward the edges. The outer radial regions exhibit higher oxygen content, reaching up to 0.22–0.24, consistent with strong entrainment of ambient air. These trends suggest that oxidiser has diffused inward from the surroundings at this height, but the centreline still reflects oxygen-depleted conditions from prior combustion.

CO_2 Mass Fraction

As shown in Figure 6-17, CO_2 concentrations remain highest just off the centreline, with values peaking at approximately 0.12, similar to the mid-flame results. However, the profile appears more asymmetrical and tapers more gradually toward the outer zones. The shape and persistence of these elevated values indicate that combustion products remain well distribut**ed** throughout the upper portion of the flame, though production of new CO_2 has decreased relative to lower heights

CH_4 Mass Fraction

The methane profile (Figure 6-17) is more flattened than at Y = 0.6 m, with a lower central peak of approximately **0.33**. The mass fraction decreases steadily with radial distance, approaching zero near the flame edges. This suggests that methane has been substantially consumed by this height, though residual fuel is still present in the core region. The reduced CH_4 levels, along with diminished temperature, point to the end stages of combustion, where flame extinction and mixing dominate.

Interpretation:

The analysis of temperature and species concentrations at Y = 0.9 m (Figure 6-17) reflects the burnout region of the buoyant diffusion flame. Compared to the mid-flame zone, the data show reduced peak temperatures**,** flattened CH_4 and CO_2 profiles, and increased O_2 levels**,** all indicating that combustion is less active and mixing processes are more dominant. These results are consistent with the expected behaviour of upward-propagating diffusion flames, where most fuel has already reacted and hot gases continue to rise while cooling and entraining ambient air. The FireFOAM simulation effectively captures these transitions in species and thermal structure toward the flame tip, reinforcing its ability to model late-stage combustion dynamics.

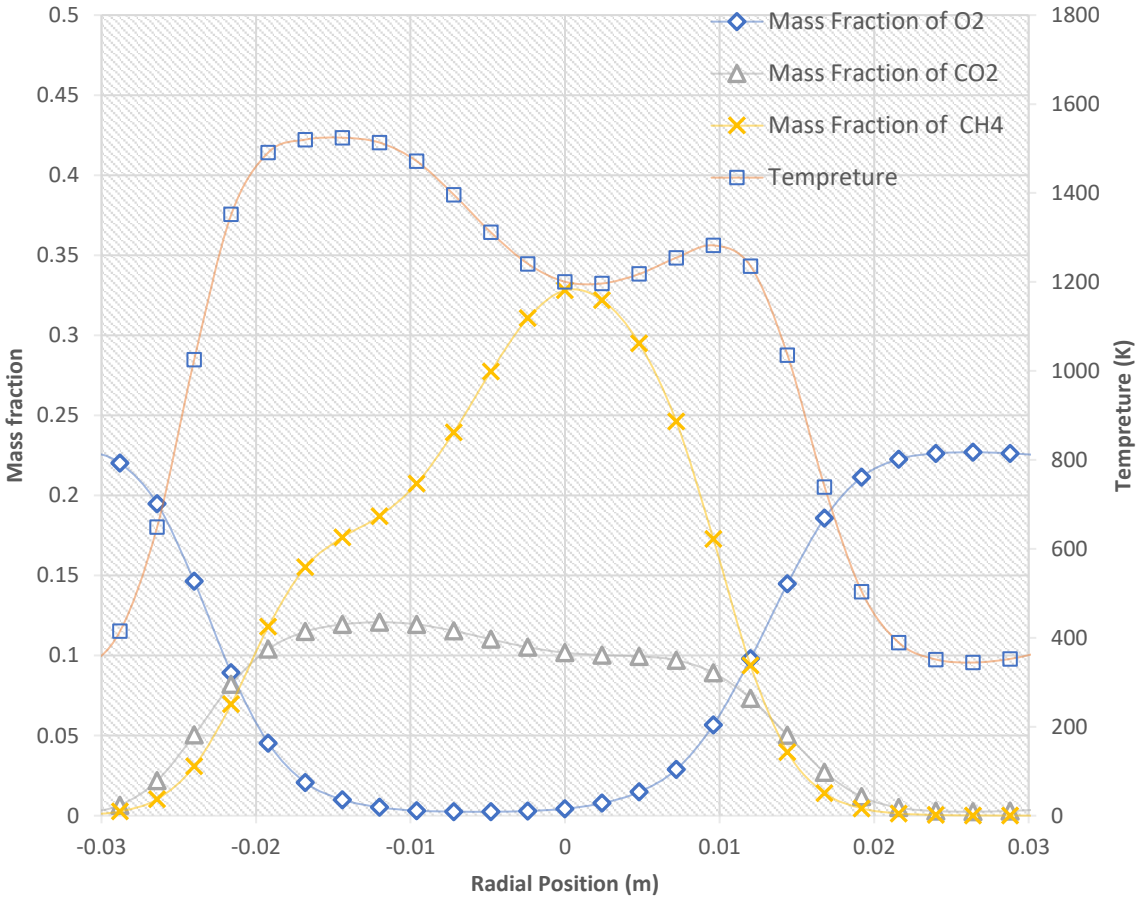

Figure 6-17 Radial Profiles of Species Mass Fractions and Temperature

6.6.5.3 Influence of Turbulence and Buoyancy on Flame Structure

The flame structure generated in this simulation is strongly influenced by both turbulence and buoyancy-driven flow. Turbulence plays a central role in enhancing the mixing between fuel and oxidiser, which in turn governs the rate and spatial distribution of combustion. The Large Eddy Simulation (LES) approach, implemented using the one-equation eddy viscosity model, enables the resolution of large-scale turbulent motions while modelling the effects of unresolved sub-grid fluctuations. These fluctuations influence flame front wrinkling, reaction zones, and thermal gradients.

The FireFOAM simulation outputs as shown in Figure 6-16 & Figure 6-17, including temperature contours, streamline fields, and species distributions, reveal the formation of vortex structures near the burner exit and the presence of a characteristic annular flame. This structure is confirmed by the radial temperature and species profiles extracted at Y = 0.6 m and Y = 0.9 m. At Y = 0.6 m, the flame exhibits a double-peaked temperature profile with elevated CO_2 mass fractions in the annular region, oxygen depletion around the high-temperature zones, and centralised CH_4 concentrations. This configuration indicates a toroidal reaction zone, where intense combustion occurs in the outer layers surrounding a fuel-rich core. At Y = 0.9 m, the profiles show reduced combustion intensity, with lower peak temperatures, a more uniform methane distribution, and increased oxygen mass fractions. These results reflect the burnout phase of the flame, where mixing and entrainment become more dominant, and combustion weakens.

These numerical results match well with the experimental observations shown in Chapter 4 [112]. The high-speed OH-PLIF and Mie scattering images from the experiments showed that, when turbulence is present on the fuel side, the flame begins to wrinkle early, loses its symmetry, and draws in more air from the surroundings. The simulation also shows a wider range of flame front shapes (curvature), especially near the burner, which is a typical effect of moderate turbulence.

For Flame F2 in particular, the simulation shows the early signs of pinch-off instability, similar to what was described by Xiao et al. [112]. This type of instability, known as the varicose mode, is when the flame neck stays symmetric on both sides, and two swirling motions (vortices) form that pull the flame apart. This causes the top part of the flame to separate and move upward as a flame pocket. These behaviours appear in the simulation as widened high-temperature zones and small vortex-like shapes, closely matching what was observed in the experiment for Flame F2.

6.6.6 Velocity Field Distribution and Analysis

Understanding the velocity distribution within the flame is essential for characterising the flame dynamics, including the effects of turbulence and buoyancy. This subsection presents the velocity contour across the domain, as well as radial velocity profiles at two vertical positions: Y = 0.6 m (mid-flame height) and Y = 0.9 m (near flame tip).

6.6.6.1 Velocity Contour

The instantaneous velocity magnitude contour is shown in Figure 6-18, derived from the FireFOAM simulation. The velocity field exhibits a strong upward jet originating from the burner exit, with high-velocity regions (up to approximately 7.7 m/**s**) forming the flame core. The velocity decays with height due to viscous dissipation and the effects of buoyancy. The observed plume bending and lateral spreading suggest the presence of vortical structures and turbulent mixing.

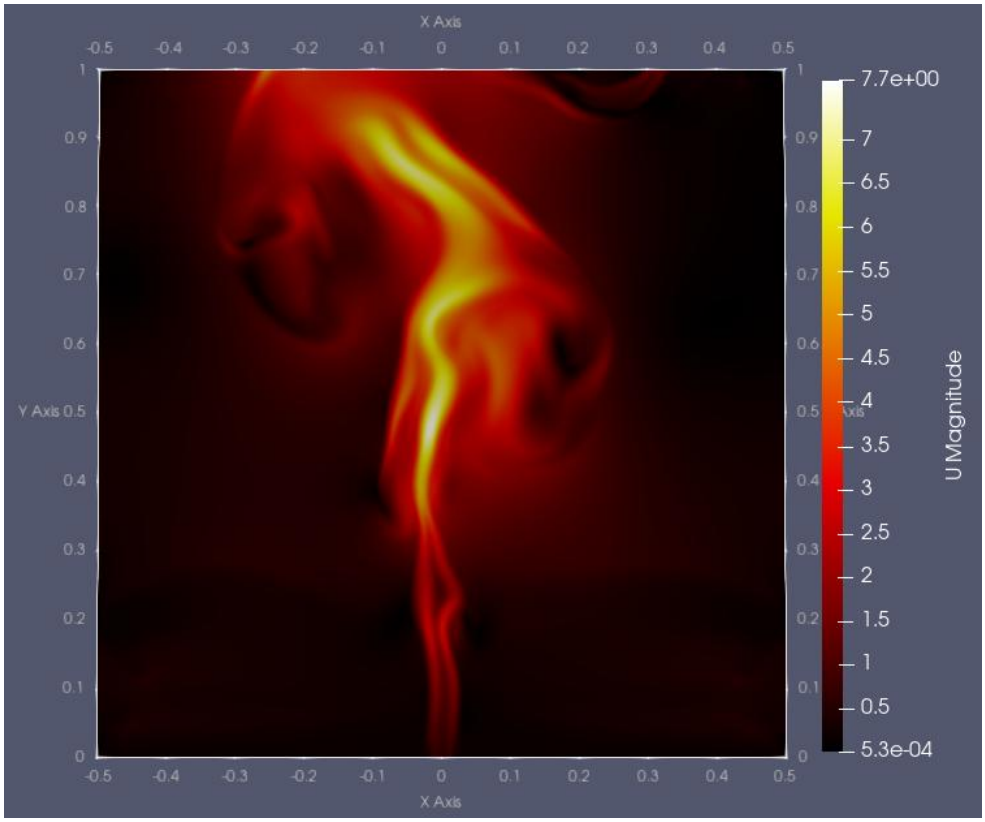

Figure 6-18 Velocity contour

6.6.6.2 Velocity Profile at Mid-Flame Height (Y = 0.6 m)

The velocity profile at Y = 0.6 m is presented in Figure 6-19. The profile exhibits a pronounced centreline peak of approximately 5.4 m/s**,** corresponding to the upward momentum of the central jet. On either side of the centreline, smaller secondary peaks emerge, resulting in a multi-lobed shape. These lobes suggest the influence of coherent vortical structures and strong lateral mixing induced by turbulence.

6.6.6.3 Velocity Profile Near Flame Tip (Y = 0.9 m)

The velocity profile at Y = 0.9 m is shown in Figure 6-19. At this height, the centreline velocity has decreased to around 5.0 m/s, reflecting the combined effects of momentum loss, turbulent dispersion, and buoyancy-induced expansion. Unlike the more structured profile at mid-height, this distribution is broader and more symmetric, with a smooth decay from the centreline toward the edges. The flattening of the profile suggests a transition toward the burnout zone, where combustion intensity diminishes, and the flow becomes more diffused.

These numerical velocity profiles at Y = 0.6 m and Y = 0.9 m are qualitatively consistent with the experimental measurements reported by Xiao et al. [112]. At Y = 0.6 m, the simulation captures the characteristic double-peak radial structure with peak velocities exceeding 5 m/s, indicative of strong entrainment and toroidal vortex formation. At Y = 0.9 m, the reduced and flattened velocity profile aligns with the experimental observation of burnout effects and buoyancy-driven lateral spreading in the flame tip region.

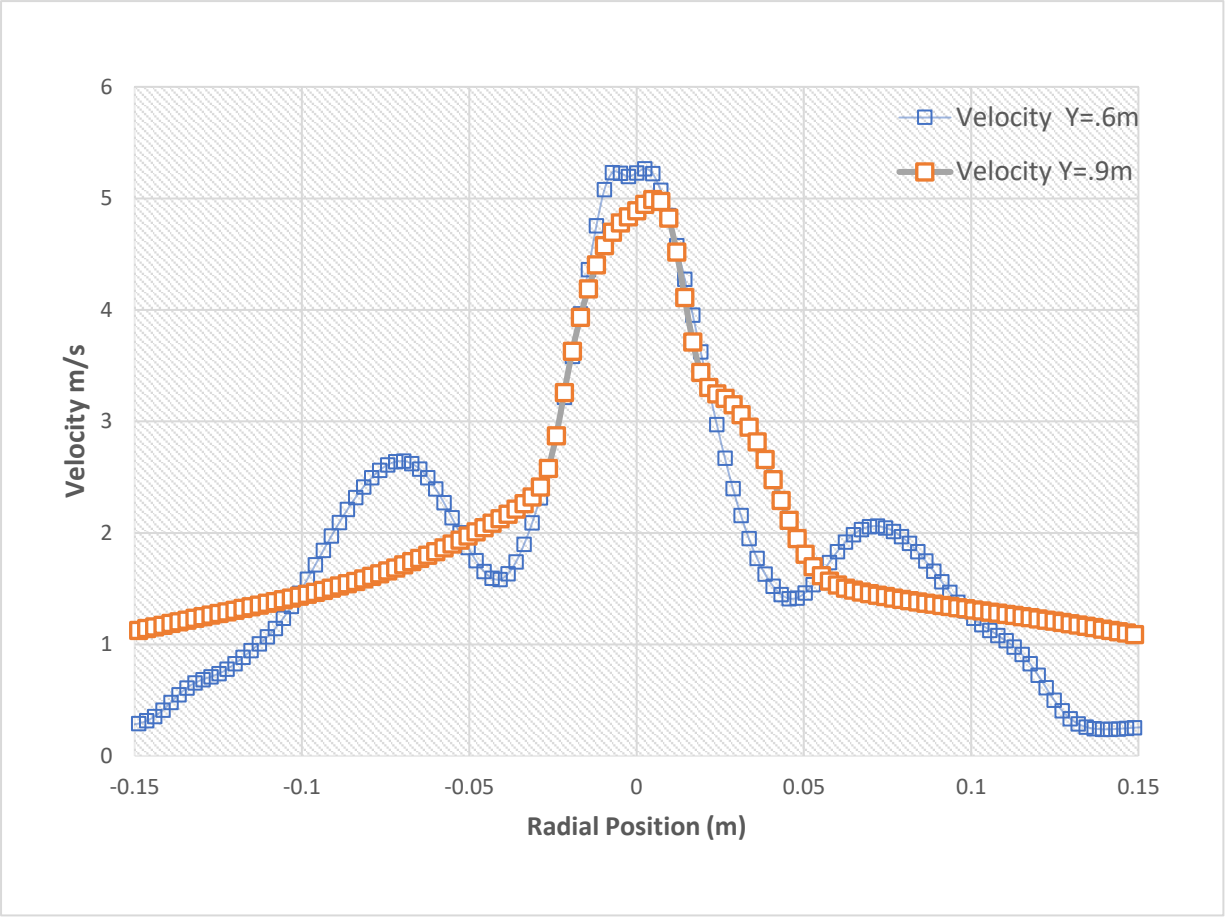

Figure 6-19 Radial velocity profile at Y = 0.6 m & .9m

6.6.6.4 Turbulence and Buoyancy Effects

The velocity field analysis confirms that the flame structure is governed by the combined influence of turbulence and buoyancy. The presence of a central high-velocity jet, clearly visible in both the velocity contour and the radial profiles, reflects the upward momentum imparted by fuel injection and sustained by turbulent momentum transfer. Buoyant forces further accelerate the vertical flow of hot combustion gases while inducing radial entrainment of surrounding ambient air.

At the mid-flame height (Y = 0.6 m), the radial velocity profile exhibits a distinct multi-lobed structure with a sharp centreline peak of approximately 5.4 m/s and secondary peaks on either side. These features are characteristic of shear-layer instabilities and suggest the presence of coherent vortical structures and enhanced turbulence near the flame core. The steep velocity gradients and symmetrical lobes highlight strong entrainment effects and turbulent mixing, both of which contribute to sustaining combustion in the primary reaction zone.

By contrast, at the upper axial location (Y = 0.9 m), the velocity profile becomes more uniform and symmetrical, with a smoother distribution and a reduced centreline peak of around 5.0 m/s. This shift indicates a transition toward lower turbulent momentum and increased dominance of buoyancy, where combustion weakens and mixing becomes more diffusive. The flattening of the velocity profile reflects the expansion and dilution of the flame plume as hot gases rise and ambient air is entrained radially into the outer regions of the flow.

Together with the temperature and species profiles, the velocity distribution validates the dynamic interplay between turbulence and buoyancy across the flame height.

6.7 Chapter Conclusion

This chapter presented a comprehensive numerical investigation of a buoyant diffusion flame produced by the University of Sydney (USYD) Burner using the FireFOAM solver within the OpenFOAM framework. Through carefully defined computational geometry, mesh sensitivity analysis, and boundary condition setup, the model was constructed to replicate key features of the experimental configuration.

The use of Large Eddy Simulation (LES), combined with the one-equation eddy viscosity turbulence model and the Eddy Dissipation Model (EDM) for combustion, enabled the prediction of turbulent flow behaviour and flame structure with good accuracy. Radiation effects were incorporated through a simplified fvDOM approach, which significantly influenced the flame temperature distribution and improved agreement with physical observations.

Validation efforts were conducted through comparisons of velocity profiles between FireFOAM, Fluent, and experimental data, demonstrating strong consistency across all cases. The simulation successfully captured the distinctive features of buoyant diffusion flames, including high central velocities, strong temperature gradients, species transport behaviour, and the role of turbulent mixing. Species concentration profiles at two axial locations, Y = 0.6 m and Y = 0.9 m, revealed expected trends of effective fuel consumption, oxygen depletion, and carbon dioxide generation, confirming the simulation's ability to replicate fundamental combustion processes.

Moreover, the analysis demonstrated the impact of the turbulence-generating perforated plate, which introduced enhanced mixing, flame wrinkling, and an increase in flame height and radiative heat losses. The velocity field profiles further highlighted the transition from a momentum-dominated jet at the mid-flame region to a buoyancy-dominated dispersion near

the flame tip. This transition reflects the dynamic interplay between turbulent momentum transfer and buoyancy-induced entrainment throughout the flame development.

In addition to the general consistency with experimental observations, the simulation also captured several key dynamic behaviours characteristic of buoyant diffusion flames. The flame structure exhibited complex vortical formations near the burner exit, which were responsible for initiating turbulent mixing and shaping the annular combustion zone. These vortex-driven interactions promoted early flame wrinkling and radial entrainment of ambient air, in agreement with the high-speed OH-PLIF and Mie scattering measurements. Time-resolved temperature contours further revealed the onset of varicose pinch-off instability in Flame F2, where symmetrical necking at the flame centreline was followed by the periodic detachment of flame pockets and upward advection. These features were especially evident around the mid-flame height and closely matched the experimental sequences presented by Xiao et al. [112].

The simulation also clearly captured how temperature and chemical species interact throughout the flame. At Y = 0.6 m, the results showed high concentrations of carbon dioxide (CO_2) and high temperatures in a ring-like pattern around the flame core. In the centre, there was a high amount of unburned methane (CH_4) and low oxygen (O_2), which confirms that the combustion mainly happens in the outer layers. This is known as a toroidal reaction zone, where the outer layers burn around a central fuel-rich core.

At Y = 0.9 m, which is closer to the flame tip, the temperature and species profiles became more spread out and even. This suggests that most of the combustion is complete, and the remaining gases are just mixing with the surrounding air. The velocity data supports this: at Y = 0.6 m, the flow showed strong shear and clear lobes (peaks on both sides), while at Y = 0.9 m, the velocity was smoother and more symmetrical.

Overall, the simulation effectively captures the dominant physical processes that govern buoyant turbulent diffusion flames. These include the combined influence of turbulence and buoyancy on combustion dynamics, the transport and distribution of major species (CH_4, O_2, and CO_2), the spatial variation of temperature throughout the flame, the onset and progression of pinch-off instabilities, and the development of flow structures from the burner base to the flame tip.

7 Flame Suppression of USYD Burner- using FireFOAM

7.1 Introduction

Fire suppression systems are essential for protecting both life and property within built environments. These systems, which function through various suppression mechanisms, are particularly important given the widespread use of water-based suppression systems in contemporary buildings[119]. Although these systems have proven to be effective, their design and optimisation remain challenging due to the complexity of accurately predicting their performance. As a result, continued research is necessary to develop a reliable analytical framework capable of forecasting suppression behaviour with greater precision. A fundamental aspect of enhancing fire safety involves understanding the interaction between flames and water sprays. This research focuses on investigating water mist suppression, which is known for its rapid evaporation and ability to reach areas that may be obstructed or shielded. Gaining a deeper understanding of these processes is vital to improving the efficiency of fire suppression methods [13, 45].

In this study, FireFOAM, which is an advanced extension of the OpenFOAM computational fluid dynamics platform, is used to simulate spray dynamics. FireFOAM applies the Lagrangian [94] particle tracking approach to represent droplets and incorporates several sub-models to simulate key physical phenomena, as discussed in details Huang [120] , including:

- Evaporation, where liquid droplets convert into vapour.
- Liquid injection, which governs how liquid enters the computational domain.
- Droplet–wall interaction, describing the behaviour of droplets upon contact with surfaces.

Despite significant advances in modelling flame extinction using Large Eddy Simulation (LES), accurately resolving the underlying physics in realistic fire scenarios remains difficult. This is due to the complex nature of flame temperature distributions, fuel and oxidiser mixing rates, and turbulence.

Flame extinction in diffusion flames can occur through three principal mechanisms[42] [121]:

- Thermal quenching, which arises from heat loss via radiation, interaction with cold surfaces, or dilution by inert gases.

- Aerodynamic quenching, which occurs when intense turbulence or high-speed flows stretch and strain the flame front, disrupting its stability and increasing the mixing rate beyond the capability of chemical reactions to sustain combustion.

- Kinetic quenching, which involves chemical reactions that interfere with chain-branching processes essential for sustaining a flame.

Modelling flame extinction can be approached through either a critical flame temperature or a critical Damköhler number. Models that rely on a critical temperature do not account for chemical time scales and may not accurately represent real flame behaviour. In contrast, models based on the critical Damköhler number include chemical kinetics and are better aligned with both laminar and turbulent combustion phenomena.

In the Fire Dynamics Simulator (FDS), flame extinction is represented by a temperature-based criterion that is suitable for capturing thermal quenching [122]. The model uses an enthalpy balance to determine whether combustion continues based on whether the heat released by the reaction can raise the mixture temperature above a critical value, typically 1600 K for hydrocarbon fuels. If the condition is not met, the reaction is suppressed by setting source terms to zero.

FireFOAM incorporates both a critical gas temperature and a critical Damköhler number to predict flame extinction. This dual criterion enables the model to more effectively capture the interplay of turbulence, mixing, and chemical inhibition under various suppression conditions.

7.2 Methodology and Numerical Solver

In this study, thermal radiation is simplified by assuming a non-scattering and non-absorbing medium, and by applying a globally defined empirical radiative loss fraction, X_{rad} , set at 23%.

FireFOAM employs a classical Lagrangian approach for spray modelling [94], where the liquid phase is represented as discrete spherical droplets injected according to specified size and velocity distributions. The model supports two-way coupling between the gas and liquid phases, allowing for dynamic interactions, although it is limited to dilute spray conditions.

The FireFOAM solver has been enhanced with a flame extinction model based on the critical flame Damköhler number and a critical gas temperature for reignition [123].

The baseline configuration for suppression modelling replicates the experimental setup of Xiao [112], where water mist is introduced from the burner base (bottom injection). In this case, droplets are injected upward into the flame core using a nozzle placed beneath the burner outlet. The interaction between the water mist and the flame plume under this configuration is visualised later in Figure 7-16, which shows the vortex formation and spray behaviour near the flame base.
This setup allows investigation of droplet-flame interaction in the near-field region where combustion is most intense. Key parameters such as droplet diameter, and velocity were selected based on the experimental characterisation [112] and Chapter 3.

Following this baseline case, an alternative configuration involving top injection is also examined. In this setup, the suppressant is introduced from above the flame, allowing comparison of flame suppression behaviour under different droplet penetration paths and momentum orientations. This top-injection configuration is particularly important as it

simulates the typical placement of ceiling-mounted sprinklers in real-life fire scenarios, enabling a more practical assessment of suppression performance in built environments.

7.2.1 Flame Extinction and Reignition Models

FireFOAM incorporates extinction and reignition mechanisms by combining the critical flame Damköhler number criterion and a reignition threshold based on gas temperature [46, 124-126]. These models are used to simulate complex interactions between turbulence, combustion, and suppression in a buoyant diffusion flame.

7.2.2 Initial Extinction Model and Transition from Mixture Fraction Formulation

The flame extinction model in FireFOAM was initially developed using the mixture fraction approach, which represents the ratio of fuel and oxidiser mass fractions and is widely used in turbulent combustion modelling [123, 125]

Although this method was effective in single-fuel, single-oxidiser scenarios, it introduced substantial complexity when extended to configurations involving multiple fuels or oxidiser streams. These situations require the introduction of multiple mixture fraction scalars, making the formulation computationally demanding and less flexible.

In this revised framework, a single-step global combustion reaction is adopted as a baseline representation of methane combustion, described as follows:

$$CH_4 + 2O_2 \rightarrow CO_2 + 2H_2O \qquad (GR1)$$

Equation 7-1

This reaction (GR1) corresponds to the primary combustion process and serves as the foundation for coupling with the flame extinction and reignition models discussed in the following sections [125].

7.2.3 Critical Flame Damköhler Number

The Damköhler number (Da) is a dimensionless parameter representing the ratio of the chemical reaction timescale to the turbulent mixing timescale. A critical threshold Dac is used to determine the onset of local extinction. If the local Damköhler number falls below this threshold, combustion cannot be sustained, and flame extinction is triggered.

Implementation in FireFOAM:

- The Damköhler number is computed using subgrid-scale (SGS) turbulence and combustion models.
- It accounts for the local turbulence mixing rate and chemical reaction rate.
- An extinction factor (FEF) is introduced to smoothly quantify the suppression process, using a hyperbolic tangent ramp function originally proposed by Marshall and Trouvé[125] in their large eddy simulations of a methane line fire exposed to air-nitrogen co-flow. This expression provides a numerically stable and physically smooth transition between active and extinguished zones based on local mixing–chemistry interactions.

$$FEF = .5 - .5\tanh\left(\frac{Da - Dac}{\Delta Da}\right)$$

Equation 7-2

Where:

Da: the local Damköhler number,

Dac: the critical Damköhler number,

ΔDa: the small interval to smooth the transition.

As the local Damköhler number drops below Dac , the extinction factor increases towards unity, indicating a higher probability of flame extinction and corresponding suppression of chemical source terms in the affected computational cells.

7.2.4 Critical Gas Temperature for Reignition

Reignition is assumed to occur when the local gas temperature exceeds a critical threshold. This threshold, typically set at 1100 K in FireFOAM, represents the minimum temperature required for the resumption of combustion reactions in methane-air systems. However, this value is not fixed and may vary depending on the fuel composition and local thermochemical conditions. A flame ignition factor (FIF) is defined to represent the local probability of reignition. The factor varies between 0 and 1, where a value of 0 denotes no possibility of reignition and a value of 1 indicates full reignition:

$$FIF = .5 + .5\tanh\left(\frac{T - T_{ign}}{\Delta T}\right)$$

Equation 7-3

as illustrated by A. Trouvé [125]

Where:

T is the filtered local temperature,

T_{ign}: is the critical ignition temperature (1100 K),

ΔT: is a smoothing interval that moderates the transition.

7.2.5 Simplifications and Future Improvements

The current reignition model in FireFOAM is relatively simplified and serves primarily as a placeholder. While it provides a basic representation of reignition, it does not yet incorporate several influential factors such as variations in chemical composition, flame stretch, or the presence of pilot flames. These factors can significantly impact the local flame behaviour and stability.

Future development should aim to integrate more detailed reignition criteria, including advanced turbulence-chemistry interaction models and detailed chemical kinetics, to better capture the physics of re-ignition and improve model fidelity under complex fire suppression scenarios.

7.2.6 Parcels in Spray Modelling

In FireFOAM, spray dynamics are captured using a Lagrangian parcel-based approach, where each parcel represents a statistically significant group of droplets that share identical physical characteristics. This abstraction avoids the computational burden of resolving every individual droplet, instead modelling the collective behaviour of droplets with similar size, velocity, temperature, and mass.

Each parcel acts as a tracking entity, advancing through the computational domain in response to local flow conditions. Their trajectories are governed by Newtonian mechanics and updated iteratively throughout the simulation.

The interaction between the liquid and gas phases is modelled through two-way coupling. As parcels move through the domain, they exchange momentum and energy with the surrounding gas, enabling the simulation of drag and convective heat transfer. This mechanism is particularly important in suppression scenarios where spray alters the thermal and velocity fields within the flame zone.

Parcels are further influenced by turbulent dispersion, which introduces randomised motion reflective of sub-grid turbulent fluctuations. This effect ensures realistic spatial spreading of droplets, which is essential in capturing mist behaviour in chaotic fire environments.

The model also accounts for droplet fragmentation. When aerodynamic forces surpass the cohesive surface tension of droplets within a parcel, secondary atomisation occurs, generating smaller droplets that enhance evaporation rates and increase surface area exposure to the flame.

Evaporation is incorporated via energy balance equations, where mass loss from the liquid phase is transferred to the gas as vapour. As evaporation progresses, parcel properties are dynamically updated to reflect changes in droplet size and mass, without altering the total number of parcels.

This parcel-based spray representation in FireFOAM effectively balances computational efficiency with physical realism, offering a robust method for capturing spray–flame interactions critical to fire suppression modelling.

7.3 Fire Suppression Model: Input Parameters and Simulation Setup

Accurate representation of fire suppression in computational simulations requires a detailed specification of the physical properties and boundary conditions governing droplet behaviour. This includes fluid thermodynamic properties, injection settings, evaporation models, and heat transfer mechanisms. These parameters directly influence the spatial and temporal evolution of droplet-vapour interactions within the fire plume, thereby determining the overall suppression performance.

7.3.1 Fluid Properties and Thermodynamic Parameters

The thermophysical characteristics of the suppressant medium, water (H_2O), are defined in the `constantProperties` block. These properties dictate the droplet's heat absorption capacity, evaporation rate, and phase transition behaviour, which are critical to thermal quenching during suppression.

Parameter	Value	Description	Units
ρ_0 (Density)	1000	Initial/reference density of water	kg/m^3
T_0 (Initial Temperature)	300	Initial temperature of the liquid before injection	K
C_{p0} (Specific Heat Capacity)	4187	Amount of energy required to raise the temperature of 1 kg of liquid by 1 K	J/(kg·K)
T_bp (Boiling Point)	373	Temperature at which water transitions to vapor	K

Table 7.1 Fluid Properties

7.3.2 Input Parameters and Experimental Basis for Spray Modelling

The mist spray parameters used in this study were primarily based on the experimental configuration described by Xiao [112], who investigated water mist suppression using bottom injection in a buoyant turbulent diffusion flame setup. Consistent with their approach, this study adopts a coneNozzleInjection model with a total injected mass of 0.01 kg per nozzle, an injection duration of 5.0 seconds, and a droplet exit diameter of 1.9e-4 m. These values reflect realistic water mist discharge rates suitable for lab-scale suppression applications.

Computational tuning was further conducted through iterative testing of the injection rate (PPS) across three values (10 million, 1 million, and 500,000 [1/s]) to identify a numerically stable and physically meaningful spray field. The resulting spray characteristics were validated through comparison with experimental observations using OH-PLIF and Mie scattering visualisations obtained at the University of Sydney. This provided qualitative confirmation of droplet distribution, flame penetration, and mist behaviour in the near-flame region.

The final configuration therefore represents a balance between experimental fidelity, numerical stability, and suppression realism, forming the basis for subsequent parametric studies in Chapter 7.

7.3.2 Injection Model and Droplet Characteristics

Droplets are introduced into the computational domain using the `coneNozzleInjection` model, which emulates conical spray patterns commonly observed in mist systems. The simulation considers two bottom-mounted nozzles and one top-mounted nozzle, representing different suppression strategies.

7.3.3 Injection Parameters

Parameter	Value	Description
Injection Type	`coneNozzleInjection`	Specifies that droplets are introduced as a conical spray
Injection Positions	(0.05 0 0) (-0.05 0 0)	Defines the spatial location of nozzles
Total Mass Injected (massTotal)	0.01 kg	Represents the total suppressant mass introduced gradually over a 3-second injection period
Injection Rate (parcelsPerSecond) (PPS)	500,000 _ 10,000,000	Number of parcels (droplets) introduced per second
Droplet Size Distribution	Rosin–Rammler; d = 90 μm, min = 1 μm, max = 150 μm	Statistical size distribution using Rosin–Rammler function with characteristic diameter and spread factor. Most droplets fall between 100–150 μm

Table 7.2 Injection Parameters

The droplet size distribution in this study is defined using the Rosin–Rammler (RR) model, as implemented in FireFOAM's spray injection module. This model statistically distributes droplets based on a characteristic diameter and spread parameter, which govern how droplet sizes are weighted around a central value. While RR theoretically spans from 0 to infinity, in practice, a minimum and maximum droplet size are specified to control the injected spray range. In this model, the diameter range was set between 1 μm and 150 μm, consistent with atomisation performance observed experimentally by Xiao [112]. The majority of droplets fall within the 100–150 μm range, matching the expected size distribution from similar cone-type nozzles used in suppression studies.

The parcelsPerSecond parameter controls droplet population density and size distribution. Lower rates promote smaller droplets with greater surface area for evaporation, while higher rates favour larger droplets capable of deeper flame penetration.

7.3.4 Evaporation and Heat Transfer Models

To capture droplet phase change and thermal interaction with the fire environment, the simulation includes coupled models for evaporation and heat transfer.

7.3.4.1 Liquid Evaporation Model

Parameter	Value	Description
Active Liquid	H_2O	Water defined as the evaporating phase.
Enthalpy Transfer Model	enthalpyDifference	Heat exchange governed by the temperature difference between droplet and gas phase

Table 7.3 Liquid Evaporation Model Parameters

7.3.4.2 Single-Phase Mixture Coefficients

Parameter	Value	Description
Phases	Liquid: H_2O: 1	Defines the suppressant as a 100% water-based liquid

Table 7.4 Single-Phase Mixture Configuration for Water Mist Suppression

This assumption simplifies the model while preserving key suppression dynamics related to evaporation and cooling.

7.3.5 Evaporation and Suppression Mechanisms

The **Ranz–Marshall model** is employed to model evaporation, capturing:

- Heat and mass transfer from flame gases to droplets.
- Droplet vaporisation rates.
- Cooling effectiveness and fire temperature reduction.

In this study, the Ranz–Marshall correlation is implemented within FireFOAM to represent convective heat and mass transfer between hot gases and liquid droplets. This model is coupled with the coneNozzleInjection spray type and a single-phase mixture of water. A simplified enthalpy transfer approach is adopted, based on the `enthalpyDifference` method.

The present model excludes additional physical complexities such as spray breakup, droplet coalescence, and radiation absorption by droplets. Furthermore, multi-component vapour interactions are not considered; only pure water droplets are simulated. These simplifications reduce computational cost while still enabling a physically meaningful representation of key suppression mechanisms. Future work may enhance model fidelity by incorporating these omitted processes for more accurate prediction of mist-flame interaction and suppression dynamics.

7.3.5.1 Liquid Evaporation Model

Parameter	Value	Description
Active Liquid	H_2O	Specifies that water is the evaporating phase
Enthalpy Transfer Model	enthalpyDifference	Determines heat transfer between the droplet and surrounding gas

Table 7.5 Parameters for Enthalpy-Based Evaporation Model

The enthalpy transfer model is set to enthalpyDifference, meaning that heat exchange is calculated based on the temperature difference between the suppressant and the fire environment. This governs how efficiently the suppressant absorbs thermal energy, leading to droplet evaporation and fire suppression.

7.3.5.2 Single-Phase Mixture Coefficients

Parameter	Value	Description
Phases	Liquid: H_2O: 1	Defines the suppressant as a 100% water-based liquid

Table 7.6 Phase Definition for Single-Component Liquid Suppression Model

This setting ensures that only water is modelled in the simulation, simplifying phase interactions while maintaining realistic suppression behaviour.

7.3.6 Evaporation and Suppression Mechanisms

The combination of cone nozzle injection, phase-change modelling, and heat transfer calculations provides a detailed representation of water mist suppression efficiency under different injection conditions. However, due to the complexity of the suppression model, this study simplifies certain input parameters. Future research will be needed to refine the model by incorporating more detailed physical interactions and improving predictive accuracy.

7.3.7 Summary of Input Parameters

Category	Parameter	Value	Description
Liquid Properties	Density (ρ_0)	1000 kg/m³	Initial water density
	Initial Temperature (T_0)	300 K	Temperature before injection
	Specific Heat (C_{p0})	4187 J/(kg·K)	Determines heat absorption capacity
	Boiling Point (T_bp)	373 K	Phase transition temperature
Injection Settings	Injection Type	coneNozzleInjection	Spray configuration
	Nozzle Positions	(0.05 0 0) (-0.05 0 0)	Location of injectors
	Total Injected Mass	0.01 kg	Water introduced per nozzle
	Injection Rate (PPS) [1/s]	500,000 - 10,000,000	Number of droplets introduced per second
Phase-Change Models	Active Liquid	H_2O	Defines suppressant phase

	Evaporation Model	Ranz-Marshall	Heat and mass transfer during evaporation

Table 7.7 Summary of Thermophysical Properties and Injection Parameters for Suppression Modelling

These input parameters govern droplet formation, distribution, and interaction with the fire plume, directly influencing the effectiveness of suppression mechanisms.

7.3.8 Transition to Suppression Scenarios

With the key input parameters now defined, the study advances to the implementation of two suppression strategies: top injection and bottom injection. In Section 7.4, the simulation setup for top injection is presented, detailing nozzle positioning at the upper boundary, conical spray configuration, and solver settings. Suppression performance is evaluated across three injection rates: 10,000,000, 5,000,000, and 1,000,000 Parcels Per Second (PPS). A Rosin–Rammler distribution is applied to define the droplet sizes, with a minimum droplet diameter of 1 μm, a maximum of 150 μm, and a mean diameter (d) of 150 μm. This size distribution influences droplet penetration, mist dispersion within the fire plume, and ultimately, flame cooling effectiveness. Each case is analysed in terms of droplet penetration, mist dispersion within the fire plume, and flame temperature reduction.

A corresponding structure is applied in Section 7.5, where the same model configuration is used for bottom injection, with nozzles positioned at the domain base. Two injection rates, 2,000,000 PPS and 500,000 PPS, are assessed, capturing the dynamics of upward mist transport, plume interaction, and suppression impact from below.

This unified framework enables a direct comparison between the two approaches. It supports the evaluation of how injection orientation, mist density, and evaporation behaviour influence flame disruption, and overall suppression efficiency.

7.4 Fire Suppression from Top: Simulation Setup and Visualization

Following the definition of key input parameters, this section presents the numerical configuration and visual assessment of water mist suppression when injected from the top of the computational domain as shown in Figure 7-1. A conical nozzle spray model is employed, with the analysis focusing on how varying injection rates influence droplet distribution and interaction with the buoyant diffusion flame.

Figure 7-1 includes coloured contours and particle representations. In this plot, white dots indicate the water mist droplets, yellow-orange zones represent the high-temperature core of the flame, purple regions highlight the flame boundary, and black areas indicate low-temperature ambient zones. A legend is provided below to guide interpretation.

Feature	Description
White Particles	Spray droplets (water mist parcels)
Yellow-Orange Region	High-temperature flame core
Purple Region	Moderate temperature / flame boundary
Black Background	Ambient air / low-temperature zone
Central Vertical Jet	Top-injected water mist penetrating downward into the flame plume

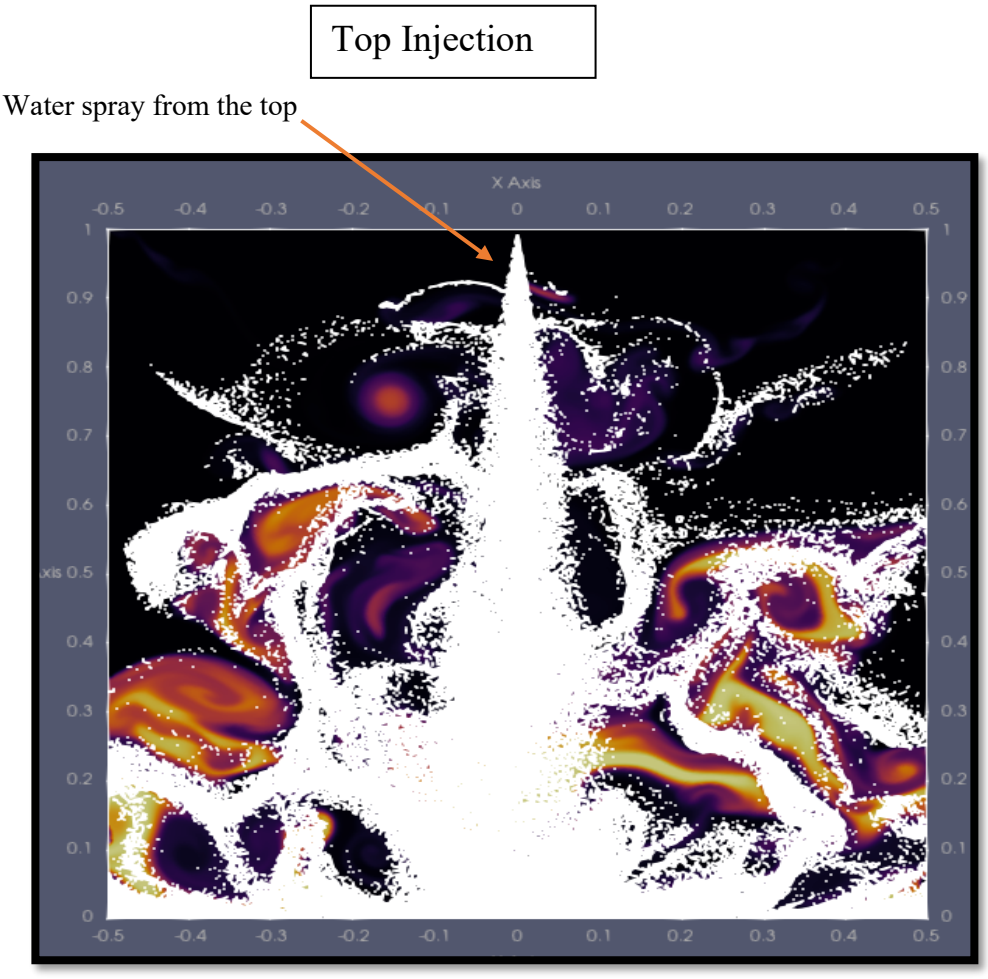

Figure 7-1 Top Injection Configuration: Droplet Penetration into Buoyant Flame

7.4.1 Spray Model Development and Optimization

The suppression setup was developed through a series of iterative spray model refinements, involving parametric adjustment of injection settings. The development process focused on three main targets: (i) improving injection accuracy, (ii) achieving numerical stability, and (iii) ensuring consistent and physically meaningful interaction between the spray and the flame zone. The refinement involved testing different droplet population densities (parcels per second, PPS), nozzle geometries, and spray durations to examine their influence on stability and suppression behaviour. In particular, three droplet injection rates (10 million, 1 million, and 500,000 [1/s] PPS were tested under identical total mass conditions (mass total =0.01 kg). The 10 million PPS case offered very fine droplets and intense evaporation but introduced high computational cost and occasional convergence issues. On the other hand, the 500,000 PPS case led to incomplete suppression due to reduced mist penetration. The intermediate rate (1 million PPS) provided a balance between droplet spread, evaporation efficiency, and model convergence**.**

The final model configuration represents an optimised case, capable of capturing the suppression dynamics across a range of spray conditions. The finalised spray parameters for top injection are outlined below:

Parameter	Value	Description
Injection Type	`coneNozzleInjection`	Defines a conical spray pattern
Total Mass Injected (massTotal)	0.01 kg	Mass of water injected per nozzle
Outer Diameter	1.9e-4 m	Defines droplet exit diameter
Inner Diameter	0 m	No internal flow restriction
Injection Duration	5.0 s	Total duration of water injection.
Injection Rate (parcelsPerSecond) [1/s]	10,000,000; 1,000,000; 500,000	Number of injected droplets per second

Table 7.8 Summary of Spray Injection Parameters for Top Suppression Model

This optimised model enables a consistent analysis of suppression performance across various injection scenarios, providing insights into how droplet population density and mass flow influence flame cooling and extinguishment mechanisms.

7.4.2 Fire Suppression Performance and Visualization

The suppression performance is evaluated using visual outputs from ParaView, focusing on the interaction between water mist and the buoyant flame. Three representative injection rates were selected to explore the influence of spray intensity on suppression behaviour:

Case 1: 10,000,000 Parcels Per Second (PPS) at mass total= 0.01 kg

Case 2: 1,000,000 Parcels Per Second (PPS) at mass total= 0.01 kg

Case 3: 500,000 Parcels Per Second (PPS) at mass total= 0.01 kg

Each case is examined over a time interval from 2.1 to 2.6 seconds, capturing the development of suppression dynamics during active spraying. The visualisations include contours of temperature reduction, spray penetration, and mist dispersion within the flame region. Emphasis is placed on flame height reduction, cooling efficiency, and the spatial extent of mist coverage during top-down suppression.

7.4.2.1 Visualization of case 1: at 10,000,000 Parcel Per Second (PPS)

Time= 2.0 second:

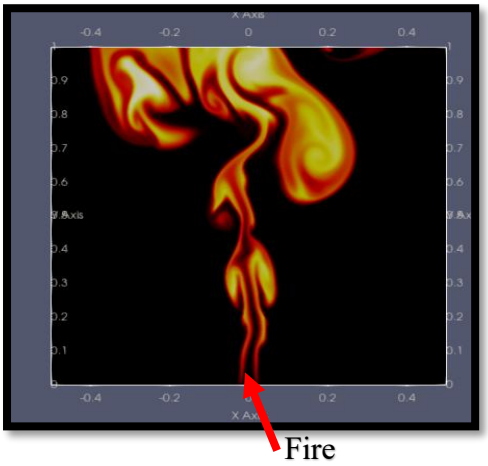

Figure 7-2 : without suppression.

Time= 2.1 second:

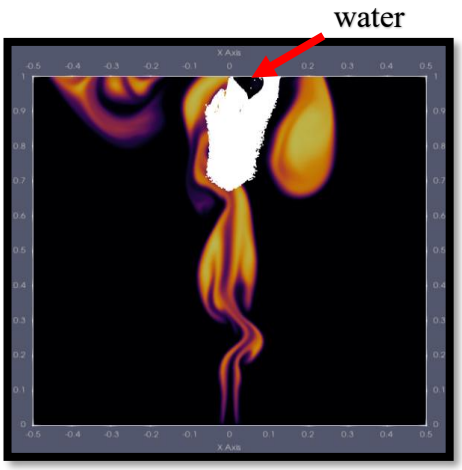

Figure 7-3: shows the initial introduction of water suppression into the fire.

Time= 2.2 second

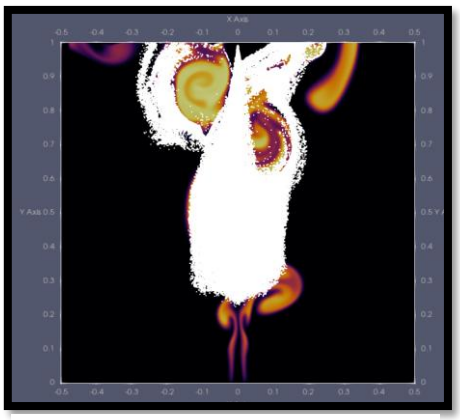

Figure 7-4: the water droplets penetrate deeper into the flame

Time =2.3 second

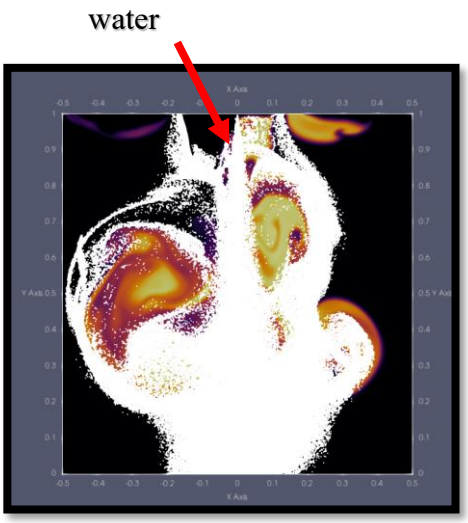

Figure 7-5: Water droplets have penetrated the central core of the flame.

Time =2.4 second

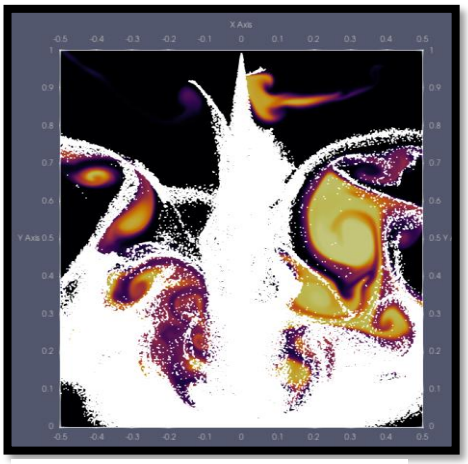

Figure 7-6: T*he flame has been* significantly suppressed

Time =2.5 second

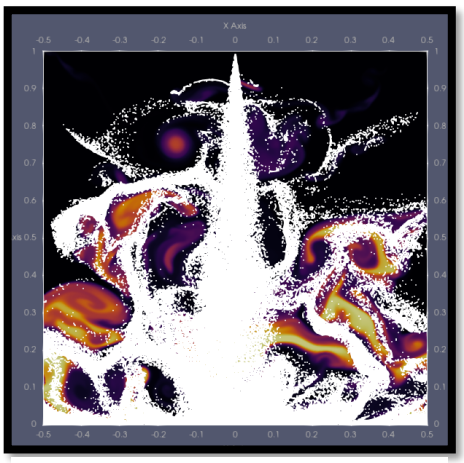

Figure 7-7: The water droplets are now reaching the lower portions of the fire

Time =2.6 second

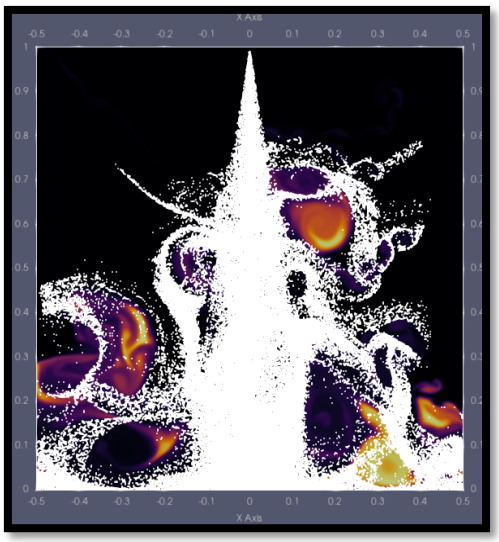

Figure 7-8: Almost the entire flame has been suppressed.

Time =2.7 second

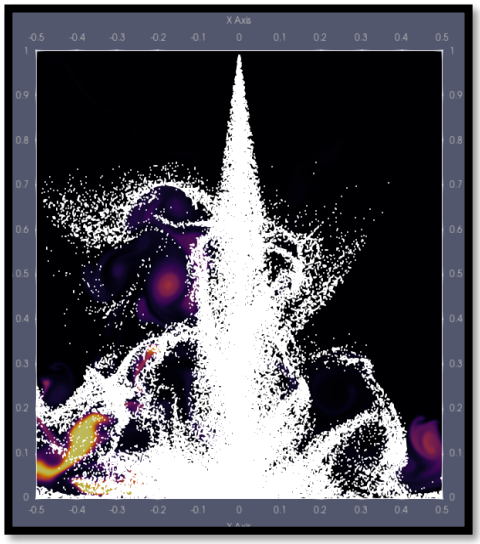

Figure 7-9: The water spray has successfully reduced the fire's size

Time = 2.8, 2.9, and 3.0 second

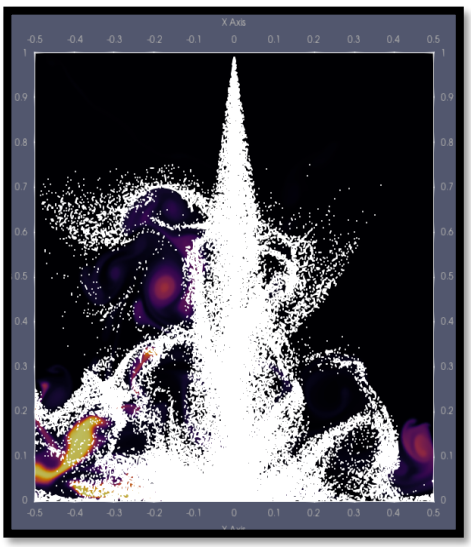

Figure 7-10: Nearly all major combustion regions have been extinguished.

Observations:

At 2.1 seconds, water mist is initially introduced into the domain, and the spray begins to interact with the upper region of the flame, initiating early suppression dynamics.

By 2.2 seconds, water droplets have penetrated deeper into the flame zone, causing visible disturbances in the flame structure.

At 2.3 seconds, the droplets reach the central core of the flame, disrupting the buoyant plume and initiating structural collapse.

By 2.4 seconds, the flame undergoes significant reduction in height and intensity, indicating the onset of effective suppression.

At 2.5 seconds, the flame has fragmented into smaller combustion pockets, with a marked decrease in radiative and convective heat signatures.

By 2.6 seconds, nearly the entire flame has been suppressed, with only residual combustion activity observed at the periphery.

From 2.7 to 3.0 seconds, the domain shows sustained suppression, with minimal to no active flame regions remaining.

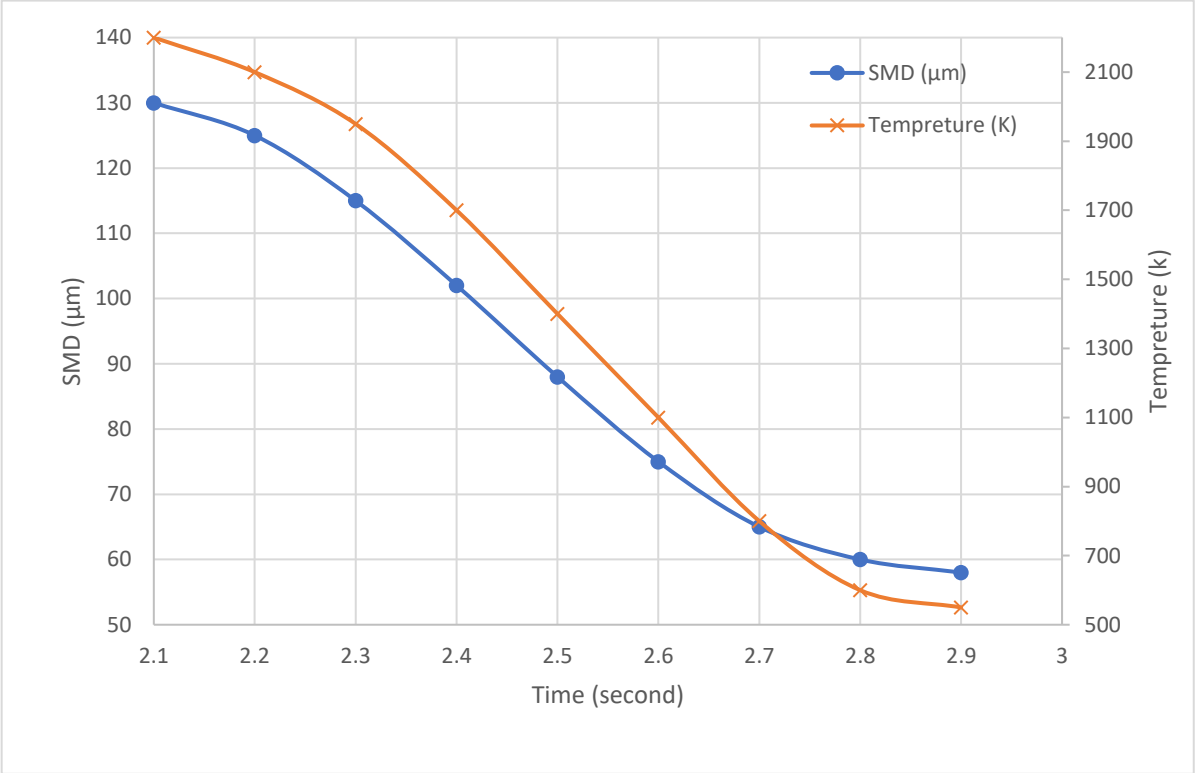

Figure 7-11 Temporal Evolution of Sauter Mean Diameter and Flame Temperature During High-Rate Top Injection (10M PPS)

Figure 7-11 shows how the Sauter Mean Diameter (SMD) and temperature change over time for the 10,000,000 PPS top injection case. The plotted values represent spatial averages taken from a central plane at Y = 0.5 m (mid-flame region), where droplet–flame interaction is most intense. Both the SMD and gas temperature were extracted and averaged across the X–Z slice at this fixed axial height over time. Between 2.2 and 2.6 seconds, both the SMD and temperature drop quickly. This means the droplets are evaporating fast and cooling the flame effectively. At 2.6 seconds, the droplet size becomes more stable, which matches the observation in Section 7.4.8 that the spray becomes more balanced and smaller enough to cool, but still strong enough to reach deep into the flame. This helps explain why the highest injection rate achieved the best and fastest suppression, with most of the flame collapsing by 2.6 seconds.

Summary:

These observations demonstrate that top injection at a rate of 10,000,000 PPS enables rapid and effective suppression, significantly reducing flame size and intensity within approximately 2.6 seconds from injection onset.

7.4.2.2 Visualization of case 2: at 1,000,000 Parcel Per Second (PPS)

Time =2.1 second

Time =2.2 second

Time =2.3 second

Time =2.4 second

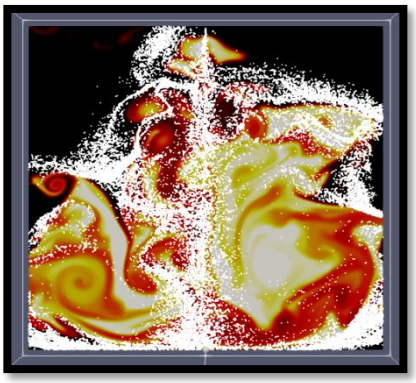

Time =2.5 second

Time =2.6 second

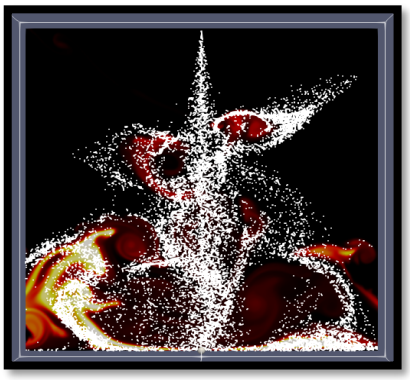

Observations:

At 2.1 seconds, water mist enters the fire zone; however, the initial interaction appears less aggressive compared to the higher injection case.

By 2.2 seconds, droplets begin to infiltrate the flame envelope, although the suppression effects remain limited at this stage.

At 2.3 seconds, early disturbances in the flame structure are observed, yet the flame retains much of its integrity.

By 2.4 seconds, noticeable reductions in flame height and intensity occur, although substantial combustion zones still persist.

At 2.5 seconds, suppression effects are increasingly evident, but the flame core continues to exhibit active burning.

By 2.6 seconds, significant suppression has been achieved, though minor residual flame pockets remain.

From 2.7 to 3.0 seconds, the domain shows sustained suppression, with minimal to no active flame regions remaining

7.4.2.2.1 Temporal Contour Snapshots of water Droplet: 2.1–2.6 s

Time =2.1 second

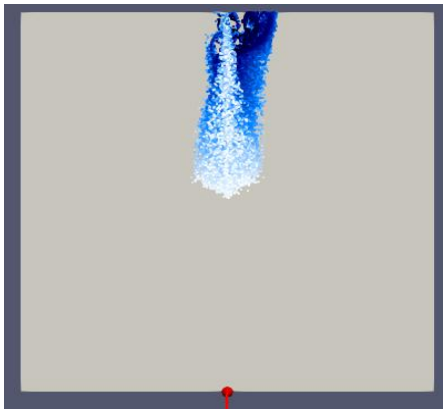

Time =2.2 second

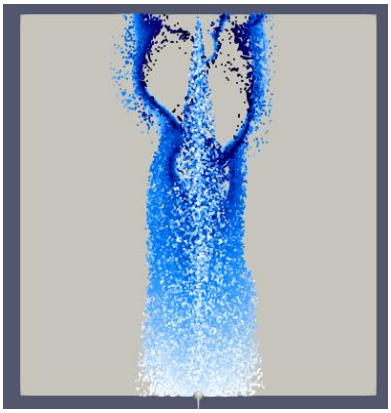

Time =2.3 second

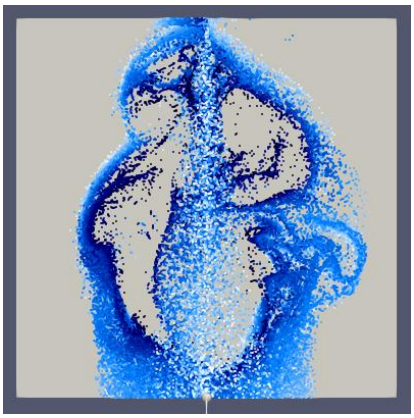

Time =2.4 second

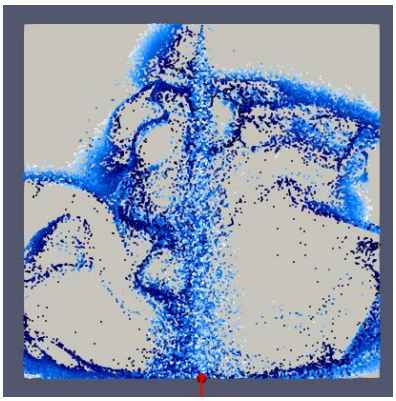

Time =2.5 second

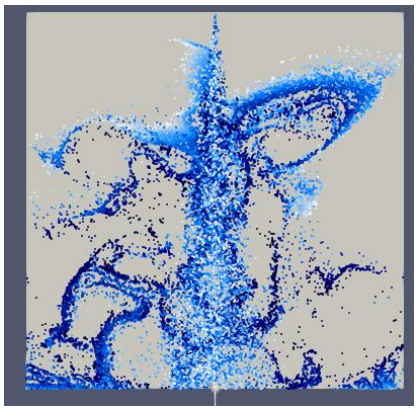

Time =2.6 second

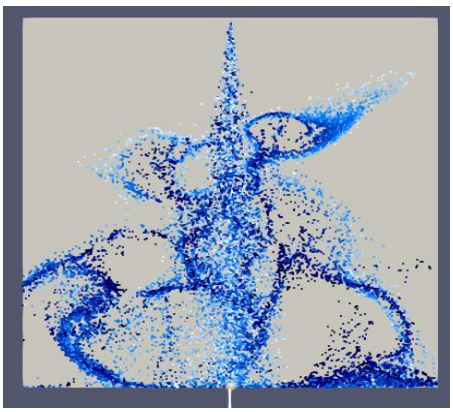

Summary:

Injection at 1,000,000 PPS achieves moderate suppression effectiveness, with a more gradual reduction in flame size and intensity compared to Case 1. While suppression is evident by 2.6 seconds, full extinguishment is not yet complete, suggesting that higher injection rates offer faster and more comprehensive fire control in top-down scenarios.

7.4.2.3 Visualization of case 3: at 500,000 Parcel Per Second (PPS)

Time =2.1 second

Time =2.2 second

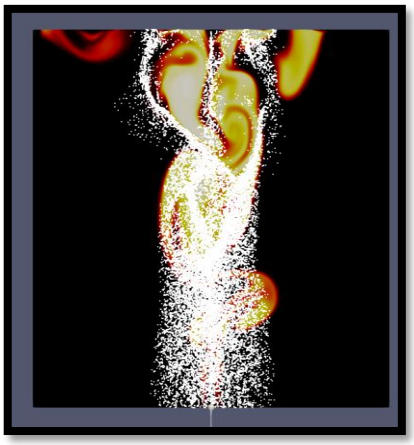

Time =2.3 second

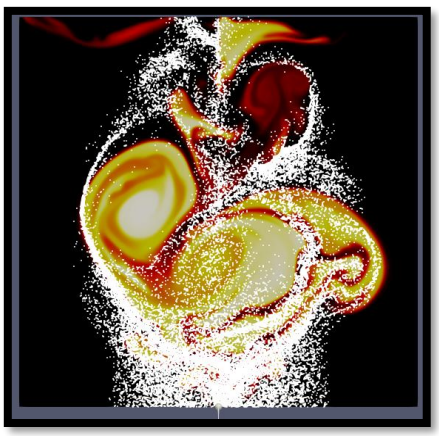

Time =2.4 second

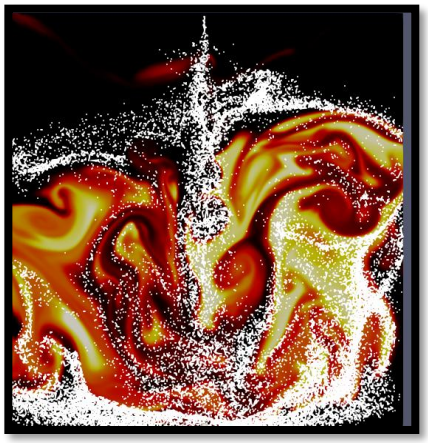

Time =2.5 second

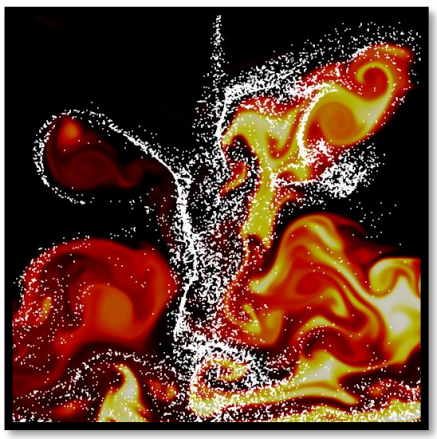

Time =2.6 second

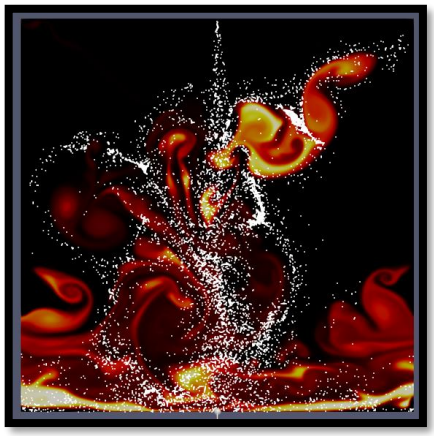

Observations:

At 2.1 seconds, the flame remains fully developed, and the water mist begins entering the domain with minimal immediate effect.

By 2.2 seconds, early signs of cooling are observed, but the flame structure remains largely intact.

At 2.3 seconds, droplet penetration is limited, resulting in only minor disruptions to the flame envelope.

By 2.4 seconds, suppression effects start to emerge, but the core structure of the flame is still clearly visible.

At 2.5 seconds, partial suppression occurs, with active combustion persisting in large portions of the domain.

By 2.6 seconds, further flame reduction is visible-but remains incomplete compared to the higher PPS cases.

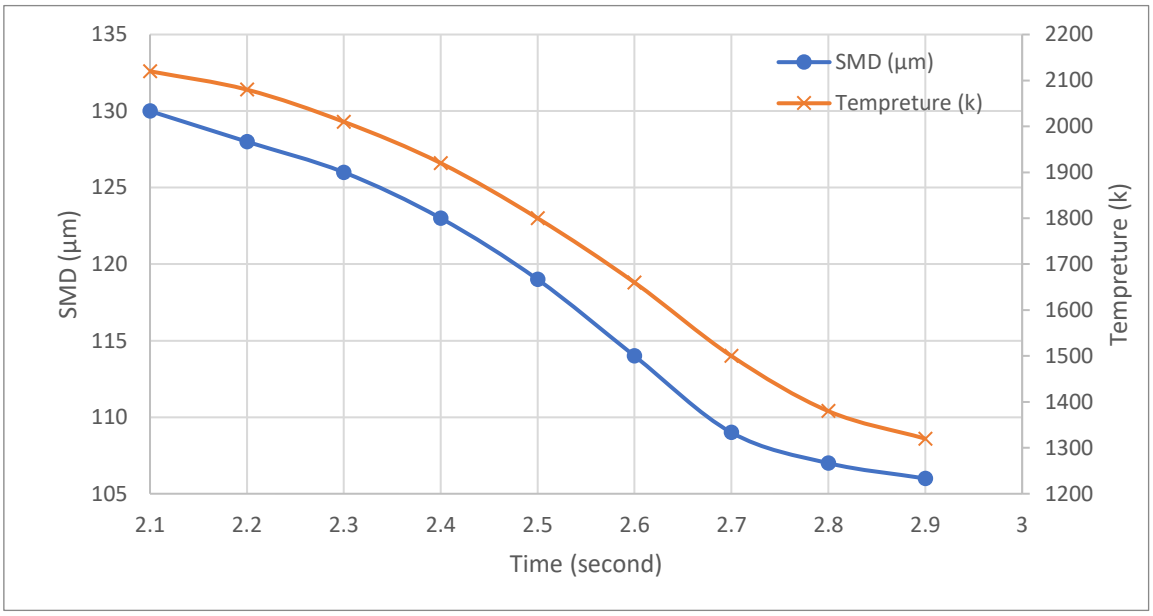

Figure 7-12 Temporal Evolution of Droplet Size and Flame Temperature – 500,000 PPS Top Injection

Figure 7-12 shows how the droplet size (SMD) and flame temperature change over time when water mist is injected from the top at a low rate of 500,000 parcels per second. The SMD only decreases slightly, staying above 105 µm, which means the droplets are not evaporating quickly. At the same time, the flame temperature decreases slowly and stays above 1300 K at the end of the sequence. This suggests that the mist could not reach or cool the flame core effectively. Overall, the suppression with limited cooling and delayed flame disruption.

Summary:

Injection at **500,000 PPS** provides limited suppression performance. The mist lacks sufficient density and momentum to penetrate deeply into the flame, resulting in a slower and less effective suppression process compared to higher injection rates. This scenario highlights the importance of injection strength when designing top-down suppression systems.

7.4.2.4 Key Observations

The comparative analysis of suppression performance at different injection rates provides the following key insights:

1. High injection rate (10,000,000 PPS) leads to the most rapid and effective suppression, with near-complete flame collapse observed by 2.6 seconds. The mist penetrates deeply, enabling widespread cooling and flame disruption.

2. Moderate injection rate (1,000,000 PPS) achieves suppression, albeit at a slower rate. Significant flame activity persists until later stages, indicating a gradual rather than immediate extinguishment process.

3. Low injection rate (500,000 PPS) results in limited suppression. The mist shows constrained penetration and reduced interaction with the flame core, leaving large combustion regions active throughout the time sequence.

The injection rate is a dominant factor influencing suppression efficiency. Higher parcel-per-second values enhance mist penetration, increase droplet interaction with the fire plume, and accelerate thermal quenching. Conversely, lower rates lead to delayed and less complete flame suppression.

These findings underscore the critical role of spray rate selection in mist-based suppression systems.

7.4.3 Importance of Droplet Size Distribution in Fire Suppression

Droplet size distribution plays a crucial role in determining the efficiency of a fire suppression system. The effectiveness of water mist suppression depends not only on the total mass injected but also on how the size of the droplets influences their evaporation rate, penetration depth, and interaction with the fire plume.

This subsection examines the distribution of droplet sizes under different injection conditions, focusing on the following key aspects:

Identifying Trends in Spray Effectiveness Across Different Injection Rates

Higher injection rates typically generate a wider range of droplet sizes, influencing how the water mist interacts with the flame structure.

Lower injection rates may lead to a narrower distribution of droplet sizes, potentially affecting suppression efficiency.

Balancing Mist Coverage, Evaporation, and Fire Interaction

Achieving an optimal balance between fine mist for cooling and larger droplets for penetration is essential for maximising fire suppression efficiency.

Droplet size distributions must be carefully analysed to ensure effective fire control across different fire scenarios.

The following section will present a detailed analysis of droplet size distribution and its implications for spray effectiveness, cooling efficiency, and overall suppression performance.

7.4.4 Droplet Distribution and Suppression Effectiveness in Top Injection

As established in the previous section, droplet size plays a pivotal role in defining the overall suppression performance. The ability of water mist to evaporate rapidly**,** absorb heat**,** and reach the core of the flame is heavily influenced by the size and distribution of the droplets. This section investigates droplet behaviour in the top injection scenario, focusing on how different spray densities affect suppression outcomes.

7.4.5 Droplet Size Distribution in Top Injection

The distribution of droplet sizes directly affects fire suppression by influencing heat absorption, evaporation, and fire penetration. In this study, the droplet size distribution was visualized in ParaView[127] using bin-based histograms. Each bin represents a specific droplet size range, capturing variations from small (micron-scale) to large droplets.

The visualisation and data extraction were conducted based on the following characteristics:

Bin Extents: 50 size categories were defined, spanning from fine mist particles to larger droplets.

Bin Values: Represent the number of droplets falling into each size range.

Temporal Evolution: Profiles were tracked at specific intervals to assess how the distribution changed during suppression.

This methodology allows the identification of how well the spray balances surface-level cooling (fine mist) with deep flame penetration (larger droplets), ultimately revealing the ideal suppression configuration for top-down systems.

7.4.6 Evaluation of Suppression Performance at Varying Injection Rates

To assess the impact of injection density on droplet distribution and suppression effectiveness, three top injection scenarios were analysed as presented in Figure 7-13, Figure 7-14 and Figure 7-15:

- 10,000,000 Parcels Per Second (PPS)
- 5,000,000 Parcels Per Second (PPS)
- 1,000,000 Parcels Per Second (PPS)

These cases offer a comparative framework to understand how spray rate influences the formation, distribution, and behaviour of the droplet field during fire interaction

7.4.6.1 Input Configuration

The spray model configuration used for all cases is consistent to ensure fair comparison, with parameters defined as follows:

Droplet Size Range:

Minimum Diameter: 1×10^{-6} m (1 micron)

Maximum Diameter**:** 1.5×10^{-4} m (150 microns)

Injection Type: coneNozzleInjection

Total Injected Mass	0.01 kg	**Inner Diameter**	0 m
Outer Diameter	1.9×10^{-4} m	**Injection Duration:**	5.0 s

The analysis focuses on the 2.4 to 2.6 second time window, an interval during which suppression is actively occurring and droplet behaviour is most dynamic.

7.4.7 Overview of Droplet Distribution Over Time

The droplet size evolution is presented in the form of histograms, illustrating how distribution shifts as suppression progresses. These are interpreted as follows:

- **X-Axis**: Droplet size (in micrometres), grouped into 50 bins.
- **Y-Axis**: Number of droplets within each bin.
- **Time Axis**: Snapshots taken at multiple time steps between 2.4 and 2.6 seconds.

In these figures, the term “PPS” in the legend refers to the injection setting used in the model, which defines the number of parcels introduced per second. In contrast, the Y-axis presents the actual number of droplets resolved within each bin, based on simulation outputs. This distinction highlights the difference between user-defined input parameters and the physical droplet distribution observed during the suppression process.

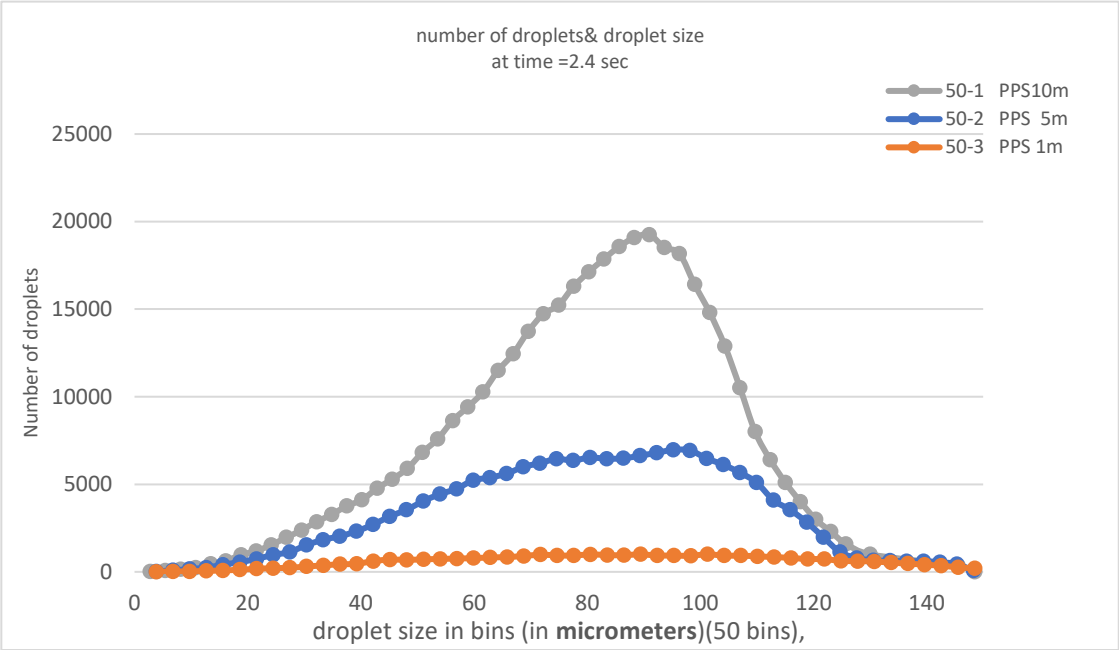

Figure 7-13 Number of droplets& droplet size
at time =2.4 sec

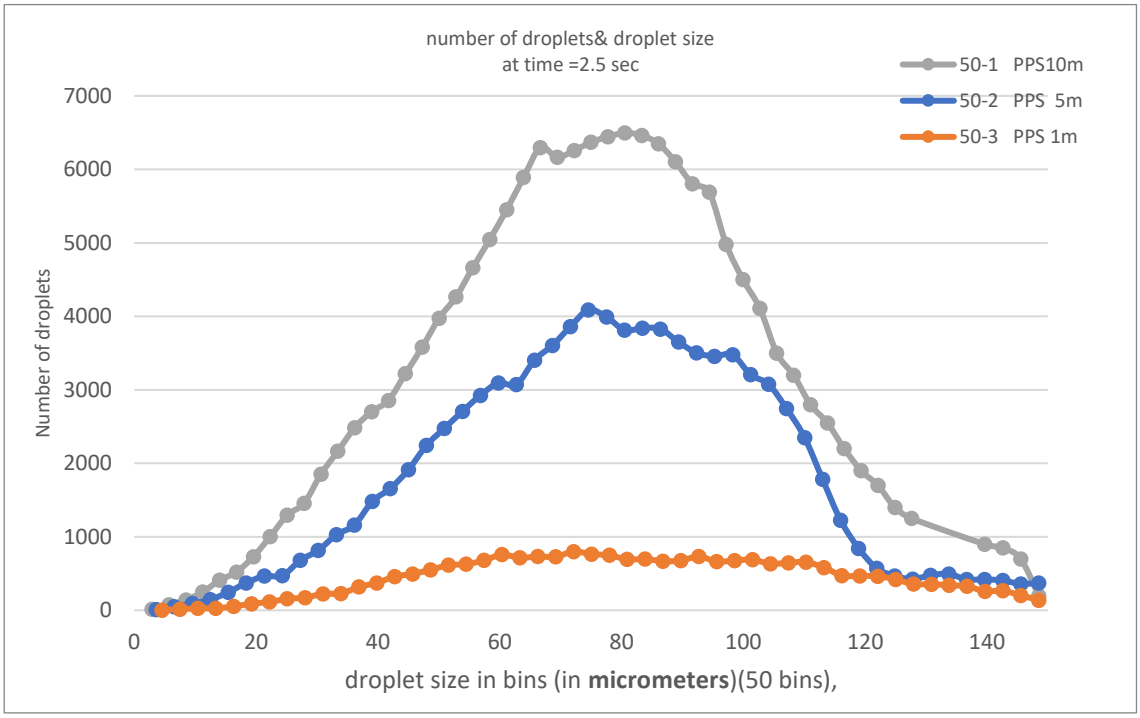

Figure 7-14 Number of droplets& droplet size

at time =2.5 sec

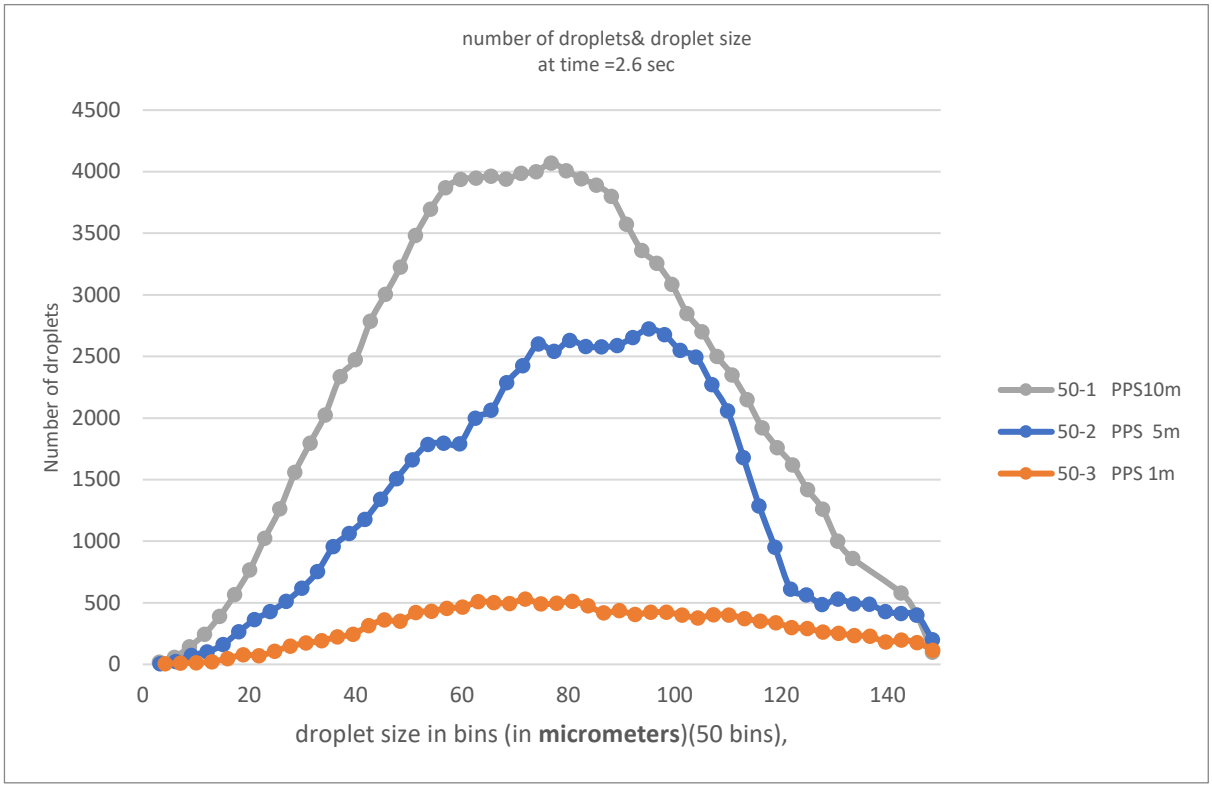

Figure 7-15 Number of droplets& droplet size

at time =2.6 sec

7.4.8 Key Observations from Droplet Size:

The analysis of droplet size distribution across time steps 2.4, 2.5, and 2.6 seconds reveals distinct trends in mist behaviour and its relationship with suppression effectiveness:

1. **At Early Stages (2.4 sec):**

Higher injection rates (10M and 5M PPS) exhibit broader size distributions, comprising a mix of both small and large droplets.

In contrast, the 1M PPS case displays a narrower distribution dominated by smaller droplet populations and fewer large droplets, indicating limited spray momentum

2. **At Intermediate Stages (2.5 sec):**

Smaller droplets (<80 μm) dominate in high PPS cases, contributing to faster evaporation and cooling.

Larger droplets (>100 μm) are more pronounced in lower PPS cases, improving deeper penetration but reducing surface cooling.

3. **At Later Stages (2.6 sec):**

The droplet distribution in the 10M PPS case begins to stabilise, suggesting an optimal balance between mist coverage and fire plume penetration.

The 5M PPS case retains some broader distribution but shows signs of depletion in the smaller droplet range.

The 1M PPS case exhibits the lowest droplet count and least variability, indicating limited suppression reach and coverage.

7.4.9 Cooling vs. Penetration Dynamics

Understanding the physical role of droplet sizes in fire suppression reveals two dominant mechanisms:

Smaller Droplets (< 80 µm)	Larger Droplets (> 100 µm)
Exhibit a high surface-area-to-volume ratio, promoting rapid evaporation and convective heat absorption.	Heavier droplets travel deeper into the fire plume, increasing fire penetration but with reduced evaporation efficiency.
Enhance cooling of surface layers and flame periphery but are limited in momentum and penetration depth.	Contribute more to the quenching of the core flame structure rather than rapid surface cooling.

Table 7.9 Comparative Roles of Small and Large Droplets in Fire Suppression Dynamics

7.4.10 Conclusion

Cooling Efficiency: At the initial stages, smaller droplets dominate, leading to **efficient cooling** of the fire's surface layers.

Penetration Capability: As suppression progresses, larger droplets play a key role in reaching deeper fire zones, enhancing suppression at the core.

Smaller Droplets: The higher surface-area-to-volume ratio enhances evaporative cooling. During the initial seconds, they dominate the profile, rapidly reducing the temperature in the vicinity.

Larger Droplets: As suppression proceeds, the shift towards larger droplets ensures deeper penetration into the fire plume, tackling the fire source effectively.

The balance between smaller and larger droplets is required as smaller droplets handle surface cooling, while larger ones penetrate the plume.

7.5 Droplet Distribution and Suppression Effectiveness - Upward (Bottom) Injection

This section explores the suppression behaviour of water mist introduced upward from the bottom of the fire domain, simulating a configuration where droplets are injected vertically from below the flame. This approach allows mist to directly interact with the high-temperature core near the fuel source, enhancing early-stage flame disruption.

Droplet size distribution is analysed as a key factor influencing the suppression outcome. Using bin-based histograms generated in ParaView, the study captures how droplet sizes evolve over time and interact with the flame. The analysis focuses on key differences between low and high injection rate.

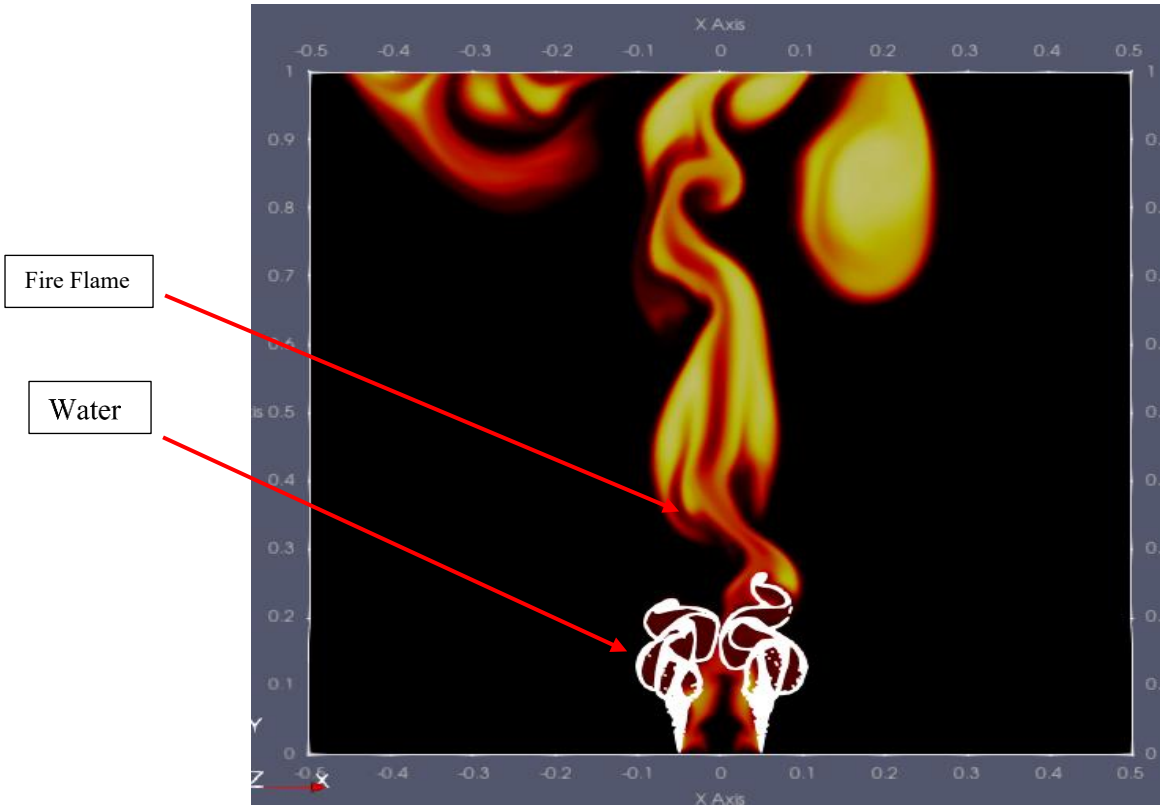

Figure 7-16 Bottom- Suppression and Vortex Interaction with Fire Plume

7.5.1 Droplet Size Distribution

In bottom injection, droplet dynamics differ due to opposing gravitational and buoyant forces. Droplet distributions are visualised using histograms, where each bin corresponds to a defined size range. This allows assessment of the balance between fine mist (for surface cooling) and larger droplets (for deeper fire penetration). The analysis focuses on three time steps 2.4s**,** 2.5s, and 2.6s to track how droplet behaviour evolves during suppression.

7.5.2 Input Configuration

The injection parameters for bottom suppression were defined as follows:

Parameter	Value	Description
Min Droplet Size	1×10^{-6} m	Minimum droplet diameter
Max Droplet Size	1.5×10^{-4} m	Maximum droplet diameter
Injection Model	coneNozzleInjection	Defines conical spray distribution
Mass Total	0.01 kg	Mass injected per nozzle
Outer Diameter	1.9×10^{-4} m	Nozzle spray width
Inner Diameter	0 m	Nozzle core diameter
Injection Duration	5.0 s	Total injection time

7.5.3 Fire Suppression Performance and Visualization

The suppression performance is evaluated using visual outputs from ParaView, focusing on the interaction between water mist and the buoyant flame. Two representative injection rates were selected to explore the influence of spray intensity on suppression behaviour:

500,000 Parcels Per Second (PPS = 500K)

2,000,000 Parcels Per Second (PPS = 2M)

These cases reveal how the injection rate impacts droplet formation, evaporation, and suppression efficiency. The analysis spans the time range **2.4s to 2.6s**, capturing the evolution of droplet distribution and suppression performance

7.5.3.1 Visualization of case 1: at 500,000 Parcel Per Second (PPS)

Time =2.1 second	Time =2.2 second	Time =2.3 second
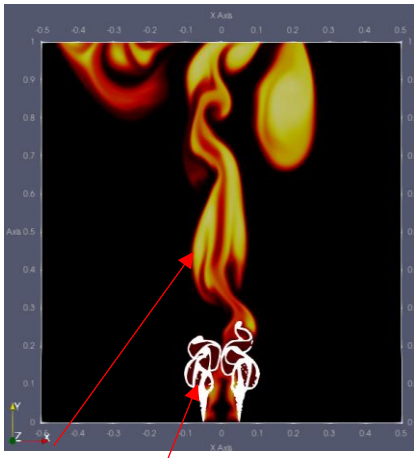 Fire Water	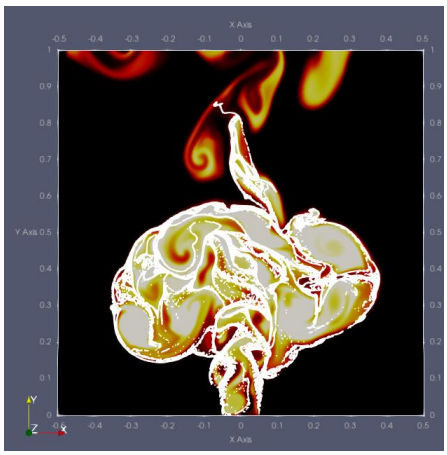	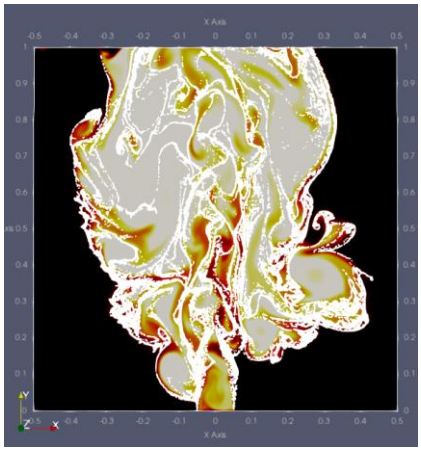
Time =2.4 second	**Time =2.5 second**	**Time =2.6 second**
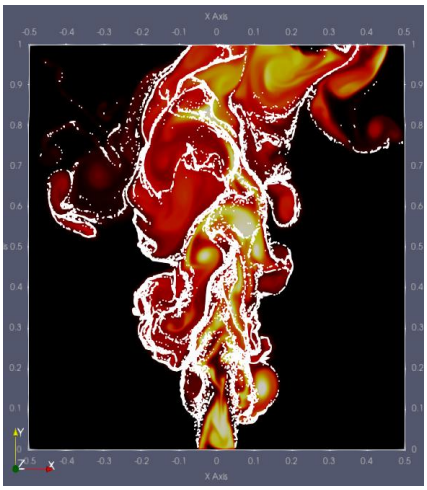	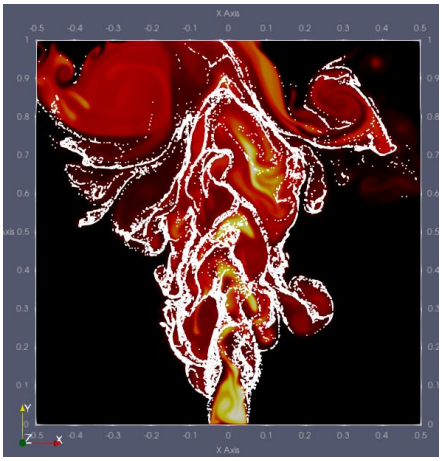	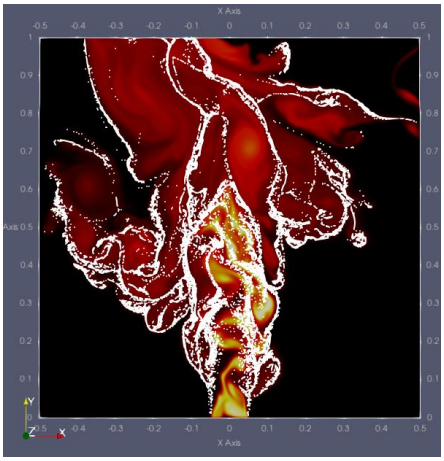

Time =2.7 second	Time =2.8 second	Time =2.9 second
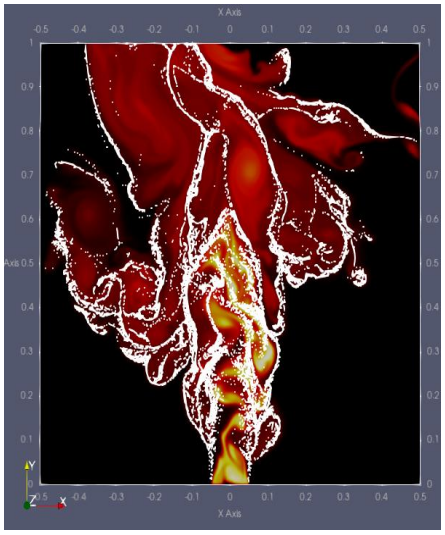	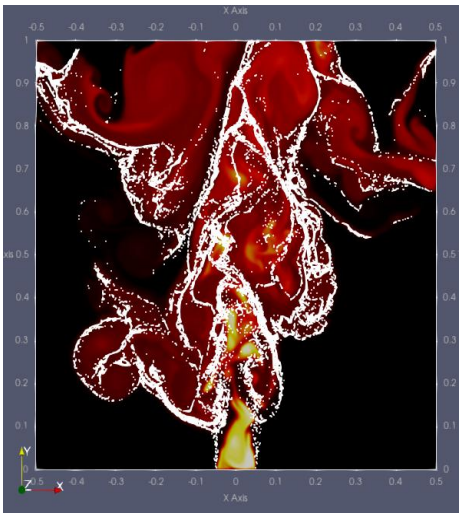	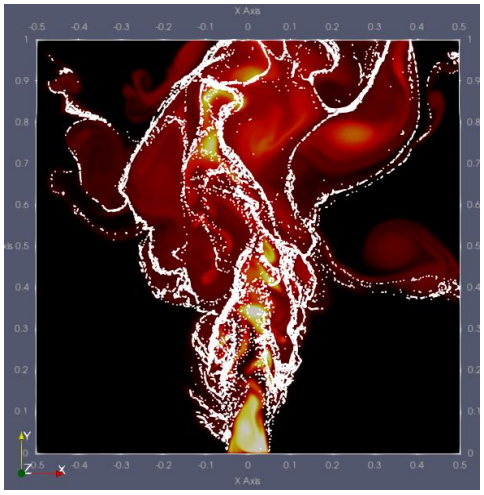

Observations: Case 1 – Bottom Injection at 500,000 PPS

At 2.1 seconds:

Water mist is first introduced from the bottom nozzles. Initial interaction between the fine mist and the base of the buoyant flame begins. Vortex structures appear around the nozzles, showing early mixing.

At 2.2 seconds:

The spray starts to lift into the lower region of the flame. Some entrainment of mist within the fire plume is observed, but upward progress is slow due to buoyant counterflow.

At 2.3 seconds:

Droplets disperse laterally and begin to occupy more volume. Fine mist particles interact with the outer flame structure, showing signs of local cooling at the flame base.

At 2.4 seconds:

The mist expands into the lower-to-mid flame region. Partial suppression appears around the periphery.

At 2.5 seconds:

Suppression strengthens at the lower zone, with reduced flame intensity. Some pockets of fire show visible disruption, though upper regions remain unaffected.

At 2.6 seconds:
The mist reaches higher regions. Flame structure begins to fragment, but not fully extinguished. Droplet dispersion improves, but suppression is limited in vertical reach.

From 2.7 to 2.9 seconds:
Localised suppression is observed, with flame reduction near the injection zone. However, the upper flame continues to burn, indicating limited deep penetration due to low injection strength. Mist disperses widely at the base but fails to dominate the fire plume.

7.5.3.2 Visualization of case 1: at 2,000,000 Parcel Per Second (PPS)

Time =2.1 second 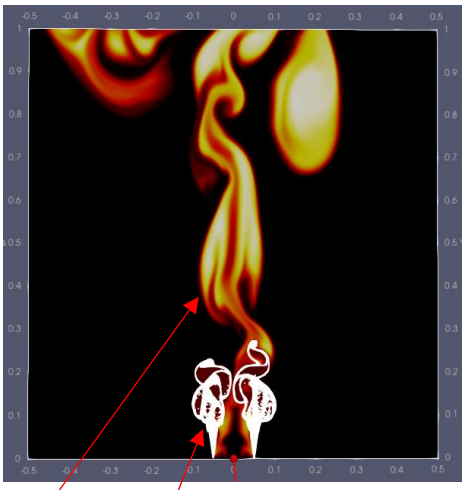 	Time =2.2 second 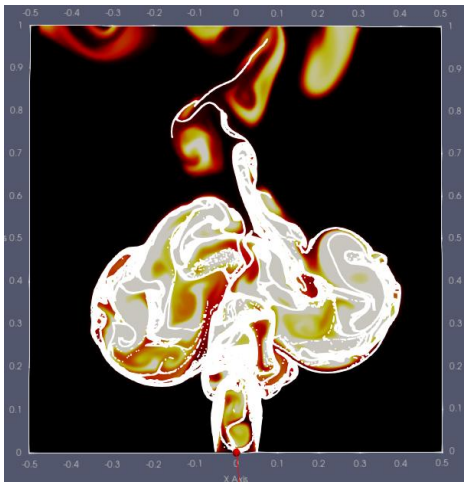	Time =2.3 second 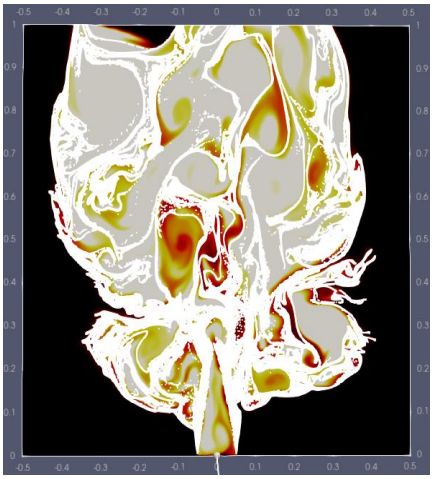
Time =2.4 second 	Time =2.5 second 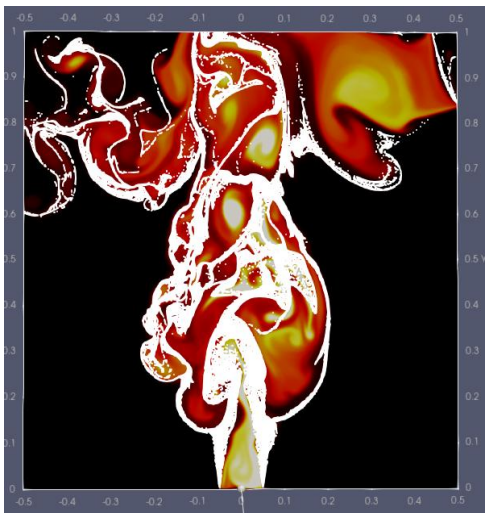	Time =2.6 second 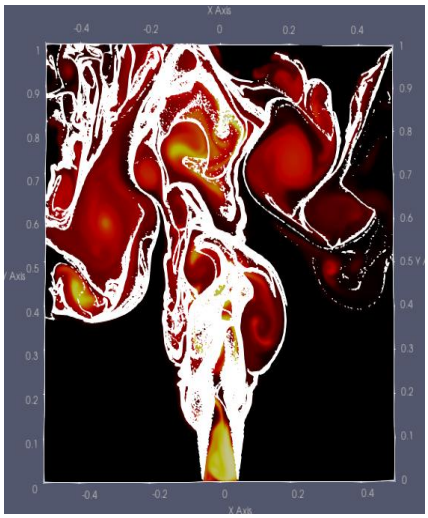

Time =2.7 second	Time =2.8 second	Time =2.9 second
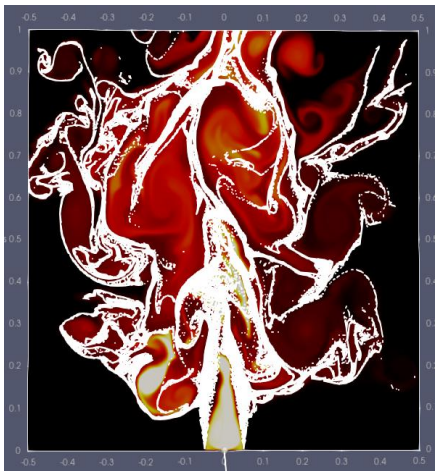	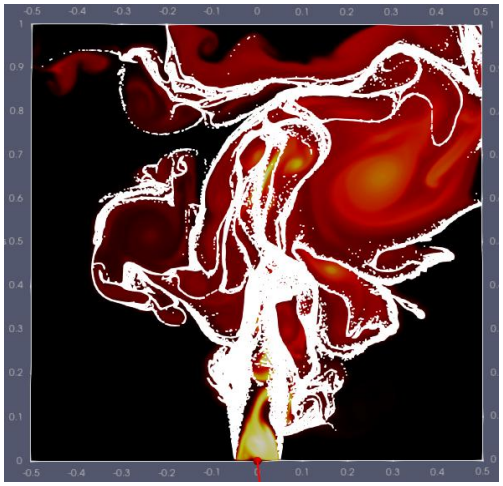	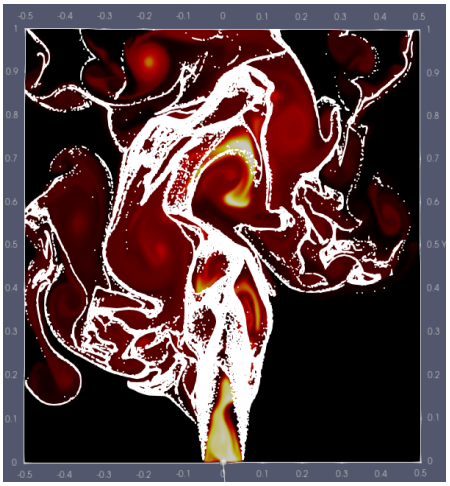

Observations: Case 2 – Bottom Injection at 2,000,000 PPS

At 2.1 seconds:

Water mist begins to emerge from the bottom nozzles with noticeably denser concentration compared to the 500,000 PPS case. The initial plume interaction appears stronger, with visible droplet clustering near the base.

At 2.2 seconds:

The mist column ascends further into the flame zone, maintaining coherence. Droplet penetration improves, aided by increased injection momentum. Early flame disruption is seen at the lower boundary.

At 2.3 seconds:

Flame deformation becomes more apparent. Larger volumes of droplets reach mid-height, engaging more effectively with the fire plume. Suppression begins to spread laterally as well.

At 2.4 seconds:

The lower flame structure begins to collapse, with broader mist dispersion. Compared to the 500K case, there is more consistent suppression in the mid and lower regions.

At 2.5 seconds:

Flame pockets start fragmenting, indicating enhanced suppression in areas directly above the nozzle zone. Flame turbulence increases as the mist pushes into the core region.

At 2.6 seconds:
Significant portions of the mid-flame region show disruption. The mist maintains vertical reach, and the boundary between suppression-affected and unaffected regions begins shifting upward.

From 2.7 to 2.9 seconds:

The suppression field becomes more stable. Fire intensity is visibly reduced across a broader section. However, a few persistent combustion zones remain at upper heights, though less pronounced than in the 500K case.

7.5.3.3 Comparative Insights: 500K vs 2M PPS (Bottom Injection)

The following table compares suppression behaviour between bottom injection rates of 500,000 PPS and 2,000,000 PPS. It highlights key differences in mist density, penetration depth, and flame interaction. The comparison demonstrates how increasing the injection rate improves vertical reach and enhances suppression effectiveness across a broader flame region.

Observation Area	500,000 PPS	2,000,000 PPS
Mist Density	Sparse, low-pressure mist	Denser, more coherent mist
Vertical Reach	Limited, stays in lower zones	Improved, reaching mid to upper flame layers
Flame Suppression	Localised, mainly at base	Broader, extends to mid-height
Turbulence Effects	Minimal impact on core flame	Induces strong flame deformation
Suppression Timeframe	Slower suppression, incomplete at 2.9s	Faster suppression, more effective by 2.9s

Table 7.10 Comparative Analysis of Fire Suppression Performance for Bottom Injection at 500K and 2M PPS

Summary Observation:

The 2,000,000 PPS bottom injection case demonstrates enhanced suppression efficiency compared to 500,000 PPS. The higher injection rate provides improved vertical penetration and mist coverage, enabling more effective interaction with the buoyant flame. Although complete suppression of the upper flame region is still limited due to upward convective resistance, the fire's mid-zone is significantly disrupted, indicating a more promising suppression profile.

7.5.4 Evaluation of Suppression Performance at Varying Injection Rates

To assess the influence of injection rate on droplet distribution and suppression behaviour during bottom injection, two representative cases were examined using histogram plots of droplet size and count at three key time steps (2.4, 2.5, and 2.6 seconds), as shown in Figures 7-17 to 7-19. These visualisations illustrate how injection density affects the evolution of mist characteristics, flame interaction, and suppression reach.

500,000 Parcels Per Second (PPS)

2,000,000 Parcels Per Second (PPS)

The comparison offers a direct framework to understand how bottom spray systems behave under different mass flow intensities and how this influences mist formation, dispersion, and fire plume penetration.

7.5.4.1 Input Configuration

To ensure consistent analysis of droplet distribution and suppression dynamics, the bottom injection cases were configured using the following parameters:

Parameter	Value	Description
Injection Model	`coneNozzleInjection`	Defines conical spray pattern
Total Injected Mass	0.01 kg	Mass of water introduced into the domain
Outer Diameter	1.9×10^{-4} m	Diameter of nozzle outlet
Inner Diameter	0 m	Nozzle core diameter (no internal restriction)
Injection Duration	5.0 s	Total mist injection time
Droplet Size Distribution	`RosinRammler`	Statistical model defining droplet size variation
Mean Diameter (d)	30×10^{-6} m (30 μm)	Average droplet diameter used in Rosin–Rammler model

Table 7.11 Spray Configuration and Droplet Properties for Mass Flow Rate Suppression Analysis

The analysis focuses on the active suppression window from **2.4 to 2.6 seconds**, a critical phase during which the mist interacts intensely with the fire plume.

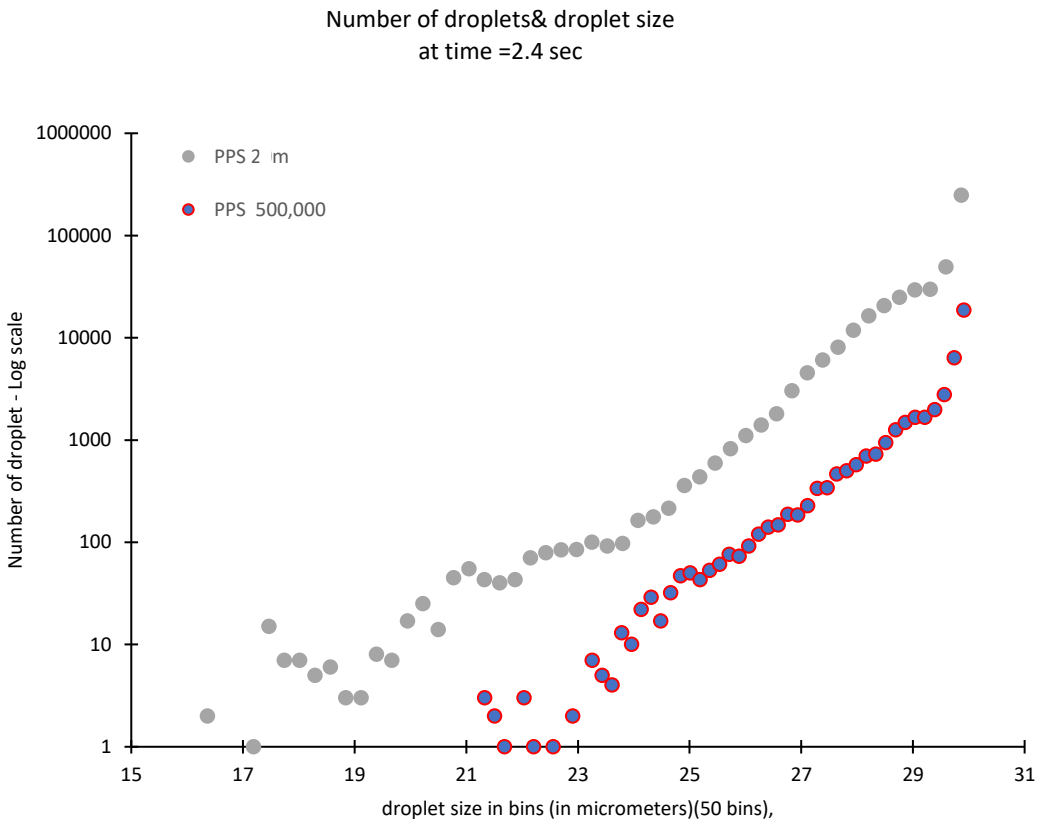

Figure 7-17Number of droplets& droplet size

at time =2.4 sec

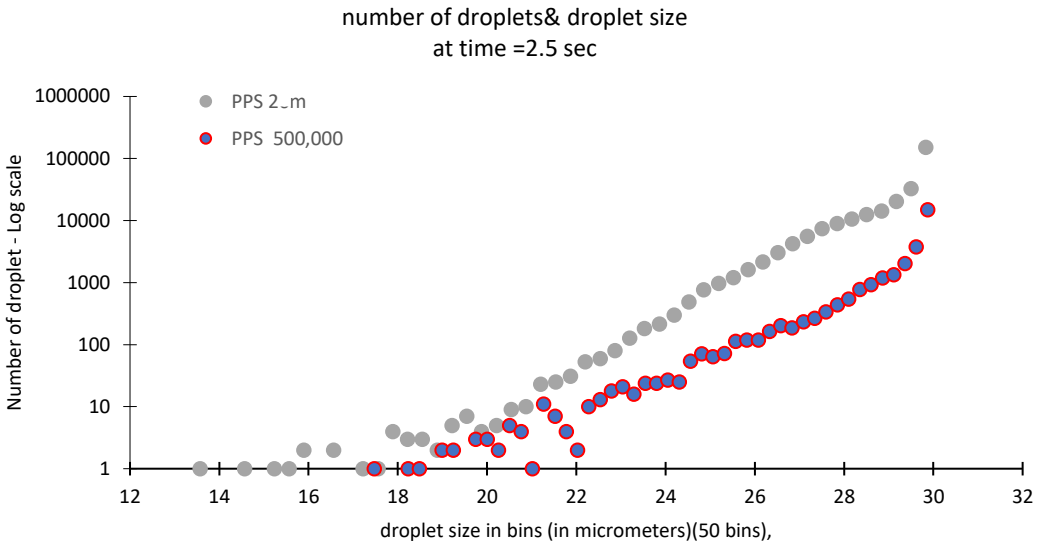

Figure 7-18 Number of droplets& droplet size

at time =2.5 sec

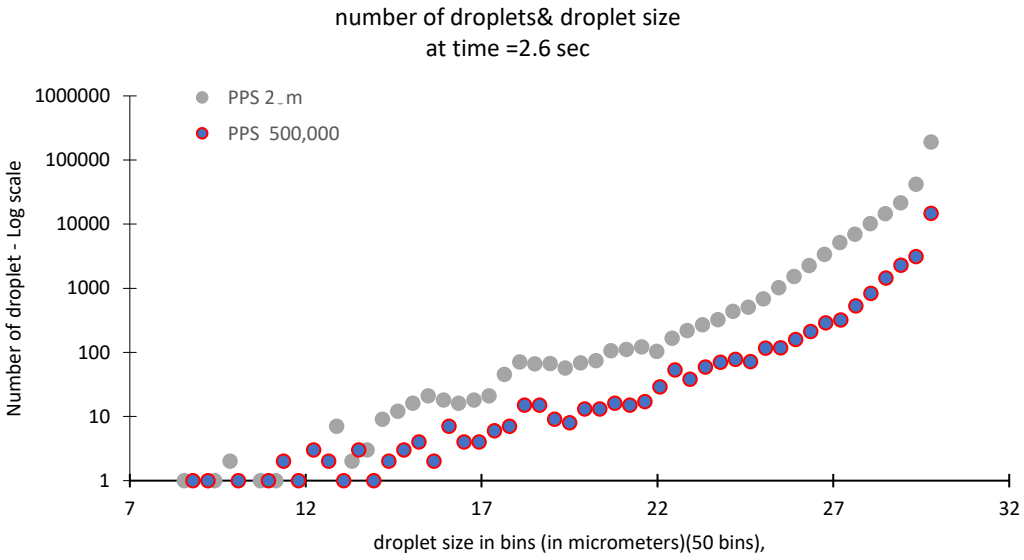

Figure 7-19 Number of droplets& droplet size

at time =2.6 sec

7.5.5 Overview of Droplet Distribution Over Time:

The histogram plots reflect the dynamic changes in droplet population and size distribution during suppression:

- **X-Axis**: Droplet diameter in micrometres, grouped into uniform size bins
- **Y-Axis**: Number of droplets present in each bin
- **Time Points**: Snapshots are taken at 2.4 s, 2.5 s, and 2.6 s for comparative analysis

From the figures:

In the 2M PPS case, a sharp peak emerges at approximately 30 μm, showing the dominance of larger droplets.

In the 500K PPS case, the droplet count is lower but more uniformly distributed across a broader range of smaller and mid-sized droplets.

As time progresses, evaporation and dispersion impact both cases differently larger droplets remain concentrated and persistent in the 2M case, while the 500K case supports finer misting and wider coverage.

7.5.6 Interaction with Fire Plume Dynamics

The upward motion of hot gases in a fire plume introduces another layer of complexity in droplet transport:

Top Injection:

The descending mist intersects with rising flame gases, leading to turbulent mixing that enhances lateral dispersion. This promotes a wider range of droplet **sizes** interacting with different flame zones, improving overall suppression coverage.

Bottom Injection:

Droplets are injected directly into the strongest convective currents at the flame base.

The high turbulence causes fine droplets to be rapidly lifted and scattered, often missing their intended suppression target.

7.5.7 Comparative Summary of Observed Differences

The following table summarises the key differences observed between top and bottom injection methods, focusing on how droplet size, residence time, and interaction with the fire plume influence suppression performance.

Aspect	Top Injection	Bottom Injection
Droplet Size Spread	Broad (small and large droplets coexisting)	Narrower; concentration of smaller droplets near injection point
Residence Time	Short for small droplets; rapid evaporation	Longer for small droplets; sustained mist in lower zones
Penetration Depth	High – reaches deep flame regions	Limited – effective mainly in lower/mid zones
Fire Plume Interaction	Droplets decelerated and dispersed within flame	Strong upward plume disperses fine mist prematurely
Suppression Pattern	Well-distributed suppression with vertical coverage	Localised suppression near base; reduced upper zone impact

Table 7.12 Comparative Summary of Droplet Behaviour and Suppression Dynamics – Top vs Bottom Injection

7.6 Effect of Mass Flow Rate on Suppression from Top Injection

To evaluate the influence of mass flow rate on suppression performance, this study investigates three scenarios using the same nozzle and injection model while varying only the total mass of water introduced.

The examined cases are:

Case M1: massTotal = 0.01 kg

Case M2: massTotal = 0.002 kg

Case M3: massTotal = 0.001 kg

These cases offer a framework to assess how increasing or decreasing the injected water volume impacts suppression effectiveness.

7.6.1 Temperature and Suppression Performance

Figure 7-20 and Figure 7-21 illustrate the impact of different mass flow rates on flame temperature and suppression efficiency. The first figure shows the temperature evolution over time, providing insights into suppression trends. The second figure presents a comparison of the final temperature at a fixed time, highlighting the effect of each mass flow rate

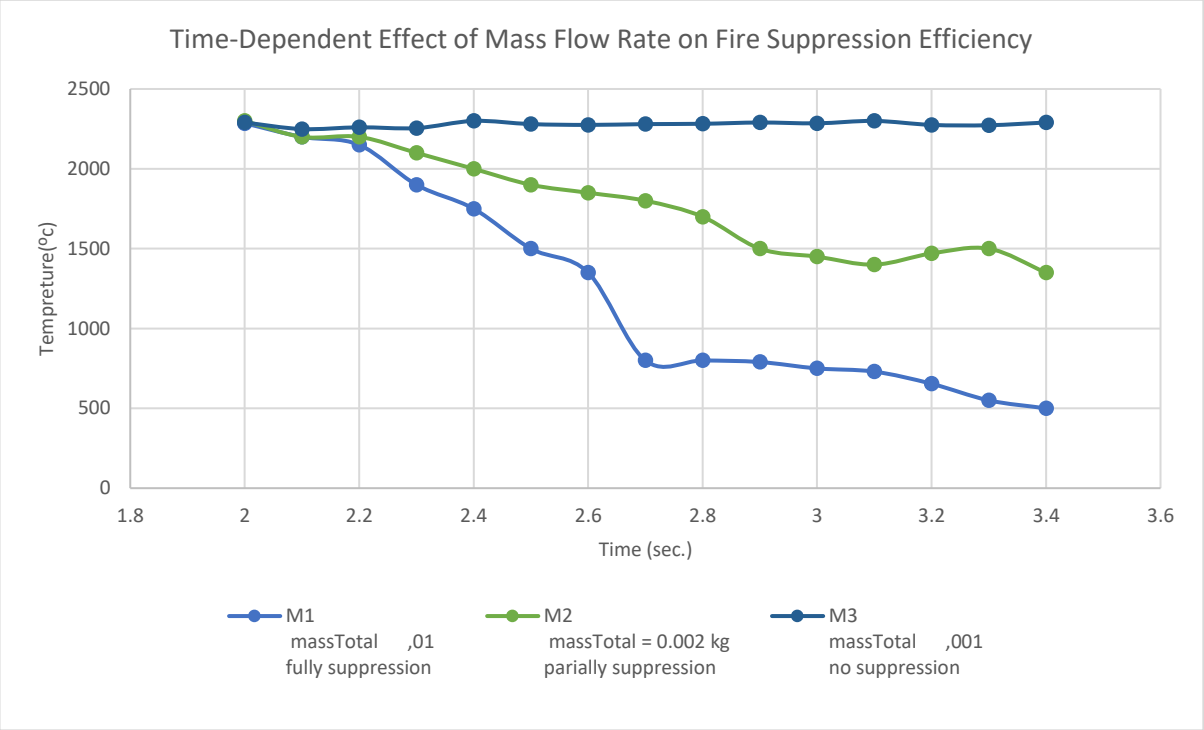

Figure 7-20 Time-Dependent Effect of Mass Flow Rate on Fire Suppression Efficiency

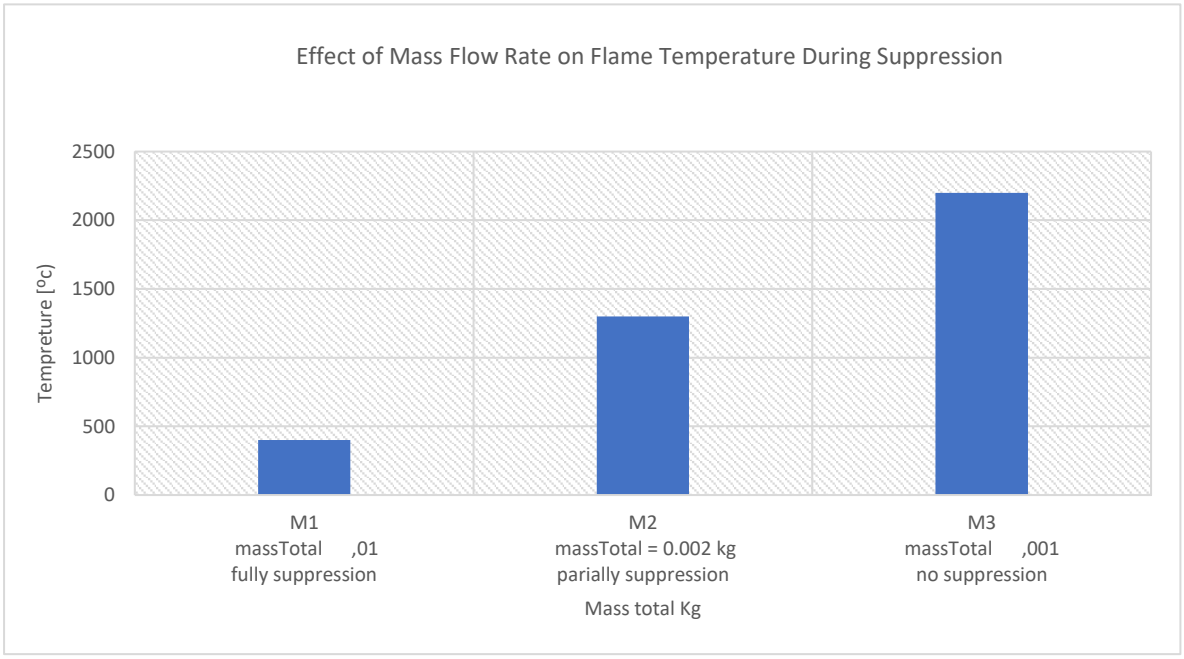

Figure 7-21 Effect of Mass Flow Rate on Flame Temperature During Suppression

Parameter	Case M1 (0.01 kg)	Case M2 (0.002 kg)	Case M3 (0.001 kg)
Flame Temperature	Low (400°C)	Moderate (1300°C)	High (2200°C)
Evaporation Rate	High - significant steam formation	Moderate	Low - minimal steam formation
Fire Plume Disruption	Strong - major turbulence and breakdown	Moderate partial suppression	Weak - plume remains largely intact
Oxygen Displacement	More effective	Less effective	Minimal displacement
Suppression Effectiveness	Strong – full suppression	Partial suppression	Weak- no significant suppression

Table 7.13 Comparison of Fire Suppression Effectiveness at Different Mass Flow Rates

These results show that:

Case **M1 (0.01 kg)** achieves full suppression due to enhanced mist dispersion, strong evaporation, and efficient cooling.

- Case **M2 (0.002 kg)** provides partial suppression, reducing flame temperature but leaving some regions unaffected.

- Case **M3 (0.001 kg)** demonstrates ineffective suppression, as the lower mist density fails to disrupt the fire.

7.6.2 Observations on Suppression Mechanisms

The variation in suppression performance is linked to several physical mechanisms:

Cooling Efficiency

Higher mass flow rates generate dense mist clouds, rapidly reducing flame temperature.

Lower rates lead to weak cooling, allowing flames to sustain.

Evaporation and Steam Generation

In M1, substantial evaporation produces steam that displaces oxygen, aiding flame inhibition.

M3 yields minimal evaporation, limiting both cooling and oxygen displacement.

Plume Disruption and Momentum Effects

M1 induces turbulence and breaks the flame structure.

Lower rates fail to disrupt the fire plume, resulting in persistent combustion zones.

Droplet Density and Mist Coverage

M1 produces high droplet density across the domain, increasing the probability of fire-droplet interaction.

Sparse mist in M3 limits coverage, reducing suppression efficacy.

7.6.3 Summary

The findings confirm that mass flow rate is a critical determinant of fire suppression effectiveness in top injection scenarios. A higher water mass leads to:

Enhanced droplet population

Improved cooling via evaporation

Greater disruption of flame structure

More effective oxygen displacement

In contrast, low mass injection rates result in weak mist fields, poor evaporation, and limited suppression reach. This underscores the importance of selecting an optimal mass flow rate tailored to the fire intensity, geometry, and application context.

By refining the mass flow rate selection, future studies can optimize suppression strategies, ensuring reliable fire control in large-scale fire scenarios.

7.7 Effect of Mass Flow Rate on Suppression from bottom Injection

To evaluate the influence of mass flow rate on fire suppression effectiveness, this study examines three different mass injection rates while keeping all other parameters constant.

The following scenarios are considered:

Case M1: massTotal = 0.01 kg

Case M2: massTotal = 0.002 kg

Case M3: massTotal = 0.001 kg

The objective is to investigate how changes in mist density affect thermal suppression, evaporation efficiency, plume interaction, and oxygen displacement.

7.7.1 Temperature and Suppression Performance

Figure 7-22 illustrate the impact of different mass flow rates on flame temperature and suppression efficiency presents a comparison of the final temperature at a fixed time, highlighting the effect of each mass flow rate.

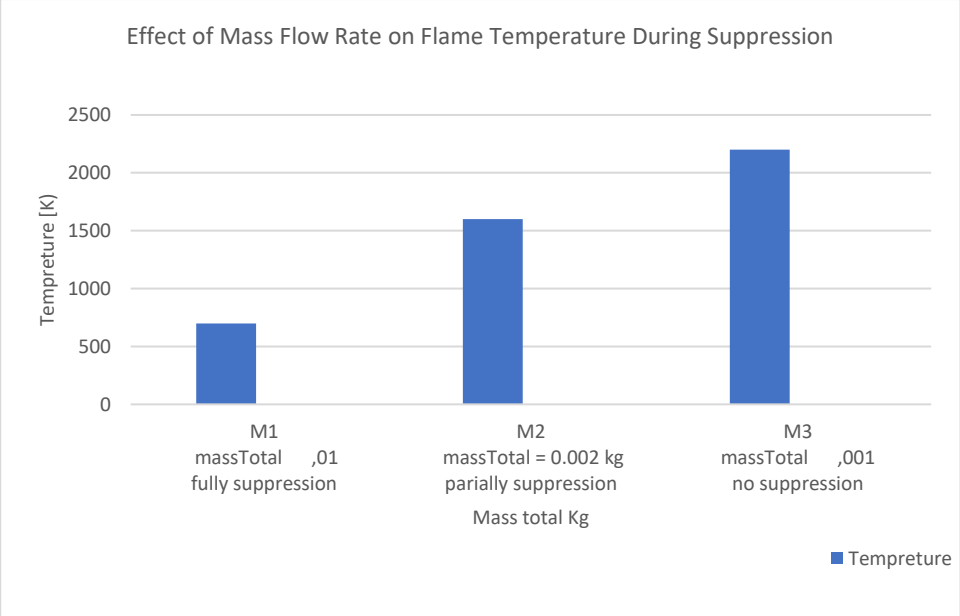

Figure 7-22 Effect of Mass Flow Rate on Flame Temperature During Suppression

Key Observations:

High Injection Rate (M1: 0.01 kg)

Achieves the most effective suppression, reducing flame temperature to approximately 400 °C.

Enables rapid mist evaporation, strong cooling, and effective oxygen displacement.

Results in significant steam formation, minimising the potential for re-ignition.

Moderate Injection Rate (M2: 0.002 kg)

Provides partial suppression, with flame temperature stabilising around 1300 °C.

Shows moderate levels of steam and mist coverage.

Causes some fire plume disruption but does not extinguish the flame completely.

Low Injection Rate (M3: 0.001 kg)

Demonstrates poor suppression, with the flame temperature remaining high (~2200 °C).

Limited evaporation and minimal mist penetration result in weak thermal suppression.

The flame remains structurally intact with minimal disruption.

7.7.2 Influence on Fire Plume Dynamics

The interaction between injected mist and the buoyant flame plays a critical role in suppression effectiveness.

M1 (0.01 kg): Produces strong turbulence at the base of the flame, disrupting the plume and collapsing flame structures.

M2 (0.002 kg): Induces moderate disruption, reducing flame size but allowing sustained combustion in upper zones.

M3 (0.001 kg): Shows minimal impact, with the fire plume remaining largely undisturbed, contributing to ineffective suppression.

7.7.3 Effect on Evaporation and Steam Formation

Evaporation serves as a dominant cooling mechanism, converting liquid mist into steam and reducing oxygen availability in the combustion zone.

High mass injection (M1) results in substantial evaporation and intensive steam formation, enhancing fire suppression and thermal quenching.

Low mass injection (M3) yields weak evaporation, leading to ineffective mist–fire interaction and a high likelihood of sustained burning.

7.7.4 Summary of Findings

The following table summarises the suppression outcomes for each mass flow rate scenario. It reinforces the importance of sufficient mist density to achieve meaningful interaction with flame dynamics and efficient oxygen displacement.

Parameter	Case M1 (0.01 kg)	Case M2 (0.002 kg)	Case M3 (0.001 kg)
Flame Temperature	Low (~400°C)	Moderate (~1300°C)	High (~2200°C)
Evaporation Rate	High – significant steam formation	Moderate	Low – minimal steam formation
Fire Plume Disruption	Strong – major turbulence and breakdown	Moderate – partial suppression	Weak – plume remains largely intact
Oxygen Displacement	More effective	Less effective	Minimal displacement
Suppression Effectiveness	Strong – full suppression	Partial suppression	Weak – no significant suppression

Table 7.14 Comparison of Fire Suppression Effectiveness at Different Mass Flow Rates

7.7.5 Conclusion:

These findings highlight that mass flow rate is a determining factor in the effectiveness of bottom-injected water mist systems. Higher flow rates improve droplet density, evaporation, and fire plume disruption, resulting in stronger suppression performance. In contrast, lower flow rates fail to produce the necessary thermal and physical interaction required for effective fire control.

Future work should explore the threshold beyond which increasing the flow rate no longer improves performance, due to oversaturation or droplet fallout, and investigate adaptive control mechanisms that dynamically adjust mass flow to match fire development in real time.

7.8 Suppression Temperature Over Time: Top vs. Bottom Injection

Fire suppression performance is primarily evaluated by examining how effectively the suppressant reduces flame temperature over time. This section presents a comparative analysis of **top** and **bottom** injection methods, highlighting differences in temperature reduction trends, evaporation behaviour, and overall suppression efficiency. A no suppression case is also included as a reference baseline.

7.8.1 Comparative Temperature Reduction Analysis

Temperature profiles were monitored throughout the simulation period to evaluate suppression efficiency for both injection strategies. The evolution of flame temperature over time is illustrated in Figure 7-23, comparing:

Top Injection

Bottom Injection

No Suppression (Reference Case)

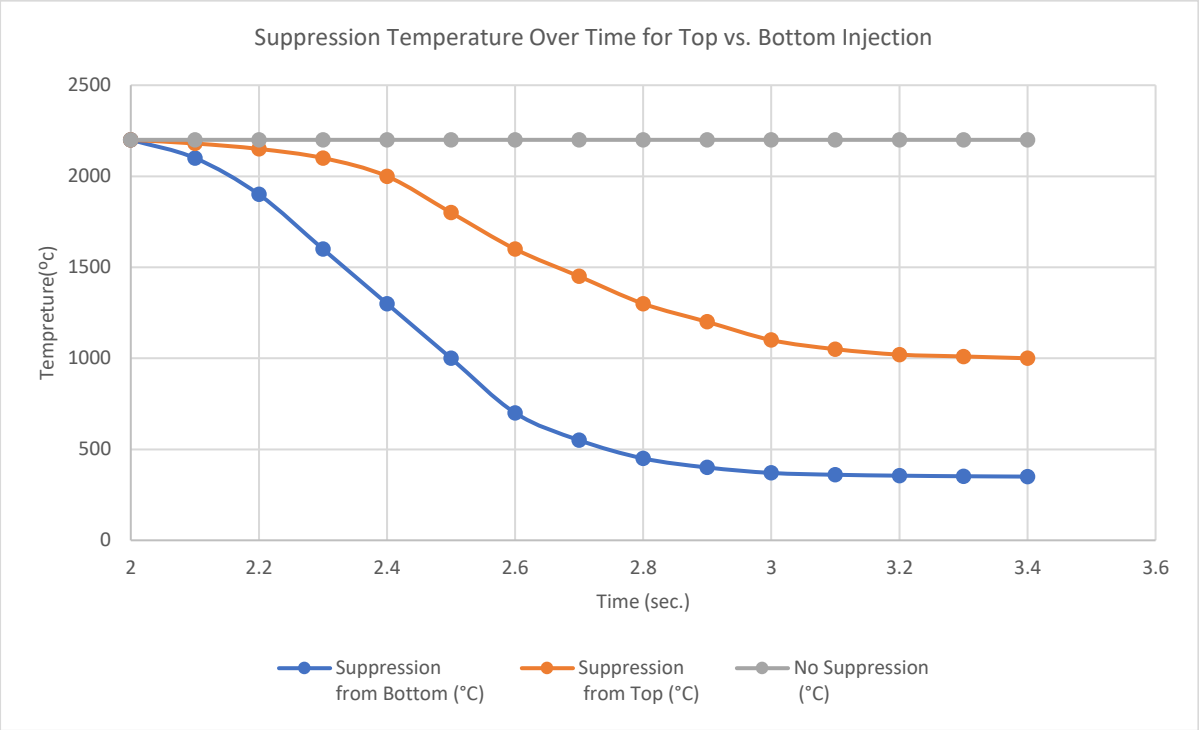

Figure 7-23 Suppression Temperature Over Time for Top vs. Bottom Injection

Key Observations:

Bottom Injection results in the most rapid and sustained temperature reduction, with significant cooling observed as early as 2.6 seconds and near-complete suppression by 3.4 seconds.

This is attributed to the direct interaction between the rising flame and the upward-injected mist, which enables efficient heat absorption and combustion disruption at the flame base.

Top Injection, while effective, exhibits slower cooling behaviour. Droplets must traverse the hot gas plume before reaching the combustion zone, leading to delayed evaporation and heat exchange.

Suppression is achieved gradually, with temperature reductions extending beyond the initial 3.4-second window.

No Suppression serves as a control case. The flame temperature remains constant at approximately 2200 °C, demonstrating the self-sustaining nature of the fire in the absence of intervention.

These results provide critical insight into the timing and positioning of suppression strategies. Bottom injection offers a faster response, making it favourable for scenarios requiring immediate flame knockdown. However, top injection remains valuable for sustained suppression coverage and cooling at multiple flame heights.

7.9 Conclusion and Future Work

This chapter has explored fire suppression performance using both top and bottom injection methods, analysing the impact of droplet distribution, injection rates, and mass flow rate variations. The findings emphasize that suppression effectiveness is significantly influenced by spray characteristics, particularly droplet size distribution, injection rate, and the volume of suppressant introduced into the system.

A simplified modelling approach was employed in this study, focusing primarily on the interaction between water mist, fire plume dynamics, and heat transfer mechanisms. While the results offer valuable insights into the suppression process, several limitations and areas for future research need to be addressed to improve the model's accuracy and applicability to real-world scenarios.

7.9.1 Key Limitations of the Current Study:

- The study simplifies turbulence-droplet interactions, which are essential in real-world suppression scenarios.
- Evaporation and phase-change mechanisms were modelled using existing sub models, but further refinements are necessary to capture localized temperature effects and heat flux variations.
- The simulations were conducted under controlled conditions, without accounting for external factors such as wind effects, ventilation variations, and different fuel types.

7.9.2 Future Research Directions:

To improve the predictive accuracy and practical application of fire suppression modelling, future studies should focus on:

1. Advanced Turbulence Modelling: Incorporating detailed turbulence-droplet interactions to better represent the entrainment of mist within buoyant fire plumes.
2. Refined Evaporation and Heat Transfer Models: Developing adaptive phase-change mechanisms that account for varying ambient conditions to enhance suppression predictions.
3. Investigation of Large-Scale Scenarios: Extending the study to full-scale fire suppression cases with different nozzle configurations, spray angles, and suppressant compositions.
4. Optimized Injection Strategies: Refining the balance between mist dispersion and penetration to determine the most efficient suppression approach for different fire intensities and environments.
5. Enhancing Computational Efficiency: Addressing the high computational cost of high-resolution simulations by exploring hybrid modelling approaches that improve efficiency while maintaining accuracy.

7.9.3 Final Remarks

This study establishes a foundation for understanding fire suppression performance, particularly in relation to spray characteristics and injection conditions. However, further research is necessary to refine the suppression model and optimize system performance under real-world fire conditions. The findings contribute to the ongoing development of advanced fire suppression strategies, supporting safer and more effective firefighting solutions.

8 Discussion

8.1 Introduction

This chapter provides a detailed reflection on the modelling results presented throughout the thesis. It connects the research objectives with the outcomes of each major phase, drawing together the literature, validation exercises, and simulation results to assess the contribution of this study to fire safety engineering. Each chapter is revisited through the lens of its relevance to the research gap and is analysed in relation to the overarching aim: to visualise, simulate, and evaluate the behaviour of turbulent buoyant flames and mist suppression using a new burner configuration that better represents realistic fire conditions.

8.2 Revisiting the Research Gap and Introducing the USYD Burner

Significant strides have been made in the field of fire modelling through collaborative international initiatives such as the Measurement and Computation of Fire Phenomena (MaCFP), which has provided a robust framework for the joint advancement of experimental and computational fire science. The MaCFP Working Group, under the auspices of the International Association for Fire Safety Science (IAFSS), has curated a series of benchmark configurations including buoyant plumes, gaseous pool fires, and solid fuel growth scenarios. Among these, the Sandia and McCaffrey burners have served as foundational cases, offering well-characterised and reproducible datasets that have been instrumental in validating numerical models, particularly for turbulent buoyant diffusion flames under controlled laboratory conditions.

These benchmark flames have enabled substantial progress in model calibration, especially in terms of heat release characterisation, scalar transport, and gas-phase dynamics. Yet, as fire safety research evolves to address increasingly complex and realistic fire scenarios, there is a growing recognition of the need for experimental platforms that can accommodate controlled

modulation of turbulence and suppression-relevant boundary conditions. While benchmark cases remain essential for ensuring reproducibility and comparability, they are often limited in their ability to simulate the interaction of turbulence with suppressant agents or fuel-side boundary phenomena in a practical fire context.

This research responds to that need by introducing a novel burner configuration developed at the University of Sydney. The University of Sydney (USYD) Burner has been designed to complement existing benchmarks by enabling the study of buoyant turbulent flame dynamics and suppression mechanisms in a setting where turbulence intensity can be systematically varied via a recessed perforated plate. Furthermore, the burner geometry is optimised to support high-fidelity diagnostics and boundary characterisation, facilitating detailed investigations into flame-suppressant interactions across a range of injection strategies.

In doing so, this study contributes to the broader fire modelling community by offering an intermediate reference case that balances the rigour of canonical configurations with the complexity needed for realistic suppression studies. It represents a methodological extension of existing efforts and aims to bridge the gap between highly idealised laboratory flames and the nuanced conditions encountered in real fire protection applications.

8.3 Benchmarking with Sandia Flame D

To ensure the reliability of the numerical methods used in this study, the simulation framework was initially applied to Sandia Flame D. This well-established benchmark flame was modelled using ReactingFoam, employing the Partially Stirred Reactor (PaSR) model for combustion and a k–epsilon turbulence model. The simulation results captured key flame characteristics including axial temperature decay, velocity profiles, and scalar mixing behaviour.

The alignment of the simulation outputs with published experimental data confirmed that the chosen solver and boundary setup were suitable for capturing the general features of non-premixed turbulent combustion. However, this exercise also highlighted the limitations of RANS-based turbulence modelling, particularly in its inability to resolve transient flow features and localised instabilities common in buoyant flames. This realisation informed the transition to a more advanced turbulence modelling approach using Large Eddy Simulation, which was applied in subsequent chapters.

The benchmarking phase was essential for two reasons. First, it demonstrated that the simulation methodology was capable of producing physically meaningful results under controlled conditions. Second, it provided a validated baseline from which more complex simulations of the USYD Burner could be developed and compared.

8.4 Characterising Turbulence with the USYD Burner

Following the benchmark validation, the USYD Burner was simulated using ANSYS Fluent to examine the impact of its perforated plate design. Simulations were carried out at two heat release rates, 20 kW and 40 kW, to investigate how varying thermal intensity affected flow development and turbulence generation.

In the absence of the perforated plate, the flow exhibited a classic parabolic profile, indicating a stable and predominantly laminar regime. The addition of the plate, however, introduced multiple zones of shear and recirculation, driven by high-velocity jets emerging from the 1 mm

perforations. This change was most pronounced near the burner outlet, where radial spreading and elevated RMS velocity were observed. These results aligned with experimental measurements and provided clear evidence that the plate was effectively enhancing turbulence in a controlled manner.

The ability to modulate turbulence through burner geometry is particularly important in fire research. It allows for the controlled study of flame response to shear, mixing, and instability. The USYD Burner thus offers a platform that not only supports combustion studies under well-defined conditions but also enables reproducible experimentation in suppression performance under varying flow dynamics.

8.5 LES-Based Simulation of the USYD Burner

To further refine the analysis of turbulent flame behaviour, Chapter 6 employed Large Eddy Simulation using the FireFOAM solver. LES allowed for the resolution of large-scale eddies that dominate energy transfer and entrainment in buoyant flames. The inclusion of radiation modelling through the discrete ordinate's method and combustion modelling via the eddy dissipation approach ensured that the simulation accounted for the dominant physical processes.

The results captured the evolution of the flame from the base upward, showing a clear transition from a momentum-driven jet to a buoyancy-dominated plume. The inclusion of the perforated plate created localised instabilities and enhanced mixing, resulting in a broader flame structure and increased flame height. These features were consistent with experimental visualisations and validated Fluent simulations.

Species concentration profiles further supported the model's accuracy, with clear trends in oxygen depletion and carbon dioxide formation along the axial flame path. These outputs confirmed that the flame was evolving in a physically realistic manner and that the USYD Burner configuration was facilitating rich turbulence and chemistry interactions.

While the LES-based simulation of the USYD Burner has yielded detailed insights into the dynamics of turbulent buoyant diffusion flames, the numerical modelling approach was subject to several simplifications to ensure computational feasibility. These included the use of a one-equation eddy viscosity model for turbulence, which, although computationally efficient, may not fully resolve smaller-scale interactions. Similarly, a simplified radiation model was adopted to reduce simulation time, which may underestimate radiative losses in certain flame regions. Furthermore, the evaporation of suppressant droplets and soot formation processes were not included in this stage of the modelling, due to the absence of corresponding experimental validation data.

Future work should seek to address these limitations by incorporating advanced sub-grid scale models for turbulence and combustion, and by integrating droplet evaporation and radiation feedback mechanisms with higher fidelity. Incorporating soot modelling and exploring the influence of chemical additives would also enhance the representation of real fire scenarios. Experimental measurements using advanced diagnostics, such as OH-PLIF and Mie scattering, will be critical for validating these extended models. Additionally, expanding the domain vertically may allow further study of flame tip behaviour and interactions with suppressant spray, thereby supporting a more comprehensive characterisation of suppression efficiency in turbulent buoyant flames.

8.6 Suppression Modelling and the Influence of Injection Strategy

Building on the established flame model, Chapter 7 explored mist-based fire suppression using both top and bottom injection strategies. The simulations were carried out using the same FireFOAM solver, and aimed to evaluate how injection direction, droplet size distribution, and flow rate affected flame cooling and extinction.

Top injection involved the release of droplets from above the flame, requiring the mist to traverse the full height of the flame column before reaching the combustion core. This configuration mimics real-world applications such as overhead sprinklers or ceiling-mounted suppression systems. In contrast, bottom injection introduced droplets directly into the base of the flame, where the temperature is highest, and combustion is most intense. This scenario simulates nozzle placements near fuel sources or floor-based systems.

The results highlighted that suppression performance is sensitive to both injection direction and the physical characteristics of the mist. In the case of top injection, the droplets encountered significant heat and turbulence during their descent, which often led to premature evaporation. This reduced the number of droplets that reached the lower flame zones, delaying the suppression response. However, when injected at sufficiently high rates, top injection achieved uniform mist coverage and ultimately led to full suppression. The suppression effect was evident in both flame collapse and the reduction of peak temperatures.

Bottom injection, by contrast, produced a more immediate response. The droplets penetrated the combustion zone with minimal delay and contributed to strong cooling and flame disturbance near the fuel source. This led to a more rapid drop in temperature, particularly in the early stages of suppression. The direct interaction with the high-temperature core also facilitated increased steam generation, which displaced oxygen and further inhibited combustion.

The study also explored the effect of mass flow rate. Simulations showed that higher injected mass led to a denser mist field, increased evaporation, and a more rapid decline in flame temperature. At 0.01 kg of total mass injection, the model captured full suppression with significant steam formation and oxygen displacement. Lower mass cases, such as 0.002 kg and 0.001 kg, resulted in partial or negligible suppression. These findings indicate that suppression efficiency is not only a function of geometry and orientation, but also critically depends on the rate of droplet introduction and their ability to survive evaporation an route to the combustion zone.

Furthermore, the comparison between different injection rates revealed that the relationship between mist density and suppression is nonlinear. There exists a threshold below which suppression becomes ineffective due to insufficient cooling and oxygen displacement. Conversely, excessively high droplet concentrations may lead to oversaturation, where droplets coalesce or fall out of the flame zone before complete evaporation, limiting the effectiveness of heat extraction.

In conclusion, the suppression simulations demonstrated that mist-based fire control strategies must be tuned to the flame characteristics, turbulence levels, and droplet behaviour specific to the fire environment. The results from the USYD Burner showed that geometry-induced turbulence plays a critical role in determining droplet dispersion and flame interaction, and that suppression effectiveness can be significantly enhanced by aligning injection strategy with the flame structure.

8.7 Integration and Reflections

Taken together, the findings of this study represent a coherent progression from model validation to complex flame visualisation and suppression evaluation. The introduction of the USYD Burner offers a novel configuration that supports enhanced turbulence and structured suppression testing. The combined use of ANSYS Fluent and FireFOAM allowed for the calibration and cross-verification of results, while the transition from RANS to LES improved the resolution of flame–turbulence interactions.

The work demonstrates that fire suppression cannot be meaningfully studied without also understanding the underlying flame dynamics. Mist suppression performance is not solely a function of droplet characteristics, but also of how the flame structure is shaped by turbulence and buoyancy. This thesis contributes to that integrated understanding and provides a framework for future studies in fire suppression modelling.

8.8 Transition to Chapter 9: Conclusion, Limitations and Future Works

This discussion has examined the key outcomes of the thesis, highlighting the interplay between turbulence generation, flame evolution, and suppression performance. Through the development and implementation of the USYD Burner, this research has introduced a novel platform for studying buoyant diffusion flames under controlled turbulence and suppression configurations. The numerical simulations carried out using both FireFOAM and Fluent have demonstrated the capability of current CFD tools to replicate key aspects of flame behaviour and suppression dynamics when benchmarked against experimental observations.

Despite these advancements, several limitations must be acknowledged. The modelling approach relied on simplified combustion and radiation models to maintain computational efficiency. While suitable for a comparative and parametric study, these simplifications may constrain the model's accuracy in representing complex chemical kinetics, soot formation, or near-wall heat transfer. Additionally, the suppression scenarios examined in this thesis did not

include the chemical kinetics of inhibitor species, which are known to play a critical role in flame extinction. Experimental validation was limited to select parameters, and further work is required to improve model calibration across more varied operating conditions and suppressant configurations.

These limitations underline the need for further refinement in both the modelling framework and experimental setup. Future studies should explore enhanced turbulence and radiation models, include droplet chemistry and phase-change dynamics, and expand the use of high-resolution diagnostics to capture unsteady behaviours at the flame-droplet interface.

The final chapter will present a synthesis of the research contributions and their implications for fire safety engineering. It will also identify specific research opportunities that can build on this foundational work, particularly in enhancing model fidelity and extending the application of suppression simulations to more complex and realistic fire scenarios.

9 Conclusion, Limitations and Future Works

This thesis has presented a comprehensive study of turbulent buoyant diffusion flames and their suppression using numerical techniques. By developing and utilising the USYD Burner, the research introduced a novel, controllable experimental platform that enabled the systematic study of turbulence, combustion, and fire suppression. Computational models were implemented using FireFOAM and Fluent, with results benchmarked against experimental datasets to ensure physical realism and validate numerical performance. The work contributes to the field of fire safety engineering by enhancing the understanding of complex flame structures, fuel-side turbulence effects, and the dynamics of water mist and chemically enhanced suppression.

9.1 Primary findings

The recessed perforated plate burner configuration can generate enhanced turbulence levels, altering both velocity profiles and flame structure.

Large Eddy Simulation (LES) effectively captured the transition from jet-driven to buoyancy-dominated flow, and provided high-fidelity insights into flame height, species concentration profiles, and velocity distributions.

Water suppression was shown to depend critically on injection orientation, droplet size distribution, and injection mass rate, with bottom injection yielding faster and more effective cooling.

9.2 Limitations

Several limitations were inherent to the current study:

Model Simplification: The combustion model used was based on the eddy dissipation concept, which assumes infinitely fast chemistry and ignores intermediate radical reactions. This approach, while computationally efficient, limits the representation of flame extinction mechanisms involving chemical inhibition.

Radiation Treatment: Radiation modelling was simplified using the finite volume discrete ordinates method (fvDOM), which neglects wavelength dependence and may underestimate radiative heat losses in regions with high soot concentrations.

Soot and Species Tracking: Soot formation, oxidation, and transport were not explicitly resolved, which is a significant limitation when evaluating radiative feedback and near-wall heat transfer. Similarly, detailed species transport of chemical inhibitors was not included.

Droplet Interaction Physics: The evaporation model was simplified using classical Sherwood and Nusselt correlations, which assume quasi-steady heat and mass transfer. These models do not account for transient droplet heating, break-up, or coalescence.

Experimental Resolution: Although advanced diagnostics like OH-PLIF and PDA were used, the experimental measurements were spatially limited, and some boundary conditions had to be inferred, reducing the fidelity of model validation.

9.2.1 Representativeness of the USYD Burner Configuration:

While the USYD Burner offers a well-controlled platform for investigating turbulent buoyant flames and mist suppression, it differs from typical real-scale fires such as pool fires in several important ways. These differences include the use of forced fuel jets (as opposed to self-regulated surface vaporisation), enhanced turbulence generation via perforated plates

(absent in most real fires), and the lack of a feedback loop between flame radiation and fuel mass-loss rate. The Table 7.15 below summarises the key distinctions:

Feature	USYD Burner	Real Buoyant Fire (e.g., Pool Fire)
Fuel delivery	Controlled jet flow (CNG)	Surface vaporisation (e.g., liquid fuels)
Turbulence source	Forced turbulence via perforated plate	Natural buoyancy and feedback instabilities
Flame anchoring	Fixed burner location	Free-standing or moving flame base
Fuel self-regulation	Absent (constant flow rate)	Present via heat feedback and vaporisation
Stability mechanisms	Mechanically imposed	Thermally and radiatively driven

Table 7.15 Comparison of the USYD Burner Configuration and Typical Real-World Buoyant Fires

These differences are acknowledged as part of the modelling scope. The goal of this study is not to replicate uncontrolled fire scenarios but to develop a validated, repeatable platform for studying turbulence-flame interactions and suppression behaviour under quantifiable and adjustable conditions. This allows the identification of critical suppression thresholds, flame instabilities, and performance trends, offering insights that can later be extended to more complex fire environments.

9.3 Future Work

To overcome these limitations and extend the capabilities of the developed models, the following directions are proposed:

High-Fidelity Chemical Modelling: Future studies should implement detailed chemical kinetics models, including radical transport and flame extinction criteria such as local Damköhler numbers and species-based suppression thresholds. These models will be computationally expensive and should be executed on high-performance computing (HPC) platforms.

Coupled Soot and Radiation Models: Integrating soot generation and oxidation models with wavelength-dependent spectral radiation models will allow for more accurate radiative heat loss calculations. This is essential for studying flame quenching, especially in smoke-laden environments.

Transient Droplet Dynamics: Incorporate droplet collision, coalescence, and break-up models to evaluate the interaction between mist and turbulent flow fields. This will enable better representation of evaporation efficiency and local cooling rates.

Advanced Supercomputing Applications: Future simulations should use dedicated supercomputing clusters to run coupled LES-combustion-radiation-suppression models at ultra-fine resolutions. This will allow for full-scale simulation of complex fire scenarios and better capture of unsteady dynamics.

Extended Validation Campaigns: Develop new experiments with fully resolved boundary conditions and expanded measurement grids, including multiple planar imaging techniques and high-speed imaging to resolve flame-droplet-radical interactions.

By addressing these areas, future work will not only improve the predictive accuracy of fire suppression models but also contribute to the broader goal of developing efficient, scalable, and environmentally responsible fire protection systems.

Velocity Distribution Analysis: Future work should employ HPC platforms to enable stable and high-resolution post-processing of droplet velocity fields. This will support deeper insights into momentum transfer, deceleration, and the role of mist dynamics during suppression.

References

1. *Sandia/TUD Piloted CH4/Air Jet Flames*. Available from: https://tnfworkshop.org/data-archives/pilotedjet/ch4-air/.
2. Barlow, R., *Piloted CH4/Air Flames C, D, E, and F – Release 2.1* 15-JUN-2007.
3. Xiao, T., et al., *On the structure of buoyant fires with varying levels of fuel-turbulence.* Combustion and Flame, 2023. **257**: p. 112993.
4. Barlow, R., et al., *Piloted methane/air jet flames: Transport effects and aspects of scalar structure.* Combustion and flame, 2005. **143**(4): p. 433-449.
5. Drysdale, D., *An Introduction to Fire Dynamics*. 3rd ed. 2011, Somerset: Wiley.
6. Quintiere, J.G., *Fundamentals of fire phenomena*. 2006, Chichester, England: John Wiley.
7. Martin, D., M. Tomida, and B. Meacham, *Environmental impact of fire.* Fire science reviews, 2016. **5**(1): p. 1.
8. Karlsson, B. and J. Quintiere, *Enclosure fire dynamics*. 1999: CRC press.
9. de Ris, J.L., *Mechanism of buoyant turbulent diffusion flames.* Procedia Engineering, 2013. **62**: p. 13-27.
10. Runchal, A.K., *The future of CFD and the CFD of the future.* Computational Thermal Sciences: An International Journal, 2012. **4**(6).
11. *History of IAFSS*. Available from: https://iafss.org/history/.
12. *OpenFOAM*. Available from: https://www.openfoam.com/.
13. Cote, A.E. and J.L. Linville, *Fire protection handbook*. 18th ed. NFPA ; FPH 1897. 1997, Quincy, Mass: National Fire Protection Association.
14. *SFPE handbook of fire protection engineering.* National Fire Protection Association.; Society of Fire Protection Engineers.
15. Wen, J.X. and L.Y. Huang, *CFD modelling of confined jet fires under ventilation-controlled conditions.* Fire safety journal, 2000. **34**(1): p. 1-24.
16. Barber, D.H.a.R., *Performance-Based Fire Safety Design, CRC Press and SFPE, Boca Raton, 2015.* 2015.
17. *Fire modeling programs*. Available from: https://www.nist.gov/el/fire-research-division-73300/fire-modeling-programs.
18. *National Institute of Standards and Technology (NIST)*. 2005; Available from: https://www.nist.gov/system/files/documents/2017/12/20/formatted_nist_open_government_plan_2016_final.pdf.
19. Bittern, A., *Analysis of FDS predicted sprinkler activation times with experiments.* 2004.
20. *Measurement & Computation of Fire Phenomena (MaCFP Working Group)*. Available from: https://iafss.org/macfp/.
21. *GitHub*. Available from: (https://github.com/MaCFP).
22. McCaffrey, B.J., *Momentum implications for buoyant diffusion flames.* Combustion and Flame, 1983. **52**: p. 149-167.
23. MCCAFFREY, B., *Purely buoyant diffusion flames: some experimental results, National Bureau of Standards (USA).* NBSIR 79-1910, 1979.
24. *FireFOAM* Available from: https://code.google.com/archive/p/firefoam-dev/.
25. *FM Global: Open source fire modeling*. Available from: https://www.fm.com/about-us/our-engineering-approach/engineering-methods/open-source-fire-modeling.
26. Wang, Y., et al., *Numerical simulation of sprinkler suppression of rack storage fires.* Fire Safety Science, 2014. **11**: p. 1170-1183.
27. *Fighting fire with FireFOAM*. Available from: https://phys.org/news/2016-01-firefoam.html#:~:text=match%20at%20L191%20cores%20was,Wang%27s.

28. *National Institute of Standards and Technology (NIST)*. 2005: National Institute of Standards and Technology (NIST).
29. Wang, Y., P. Chatterjee, and J.L. de Ris, *Large eddy simulation of fire plumes.* Proceedings of the Combustion Institute, 2011. **33**(2): p. 2473-2480.
30. *FireFOAM*. Available from: https://www.openfoam.com/documentation/guides/v2112/doc/guide-applications-solvers-combustion-fireFoam.html.
31. *ORNL's Titan supercompute*. Available from: https://www.ornl.gov/blog/farewell-titan.
32. *High Performance Computing Facility,Operational Assessment 2015 NIST.* National Research Council, 2015.
33. Wang, Y., *CFD-Modeling-of-Industrial-Scale-Fires-using-HPC-Yi-Want.* FM Global, 2016.
34. *RISE Research* Available from: https://www.ri.se/en.
35. *RISE Fire*. Available from: https://risefr.com/about-rise-fire-research.
36. Ying Zhen Li, C.H., Johan Anderson, Robert Svensson, *Verification, validation and evaluation of FireFOAM as a tool for performance design.*
37. Brown, A., et al., *Proceedings of the first workshop organized by the IAFSS Working Group on Measurement and Computation of Fire Phenomena (MaCFP).* Fire safety journal, 2018. **101**: p. 1-17.
38. Ahmed, M.M. and A. Trouvé, *Large eddy simulation of the unstable flame structure and gas-to-liquid thermal feedback in a medium-scale methanol pool fire.* Combustion and Flame, 2021. **225**: p. 237-254.
39. Xu, R., et al., *Simulations of the coupling between combustion and radiation in a turbulent line fire using an unsteady flamelet model.* Fire Safety Journal, 2021. **120**: p. 103101.
40. Desai, A., S. Goodrick, and T. Banerjee, *Investigating the turbulent dynamics of small-scale surface fires.* Scientific reports, 2022. **12**(1): p. 10503.
41. Vilfayeau, S., et al., *Large eddy simulation of suppression of turbulent line fires by base-injected water mist.* Proceedings of the Combustion Institute, 2017. **36**(2): p. 3287-3295.
42. Poinsot, T. and D. Veynante, *Theoretical and numerical combustion*. 2nd ed. 2005, Philadelphia: Edwards.
43. Spalding, D. *Mixing and chemical reaction in steady confined turbulent flames*. in *Symposium (International) on combustion*. 1971. Elsevier.
44. Heskestad, G., *Luminous heights of turbulent diffusion flames.* Fire safety journal, 1983. **5**(2): p. 103-108.
45. Grant, G., J. Brenton, and D. Drysdale, *Fire suppression by water sprays.* Progress in energy and combustion science, 2000. **26**(2): p. 79-130.
46. Chao, B., C.K. Law, and J. T'ien. *Structure and extinction of diffusion flames with flame radiation*. in *Symposium (international) on combustion*. 1991. Elsevier.
47. Verma, S., et al., *Measured and simulated temperature statistics in a buoyancy-driven turbulent line fire.* 2017.
48. Ashgriz, N. and J. Mostaghimi, *An introduction to computational fluid dynamics.* Fluid flow handbook, 2002. **1**: p. 1-49.
49. Barlow, R.S., *EFFECTS OF TURBULENCE ON SPECIES MASS FRACTIONS IN METHANE/AIR JET FLAMES.* 1998.
50. Heskestad, G., *Scaling the interaction of water sprays and flames.* Fire safety journal, 2002. **37**(6): p. 535-548.
51. Yamashita, K., S. Karnani, and D. Dunn-Rankin, *Numerical prediction of ion current from a small methane jet flame.* Combustion and Flame, 2009. **156**(6): p. 1227-1233.

52. Smooke, M., I. Puri, and K. Seshadri. *A comparison between numerical calculations and experimental measurements of the structure of a counterflow diffusion flame burning diluted methane in diluted air*. in *Symposium (International) on Combustion*. 1988. Elsevier.
53. Jones, R.D.P.G.P.F.P.R.R.P.W.W., *Experimental Measurements of Heat and Mass Transfer from a Turbulent Diffusion Flame to a Vertical Wall.* CFAST, 1992.
54. *Sandia National Laboratories.*; Available from: https://www.sandia.gov/.
55. Davis, R., et al., *A numerical/experimental study of the dynamic structure of a buoyant jet diffusion flame.* Theoretical and Computational Fluid Dynamics, 1994. **6**: p. 113-123.
56. Reuter, C.B., S.H. Won, and Y. Ju, *Experimental study of the dynamics and structure of self-sustaining premixed cool flames using a counterflow burner.* Combustion and Flame, 2016. **166**: p. 125-132.
57. Masri, A.R., P.A. Kalt, and R.S. Barlow, *The compositional structure of swirl-stabilised turbulent nonpremixed flames.* Combustion and Flame, 2004. **137**(1-2): p. 1-37.
58. Duny, M., et al. *Experimental study on vertical fire spread along a wooden façade*. in *MATEC web of conferences*. 2016. EDP Sciences.
59. Lam, C.S. and E.J. Weckman, *Wind-blown pool fire, Part I: Experimental characterization of the thermal field.* Fire Safety Journal, 2015. **75**: p. 1-13.
60. Lam, C.S. and E.J. Weckman, *Wind-blown pool fire, Part II: Comparison of measured flame geometry with semi-empirical correlations.* Fire Safety Journal, 2015. **78**: p. 130-141.
61. DiDomizio, M.J. and E.J. Weckman, *An evaluation of methodologies for determining delay times in the cone calorimeter fire test.* Journal of Testing and Evaluation, 2016. **44**(3): p. 1050-1063.
62. Cox, G., *The challenge of fire modelling.* Fire Safety Journal, 1994. **23**(2): p. 123-132.
63. Karlsson, B. and S. Magnusson, *Combustible wall lining materials: Numerical simulation of room fire growth and the outline of a reliability based classification procedure*, in *Fire Safety Science*. 1991, Routledge. p. 667-678.
64. Novozhilov, V., *Computational fluid dynamics modeling of compartment fires.* Progress in Energy and Combustion science, 2001. **27**(6): p. 611-666.
65. McGrattan, K.B., et al., *Fire dynamics simulator--Technical reference guide*. 2000: National Institute of Standards and Technology, Building and Fire Research ….
66. Trouvé, A.; Available from: https://fpe.umd.edu/clark/faculty/601/Arnaud-Trouv%C3%A9.
67. Trouvé, A. *Cfd modeling of large-scale pool fires*. in *The Second International Energy 2030 Conference, Abu Dhabi, UAE*. 2008.
68. Tavelli, S., et al., *Numerical analysis of pool fire consequences in confined environments.* Chemical Engineering, 2013. **31**.
69. Wang, Y., et al., *Numerical and experimental validation study of flame extent of a pool fire under the ceiling.* Journal of Loss Prevention in the Process Industries, 2017. **49**: p. 652-659.
70. Pio, G., et al., *Numerical simulation of small-scale pool fires of LNG.* Journal of Loss Prevention in the Process Industries, 2019. **61**: p. 82-88.
71. Trouve, A. and Y. Wang, *Large eddy simulation of compartment fires.* International Journal of Computational Fluid Dynamics, 2010. **24**(10): p. 449-466.
72. Ren, N., Y. Wang, and A. Trouvé, *Large eddy simulation of vertical turbulent wall fires.* Procedia engineering, 2013. **62**: p. 443-452.
73. Meredith, K., et al., *A comprehensive model for simulating the interaction of water with solid surfaces in fire suppression environments.* Proceedings of the Combustion Institute, 2013. **34**(2): p. 2719-2726.

74. Vilfayeau, S., et al., *Large eddy simulation of flame extinction in a turbulent line fire exposed to air-nitrogen co-flow.* Fire Safety Journal, 2016. **86**: p. 16-31.
75. Camilo Andrés, S., et al., *Prediction of a Small-Scale Pool Fire with FireFoam.* International Journal of Chemical Engineering, 2017. **2017**.
76. Le, D., et al., *Assessment of the capabilities of FireFOAM to model large-scale fires in a well-confined and mechanically ventilated multi-compartment structure.* Journal of fire sciences, 2018. **36**(1): p. 3-29.
77. Abdalhamid, A.M., C. Devaud, and E. Weckman, *Large Eddy Simulations of a Medium-Scale Ethanol Pool Fire Using Conditional Source-Term Estimation Including Coupled Soot Radiation Effects.* Combustion Science and Technology, 2025: p. 1-29.
78. Kim, S.C. and H.S. Ryou, *An experimental and numerical study on fire suppression using a water mist in an enclosure.* Building and Environment, 2003. **38**(11): p. 1309-1316.
79. Street, J.H.F.M.P.R.L., *Computational Methods for Fluid Dynamics.* 2002.
80. Anderson, J.D., *Governing Equations of Fluid Dynamics*, in *Computational Fluid Dynamics*, J.F. Wendt, Editor. 2009, Springer Berlin Heidelberg: Berlin, Heidelberg. p. 15-51.
81. Versteeg, H.K., *An introduction to computational fluid dynamics the finite volume method, 2/E*. 2007: Pearson Education India.
82. Patankar, S., *Numerical heat transfer and fluid flow*. 2018: CRC press.
83. Biswas, G. and V. Eswaran, *Turbulent flows: fundamentals, experiments and modeling*. 2002: CRC Press.
84. Kadar, A.H., *Modelling turbulent non-premixed combustion in industrial furnaces*. 2015.
85. guide., O.U., *OpenFOAM: User guide.*
86. Wang, A.T.a.Y., *Large eddy simulation of compartment fires.* 2010.
87. Ken-ichi Abe, T.O., *An investigation of LES and Hybrid LES/RANS models for predicting 3-D diffuser flow.* 2010.
88. Zoheb Khan, J.B.J., *Comparison of k–ε, RSM and LES models for the prediction of flow pattern in jet loop reactor.* 2015.
89. Ren, N., Wang, Y., *Large Eddy Simulation of Turbulent Wall Fires.* 2013.
90. Magnussen, B.F. and B.H. Hjertager. *On mathematical modeling of turbulent combustion with special emphasis on soot formation and combustion*. in *Symposium (international) on Combustion*. 1977. Elsevier.
91. Lia, Z., *Finite-rate chemistry modelling of non-conventional combustion regimes.*
92. Wellons, M., *The Stefan-Boltzmann Law.* 2007.
93. J.C.CHAI, *Handbook of Numerical Heat Transfer - 2000 - Minkowycz - Discrete-Ordinates and Finite-Volume Methods for Radiative Heat.*
94. Subramaniam, S., *Lagrangian-Eulerian methods for multiphases-Suppression modelling.* 2013.
95. Çengel, Y.A. and A.J. Ghajar, *Heat and mass transfer : fundamentals & applications / Yunus A. Çengel, Afshin J. Ghajar*. 4th ed. 2011, New York: McGraw-Hill.
96. Ho¨ hne, T., S.r. Kliem, and R. Vaibar. *Experimental and numerical modeling of transition matrix from momentum to buoyancy-driven flow in a pressurized water reactor*. in *International Conference on Nuclear Engineering*. 2008.
97. Wu, Y., *The Critical Velocity and the Fire Development-page 408.* 2010.
98. Li, J., et al., *Numerical prediction of combustion instability limit cycle oscillations for a combustor with a long flame.* Combustion and Flame, 2017. **185**: p. 28-43.
99. Barlow, R.S. and J.H. Frank. *Effects of turbulence on species mass fractions in methane/air jet flames*. in *Symposium (international) on combustion*. 1998. Elsevier.

100. Barlow, o.S. *The third International Workshop on Measurement and Computation of Turbulent Nonpremixed Flames*. 1998; Available from: https://tnfworkshop.org/wp-content/uploads/2019/01/TNF3_Proceedings.pdf.
101. Nguyen, Q.V., et al., *Raman-LIF measurements of temperature, major species, OH, and NO in a methane-air bunsen flame.* Combustion and flame, 1996. **105**(4): p. 499-510.
102. Lysenko, D.A., I.S. Ertesvåg, and K.E. Rian, *Numerical simulations of the sandia flame d using the eddy dissipation concept.* Flow, turbulence and combustion, 2014. **93**(4): p. 665-687.
103. Veynante, D. and L. Vervisch, *Turbulent combustion modeling.* Progress in energy and combustion science, 2002. **28**(3): p. 193-266.
104. Launder, B.E., & Spalding, D. B., *The Numerical Computation of Turbulent Flows. Computer Methods in Applied Mechanics and Engineering, 3(2), 269–289.* 1974.
105. Delić, F., *Three-dimensional numerical simulation of combustion in a jet engine combustion chamber*. 2019, Fakultet strojarstva i brodogradnje.
106. Chomiak, J., *Combustion: a study in theory, fact and application.* 1987.
107. Nordin, P.N., *Complex chemistry modeling of diesel spray combustion*. Vol. 18. 2001: Chalmers University of Technology Sweden.
108. Pang, K.M., *Development and validation of a local time stepping-based PaSR solver for combustion and radiation modeling.* 2013.
109. *GRI-Mech 3.0 Source Files.*; Available from: http://combustion.berkeley.edu/gri-mech/version30/text30.html.
110. Meares, S. and A.R. Masri, *A modified piloted burner for stabilizing turbulent flames of inhomogeneous mixtures.* Combustion and flame, 2014. **161**(2): p. 484-495.
111. Delichatsios, M., *Transition from momentum to buoyancy-controlled turbulent jet diffusion flames and flame height relationships.* Combustion and Flame, 1993. **92**(4): p. 349-364.
112. Xiao, T., *The Dynamics of Buoyant Fires and their Suppression with Chemically Enhanced Water Mist*. 2025.
113. OpenFOAM. *OpenFOAM*. Available from: https://cpp.openfoam.org/v11/.
114. OpenFOAM. *OpenFOAM* Available from: https://openfoam.org/.
115. Hrvoje, J., *Error analysis and estimation for the finite volume method with applications to fluid flows.* Imperial College: London, UK, 1996.
116. White, J., et al., *Radiative emissions measurements from a buoyant, turbulent line flame under oxidizer-dilution quenching conditions.* Fire Safety Journal, 2015. **76**: p. 74-84.
117. Ouyang, Y., et al., *Numerical study of hydrogen/methane buoyant fires using FireFoam.* International Journal of Hydrogen Energy, 2020. **45**(24): p. 13551-13558.
118. Zhang, Y., et al., *Surface inclination effects on heat transfer during flame spread acceleration based on FireFOAM.* Case Studies in Thermal Engineering, 2022. **32**: p. 101905.
119. McGRATTAN, K., *Fire Modeling: Where Are We? Where Are We Going?* . Fire Safety Science, 2005. **8**: p. 53-68.
120. Huang, C., *Numerical Modelling of Fuel Injection and Stratified Turbulent Combustion in a Direct-Injection Spark-Ignition Engine Using an Open Source Code.*, in

2014.
121. Law, C.K., *Combustion Physics*. 1 ed. 2006, Cambridge: Cambridge University Press.
122. Hewson, J.C., *CFD MODELING OF FIRE SUPPRESSION AND ITS ROLE IN OPTIMIZING SUPPRESSANT DISTRIBUTION.* 2003.
123. Vilfayeau, S., *Numerical simulation of under-ventilated liquid-fueled compartment fires with flame extinction and thermally-driven fuel evaporation.*

124. TROUVÉ, V.R.L.P.N.H.R.B.A., *Local Extinction of Diffusion Flames in Fires.* FIRE SAFETY SCIENCE-PROCEEDINGS OF THE TENTH INTERNATIONAL SYMPOSIUM, 2011: p. 583-596.
125. Vilfayeau, S., et al., *Large eddy simulation of flame extinction in a turbulent line fire exposed to air-nitrogen co-flow.* Fire Safety Journal, 2016. **86**: p. 16-31.
126. Yu. Snegirev, A., *Perfectly stirred reactor model to evaluate extinction of diffusion flame.* Combustion and flame, 2015. **162**(10): p. 3622-3631.
127. Paraview. Paraview; Available from: https://www.paraview.org/.